# DESIGN AND ANALYSIS OF A STAGED COMBUSTOR FEATURING A PREMIXED TRANSVERSE REACTING FUEL JET INJECTED INTO A VITIATED CONFINED CROSSFLOW

by

**Oluwatobi Busari**

**A Dissertation**

*Submitted to the Faculty of Purdue University*

*In Partial Fulfillment of the Requirements for the degree of*

**Doctor of Philosophy**


School of Aeronautics and Astronautics

West Lafayette, Indiana

May 2021

# THE PURDUE UNIVERSITY GRADUATE SCHOOL
# STATEMENT OF COMMITTEE APPROVAL

**Dr. Robert P. Lucht, Chair**

School of Mechanical Engineering

**Dr. Steven Heister**

School of Aeronautics and Astronautics

**Dr. Timothee Pourpoint**

School of Aeronautics and Astronautics

**Dr. Gregory Blaisdell**

School of Aeronautics and Astronautics

**Approved by:**

Dr. Gregory Blaisdell

Dedicated to my mum, she would have loved to see it with her feet on the ground. I hope you get the best seat up there! To my dad, who listened to me as I grew up and taught me to be generous.

# ACKNOWLEDGMENTS

I thank my advisor professor Robert Lucht who chose me to run the Siemens rig and funded my graduate career at Purdue. It had its ups and downs but you never gave up. I thank God most of all for loving me well, I never thought I would see the day I turned in my dissertation. Thanks Scott Meyer, for teaching me aerospace engineering. There were many design reviews, many visits to your office revisiting designs, capturing lesson learned or discussing paths forward. I thank my committee; professor Gregory Blaisdell for his thorough and accurate review of my fluid dynamics inferences, professor Timothee Pourpoint for his attention to detail and uncertainty quantification and professor Steven Heister for his insightful questions. Thanks Rob McGuire for working magic to my hand made drawings.

I thank my friends who stuck with me through thick and thin, an unfinished list including Hannah and Josh, Elisabeth and Horane, Marquetta, Jaron, Eboni, Henry, Derrick, Jerica and Olatunji, Thembi, Danae, Evidence and Jessi, Ibukun, Michael, Naveen, Femi, Moses, Tiffany, Marlou, Jeremy.

I thank my colleagues Dr. Pratikash Panda, Yibiao Ying, Dr. Neil Rodrigues, Michael Arendt, William Senior, Colin McDonald you guys taught me most of the things I hoped to teach you. Andrew Pratt, Dr. Rohan Gejji, Dr. Robert Zhang and professor Carson Slabaugh are few individuals whose doors remained open when I needed technical guidance, from preparing for my quals to diagnosing data system problems. Zucrow students and staff have also been there to help make purchases, lift heavy hardware, drive me to the hospital, celebrate my wins, or join in technical banter through which many ideas were clarified and techniques were gained.

To my family Damisi, Subomi, Aunt Kike, Uncle Remi, Doyin, Dunni, Funto, Kosi, you prayed with me, sang with me cried for me and laughed at my jokes ... you loved me well. All the joys of our times together will only increase.

This work was sponsored in large part by Siemens Energy. I appreciate all the effort and time from Ray Laster, Andrew North, Yuntao Chen, Melanie Abou-Jaoude and the other personnel at Siemens Energy Florida.

# PREFACE

Combustion phenomena are complex in theory and expensive to test, analysis techniques provide handles with which we may describe them. Just as simultaneous experimental techniques provide complementary descriptions of flame behavior, one might assume that no analysis technique for any kind of flame measurement would cover the full description of the flame. To this end, the search continues for complementary descriptions of engineering flames that capture enough information for the engine designer to make informed decisions. The kinds of flames I have encountered are high pressure transverse jet flames issuing into a vitiated crossflow which is itself generated from combustion of a gaseous fuel and oxidizer. Summarizing the behavior of these flames has required my understanding of experimental techniques such as Planar Laser Induced Fluorescence of a reaction intermediate -OH, Particle Image Velocimetry of a passive tracer in the flame and $OH^*$ chemiluminescence of another reaction intermediate. The analysis tools applied to these measurements must reveal as much information as is laden in these measurements.

In this work I have also used wavelet optical flow to track flow features in the visualization of combustion intermediates using $OH^*$ chemiluminescence. There are many limitations to the application of this technique to engineering flames especially due to the interpretation of the data as a 2-D motion field in 3-D world. The interpretation of such motion fields as generated by scalar fields is one subject matter discussed in this dissertation. Some inferences from the topology of the ensuing velocity field has provided insight to the behavior of reacting turbulent flows which appear attached to an injector in the mean field. It gives some understanding to the robustness of the attachment mechanism when such flames are located near walls.

# TABLE OF CONTENTS

# LIST OF TABLES

# LIST OF FIGURES

# LIST OF SYMBOLS

| | |
|---|---|
| $f$ | function in $L^2$ or data/reg model in variational optical flow |
| $\mathcal{F}$ | Fourier transform |
| $I$ | Intensity of image |
| $I_{\mathrm{i}}$ | First $\mathrm{i} = 0$ or second $\mathrm{i} = 1$ image of image pair |
| $\tilde{I}$ | motion compensated (warped) image used in pyramidal motion estimation |
| $J$ | Jet to crossflow momentum flux |
| $J_{data}$ | data term in variational optical flow |
| $J_{reg}$ | regularization term in variational optical flow |
| j | scale or negative exponent of resolution |
| $L^2$ | Vector space of finite energy (square integrable) signals over $\mathbb{R}$ or $[0, 1]$ |
| $m$ | mass or subscript of time-frequency atom |
| $n$ | subscript of time-frequency atom |
| $\mathcal{P}$ | projection operator - used loosely for upsampling (2 times larger) and down-sampling in images |
| $\mathbb{R}$ | field of reals often in relation to $L^2$ |
| $Re_D$ | Reynolds number based on jet diameter |
| $Re_{Dh}$ | Reynolds number based on hydraulic diameter of test section |
| $T$ | Temperature |
| $T_0$ | Total temperature |
| $\boldsymbol{v}$ | velocity |
| $\hat{\boldsymbol{v}}$ | velocity estimate |
| $\mathcal{V}$ | interrogation volume |
| $\boldsymbol{v}^{\parallel}$ | normal component of velocity with respect to image intensity gradient in variational optical flow |
| $\boldsymbol{v}^{\perp}$ | component of velocity coincident with image intensity gradient in variational optical flow |
| $w$ | window in windowed Fourier transform |
| $\mathcal{W}$ | wavelet transform |

| | |
|---|---|
| $\boldsymbol{x}$ | position typically with reference to optical flow image domain |
| $xH_2$ | mole fraction of hydrogen in fuel mixture |
| $\mathbb{Z}$ | ring of integers often in relation to tilling time-frequency spectrum |

# ABBREVIATIONS

| | |
|---|---|
| DMD | Dynamic Mode Decomposition |
| DSL | Downstream Shear Layer |
| FOV | Field of view |
| JICF | Jet in Crossflow |
| NG | Natural Gas |
| NOx | Oxides of Nitrogen |
| OH-PLIF | OH Planar Laser Induced Fluorescence |
| PIV | Particle Image Velocimetry |
| POD | Proper Orthogonal Decomposition |
| SPOD | Spectral Proper Orthogonal Decomposition |
| USL | Upstream Shear Layer |
| WOF | Wavelet Optical Flow |

# NOMENCLATURE

| | |
|---|---|
| Multiresolution analysis | Ladder of vector spaces together with closure property, unique zero intersect, a translation operation that keeps elements in the space, a dilation operation that moves elements between adjascent spaces in the ladder and a unique function called a scaling function whose dilates spans each ladder space. |
| Natural Gas | Mixture of fuel gases, mostly methane |
| Optical flow | Computer vision technique for extracting motion fields from a sequential image pair |
| Wavelet | Zero average function as defined in fourier space using filters |

# GLOSSARY

| | |
|---|---|
| Axial Stage | Secondary combustion stage, displaced downstream of primary |
| Flame | combustion event, usually as imaged |
| Wobbe Index | Ratio of higher heating value of fuel to square root of ratio of fuel density to air density $\frac{\text{HHV}}{\sqrt{\rho_{fuel}/\rho_{air}}}$ |

# ABSTRACT

In this work the images from a novel designed high subsonic Mach number combustor were analyzed using complementary techniques of OH-PLIF and OH* chemiluminescence. The analysis of internal combustion in High subsonic Mach number environments is applicable to multiple flows including the combustor discharge flow supplying the inlet guide vanes of modern stationary gas turbines. For this experimental analysis, a High subsonic combustion test rig was designed. It comprised of a head end vitiator, supplying high pressure vitiated air through a high temperature nozzle to the test section after which reaction quenching in a long mixing section provided uniform flow for emissions sampling. The High temperature nozzle design featured a regeneratively cooled and film cooled converging nozzle with vitoshinski flow profile. The survivability exceeded expectations and was the major milestone for this experimental effort. The nozzle design allowed high subsonic Mach number combustion in the test section at the high heat fluxes typical of nozzle flows. This combustor ran continuously for an average of 5 hours every test. The test section design allows secondary injection of fuel and oxidizer in a transverse fashion into the combustor. The emissions characteristics of this combustor revealed improved NOx emissions over the low subsonic Mach number behavior documented in literature.

The emissions results from the high subsonic Mach number combustion identified operating conditions for NOx abatement. To further identify why these transverse jet flames burned differently from their low subsonic counterparts motivated imaging of the spatio-tempporal behavior of the flames. Advanced imaging techniques such as kHz OH* chemiluminescence and OH-PLIF were used on these flames. Using OH-PLIF, the measurement of the transverse jet flames revealed that at the high subsonic Mach numbers for the test matrix, the fuel jet was unable to ignite in the upstream shear layer, and stabilized only in the near wake as a leeward stabilized flame, which was dependent on the subsonic boundary layer for flame attachment near the injector. Significant jet flapping in the near field was also identified. A far wake transverse jet flame was also observed, broken into flamelets that do not connect with the bottom wall of the combustor, revealing more distributed burning in the shear flow. The OH* chemiluminescence obtained at a higher repetition rate, revealed

that the dynamics of the flames in the subsonic boundary layer is largely in response to the increased strain rate field in the jet wake. In order to attach the flame at the injector, hydrogen was added to increase the reactivity of the flame. Increasing the reactivity of the fuel jet to comparatively similar chemical timescales as the flow timescales allowed the leading point of the flame to consume fuel at the injector before convection pulled the hot gasses into the jet wake for further heat release. This result also showed that any flames attached at the injector behaved similarly irrespective of the crossflow Mach number so that the flames were governed more by reactivity, with similar features in the mean field. The unattached flames were shown to be capable of attachment given sufficiently high reactivity at the same crossflow Mach number. This change in attachment was shown to have little effect on the NOx generated from these flames.

The flame displacement velocities interpreted from the $OH^*$ chemiluminescence images were quantified using a computer vision technique called optical flow. The technique allows the extraction of motion fields from a pair of scalar images, but does a better job than typical correlation algorithms used in particle displacement fields, allowing scalars to be used. Optical flow with wavelets allowed the decomposition of the velocity field into orthogonal subspaces to deal with the issue of large displacements. Imaging of the flames allowed a provides access to the motion of the flame, over the usual process which extracts flame information from the velocimetry of the underlying fluid motion. The results provided evidence that flame attachment at the wall is due to the movement of the stoichiometric surface outward for less reactive higher equivalence ratio flames.

It is expected that dulute jet flames have their stoichiometric surface closer to the shear layer where instabilities often move the flame base. It is also expected that as the convective timescales decrease in a flame, the lower reactive timescales required to reignite the flame would prove dominant as an attachment mechanism leading to autoignition stabilized flames. In this work, a test matrix was developed to compare the effects of reactivity and fuel concentration on the attachment mechanism of transverse jet flames. The low reactivity flames were the least dilute and the high reactivity flames were the most dilute. The stoichiometric sufrace did move away from the jet core as expected for the richer flames, however due to their lower reactivity, the motion of the flame base required a low timescale

ignition mechanism. For the more dilute flames, they were closer to the jet core, but their reactivity allowed consistent ignition of the flame base. This revealed reactivity as dominant for attachment over concentration.

From the motion fields from the wavelet optical flow computations, it was proposed that when the stoichiometric surface moves toward the shear layer, more rapid changes in the location of the flame base would require faster time scales for flame stabilization for the least reactive flames. Addition of low reactivity fuel into the mixture tends to move the stoichiometric surface way from the jet core, but also results in autoignition stabilized flames. For fuel rich flames, at the stoichiometric surface, the prescence of high temperature gasses and a constant source of radicals from the jet mixing with the crossflow makes it suitable for flame attachment. In addition to the flame adhering to the bottom wall, the delayed heat release of the flame due to the lower reactivity causes the flame to be more compact and heat release more localized, expanding the heat release zone primarily into the downstream shear layer. This is in contrast to the behavior of high reactivity low equivalence ratio flames which tended to burn near the downstream shear layer following the stoichiometric surface that was in those conditions closer to the jet core. It led to the flame pulling away from the wall with a thinner longer flame.

# 1. INTRODUCTION

Staged combustion in gas turbine engines is an active area of research, supplying data for model validation to original equipment manufacturers (OEMs) in the land based power generation and aircraft powerplant industry. This gas turbine technology has matured for the purpose of emissions control by staging the fuel/air injection. Fuel staging captures the design intent to transition safely between operating conditions allowing gradual increase in the peak load by diverting fuel to the staged fuel injectors. GE's DLN2+ (Dry-Low-$NO_x$) technology does this through radial staging [1][2]. Siemens' ULN (Ultra-Low-$NO_x$) combustors also reflect this design intent by adopting axial staging. The additional stage features short residence time jet in crossflow injectors with normal radial injection of fuel into the vitiated crossflow of the primary zone for emissions control and simultaneous damping of thermoacoustics. To understand the behavior of the engines, siemens engineers ran tests on a modified full scale distributed combustor at their ENEL and NRC facilities under the cooperative agreement DE-FC26-05NT42644 with the U.S. Department of Energy[3]. With measured emissions as low as 32 ppm $NO_x$ at H class conditions under distributed operation, their designs showed the emissions benefits of staging as well as for optimizing the transition from the secondary zone to the turbine inlet [4]. Some testing in this development program was performed at the test rig level featuring smaller (typically single element) combustors designed in conjunction with university partnerships to understand the physics of thermoacoustic instabilities,[5], jet in crossflow flame emissions[6], and flame-flowfield interactions,[7],[8][9].

The design process of these test rigs follows the aerospace design progression, from conceptual design to test readiness and subsequent data collection. The test rig design captures the requirements for a high mass flow system capable of transferring megawatt level thermal power to the working fluid at engine relevant temperatures and pressures. Typical measurements from high fidelity instrumentation include temperature, dynamic pressure and mass flow rates to establish operating conditions, describe heat flux, monitor safe operation, and enable red line aborts. The target measurements for the testing operations typically include

emissions measurements, high frequency pressure measurements and high repetition rate flame/flowfield measurements.

Different flame measurement configurations may include point, line, planar and volumetric measurements. Other measurements are line of sight, path integrated, capturing light from all molecules within the field of view. The point, line, planar and volumetric measurements are usually laser based measurements. These light matter interactions are either absorption, emission or scattering events. For example, laser induced fluorescence is a technique that can be configured for planar measurement capturing the incoherent emission following the laser pulse. It is well adapted to capturing flame structure and dynamics against the underlying turbulent flowfield. The level of theory used to model the emission depends on the requirement to describe coherence effects. The models in order of increasing complexity include the rate equation, the density matrix approach and methods using time dependent perturbation theory [10],[11]. The laser field is modeled using Maxwell's equations classically while the material is modeled using its quantum statistics. Since the light from the probe volume originates from the location of the laser, spatial resolution can be established by focusing the laser sheet. Light from the probe volume is scattered into the full solid angle, and the lens and collection optics capture a fraction of this light. The benefits of spatial resolution most often outweigh the limitations even when out of plane motion is expected.

One example of a path averaged measurement is chemiluminescence, an emission event following electronic excitation as a result of chemical reaction. Most engineering flames are luminous because of the presence of this mechanism in the chemistry of the fuel and oxidizer. As the light originates from all reacting portions of the flame, imaging with long depth of field may capture the full flame extent but interpretation of the flame behavior is complicated by the projection of 3-D structure on the 2-D image. Axisymmetric flowfields may lend themselves to planar reconstruction in the time average sense using Abel deconvolution. Other analysis techniques used on path averaged measurements include proper orthogonal decomposition (POD)[12], dynamic mode decomposition (DMD) [13],[14] and spectral proper orthogonal decomposition (SPOD) that captures features from the previous two [15],[16] to characterize the repeated periodic behavior of the flame or flowfield. The kinds of inferences

that can be made from these analyses include the identification or reconstruction of the frequency modes underlying the dynamics, as well as most energetic flow structures and their their growth and decay.

The previous paragraphs aim to show that test rigs and the associated image based diagnostic techniques are expensive technical efforts to generate data that enables the engine designer to make informed decisions to advance the cutting edge of technology. It is fitting to apply analysis techniques to the generated data to extract as much information from the images themselves or the post processed images of other analyses. The analysis techniques presented so far, for path averaged measurements include data based methods that use linear approximations of nonlinear phenomena by modal reduction to represent the data on a smaller subspace, and if appropriate, applying deconvolution to project an axisymmetric image to the center plane. As flame visualization measurements produce digital images, there is a natural incentive to use digital image processing techniques to describe these flame images. Some of these techniques include wavefront coding to deblur images that are blurred due to the image collection system. Image segmentation may be used to extract the flame surface from the background. Filters are typical in presenting portions of images that reveal an obscure subject. Non-classical approaches are growing in familiarity to the combustion scientist and may attempt to capture repeating aperiodic behavior using convolutional neural networks adapted to the flame images using holistic edge detection.

In recently published work [17], Zhang showed the benefit of training these network algorithms to segment patterns of a passive scalar that matches the flame location in images from a swirl stabilized flame. The algorithm called semantic segmentation, aided in computing the flame cross sectional area allowing the retrieval of the size and shape of the turbulent flame during thermoacoustic fluctuations. The algorithm performed at a level consistent with an expert, where classical methods failed. The aperiodic lift off of the flame from the burner was compared to thermoacoustic pressure fluctuations which revealed an intermittent instability linked to increased inlet velocity. This caused reduced reactivity at the flame front which coupled with a stronger precessing vortex core, strained the flame base causing lift off. The results provide improved prediction over time and phase average methods. Another example of a new non-classical approach to extracting information from (passive) scalars is the use

of computer vision techniques to extract velocity fields from flame images using a technique called optical flow. This approach offers the experimentalist the capacity to obtain motion vectors from unseeded flowfields. There are immediate difficulties in interpreting the data from these path averaged measurements as 2-D images for velocimetry, but inroads are being made [18],[19]. To push the cutting edge further, the analyses in subsequent chapters describes effort by the author to prepare high repetition rate (HRR) scalar imaging for optical flow velocimetry. As this work builds on a multi-year project for distributed combustion in a test rig operating at land based gas turbine engine relevant conditions, some description of the testing apparatus will precede the test results. Furthermore, since the fuel blend in this work is representative of efforts building on previous work for emissions reduction, some of the results from that work will be described.

# 2. JET IN VITIATED CROSSFLOW FOR GAS TURBINE COMBUSTION

In this chapter a brief review of the varied specialty literature on transverse jets will be presented. The review will cover the transverse jet features and their properties. It will also cover some aspects of transverse reacting jets and motivate the statistical description of the velocity field. Fuel composition effects are also discussed as well as emission control.

## 2.1 Flow Features

### 2.1.1 Vortices in the Leeward Side

The non-reacting flush normal unconfined gaseous JICF flow features were identified from a few visualization and numerical experiments. Experimental work preceded computational analysis by virtue of the legacy of the intractability of the Navier Stokes equation and the progress of computers. Dye visualizations by Kelso, Lim and Perry [20] for liquid JICF provides insight into the folding of vortex tubes at the downstream side of the jet associated with the formation of the counter rotating vortex pair (CVP). Their experiment also described entrainment of flow from the jet-wall boundary layer, via a few upside-down tornadoes that are now called upright wake vortices. The generation of these features is preceeded by the separation of the upstream boundary layer into what is called the horse shoe vortex. The horse shoe vortex curves around the jet and itself sheds vortices. The train of shed vortices align in the wall normal direction stirring the boundary layer fluid. The low pressure centers of the counter rotating vortex pair form a "drain" where the spinning fluid can empty into, similar to stirring water in a bathtub and opening the drain. These features carry fluid from the boundary layer into the jet core. Fric and Roshko [21] performed smoke visualization experiments on a flush unconfined gaseous JICF revealing these tornado vortices, showing their interaction in the near field of the jet wake and indicating their entrainment pattern into the jet core. These vortices were observed to originate where the crossflow boundary layer (part of the horse shoe vortex) is entrained into the jet near the jet exit plane. The boundary layer rolled up into a vortex stays connected to the wall boundary layer (vortices

cannot terminate on an open surface) and the CVP in the jet core. Furthermore, it carries fluid from the boundary layer into the jet as it is stretched and convected downstream. This was later corroborated by Schlegel et al. [22] in their numerical experiment for a constant density flow using vortex methods, that the boundary layer flow is entrained into the jet wake wrapping around the jet and lifted upwards in the wall vortices. These have also been observed in LES experiments by Zhang and Yang [23] of unconfined ambient air JICF with velocity ratios $R = 2, 4$ using isosurfaces of vorticity and helicity. Their low velocity ratio jets have a higher scalar concentration in the leeward side of the jet a condition required for ignitability in reacting jets.

### 2.1.2 Scalar Concentration

Scalar concentration PDFs revealed quicker peak drift from the jet core to lower concentrations in the near field of the jet plume for the lower velocity ratio. Measurements with passive scalars at two Reynolds numbers showed again the entrainment benefit of the leeward side of the the JICF [24]. This was corroborated by efforts by Shan and Dimotakis showing concentration PDF peak flattening with increasing Reynolds number [25]. Muppidi and Mahesh [26] showed using DNS data of passive scalars that the percentage contribution of the leeward side of the jet to total jet entrainment rises above 90% at 5 jet diameters into the jet trajectory for a density ratio of 1.1 and Schmidt number $Sc = 1.49$ and velocity ratio of 5.7. The visualization experiments by Fric and Roshko imaging the jet trajectory also show that care should be taken in interpreting visualizations since when only the wake structure of a JICF is visualized, especially when the jet is deflected significantly in the direction of the crossflow the resulting pattern of shed vortices could be well within the core of the jet.

### 2.1.3 Jet Penetration

The amount of interaction between the jet fluid and the boundary layer is dependent on the final turning angle of the jet cross section. This angle is controlled by the confinement of the jet and the amount of momentum in the jet. The ratio of the jet momentum flux to the

crossflow momentum flux J parametrizes the non-reacting unconfined JICF. Low values of J result in lower penetration or more interaction between the counter rotating vortex pair and the wall boundary layer [21]. The confined jet responds to the walls in a few ways. Lateral "sideways" confinement forces the horseshoe vortex to fold close to the jet orifice and forces the crossflow to flow over the jet fluid, similar to a low J jet. The laterally confined jet also has a higher strain rate on the windward side. The horseshoe vortex participates in mixing in the near field of the jet orifice, as seen in [23] and [20] injecting crossflow fluid into the jet tube for low J jets, or mixing jet fluid in the upstream boundary layer for high J jets. Wall normal confinement is not often encountered in internal reacting flows, but chemical engineers may use this configuration for tee-mixers the confinement of which results in increased mixedness according to Forliti [27]. Some knowledge of premixed flame behavior in the presence of turbulence is useful before we introduce the reacting jet in crossflow.

### 2.2 Transverse Reacting Jets

The flame of a reacting jet in subsonic crossflow can be attached on the windward side in which case it is fully attached as seen in the 40%/60% $H_2/N_2$ transverse jet flame in Panda et al. [28]. This happens for the most reactive fuel composition. A reduction in reactivity can cause the flame to be be attached at the leeward side and lifted on the windward side with potentially unstable attachments at the windward side [28],[29]. Further reduction in the reactivity of the fuel jet results in a transverse jet flame fully attached on the leeward side [30],[31], with a fully detached flame [32] as the final stage before blowoff. The propensity for attachment can be improved by increasing the fuel reactivity or increasing the crossflow temperature. Increasing the fuel reactivity decreases the chemical time scale relative to the flow time scale increasing the likelihood of stabilizing the transverse jet flame by flame propagation. Increasing the temperature increases the likelihood of forming autoignition kernels which provides a more robust flame stabilization mechanism many times in excess of the flame displacement speed [32]. Direct Numerical Simulation (DNS) results also show that transverse jet flames are more likely to burn in the upstream shear layer if the crossflow is heated [33],[34].

Hydrodynamic instabilities are responsible for the unstable flame attachment on the windward side. Steinberg et al. [29] describe their 70%/30% $H_2/N_2$ transverse jet in non-vitiated heated air crossflow as having a lifted branch that occasionally merged with the lee stabilized portion of the flame. The leeward flame brush always displayed a thicker flame than the windward side owing to the lower velocity and the higher mixedness on the leeward side. The position of the lifted branch in the windward side responded to the unstable motion of the upstream shear layer (USL) which exhibited high extensive principal strain upstream of the closest lifted flame branch as an indication of extinction or flame quenching at that location. Furthermore, the leeward side of the jet showed a low speed recirculation bubble that decreased in velocity with an increase in jet angle or penetration. The bottom of the leeward flame branch did not interact with the bottom of the combustor. The size of this bubble was not related to other configuration parameters. This low speed region was the position of the leading edge of the leeward flame branch. Their mean jet velocity was as high as 200 m/s and no higher (or the flame blew out) in a 54m/s crossflow. From their experiments, it can be argued that the extinction of the flame following a subsequent increase in the jet velocity followed an increase in the upstream shear layer principal extensive strain due to the mismatch between jet and crossflow velocities. The high penetrating jet flame was close to the jet tube and little boundary layer mixing was found in the jet wake [29]. Experiments by Megerian et al. [35] for isodensity jets showed the effect of velocity ratio $R = U_\mathrm{j}/U_\infty$ $(= \sqrt{J = \rho_\mathrm{j} \cdot U_\mathrm{j}^2/(\rho_\infty \cdot U_\infty^2)}$ in an isodensity jet) on the growth rate of USL instabilities which decrease exponentially. Flush jets with velocity ratio less than $R_{cr} = 3.5$ showed significant growth of the fundamental frequency in the USL which transition to higher harmonics with increasing crossflow velocity. In addition, recent work by Shoji et al. [36] revealed the role of the stagnation point in the windward shear layer on the USL instability formation. As flow from the upstream stagnation streamline travels towards the wall, a counter current shear layer is formed which is unstable above $R_{1,ex} = (V_1 - V_2)/(V_1 + V_2) = 1.25$ for isodensity jets, so that jets with $J < 10$ (similar to the $R = 3.5$ from [35]) have absolute instability.

The RJICF may also be attached exclusively in the leeward side with the windward side blown off or entirely lifted perhaps owing to the instability or increased principal extensive

strain in the USL. An increase in extensive strain can contribute to flame extinction. In some cases the flame base is lifted along the jet trajectory, but stabilized in the relatively low strain rate region of the leeward shear layer [29]. Experiments by Sirignano et al. [37],[30] revealed the role of fuel reactivity and reactant diffusivity on the lift off distance of a lee stabilized flame. Their $C_2H_6$/Air or $CH_4$ doped $C_2H_6$/Air premixed jets issued out of a 6mm diameter injector into a 38mm x 114mm cross section with a vitiated crossflow with temperature 1350 or 1410K and velocity of 25.8 $\mathrm{m\,s^{-1}}$. Lifting of the lee stabilized flame occurred on the rich and lean ends of the jet equivalence ratio regime for flush and elevated jets and only attached between jet equivalence ratios of 1.5 and 3. Their experiments also emphasized results that the liftoff distance alone is not a good indicator of NOx, but when it was initiated by doping with $CH_4$, to decrease the flame speed, the amount of flame premixing was increased and the NOx was lower than comparative cases with no doping. The lifting of the jet in crossflow flame edges indicates the competition between the high strain rate at the windward side and around the lateral edges of the jet (where it interacts with the crossflow) and the turbulent burning velocity. The ignitability of the reacting jet on the leeward side is related to the low speed region in the jet wake immediately downstream of the jet and the favorable mixture fraction from the higher entrainment rate. When the jet angle was slowly decreased from 90 to 75deg an established flame in a DNS of a hydrogen RJICF is blown out in simulations by Kolla et al [38], showing similar results to those in Steinberg et al. [29].

Kolb et al. [39] indicate in the development of their liftoff mechanism, several theories underlying the displacement of a premixed flame from the orifice exit in free jets. Their flush circular JICF liftoff theory superimposes the effects of flame propagation and autoignition on the location of premixed jet flames in crossflow and ultimately compares the effects of preflame mixing, jet equivalence ratio, crossflow temperature and jet penetration. Their conclusions indicate the relevance of knowledge of the mixture state at the flame base to predict the liftoff height. Sirignano et al. [37] extend this observation to their natural gas-air crossflow flames. Their liftoff model predicts that leaner flames require shorter ignition delay times because they are hotter having entrained hot crossflow fluid. The model also indicates a strong non-monotonic dependence of the flame stabilization point on mixing - the local equivalence ratio. The ignition delay time is shown to increase at very lean and very

rich mixtures and to decrease with increasing temperature and pressure. Similar displaced flames were encountered in the Mach 0.6 vitiated crossflow $C_2H_4-H_2$ jet flames by Micka et al. [31]. The flames are described to extend into the space downstream of the downstream shear layer of the jet.

Density gradients due to fuel composition and heat release contribute additional perturbations to the dynamics of the jet in crossflow. The added buoyancy causes dilatation of the jet streamlines downstream of the lifted flame base [40]. The jet entrainment rate is thus immediately affected by the presence of the flame. As in the non-reacting case, it depends on momentum flux ratio (penetration and mixing), but here also on the fuel composition (reactivity) and equivalence ratio (temperature). Mungal and Hasselbrink [41] found in their experimental work on reacting jets issuing normally from an elevated injector that the product of density and squared velocity is conserved between reacting and non-reacting cases. This implies that any increase in velocity follows the decrease in density or increase in temperature. They note that the core of the jet expands with the presence of the flame. They also point out that the base of the flame points into the crossflow. They note that the peak velocity fluctuations occur in the jet shear layer and that the vertical velocity fluctuations increase in the flame envelope. Finally their data reveals that the mass entrainment between non-reacting and reacting cases decreases by the square root of the temperature ratio due to the velocity ratio between burned and unburned fuel. Their data indicates that compressive strain and vorticity are good markers for heat release location [41]. Since

$$\frac{\mathrm{D}\omega}{\mathrm{D}t} = -\omega(\nabla \cdot \boldsymbol{v}) + \frac{\nabla\rho \times \nabla p}{\rho^2} + (\omega \cdot \nabla)\boldsymbol{v} + \frac{1}{\mathrm{Re}}(\nabla^2\omega) \tag{2.1}$$

the mechanisms of vorticity $\omega$ dynamics in this reacting flow are the dilatation (first term on rhs), the baroclinic torque (second term on rhs) and the decrease in local fluid Reynolds number from temperature rise. Wagner et al. [40] found in their confined ethylene air crossflow jet flame that the role of heat release in reducing entrainment rates was captured by the local increase in fluid viscosity leading to a reduced shear layer rollup - which may be attributed to the first and last terms on the rhs of eq 2.1. The shear layer rollup is also important in starting the counter rotating vortex pair (CVP). The delayed initiation of the

CVP reduces the entrainment of crossflow fluid from the jet wake. The leeward shear layer also suffers from lower entrainment from the flow expansion contributing to the slowing down of vortex rollup.

### 2.3 Turbulent Statistics

The JICF flowfield contains both wall bounded features as well as features characteristic of free shear flows. The interaction of these features complicates the purely theoretical study of the flowfield. It has been sucessfully studied using computational tools, but here we aim to describe it using results from vorticity dynamics and with a statistical treatment. The third term on the rhs of eq 2.1 is responsible for the transfer of energy in turbulent flowfields. It is called the vortex-stretching term because it acts on already available vorticity by actions of the mechanisms in the strain rate field. The smallest eddies are generated by a distortion caused by the largest eddies. The available mechanisms by which energy is transferred include the different terms in the acoounting of vorticity dynamics triggered by instabilities and dynamics of coherent structures. The transfer of energy between scales is often described using the language of statistics, partly because the conservation equations that describe the flow are highly dissipative and highly nonlinear. The result is that solutions of these equations to similar initial conditions are known to diverge given sufficient separation from the initial time. The statistical theory serves to describe the behavior of average features in the flowfield that behave similarly irrespective of initial conditions. The formulation models the spectrum of energy containing eddies which differ in scale. The Fourier transform of the conservation equation provides a model from which spectra can be analyzed. In particular, quantities in the conservation equation form Fourier transform pairs with single and two point correlations. The portion of the energy spectrum whose behavior is independent of initial conditions is called the inertial region. This size of this region can be increased at the same length scale by increasing the velocity or decreasing the dynamic viscosity. To describe

these eddies deterministically would require models with a large number of degrees of freedom for the Reynolds numbers typical of engineering flows. Moments of velocity differences

$$S_n = \int_0^\infty \mathrm{d}r((\boldsymbol{v}(\boldsymbol{r},t) - \boldsymbol{v}(\boldsymbol{0},t)) \cdot \boldsymbol{r}/r)^n = \langle (\delta v_r)^n \rangle \tag{2.2}$$

are two point correlations called *structure functions* that reproduce quantities related to the energy content of portions of the flow. For example the second order structure function captures the energy contained in all Fourier modes with wavenumbers larger than $1/r$. Kolmogorov obtained a closed form expression for the third order moment in isotropic turbulence, the celebrated four-fifths law

$$S_3 = r\frac{4}{5}\langle \epsilon \rangle \tag{2.3}$$

With $\langle \epsilon \rangle$ the viscous dissipation of turbulent kinetic energy. This function is independent of the origin of the coordinate system, where the statistic is computed an indication of isotropy. When the two points coincide, the temporal changes in these correlations where they exist are determined by viscous effects, by convective diffusion due to inhomogeneities in the flow, by production or transfer of energy through turbulent shear stresses and by the effects of correlations in pressure fluctuations and that of velocity or its derivatives.

The contributions from pressure-velocity gradient correlations tend to make the flowfield more isotropic by transferring energy from one velocity component to the others if local incompressibility is valid. The effect of the production of turbulent kinetic energy is to increase the autocorrelation of the $u'_{\mathrm{i}} = \sqrt{\overline{u_{\mathrm{i}}}^2}$ making the flowfield non-isotropic. $\bar{\cdot}$ represents ensemble average and the $\cdot'$ represents the turbulence intensity or the root mean square of the fluctuation. The production term makes a negative contribution to the temporal change in the cross correlation, the turbulent shear stress $\overline{u_{\mathrm{i}}u_{\mathrm{j}}}$, however for this to happen, the velocity gradient is positive and the cross correlation is of the opposite sign, and hence the negative contribution increases the value of the cross correlation. The effect of the pressure-velocity gradient correlation is to decrease the absolute value of the cross correlation. The turbulent shear stresses are created in non uniform main flows - with inhomogeneity.

The two point second order correlation is dependent on the root mean square of the component fluctuation $u_{\mathrm{i}}'$ (which is identical in all directions) and the longitudinal and lateral correlation functions $\mathbf{f}, \mathbf{g}$. These functions $\mathbf{f}, \mathbf{g}$ reveal the size of the smallest eddies because

$$\frac{1}{\lambda_g^2} = -\frac{1}{2}\left[\frac{\partial^2 \mathbf{g}}{\partial x_2^2}\right]_{x_2=0} = \frac{1}{2u_1'^2}\overline{\left[\frac{\partial u_1}{\partial x_2}\right]_{x_2=0}^2} \tag{2.4}$$

and size of the longest correlation distance or the largest eddies because

$$\Lambda_g = \int_0^\infty \mathrm{d}x_2 \mathbf{g}(x_2) \tag{2.5}$$

where $\lambda_g$ is the micro scale of the smallest eddy, and $\Lambda_g$ is the (integral) macro scale of the largest eddy. The expressions are identical for $\lambda_f$ and $\Lambda_f$ with $x_2$s replaced with $x_1$s. The statistical theory describes the distribution of energy $\mathbf{E_{i,j}}(\mathbf{k})$ in the three dimensional flowfield and provides relations for the one dimensional energy spectrum $\mathbf{E_i}(k_{\mathrm{i}})$ due to limitations of experimental measurements. There are also extensions to frequently used energy spectrum functions $\mathbf{E}(k) = 2\pi k^2[\mathbf{E_{i,j}}(\mathbf{k})]_{av}$ constructed from the contracted 3-D functions after averaging over spherical shells and simplified for legibility. The distribution of energy is understood to describe some energy spectrum function in terms of scales. The equations that govern the transport of energy between scales is beyond the scope of this review, but recent reviews show that the transfer of energy is nonlocal - the closest scales do not transfer energy between each other. Choosing $\mathbf{E}(k)$ is beneficial as simple integrals reveal familiar terms like the turbulence kinetic energy and the turbulence shear stresses. The lateral and longitudinal functions also provide insight into the one dimensional energy distributions in fact they are Fourier transforms of the 1-D energy distributions in each component of velocity. Experimental evidence has shown that in high Reynolds number anisotropic turbulent flows, the high wavenumber range behaves isotropically. This led Kolmogorov [42] to hypothesize that the range of high Reynolds number flows where turbulence is statistically in equilibrium is universal and parametrized by two quantities; viscosity and the supply of energy.

In compressible isotropic flowfields, it has been suggested by Hinze [43] to use the turbulence intensity of the velocity components as the velocity scale for the Mach number. Using this definition, compressibility contributes to the mean motion in addition to the turbulent shear stresses through double and triple correlations involving the fluctuation in density. Chandrasekhar [44] found from equations of motion of the second order correlation of fluctuations in density that the dynamics of this correlation can be expressed as a superposition of spherical waves propagating with a finite velocity. Implying that there exists one new path for energy transfer between scales, following these spherical waves and eventually dissipating into heat. Compressibility thus contributes energy dissipation to the flowfield.

Non-isotropic flowfields are marked by significant interaction between turbulence and the shear flow driving it. Some of the effects of non-isotropic flowfields may be ignored if the region of interest is small enough so as to be interpreted as locally isotropic.

In wall bounded flows the energy spectrum shows different behavior across the low-intermediate wavenumber ranges. The main motion of the largest scales supplying the energy has an additional role in addition to that of homogeneous or isotropic flowfields. Here the organized motion due to its high vorticity may interfere with the underlying turbulence. This effect results in a different energy spectrum especially in the low to intermediate wavenumber range where the interaction between the main flow and the underlying turbulence occurs.

## 2.4 Fuel Composition Effects

The premixed gaseous fuel jet in crossflow is a mixture scalar field whose non-reacting local properties are regime dependent with parameters including penetration depth, level of premixedness, Reynolds number etc. There is incentive to blend multiple fuels into the premixed flame environment to benefit from properties of both fuels. The design of these systems would account for the changes in volumetric flow rate, heat release rate, vortex shedding, reactivity, burnt gas temperatures, and static and dynamic flame stability to prepare fuel injectors for blending [45]. One such case is the reacting jet in high subsonic-Mach-number crossflow. High Mach number jet flames in crossflow are highly strained flames which benefit from increased mixing and lower static temperatures for emissions control. The

drawback is that the ignitability and flame stabilization mechanisms need to be augmented in order to establish a robust flame. Blending the fuels for composition design meets the requirement to increase the flame speed of the base fuel. The absence of the supersonic flow features simplifies analysis of the flowfield, however the OEM is tasked with the control of the flame location for flashback mitigation.

### 2.4.1 Carbon Neutral Emission Goal and Hydrogen Combustion

The increased reactivity of the fuel blend can benefit from higher H/C ratios. This is especially evident in hydrogen blending into gaseous hydrocarbon fuels. The shorter ignition delay suggests earlier onset of preheat reactions in the fuel, supporting CO burnout and lower amounts of unburned hydrocarbons (UHCs) that would otherwise escape from the injector face. This is evidenced by lower flame liftoff heights. The addition of hydrogen into hydrocarbon fuels reduces the carbon footprint. Some fuels like natural gas have a similar Wobbe Index[1] to hydrogen, permitting their interchangeability. The injection of premixed fuels into the crossflow also reduces the drastic effect of changing the volumetric flow rate of the fuel since air accounts for the mass of the jet.

## 2.5 Emissions Control

The regulation of emissions from national and global environmental agencies has prompted the ongoing design of gas turbine engines with increasingly stricter emissions goals in aircraft architectures or for power generation. The most regulated emission species are known as $NO_x$, a collection of oxides of nitrogen which act as a reducing agent depleting stratospheric ozone($N_2O$), generating tropospheric ozone($NO_2$) and contributing to acid rain, to name a few large scale effects. Natural gas combustion contributes to 68% of that amount. National ambient $NO_2$ concentrations are near 15ppb well below the quality standard of 53ppb, but the average does not indicate how much removed some regions are from this value. Short and long term exposure on the human scale causes health issues connected to traffic-related pollutants [46]. The majority player in the generation of $NO_x$ is highway vehicles, with off

[1]↑The Wobbe Index is the ratio of the higher heating value to the square root of the density ratio. $\frac{\text{HHV}}{\sqrt{\rho_{gas}/\rho_{air}}}$

highway vehicles (trains, planes etc) coming in as a close second. The average nationwide percentage for a representative year proves about 14% of the total $NO_x$ comes from power generation units (in fourth place), with a quantity of about 2 million tons. This statistic was sampled from the 21 largest statistical areas in the U.S.A. each with a population of more than 2.5 million. These power generation combustion devices are termed stationary combustion sources. Of these, land based gas turbine engines comprise a small majority. According to monitoring by the United States EPA - Cross-State Air Pollution Rule (CSAPR) NOx annual program of 2019, gas fired combustors generated about 631.74 million MWh with low $NO_x$ burners and other combustion control technology (not including post combustion controls) contributing to 17.13% of the total power generated.

Distributed combustion or staging is one such technology used by gas turbine OEMs to create environments in the combustor that generate high enthalpy working fluid which minimizes emissions without jeopardizing performance. Although radial and circumferential staging technologies exist, we shall focus on axial staging. As a disambiguation against other arrangements called axial staging, this terminology describes the arrangement of the main (primary) combustion zone upstream of the secondary zone. In this configuration, fuel, air or both fluids are distributed along the length of the combustor. Air staging typical of an RQL combustor may feature a fuel rich primary zone, with most of the air diverted around the primary zone, to be injected downstream in the secondary zone providing oxygen to burn the hydrocarbon fragments generated in the oxygen deficient primary zone [47],[48]. In fuel staging, most of the fuel is injected into the primary zone where it is burnt and some additional fuel may be added downstream. The primary zone is operated fuel lean, a configuration designed to help minimize $NO_x$ formation [49],[50]. The fuel lean primary zone features combustion in excess air supplying a vitiated supply of air with available $O_2$ to ignite the added fuel in the secondary zone. Fuel staged distributed combustor operation features lower overall peak gas temperatures at the same thermal power and as such lower $NO_x$.

Parameters governing the secondary zone flame behavior of these staged combustion systems may be flowfield based such as the penetration of the jet fluid, as well as the temperature and pressure of combustion environment. Some parameters are geometry based such as the

confinement by the walls, the amount of premixing, governed by the location and orientation of premixer fuel injectors, and the residence time of the working fluid. Other parameters are chemistry based such as the chemical composition of the fuel, and the chemical environment of the flame (its local equivalence ratio which may be based on premixing or entrainment). The difficulty of instrumenting full scale engines to extract these measurements capturing the role of independent parameters has given rise to subscale testing. Results from such test rigs provide the bulk of the literature on these parameters. Hayashi and Yamada [51] ran an atmospheric pressure methane air staged combustion rig with the primary stage flame stabilized on a perforated plate burner and the second stage a jet in vitiated crossflow flame. The $NO_x$ emission index was shown to decrease up to a minimum and then increase with further increase in secondary stage fuel. The initial decrease was attributed to the reducing environment created by the added hydrocarbons causing the reduction of $NO_x$ to molecular $N_2$, with the final chemical heat release located a short distance before the combustor exit. As the flame temperature increases (with stage equivalence ratio) the jet in crossflow flame length and liftofff height shortens and the post flame gases have a longer residence time. Similar results were found in a radial injection staged combustion rig burning natural gas and air in an industrial gas turbine burner at elevated pressure by Geigle et al. [52]. In their experiment, addition of about 15% of the total combustor fuel into the secondary zone decreased the corrected $NO_x$ to well below the reference value, before the subsequent increase with further increase in staging ratio. Therkelsen et al. [53] ran a full scale distributed combustion engine at 4 atm with a hydrogen/natural gas mixture with angled premixed injection for both the main and secondary stages. The fuel composition was swept from pure natural gas to pure hydrogen in both primary and secondary zones. The engine was run with three modified fuel injectors. In each case, the premixer fuel lance was offset from the injector face by some distance, or injected into the airstream at a different angle. They found that the amount of premixing controlled to a large extent the amount of $NO_x$ generated. For example, when the base load was increased from 5kW to 60kW, the $NO_x$ levels stayed relatively the same.

Recent work by Rodrigues et al. details the emission benefit for high Mach number combustion in the secondary stage [6], and as high Mach number flowfields are high strain

rate flowfields, flame stability is an important metric to establish for these flames. Higher reactivity fuels satisfied the requirements for stable flames in this high strain rate field. Natural gas/hydrogen fuel blends were used in the subsequent phase of the project to improve the stability of the flame [54]. The addition of hydrogen was shown to increase the available reactive species in the crossflow entrained jet under reacting conditions allowing an upstream drift of the average flame position in the unanchored stabilization mode. The anchored flame behaved as expected with rearward drift in the mean anchor point with increase in hydrogen content.

# 3. OPTICAL MEASUREMENTS OF HIGH PRESSURE COMBUSTION

High pressure environments are naturally confined. The measurement of temperature or pressure is traditionally done using probe or transducer instrumentation. Computational tools may also provide insight into flow behavior at comparatively cost effective prices. Optical measurements in high pressure combustion are important due to the Reynolds number scaling of the smallest fluctuations and the large number of scales that immediately become available in high density flows. Optical measurements are thus still used to validate computational models. The 2-D data provides information about temporal correlation in the image domain without having to result to Taylor's hypothesis. Optical measurements are also necessary for probing data in harsh environments and are natural to some flowfields. Probe techniques provide higher precision data in wind tunnel experiments, but are not conducive to high temperature flows like combustion. These optical measurements are the interpretation of some natural or forced photon emission, absorption or scattering within the flowfield. Depending on the scalar being measured, laser techniques could be used to make measurements of flowfields. The laser technique is usually suited to the scalar. Laser techniques benefit from spatial resolution within the limits of the collection optics. They could be extended to line and sheet measurements given the right light collection optics. As lasers are expensive, natural emission from the flowfield can also be used for visualization. In this report, 2-D OH PLIF measurements are used to qualitatively describe the reacting layers in a turbulent premixed reacting jet in crossflow. 2-D $OH \cdot$ chemiluminescence measurements are used to qualitatively locate the fluid undergoing heat release in the same turbulent premixed reacting jet in crossflow.

Dynamic pressure measurements may accompany high repetition rate imaging where the imaging technique does not also provide pressure data. This accompanying measurement could provide a comparison to verify theoretical claims. Optical measurements may provide species concentration. In the absence of such techniques, emissions measurements may accompany optical measurements to help engine designers identify unwanted flame behavior either paying NOx, CO or unburned hydrocarbon penalties.

## 3.1 Turbulent Premixed Flames

This section provides some introduction to turbulent flames in high pressure combustion. In general it is impossible to predict even with a-priori knowledge of the local rms. turbulence velocity $u = \sqrt{u'^2}$, whether a turbulent premixed flame will be extinguished or propagate faster. Given a small enough $u$ the "turbulent flame speed" $S_t$ does increase, however there is a maximum experimentally observed turbulent flame speed $S_{tm}$ associated with a height of velocity fluctuation $u_m$. Subsequent increase in $u$ results in a decrease in $S_t$ with further increase resulting in eventual flame extinction. The general dependence of this maximum on the turbulence intensity is not yet theorized. Also the transport of the deficient reactant and heat, and the flame speed of the premixed fuel are parameters that change the turbulence fluctuation associated with the maximum turbulent flame speed at a particular premixed fuel composition.

The main contribution of flamelet ideas to the turbulent premixed flame literature is that the only effect of turbulence is to wrinkle an otherwise laminar flame. Two diffusive-thermal mechanisms by which the local flame area in turbulence enhanced laminar flames is increased are the Lewis number effect and preferential diffusion. The maximum turbulent flame speed or burning rate of premixed fuels is reached on the *leaner* side of the equivalence ratio range compared to the laminar flame speed, if the mass diffusivity of the fuel is higher than that of the oxidizer because in turbulent flows, the wrinkling of flames often creates concave bulges towards the unburned mixture, into which the fuel diffuses faster towards establishing stoichiometry. This result is separate from but adds to the Lewis number ($Le = \kappa/D_d$) effect where provided the molecular diffusivity $D$ is larger than the thermal diffusivity $\kappa$ (low Le) in the premixed reactant, chemical energy is supplied to the bulge faster than it is lost to molecular diffusion increasing the turbulent flame speed and thus the penetration of the bulge. As the two mechanisms are dependent on the single parameter $D_d$, they are impossible to distinguish in experiments. In addition to the thermal instability, a hydrodynamic instability - the Darrius Landau instability - was theorized to wrinkle laminar flames in the presence of turbulence. The theory proposed is as follows: If a laminar premixed flame encounters turbulence that bulges it towards and away from the reactants, the portion

bulging towards the reactants will produce streamlines that diverge away from the bulge, the reactants are slower than the flame speed and the bulge increases. Similarly the bulge away from the products produces streamlines that converge towards the bulge, increasing the reactant speed higher than the flame speed and the bulge increases in the opposite direction. In summary the effect of turbulence on laminar premixed flames produces an unconditional instability[55]. To explain the discrepancy between this theory and the observed stability of laminar premixed flames, we consider both instability mechanisms since the thermal mechanism can have an amplitude reducing effect. The practicality of this wrinkled flamelet theory would be revealed in its predictive power to describe premixed turbulent combustion. The models proposed to account for the hydrodynamic instability either capture them using weak perturbations using the concept of the Markstein number $Ma = \ell/\delta_L$ or strong extinction perturbations parametrized by the critical stretch rate. Using the developed models based on $Ma$ or critical stretch rate, the prediction of the values of $u_m$ for which $S_{tm}$ is reached does not agree with experimental results. The various models built on this theory have been tested to reveal the effect of $D_d$ on $S_t$ but a clear effect is not shown. There are also other theories that describe the experimentally observed results such as the leading point theory [56].

Leading point ideas of turbulent premixed flames describe the flame using its portions that move furthest towards the unburned reactants and describes them as independent of turbulence in the flowfield. Leading point flamelets are critically stretched since they are exposed to the strongest non-quenching perturbations. The claim is that the structure of these flamelets is universal. The diffusive-thermal mechanisms described in the previous paragraph produce the leading points in a flame pushing against the convection of the leading points by large eddies. The concepts of critically strained flamelets and critically curved flamelets are employed to describe the structure of leading points. If the diffusive-thermal effects are larger than convection effects ($Le < 1$), the leading point structure is that of a critically strained flamelet and the previous arguments for the progress of bulges into the reactants capture the direction of the leading points. If on the other hand $Le > 1$ the burning rate only increases if the bulge proceeds into the products which does not favor the geometrical definition of leading points. The leading points where $Le > 1$ then correspond

to the flamelets wrinkled by turbulence which have an increased surface area to increase the local burning rate above the reduction due to the diffusive-thermal effect of the bulge. The critically curved flamelet predicts the strong effect of $D_d$ on $S_t$ in $Le < 1$ flames which the critically strained flamelets are incapable of reproducing. The idea is quantified using a chemical timescale $\tau_{lp}$ for the burning rate of a spherical flame ball, which when $Le > 1$ $\tau_{lp} = \tau_c = \kappa_u / S_L^2$ and when $Le < 1$ $\tau_{lp} = \tau_c \cdot S_c / \min(S_c)$ weighted by the consumption speed $S_c$. The models based on this theory have been successful in describing the strong effect of $D_d$ on $S_t$. Furthermore, the hydrodynamic instability is quantitatively predicted in the medium turbulence case. The values of $u_m$ for which $S_{tm}$ is reached is not predicted in the theory [56]. Hawkes and Chen [57] showed that the combined effect of preferential diffusion and shorter flame time scales accounts for an enhanced flame area in a hydrogen enriched lean methane air flame. In addition the enriched flame was shown to be diffusively thermally stable and more resistant to quenching owing to the preferential diffusion increasing the curvature of the flame.

## 3.2 HRR OH-PLIF

### 3.2.1 LIF Physics

OH-PLIF is a laser based emission measurement of OH in chemical environments where it is generated since it only exists as a reaction intermediate. The laser sheet is tuned to the absorption line of OH at the measurement location. Fluorescence occurs spontaneously, some time after the laser excites the electrons to their excited state. The light from the fluorescence event is collected at right angles to the laser sheet path. Because the fluorescence event follows the laser pulse, the data is highly resolved to the probe volume $V$: the intersection of the laser sheet and the OH. High repetition rate studies can be performed by using high repetition rate laser and array detectors such as (intensified) camera systems. The theory of laser induced fluorescence in flames is captured by two transitions namely; the electronic absorption transition of electrons in the outermost shells of some specie from state 1 with

population $n_1^0$ to state 2 followed by a radiative transition from state 2 the excited state with population $n_2$ to a lower state. The signal strength (number of photons per second)

$$
\begin{aligned}
S_F &= n_2 \cdot V \cdot A_{21} \cdot \frac{\Omega}{4\pi} \\
&= \underbrace{\left(n_1^0 V\right)\left(W_{12} = \overbrace{B_{12}\frac{I_v}{c}g(v)}^{\text{probability of absorption/s}}\right)}_{\text{photons absorbed/s}} \cdot \underbrace{\left(\frac{A_{21}}{W_{21}+A_{21}+Q_{21}}\right)}_{\text{fluorescence quantum yield}} \cdot \underbrace{\left(\frac{\Omega}{4\pi}\right)}_{\text{light fraction collected}}
\end{aligned} \tag{3.1}
$$

It is proportional to $A_{21}$ the probability per second of spontaneous radiative transfer from state 2 to 1, to $\Omega$ the solid angle of the collection optics and inversely proportional to $Q_{21}$ the rate of non-radiative transfer of electrons out of state 2 of which fast rotational transfer dominates. Absorption is governed by quantum mechanical selection rules describing the allowed transitions or the total change of the wavefunction of the molecule following the transition. The transition is described using the laser wavelength and intensity, the vibrational band, the Einstein coefficient for the transition of the molecule of interest. The term symbol for describing the transition is

$$
\begin{aligned}
&{}^{X}Y_{\alpha\beta}(J\text{" or } N\text{"}) \text{ where} \\
&Y - \Delta J(O, P, Q, R, \text{ or } S, -2 \text{ to } 2) \\
&X - \Delta N(P, Q \text{ or } R, -1 \text{ to } 1) \\
&\alpha - \text{i for } F_{\text{i}}\text{"} \\
&\beta - \text{i for } F_{\text{i}}' \\
&F - \text{i Spin split state with same } J \\
&\qquad \text{(orbital) but different spin angular momentum}
\end{aligned} \tag{3.2}
$$

For example ${}^{P}Q_{12}(13)$ in a spin doublet transition corresponds to transition from $N\text{"} = 13$ or $J\text{"} = 12.5$ in $F_2\text{"}$ to $N\text{"} = 12$ or $J\text{"} = 12.5$ in $F_1'$. Either $P$ or $Q$ is used typically and the other is omitted. Similarly if $\alpha = \beta$, one is omitted. Finally $N\text{"}$ is most often used in literature.

The laser sheet induces an absorption transition which precedes the spontaneous fluorescence transitions. Furthermore, the areas of the laser sheet where absorption does not occur return little signal. As a result in some cases, as a benefit of the technique, the LIF signal is obtained against a dark background. In others large portions of the laser energy are absorbed along the direction of the sheet reducing the high SNR portion of the image to the regions where absorption occurs. The dark background may also be slightly illuminated by chemiluminescence at the same frequency. Other difficulties in measurement include the dependence of LIF on high number density in the ground electronic state of the molecules being probed, reabsorption of LIF signal by surrounding gas prior to detection, beam steering out of focal plane of camera for low depth of field optics – due for example to changing refractive indices around a flame. Detection limits can be calculated based on the available number density of the species being measured and the quantum efficiency of the collecting optics. Molecules typically fluoresce when irradiated with UV photons, so frequency doubled output from dye lasers are typically used for these measurements.

### 3.2.2 OH Formation Chemistry

In turbulent flames, OH PLIF can provide gradient and spatial structure of the flame. The reactions responsible for generating OH include

$$\mathrm{H} + \mathrm{O_2} \rightarrow \mathrm{OH} + \mathrm{O} \tag{R 3.1}$$

the most important chain branching reactions at high temperatures as well as the chain terminating

$$\mathrm{H} + \mathrm{O_2} + \mathrm{M} \rightarrow \mathrm{OH} + \mathrm{O} + \mathrm{M} \tag{R 3.2}$$

Flame propagation depends on reaction R 3.1 however since the OH concentrations persist into the reactants and products when convected, knowledge of the flowfield is important to interpret the results.

## 3.3 HRR OH*-Chemiluminescence

$OH^*$ chemiluminescence is an emission of light from electronically excited OH-producing chemical reactions which are themselves inelastic scattering of molecules off each other. There has been some progress on the scattering theory of some chemical reactions. In most cases however the theory is behind the practice and we are forced from the spectra of these emission events to draw simple conclusions such as the identity of colliding partners, that of the newly formed molecules and their quantities in the reaction zone. In combustion, particular attention is placed on reactions whose progress parallels the release of significant fractions of the total heat released in the full reaction chain.

### 3.3.1 OH* Formation Chemistry

The reactions responsible for $OH^*$ formation on in hydrocarbon mixtures are

$$CH + O_2 \rightarrow CO + OH^* \tag{R 3.3}$$

with addition of hydrogen, hydrogen/methane flames see additional $OH^*$ from

$$H + O + M \rightarrow M + OH^* \tag{R 3.4}$$

Reaction R 3.3 is proposed by Krishnamachari and Broida who studied the emission spectra of oxygen acetylene flames at low pressures. The activation energy of $OH^*$ from the reactions is estimated as 17.38kJ/mol obtained from shock tube studies at high temperatures by Hall et al. with a rate coefficient as high as $1.8\text{x}10^{11}\,\text{cm}^3/\text{mol}/\,\text{sec}$ at flame temperature. Just as easily as $OH^*$ is generated, it is quenched by collisional partners $M = N_2, H_2, H_2O$ with quenching rates at least one order of magnitude higher than the generation rate coefficient [58]. Najm et al. compared the measurements of heat release and the occurrence of $OH^*$ chemiluminescence and arrived at conclusions identifying that the location of the the one was sufficient to infer the other [59]. Sardeshmukh et al. [60] also carried out analysis to identify the transported $OH^*$ with heat release in a model rocket combustor. Qualitative

approaches to the measurement of chemiluminescence are thus one way to describe locations and or frequency of heat release in the combustor. The 2-D measurements resulting from these measurements identify space and time resolved locations of heat release.

OH* is chemically excited OH present in reacting flows of hydrocarbon fuels. As a radiant product of the flame, its luminescence provides a signal for flowfield visualization especially since it is quenched relatively quickly and hence is a good flame/heat release marker [60] and does not require expensive lasers. Quantitative chemiluminescence often deals with laminar "laboratory flames" or heat release following shock compression where direct measurement is accessible without the complexities of turbulence. Turbulent combustion in literature often uses qualitative chemiluminescence for a general description of the flame location. We shall attempt to make this more formal for the ensuing discussion. The chemical activation of OH to OH* is not an efficient process, so that a small fraction of the available OH is chemically excited for radiating photons. The low SNR coupled with the multiple available chemical pathways for its generation makes the sensitivity analysis of this specie difficult. This means the sampling of OH* molecules by chemiluminescence does not correlate uniquely with the OH in the flowflield. The reactivity of the flame determines the capacity for the visualization to be adapted to the statistical theory of passive scalars. If the reactive portion of the flow is isolated to nearby portions of the shear layer where OH* is generated, the rest of the flow may still be illuminated by the activated OH* in superequilibrium given short enough integration times. The OH* is thus merely convected and can be interpreted as a contaminant being flushed from the flame front.

### 3.3.2 Imaging of OH* Chemiluminescence

Chemiluminescence is a path averaged measurement. As a light source for flowfield imaging, it is important to note that the luminescence originates from multiple nearby sources in the flow, so that spatial structure and contrast in the image may result from back projection of separated features through the depth of the reacting flow. Contributors to lower contrast for chemiluminescence include the integration time of image acquisition, which is of the order of a few microseconds, up to two orders of magnitude longer than LIF to increase

the signal levels. This often results in the familiar time-lapse blurring. The deblurring of these features is possible using deconvolution methods. Decrease in sharpness in chemiluminescence images may also follow increase in pressure as the heat release reaction path is pressure dependent for C1-C4 alkanes. There is a double peak in the heat release reactions, one associated with partial oxidation to CO at lower temperatures and the other following CO burnout. Increased pressure increases the fraction of the heat release associated with partial oxidation reactions which broadens the region of luminescence resulting in a dimmer radiance, perhaps moving from a flamelet to a thickened flame regime. The analysis of chemiluminescence images using the tools of passive scalar statistics is hindered by the long integration time, coupled with the possible generation and quenching of OH* in the image domain. When chemiluminescence is used for visualization, care will be taken to describe the pre/post processing and simultaneous measurements that were performed to make sufficient inferences from the data.

The OH* chemiluminescence will originate from a turbulent premixed reacting jet in crossflow RJICF. The transverse jet flame may release heat along shear layers of the turbulence induced bulk fluid mixing. Since the chemiluminescence will illuminate the coherent structures, one question this experiment addresses is where the crossflow is mixed into the jet at sufficient conditions for ignition. Conditions with rapid mixing are of interest, and may coincide with short flame liftoff distances to the injector orifice. This would need to be balanced with NOx performance. Further inference on the location of the flame on the upstream or downstream shear layer of the jet will indicate which stabilization mechanisms are preferred. Qualitative flame behavior may be inferred from the chemiluminescence such as flame brush shape and size. That the fuel jet is premixed means that the flame will be established as a partially premixed flame. Since the jet fluid contains a mixture of hydrogen and natural gas, the properties of one fuel may appear at a separate location from that of the other. Hydrogen being very diffusive and reactive may preferentially burn earlier. Jet momentum is mostly contributed to by air, the working fluid, so changes in chemical composition of the jet should not significantly alter the jet penetration apart from effects of heat release.

# 4. OPTICAL FLOW

Direct numerical simulation (DNS) of turbulence has improved significantly with the development of large supercomputers and their multicore computational capacity. The development of this technology has been driven by the lack of analytical solutions to the Navier Stokes equation

$$\frac{\partial \rho \boldsymbol{v}}{\partial t} + \nabla \rho \boldsymbol{v}\boldsymbol{v}^T = -\nabla p + \nabla \cdot \left( \mu \left( \nabla \boldsymbol{v} + (\nabla \boldsymbol{v})^T - \frac{2}{3}(\nabla \cdot \boldsymbol{v})\boldsymbol{I} \right) \right) \tag{4.1}$$

which models fluid flow - the velocity field, and the need for computational solutions. Despite its significant capability, DNS results are limited in scope of Reynolds number and spatial extent. Simulations of fluid flow at engine relevant conditions are best carried out by models that require detailed validation. Experimental approaches are often designed to improve the accuracy of a model or describe the engine conditions per se. Optical experimental methods have the added capacity to reveal the spatial behavior of the flowfield often producing instantaneous 2-D datasets. Data from optical methods provide natural input to velocimetry techniques such as optical flow.

Optical flow is a method of inferring apparent three dimensional motion from moving brightness patterns in an image sequence. Each image is interpreted as a scalar field of digitized brightness values whose patterns are identified by consistent features between image frames - this is the brightness constancy assumption. Using a rectangular grid, we may decompose the expected motion into two scalar fields correcting the vertical and horizontal motion components of the pixels in the first frame belonging to features we wish to identify in the second. When the displacement in pixels is *small*, such motion that can be inferred from the motion field include solid body translations and rotations, deformations, and expansions. Optical flow is a dense motion estimation technique in that it describes the motion between corresponding pixels in an image pair, contrary to other techniques that use windows of pixels such as correlation methods and "windowed" optical flow. Two assumptions have been listed under which a pair of images with identifiable brightness patterns could be used to recover the underlying motion field namely: Small displacements and constant brightness of the features in the pattern. In fact a few more assumptions are implied such as the interpretation of 3-D motion with a 2-D image, others will be indicated as we proceed

with the theory. Regarding the brightness constancy assumption, any changes to brightness patterns outside the listed assumptions would require some adjustment of the theory as stated. This is however often the case: Occlusions, large displacements, layered motions and the aperture problem are a few occurrences where the assumptions are not satisfied. Further complexity comes when physics of material properties needs to be employed to interpret the results such as reflections, shadows, and transparencies [61]. Occlusions occur when the brightness pattern from an object is hidden behind another object or feature in the image, this occurs at the edges of an image if objects exit the image domain. Layered motions are another type of occlusion, where multiple objects with identifiable brightness patterns are overlaid above one another, with segmentation and motion in independent directions.

The aperture problem is fundamental to dense techniques. The mathematical expression uses a few quantities that need definition. We will describe the mathematical interpretation of the optical flow problem as we explain the aperture problem. The equation that links the input data (images) to the underlying motion field is called the data term. The link involves algorithmic manipulation of the images by casting them as input to a function to be optimized. The brightness constancy constraint sets the intensity field

$$I(\boldsymbol{x}) = I(\boldsymbol{x} + \boldsymbol{v}t) \tag{4.2}$$

such that there exists a motion field $\boldsymbol{v}(\boldsymbol{x})$ that satisfies the brightness constancy eq. 4.2, so that when applied to the first frame, it recovers the next. A linearization of eq. 4.2

$$\frac{\mathrm{d}I(\boldsymbol{x},t)}{\mathrm{d}t} + \boldsymbol{v} \cdot \nabla I(\boldsymbol{x},t) = 0 \tag{4.3}$$

obtains a form that when manipulated as

$$\frac{\mathrm{d}I(\boldsymbol{x},t)}{\mathrm{d}t} \frac{1}{\|\nabla I(\boldsymbol{x},t)\|} + (\boldsymbol{v}^{\parallel} + \boldsymbol{v}^{\perp}) \cdot \frac{\nabla I(\boldsymbol{x},t)}{\|\nabla I(\boldsymbol{x},t)\|} = 0 \tag{4.4}$$

yielding a solution

$$\boldsymbol{v}^{\perp} = -\frac{\mathrm{d}I(\boldsymbol{x},t)}{\mathrm{d}t} \frac{\nabla I(\boldsymbol{x},t)}{\|\nabla I(\boldsymbol{x},t)\|} \tag{4.5}$$

in the direction of the gradient vector, but this leaves the solution to the orthogonal complement velocity component $\boldsymbol{v}^{\parallel}$ floating [62] meaning all values are valid. This is especially visible when the features that participate in that motion are small and unconnected or partly hidden behind other features hence the name "aperture" as seen in Fig. 4.1. It is obvious

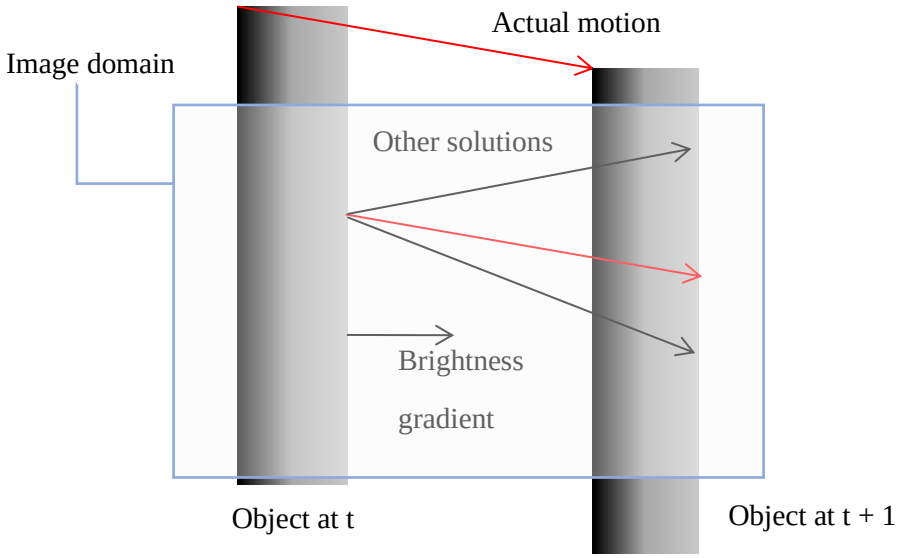


**Figure 4.1. :** Aperture problem.

that no solutions are found if the gradient $\nabla I(\boldsymbol{x}, t)$ vanishes, this is another issue that needs to be accounted for. Objects that appear in one frame and disappear in another also pose issues. This is a type of occlusion say at the edges of the image domain, but also evident in planar images with out of plane motion.

Experimentalists familiar with seeded flowfield imaging for velocimetry observe that the aperture problem does not arise in the correlation algorithm which samples a range of pixels to obtain a single velocity vector. Such methods are not dense methods, in that they do not generate displacement fields for each pixel. This limits the resolution of the motion field and introduces smearing errors especially when derivatives are to be computed based on spatial variation.

Horn and Schunck (HS) [62] were early adopters of the brightness constraint. They proceed in their paper using the linearized brightness constancy expression eq. 4.3. They identified following a similar analysis as was done in eqs. 4.3, 4.4 and 4.5 that using the

brightness constancy assumption alone, the motion field solution to optical flow constitutes an ill-posed problem, namely one that attempts to identify two components of displacement from a single scalar equation. HS thereafter impose a series of smoothness constraints, additional heuristic equations that lift the ill-posedness of the inverse problem. Practically it means neighboring vectors point in the same general direction, within some region. This smoothness equation provides "regularization" to this ill-posed problem. Not only does it fill in solutions where it is ill posed, it also fills in solutions where the gradient vanishes, or significantly exceeds the local values such as the disappearing object.

In practice, the problem is solved using a variational approach modeled with an energy functional that penalizes the deviation from brightness constancy (data term - $f_{data}$) as well as deviations from smoothness (regularization - $f_{reg}$). The formulation of these energy functionals is typically done using three parameters that can contribute to the definition of an "error" or model residuals in the estimation of the motion field. These are the data term, the regularization and the penalty function. We start with the penalty function. HS use a quadratic functional, with an estimator

$$\begin{aligned} \hat{\boldsymbol{v}} &= \arg\min_{\boldsymbol{v}} J_{data}(I(\boldsymbol{x}), \boldsymbol{v}(\boldsymbol{x})) + \alpha J_{reg}(\boldsymbol{v}(\boldsymbol{x})) \\ &= \arg\min_{\boldsymbol{v}} \frac{1}{2} \int \left[f_{data}(I(\boldsymbol{x}), \boldsymbol{v}(\boldsymbol{x}))\right]^2 \mathrm{d}\boldsymbol{x} + \alpha \left[f_{reg}(\boldsymbol{v}(\boldsymbol{x}))\right]^2 \mathrm{d}\boldsymbol{x} \end{aligned} \tag{4.6}$$

also known as the $\mathbf{L}^2$ norm, which provides a non negative convex optimization problem suitable for minimization. Using the $\mathbf{L}^2$ norm implies an assumption that the model residuals follow the normal distribution, in other words, deviations from the minimum can be modeled as Gaussian noise which is not often the case. The quadratic functional is also problematic because it is flat near zero which is where the error accumulates. To obtain better results, the optimization algorithm should require functionals with less strict penalization wherever the residual values accumulate. It should also require that the function be insensitive to outliers from the assumed model - termed robustness, since they are less sensitive to model outliers namely spatial discontinuities in the motion field. Improvements tend to result in functions with finite limit at infinity. Optimization of energy functionals formulated in terms of the $\mathbf{L}^1$ norm require gradual solutions because a straight line is both convex and non-convex. Early

on Black and Rangarajan implemented a non-local smoothing penalization which preserves edges using line processes adapted to robust estimation [61]. The line process locates the occurrence of discontinuities. The modified penalty function adjusts to keep the discontinuity dominant against smoothness wherever present. Some more-robust penalizations were considered such as the Charbonier function similar to the family proposed by Geman and Reynolds [63]

$$g_c(f_{data}, \sigma) = \left[f_{data}^2 + \sigma^2\right]^{0.5} \tag{4.7}$$

the function proposed by Geman and McClure [64], for line processes for edge preserving image restoration

$$g_{gm}(f_{data}, \sigma) = \frac{f_{data}^2}{f_{data}^2 + \sigma^2} \tag{4.8}$$

the exponential function proposed by Leclerc [65],

$$g_l(f_{data}, \sigma) = 1 - \mathrm{e}^{-f_{data}^2/\sigma^2} \tag{4.9}$$

and a function based on minimizing the model residuals. In practice, the minimization is replaced by a minimization in terms of associated optimal weight functions which for the robust penalization of model residuals is

$$w_{mr}(f_{data}, \sigma) = \frac{\sigma^2}{f_{data}^2 + \sigma^2} \tag{4.10}$$

and for the robust penalization by Leclerc is

$$w_l(f_{data}, \sigma) = \mathrm{e}^{-f_{data}^2/\sigma^2} \tag{4.11}$$

for example. The estimate is obtained by replacing the quadratic $g$ for the data term in eq. 4.6 for example with a minimization of the form

$$\begin{aligned}
\hat{\boldsymbol{v}}(w) &= \arg\min_{\boldsymbol{v}} \int \left( \mathrm{d}\boldsymbol{x} \tau w f_{data}(I, v(\boldsymbol{x}))^2 + \psi(w) \right) \\
&= \arg\min_{\boldsymbol{v}} \int \left( \mathrm{d}\boldsymbol{x} \tau w f_{data}(I, v(\boldsymbol{x}))^2 \right) \text{ for stationary } w \\
&\quad \text{and with stationary } f_{data} \\
\hat{w} &= \frac{g'(f_{data}(I, v(\boldsymbol{x})))}{2\tau f_{data}(I, v(\boldsymbol{x}))} = \sigma^2 \phi'(f_{data}(I, v(\boldsymbol{x})^2) \\
\psi &= \phi \circ (\phi')^{-1}(\tau w) - (\tau w)(\phi')^{-1}(\tau w),\ \sigma^2 = \tau^{-1} \\
&\quad \text{if } \phi = g(\sqrt{f_{data}(I, v(\boldsymbol{x}))}),\ \tau = \lim_{f_{data} \to 0} \phi' < \infty
\end{aligned} \tag{4.12}$$

since both estimations have the same global minimum in $\boldsymbol{v}$[66]. The optimal weight function is quadratic for stationary $w$ because the graph of $g$ is the inferior envelope of a family of parabolas continuously indexed by $w$ [66]. One benefit of the replacement of the penalty function $g$ with a quadratic is that the derivatives of the quadratic are linear in the data term which is not costly to implement. In this work, we chose the **Leclerc** penalization for the data term and the quadratic penalization for the regularization term for ease of implementation. We may now restate the definition of optical flow as a method that obtains apparent *dense* motion fields from a pair of image frames using a global minimization algorithm. In addition to the aperture problem there is also the issue of interpreting from the optical flow the relative motion between the camera and the object in focus. In this work, all images are obtained from a fixed camera and fixed test rig. The entire motion field is thus contributed to from the motion of the tracer in the flow.

## 4.1 The Data Term and Regularization

There are two terms in the energy functional for variational optical flow. The first is the data term. Two kinds are treated here with some detail. They are the displaced frame

difference (dfd) data term based on eq.4.2 and the optical flow constraint (ofc) data term based on

$$I_1(\boldsymbol{x}) - I_0(\boldsymbol{x}) + \boldsymbol{v}(\boldsymbol{x}) \cdot \nabla I_1(\boldsymbol{x}) = 0 \tag{4.13}$$

The data term is a difference that models the residual error. The terms $I_0(\boldsymbol{x})$ and $I_1(\boldsymbol{x})$ are the first and second frames used for motion field extraction. The partial time derivatives have been replaced with the difference $I_1(\boldsymbol{x}) - I_0(\boldsymbol{x})$: Either interpreting the difference as over unit time, or the motion field as displacement vectors. Regularization compensates for the incompleteness of the dense optical flow by filling in vectors in locations where the aperture problem and the vanishing gradient return no useful solutions for the data term. The dfd data term is more accurate with small displacements, and though the ofc data term is less accurate for small displacements, it produces less residual errors for high displacements.

There are a few regularization models as well. HS implemented a smoothing model that penalizes strong gradients of the velocity components.

$$J_{regHS}(\boldsymbol{v}) = \frac{1}{2} \int |\nabla v_1(\boldsymbol{x})|^2 + |\nabla v_2(\boldsymbol{x})|^2 \mathrm{d}\boldsymbol{x} \tag{4.14}$$

Penalization of smoothness is not restricted to the gradients of the components, penalizing combinations of the gradient and/or divergence of the vector field has also been done. The gradient of divergence regularization

$$J_{regGD}(\boldsymbol{v}) = \frac{1}{2} \int |\nabla \nabla \cdot \boldsymbol{v}(\boldsymbol{x})|^2 \mathrm{d}\boldsymbol{x} \tag{4.15}$$

is one such example. There are also regularizations that penalize the $\mathbf{L}^2$ norm of the components of the vector

$$J_{regL2}(\boldsymbol{v}) = \frac{1}{2} \int |v_1(\boldsymbol{x})|^2 + |v_2(\boldsymbol{x})|^2 \mathrm{d}\boldsymbol{x} \tag{4.16}$$

In this work, the **Horn and Schunck** regularization used was implemented with the quadratic penalty model to prevent loss of information by enforcing a constant source in the continuity equation $\nabla \cdot \boldsymbol{v} = c$ as in incompressible flows. There is also the requirement to balance the effects of smoothing where the results are valid. This is captured by the

$\alpha$ parameter in eq. 4.6 although the choice of this parameter is data specific. It may be beneficial to use non-local smoothing with line processes like the penalty functions described in the previous section. More recent methods developed from identifying that better optical flow statistics were obtained when a pre-smoothing operation is carried out prior to using the optical flow algorithm. This pre-smoothing increases the contribution of far away lattice points to the regularization at any one point. In fact when the pre-smoothing operation is carried out, the energy or error is larger than that of the un-smoothed data, indicating that the energy functional is as it is cast, is not what is truly minimized for increased accuracy. The non-local penalty function in the work by Sun, Roth and Black formalizes this [67]. In this work all data is **pre-smoothed with a Gaussian filter** with a 2.5 pixel kernel radius.

## 4.2 Pyramidal Approaches to Large Displacements

The assumption of small displacements can be made more quantitative. In recent validation efforts on a fluid dedicated optical flow code by Derian, [68] it was identified that the maximum displacement in pixels where the average RMS error

$$RMSE(\boldsymbol{v}) = \sqrt{\left(\frac{1}{N_{pix}}\sum_{\boldsymbol{x}} |\hat{\boldsymbol{v}}(\boldsymbol{x}) - \boldsymbol{v}_{gt}(\boldsymbol{x})|^2\right)} \tag{4.17}$$

was minimized was of the order of 5 pixels. The RMS error is one quantity in the work by Derian that was used to compare the optical flow results from a slice of the DNS scalars to the DNS velocity field from that sclice. The terms in the difference are the flow velocities $\boldsymbol{v}_{gt}(\boldsymbol{x})$ (ground truth) and the estimated velocities $\hat{\boldsymbol{v}}(\boldsymbol{x})$. Data from a free shear flow (Inhomogeneous turbulence) experiment and a wall bounded flow (cylinder wake) experiment were used for this validation visualized with *particles* of size less than 2 pixels. These particles were generated from passive scalars from a DNS dataset whose statistics are quite similar to that of experimental DNS. The particles are also obtained from a single plane. Using the passive scalars, the error did not increase significantly after the initial decrease, however the minimum error obtained using the scalars is higher than that using particles.

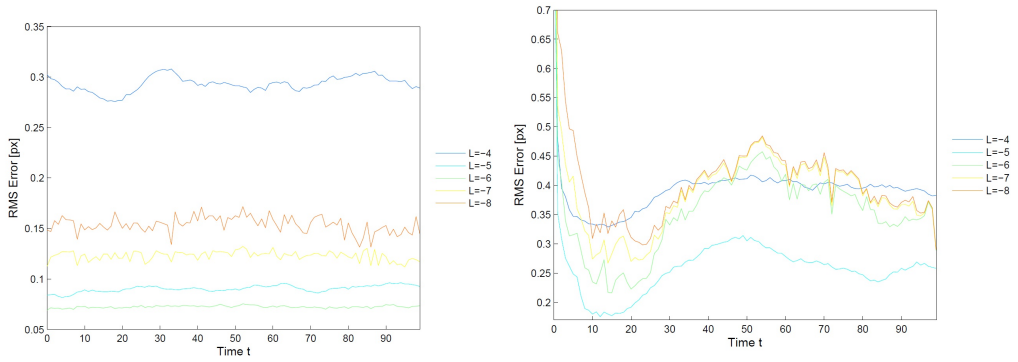


**(a)** Particles **(b)** Scalars

**Figure 4.2. :** Finding the optimum displacement from synthetic particles and scalars. Lines with different values of L indicate different fine level reconstructions. Reproduced from Derian [68]

Derian's work [68] forms the basis on which the velocimetry portion of this work is outlined. The wavelet optical flow code authored by Derian and coworkers at HAL INRIA the french national institute for research in digital science and technology, was generously shared as is to the author. In Derian's validation, it was further emphasized that for optical flow computations where "ground truth" or another method of computing motion field vectors is unavailable, qualitative methods need to be used to identify good enough displacement for accurate vectors. *Particles* have sharper edges, than *scalars*. This work uses **scalars** to capture the motion field of a turbulent combusting flowfield.

The optimal displacement estimate can be used in the design of a high velocity visualization experiment. For example, in a high subsonic Mach number jet in crossflow optical experiment, an estimate of the pixel displacement required to resolve the flow provides guidance on the design repetition rate. Suppose the flow has a static temperature of 1700K, with air as the working fluid at Mach 0.6, the velocity is about 480m/s or 480000mm/s. A typical magnification of 10 pixel/mm converts this to 4800000 pixel/s. An adequate repetition rate required to resolve displacements between two images is 4.8/5MHz or 1µs between frames. Working with a high speed camera, a sufficient field of view (FOV) of the flowfield from a 5mm jet is 38.4mm x 28.8mm, which corresponds to 384 x 288 pixels. This repetition rate would limit the acquisition of such images to MHz type cameras. In this work the

images were obtained at 150kHz or 6.67μs between frames, "one order of magnitude" lower repetition rate than would be suggested heuristically from the estimate above. Said another way, it implies the interframe displacement is about 35 pixels. In order to capture the large displacements in comparison to the estimated optimal displacement, an approach is needed to bring patterns displaced $> 5$ pixels away closer together.

Pyramidal approaches are implemented in optical flow to cater to large displacements by filtering and subsampling. The more familiar pyramidal approach starts with the finest resolution, the image pair, low pass filtering prior to subsampling returns an image with half the length and width of the original image, possibly bringing any displaced brightness patterns within the optimal displacement range. The process is repeated on the subsampled image if necessary - forming the pyramid.

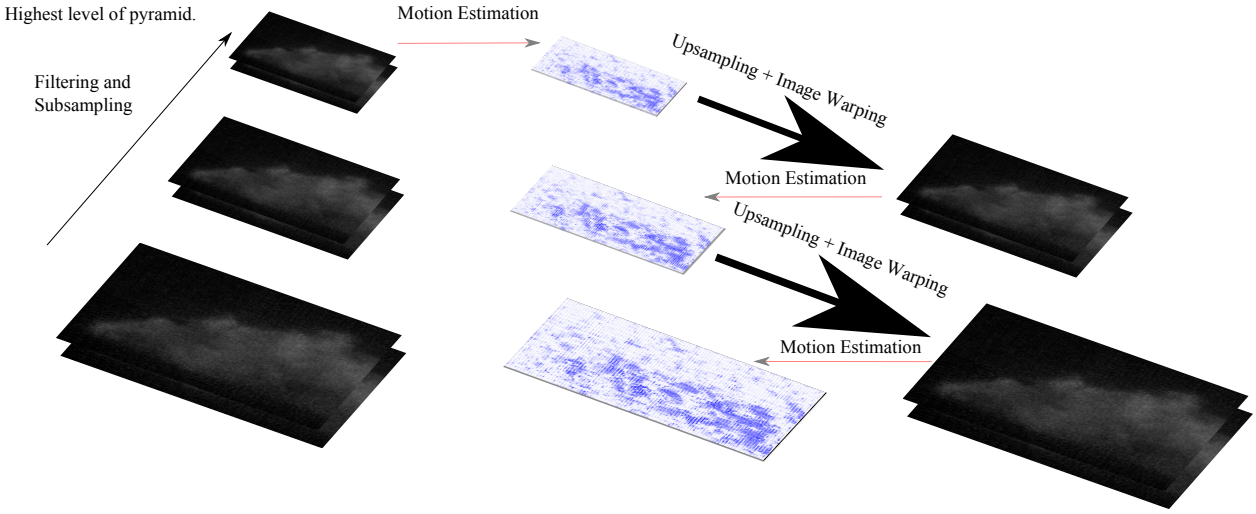


**Figure 4.3. :** Classical pyramid technique for dealing with large displacements.

The coarsest resolution, the smallest image pair is used for motion estimation. At this pyramid level, the motion field generated corresponds to the largest features in the image pair. Fine details are lost as a result of the smoothing operation prior to subsampling. If these features are only present at lower pyramid levels, they may still suffer from the large displacement problem. The motion field from the smallest image pair is upsampled to the size of the next level below and used to dewarp the second image of the pair to be ideally closer to the first. The concept of scale is useful for the mathematical formulation. By scale,

$\mathrm{j} \leq 0$ it is meant the exponent of base 2 in a $2^{-F} \times 2^{-F}$ image, such that to downsample is to increase the scale. The zero scale corresponds to the coarsest resolution. The resolution is expressed in terms of exponents of the scale. A scale $\mathrm{j} = -3$ corresponds to a resolution $2^{-\mathrm{j}} = 2^3 = 8$. Downsampling reduces the number of pixels to a quarter of the original image size, half in each dimension. In the case of the pyramidal approach, each motion field at scale j obtained on the way down the pyramid is computed from the motion compensated (dewarped) image pair (see Fig. 4.3). Each pyramid level thus contributes an increment $\delta \boldsymbol{v}^{\mathrm{j}}$ to the previous motion field at scale j.

$$\begin{aligned} \boldsymbol{v}^{\mathrm{j}} &= \tilde{\boldsymbol{v}}^{\mathrm{j}} + \delta \boldsymbol{v}^{\mathrm{j}}, \\ \text{where } \tilde{\boldsymbol{v}}^{\mathrm{j}} &= \sum_{\mathrm{j}<k} \mathcal{P}_{\mathrm{j}}(\delta \boldsymbol{v}^{k}) \text{ is the upsampled motion field} \end{aligned} \tag{4.18}$$

So that for at each resolution, using the optical flow constraint the contribution to the motion field satisfies

$$\begin{aligned} &\tilde{I}_1^{\mathrm{j}}(\boldsymbol{x}) - I_0^{\mathrm{j}}(\boldsymbol{x}) + \delta \boldsymbol{v}^{\mathrm{j}}(\boldsymbol{x}) \cdot \nabla \tilde{I}_1^{\mathrm{j}}(\boldsymbol{x}) = 0 \\ &\text{where } \tilde{I}_1^{\mathrm{j}}(\boldsymbol{x}) \stackrel{\text{def}}{=} I_1^{\mathrm{j}}(\boldsymbol{x} + \tilde{\boldsymbol{v}}^{\mathrm{j}}(\boldsymbol{x})) \text{ is the motion compensated } (\textit{dewarped}) \text{ image} \end{aligned} \tag{4.19}$$

and the final motion field contains contributions from upsampled motion fields up to the finest scale.

For the development of the non-classical pyramidal estimation, we need tools from a different analysis method called time frequency analysis.

## 4.3 Wavelet Based Optical Flow

### 4.3.1 Wavelets and Time-Frequency Analysis

A wavelet is a function comprised of a finite oscillation that is usually localized in space/time. It has origins in seismology, quantum mechanics, signal processing to say a few. It is defined such that this single function can be stretched and positioned in different portions of the time or frequency spectrum of a signal to capture local features. When fre-

quency analysis is required, scientists typically apply the tools and techniques of the Fourier transform

$$\hat{f} = (\mathcal{F}f)(\omega) = \int \mathrm{d}x f(x)\mathrm{e}^{-\mathrm{i}\omega x} \tag{4.20}$$

or the discrete version,

$$(\mathcal{F}f)_n = \int \mathrm{d}x f(x)\mathrm{e}^{-\mathrm{i}n\omega x} \tag{4.21}$$

to capture component frequencies either in the full signal or in a windowed portion of it. We will proceed from here with discrete analogs of these tools. To motivate the use of the wavelet transform, we will describe the behavior and shortcomings of Fourier transform to image analysis. While the Fourier transform of a signal does poorly in identifying local features, the windowed Fourier transform

$$(\mathcal{F}f)_{m,n} = \int \mathrm{d}x f(x)\mathrm{e}^{-\mathrm{i}n\omega x} w(x - m\tau) = \int \mathrm{d}x \langle f, w_{m,n}\rangle \tag{4.22}$$

as its name implies is defined with partly overlapping windows

$$w(x - m\tau) \text{ s.t.} \int \mathrm{d}x \|w(x)\|^2 = 1 \text{ with } \omega\tau = 2\pi \tag{4.23}$$

with soft decay reducing the artifacts of the tool at the expense of resolution. We have here a discrete transform that creates an $(m, n) \in \mathbb{Z}^2$ lattice in the time-frequency plane. The window is translated by $m\tau$ in time and by $n\omega$ in frequency so that within the window, higher frequency content are captured by increasing $n$ and by translating the window by $m\tau$ the full signal is captured. We can think of the window as a time-frequency atom that cannot be made arbitrarily small. This windowed Fourier transform is unitary, in that it maps the $L^2(\mathbb{R})$ vector space of functions of time onto the $L^2(\mathbb{R})$ vector space of functions of frequency. And because the window function can be chosen such that $\omega\tau = 2\pi$ so that $w_{m,n}(x) = w(x - m\tau)\mathrm{e}^{-\mathrm{i}n\omega x}$ is an orthonormal basis for the unit interval, it implies that the Fourier transform of the window function $\hat{w}_{n,m}(\xi) = (\mathcal{F}w)_{n,m} = \hat{w}(\xi + n\omega)\mathrm{e}^{-\mathrm{i}m\tau\xi}$ is in fact a window function in the frequency domain. Much like the Fourier transform, the windowed Fourier transform captures all the features of the original signal by filling the

window with higher frequency oscillations. It captures the $\mathbb{R}$ line by translating the window to new locations so that

$$\int \mathrm{d}x \|f(x)\|^2 = \int \mathrm{d}x \langle f, f \rangle = \sum_{m,n} \|(\mathcal{F}f)_{m,n}\|^2 \tag{4.24}$$

The r.h.s of the first equality identifies the square integral as an inner product. The second equality identifies the $\mathbf{L}^2$ norm with the $l^2$ norm. Replacing an integral with a finite sum of coefficients. This is brought about by the orthonormality of the windowed Fourier transform.

We want a similar behavior from wavelets that is, tilling the time-frequency plane, but perhaps with better properties.

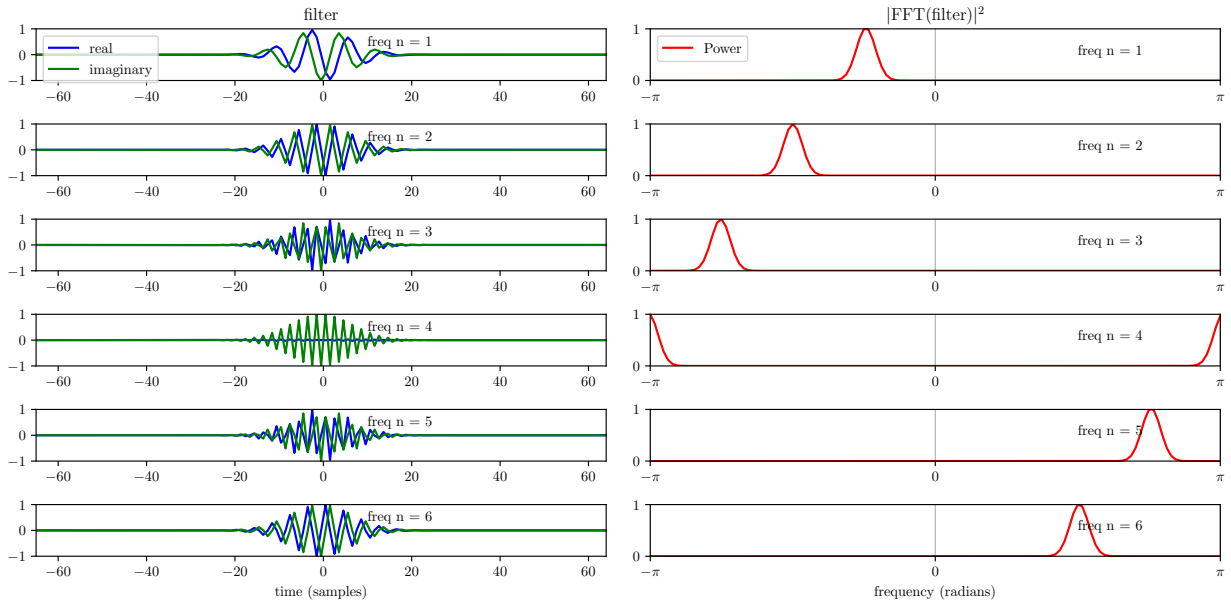


**(a)** Windowed Fourier transform captures frequency components by filling the same envelope with faster fluctuations

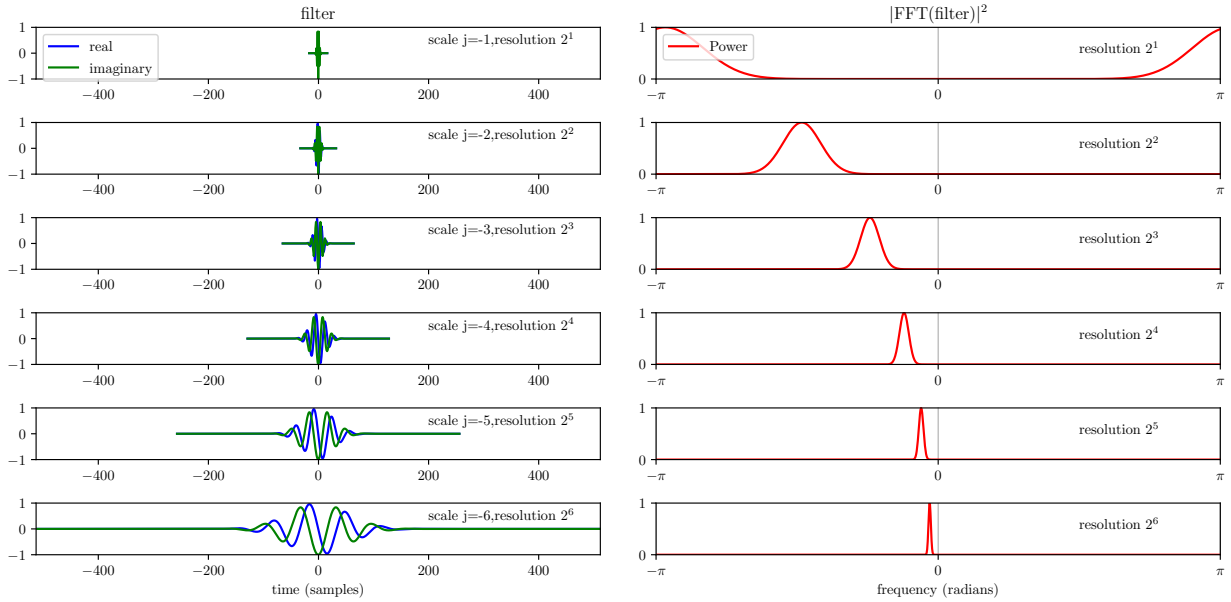


**(b)** Wavelet transform captures different scales of a signal by stretching the same function

**Figure 4.4. :** Correspondence between frequency (scale) and time. Comparison between complex Morlet wavelet with Bandwidth of 1.5 and center frequency of 1.0 and windowed Fourier transform.

In fact the wavelet replaces the window $w_{m,n}(x) = w(x - m\tau)\mathrm{e}^{-\mathrm{i}n\omega x}$, and since we expect it to tile the frequency spectrum, we find it is also indexed by two integers $(m, n) \in \mathbb{Z}^2$ so that we can also recover the full signal by translations in time and *some other* operation in frequency.

There exists a continuous analog of the discrete wavelet transform that allows us to reconstruct the signal from its time-frequency atoms. Although the discrete version is an extension of the continuous transform, in fact there is no unique formula for reconstructing the signal from its discrete transform - there are many. The discrete wavelet transform like the discrete Fourier transform takes the inner product of a function $f$ with a scaled and translated function $\psi$

$$(\mathcal{W}f)_{m,n} = \int \mathrm{d}x \langle f, \psi_{m,n} \rangle = \int \mathrm{d}x f(x) a_0^{-m/2} \psi(a_0^{-m} x - n b_0) \tag{4.25}$$

where $a_0, b_0 > 1$, and fixed. $a_0 = 2$ for the ease of implementation in this report. The family of functions $\psi_{m,n}$ are called wavelets and $\psi$ is called the mother wavelet. It is overcomplete in the sense that it provides a two variable function for a one variable input - with a few more basis vectors than the space requires. The wavelet transform allows the study of the frequency contents of a signal at a resolution that is **scale** specific. For the reconstruction, we will use the fact that the function is redundant - overcomplete, with a tool called multiresolution analysis.

### 4.3.2 Multiresolution Analysis and Images

Images are made up of pixels of finite width and height over which the intensity is constant. Digital images make up a vector space of square integrable functions called $L^2(\mathbb{R})$ out of which the familiar Fourier analysis evolved. Our quest is to know what techniques can allow us to capture all or most of the information in a picture as well as analyze them on different scales. We wish to then construct a method of isolating information on each scale from that in all others, which is challenging since the information in one scale is usually embedded in the other, even though it may not be visible. One easy way to analyze signals in different non-overlapping regions is by using orthonormal bases. We thus wish to find

a basis set $\{\phi_i\}_{i\in\mathbb{Z}}$ that spans $L^2(\mathbb{R})$ but whose non-overlapping regions span subspaces that completely describe the information at a given scale and reconstructed recreates the original image. These are the very questions that arise in many fields of signal processing that gave rise to a multiresolution analysis. In the next few paragraphs, we will define a multiresolution analysis - a technical hurdle, identify the wavelet transform in it, motivate the choice of wavelets, and see the application to images.

The idea of a multiresolution analysis is akin to looking at averages and details of images. We expect for example that if we blur two nearby pixels of an image by averaging them and then take the difference between the original image and the blurred image, that the fine features of the original image will be what is left over. Once this is done, the resulting image could be replaced with one 4 times as small, by choosing the average value in the place of the two previous entries in each direction. Well nothing stops us from continuing this blurring and subtraction over multiple "nearby" pixels for the blurred images and identifying the details at each of these scales. We see that all these averages or approximations and details are contained in the original image and that the subsequent scales are contained in the previous ones. The unique thing about multiresolution analysis is that a single function called a scaling function, when dilated and translated fulfills all requirements of capturing all the approximations and details in every scale. This is the **wavelet version of the pyramidal approach** to large displacements. Because information can be extracted in a scale specific way, it lends naturally to calculations of velocity in flowfields since turbulence transfers energy and momentum through scales. Furthermore, some property of the multiresolution analysis that allows it to describe any space densely, will suggest the analysis of the optical flow problem in the space of wavelet coefficients. This property - that it is *dense* - means the topological closure of the union of all subspaces is the whole space. In the image analog, the addition of all the details of the images produces the original image and can be extended to images of any size.

If we look at a horizontal band through an image of height one pixel, one may obtain a line graph like Fig. 4.5

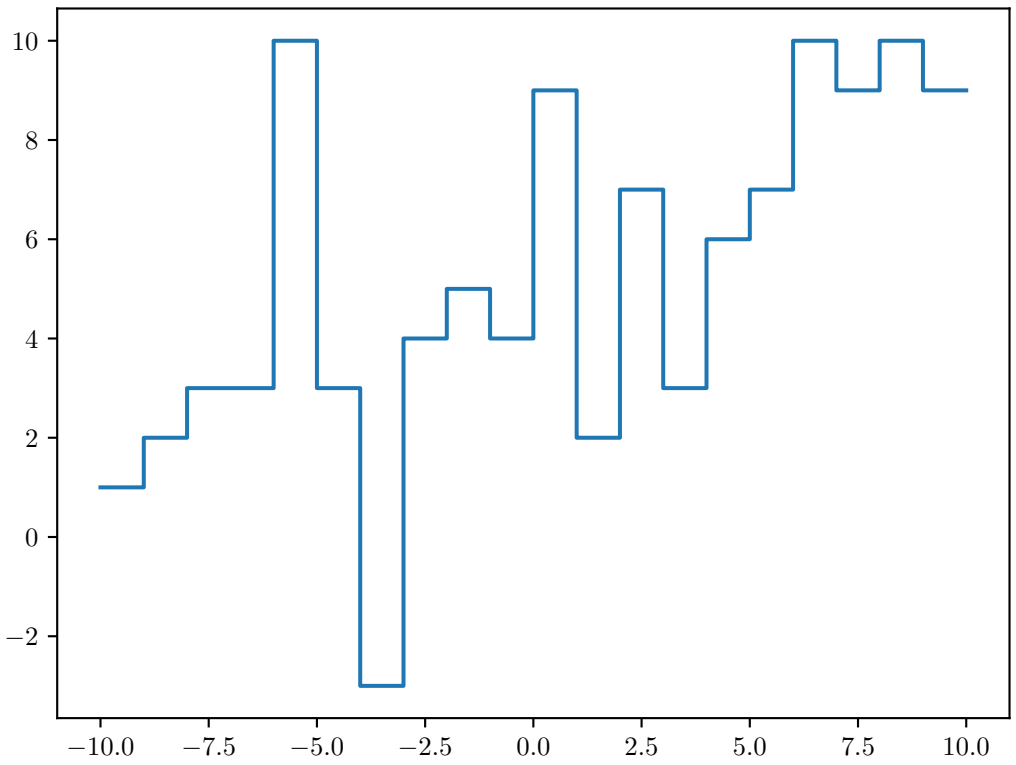


**Figure 4.5. :** Horizontal band of height one-pixel through image.

with the width of the pixels exaggerated.

Since the discrete wavelet transform provides a redundant or overcomplete approximation for individual subspaces, we will use the wavelet transform to create our orthonormal basis. The requirements for a set to construct an orthonormal basis for $L^2(\mathbb{R})$ are that

- the set $\{\psi\}_{\mathrm{j}}$ spans the space. Meaning the set contains an independent minimum number of entries equal to the cardinality of the space. It also means any element in the space can be constructed by a linear combination of these elements. If $f \in L^2(\mathbb{R})$, $f = \sum_{\mathrm{j}} c_{\mathrm{j}}\, \psi_{\mathrm{j}}$ where $c_{\mathrm{j}} = \langle f, \psi_{\mathrm{j}} \rangle$
- The inner product of any two entries in the set is zero $\langle \psi_{\mathrm{i}}, \psi_{\mathrm{j}} \rangle = \delta_{\mathrm{i,j}}$ where $\delta_{\mathrm{i,i}} = 1$ and zero otherwise.

Some definitions are going to help describe the theory. The next few paragraphs are highly mathematical (requiring proofs) and the interested reader is encouraged to read along or skip to the next section. The domain of a function that it does not map to zero is of interest here since we define wavelets as zero average functions. This region that does not map to zero is defined as the support of the function. We aim here to show that a wavelet creates a multiresolution analysis of $L^2(\mathbb{R})$ and for that we shall use a wavelet function called the Haar wavelet [69], but the results apply in general. The relationship between the wavelet and the scaling function will be revealed in the next subsection. We follow the progression in chapter 1 of Ingrid Daubechies' book "Ten lectures on wavelets"[70]. The Haar wavelet

$$\psi(x) = \begin{cases} 1 & 0 \leq x < \frac{1}{2} \\ -1 & \frac{1}{2} \leq x < 1 \\ 0 & \text{otherwise} \end{cases} \tag{4.26}$$

is part of a family of wavelets with variable scale and support $\psi_{m,n} = 2^{-m/2}\,\psi(2^{-m}x - n)$, where $\psi(x)$ is the mother wavelet. It is indexed by scale $m$ and translates $n$. Recalling section 4.3.1, the way the wavelet tiles the time frequency plane is by dilation (changing scale) and translation: the second index $n$ of the wavelet $\psi_{m,n}$ identifies how the wavelet is translated at the same scale, so that summing across that index, adds wavelets adjascent to the previous instance. What is left is to show that the $\psi_{m,n}$ are orthonormal and that they can construct any function in $L^2(\mathbb{R})$. The support of the Haar wavelet is the open interval $[2^m n, 2^m(n+1)[$, where the right open square bracket shows that the interval is open on the right. The mother wavelet $m = 0$ has a support of $[2^0 n, 2^0(n+1)[ = [0, 1[$ for n=0, and is open at $x = 1$ for example, see eq. 4.26. For an orthonormal basis, the basis functions need to have zero inner product to show independence. Because discrete wavelets are supported on intervals of fixed scale ($m = 0$ for the mother wavelet), the overlap of two Haar wavelets of different scale produces zero inner product $\langle \psi_{m,n}, \psi_{m',n} \rangle$ (see Fig. 4.6). This is evident since the product is computed with the wavelet with smaller support contained where the wavelet with larger support is constant and the wavelet has zero average.

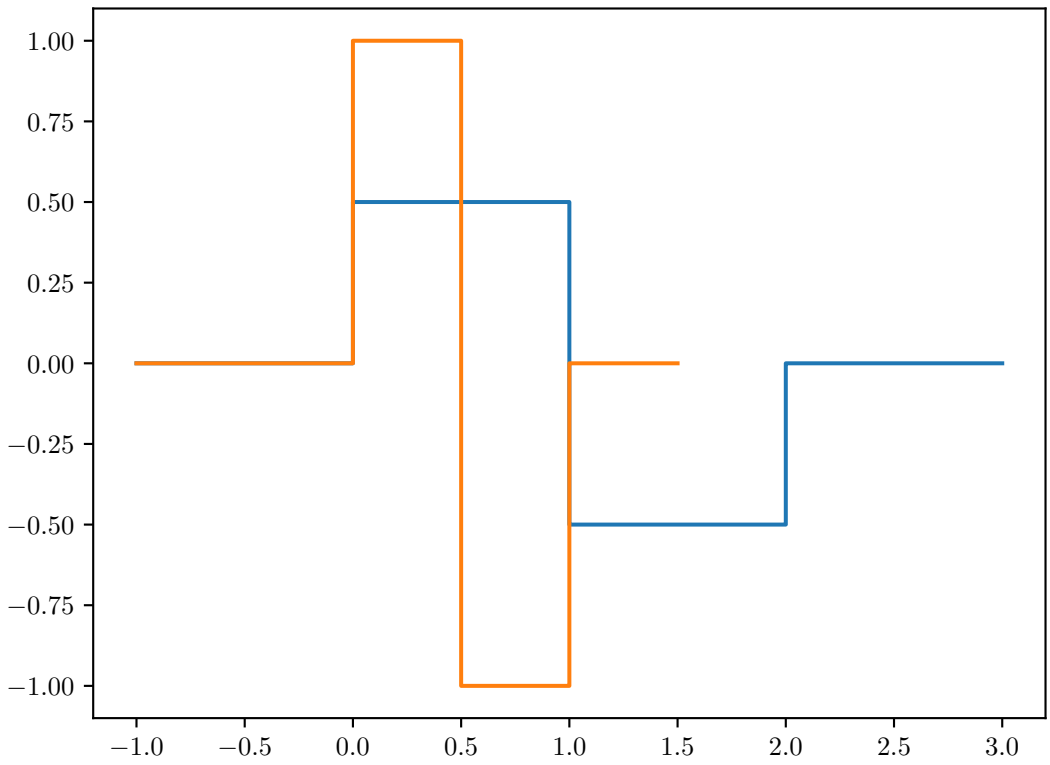


**Figure 4.6. :** Haar Wavelets of different scale with overlapping support.

Also wavelets of the same scale do not overlap.

What is left for an orthonormal basis is to show that the wavelet $\psi_{m,n}$ constructs any function $f$ in $L^2(\mathbb{R})$. For this we assume the functions $f$ are piece-wise constant since we can approximate $f$ up to any scale by making the constant portions small enough. We will use subscripts to indicate the instances of these piecewise portions. We further assume that $f$ is supported on $[-2^{J_1}, 2^{J_1}]$ and piece-wise constant on $[2^{-J_0}\ell, 2^{-J_0}(\ell+1)[$. We let $J_0$ & $J_1$ be as large as needed.

For the next few paragraphs of the proof and **only** here, we let the scale j run from 0 at the finest to $\infty$ at the coarsest. In the images, we will reverse this notation, care will be taken to show when which notation is used. We choose $f$ to take the constant value $f^0$ on each instance, the superscript defines the scale. The approach using wavelets begins

when we express $f^0$ as the sum $f^1 + \delta^1$ of two functions at a coarser scale. Then for each translate $k$ of $f^1$, $f^1|_{[k\,2^{-J_0+1},(k+1)\,2^{-J_0+1}[} \stackrel{\text{def}}{=} f^1_k$, with the $f^1_k$ given by the average at the finer scale sampled twice as often $f^1_k = \frac{1}{2}(f^0_{2k} + f^0_{2k+1})$ and the $\delta^1$ by the difference. Another way to say it is that the function is decomposed into an average and a difference (again see Fig. 4.7).

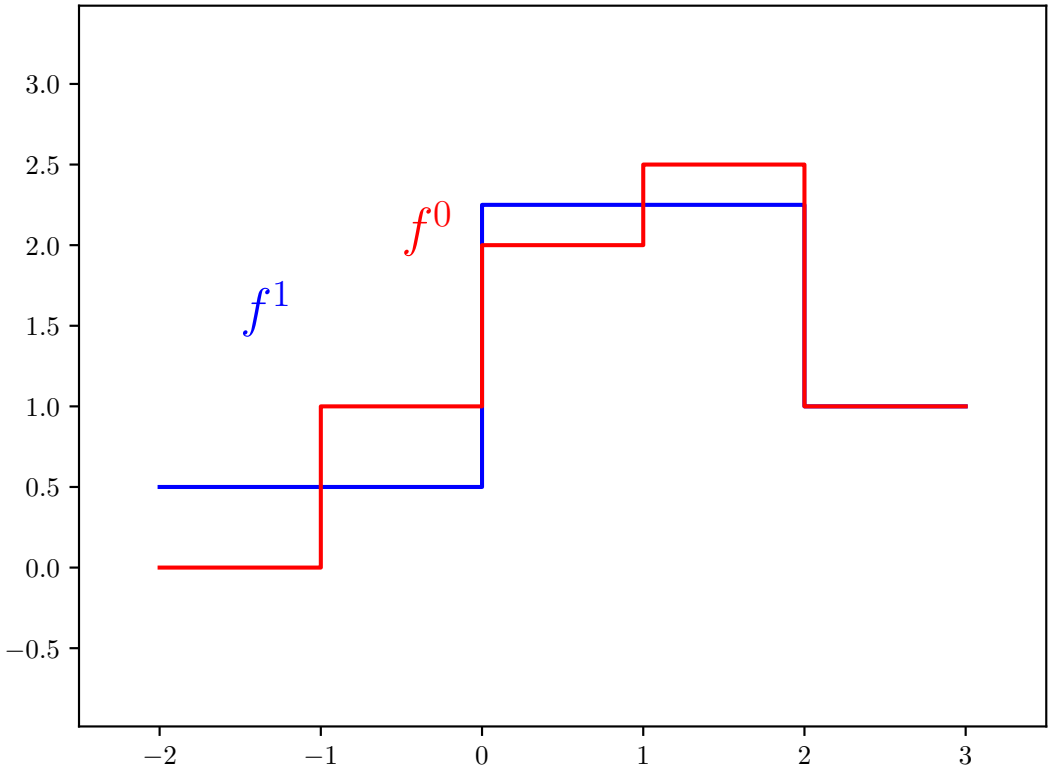


**Figure 4.7. :** Function $f$ is blurred to $f^1$. The difference highlighted.

Notice however that the $\delta^1$ have the same sampling stepwidth as $f^0$ with equal opposite values on either side of the average $f^1_k$ so though the counting is done in one scale, the sampling is done twice as often and so the index is of $\delta^1$ is $2\ell$ not $\ell$. Also

$$\begin{aligned} \delta^1_{2\ell} = f^0_{2\ell} - f^1_l &= \frac{1}{2}\left(f^0_{2\ell} - f^0_{2\ell+1}\right) \\ \text{so that the next value } \delta^1_{2\ell+1} = f^0_{2\ell+1} - f^1_l &= \frac{1}{2}\left(f^0_{2\ell+1} - f^0_{2\ell}\right) \\ &= -\,\delta^1_{2\ell} \text{ is the negative of the previous} \end{aligned} \tag{4.27}$$

We identify $\delta^1$ as a combination of Haar functions stretched and translated in the usual way. Recalling Fig. 4.7 notice that Fig. 4.8 contains the average $f^1_k$ and the differences $\delta^1$ composed to make the original function.

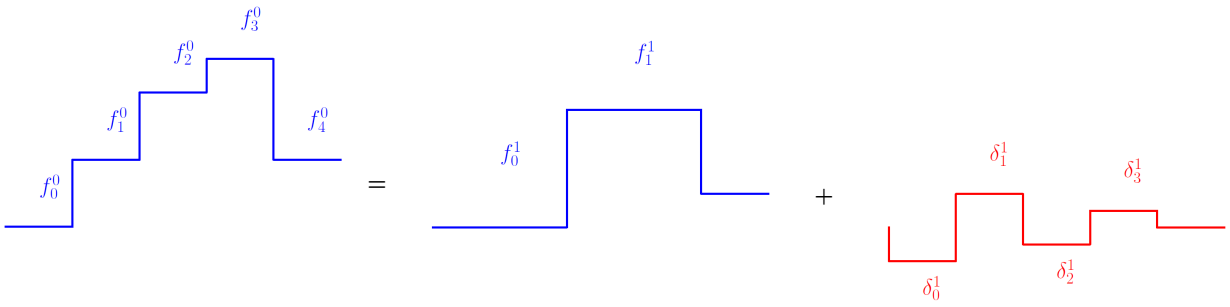


**Figure 4.8. :** Function $f$ is blurred to $f^1$. The difference is a linear combination of Haar wavelets.

The differences can be represented as a sum of Haar wavelets because the wavelets at the same scale do not overlap and the numbers $\delta^1$ are just the height of the Haar wavelet.

$$\begin{aligned} \delta^1 &= \sum_{\ell=-2^{J_1+J_0-1}+1}^{2^{J_1+J_0-1}} \delta^1_{2\ell}\,\psi\left(2^{J_0-1}x - \ell\right) \\ \text{so we may rewrite } f \text{ as } f = f^0 &= f^1 + \sum_\ell c_{-J_0+1,\ell}\,\psi_{-J_0+1,\ell} \\ \text{with the coefficients } c_{-J_0+1,\ell} &= \delta^1_{2\ell} \end{aligned} \tag{4.28}$$

It is important to note that addition of functions at one scale keep the result in that scale. $f^k_0 + f^k_1 = \sum_{\mathrm{i}} f^k_{\mathrm{i}}$ for example. The same result applies to scalar multiplication with

functions at each scale. Since there exists the identity under addition, namely the zero function and the identity under scalar multiplication namely the unit scalar, functions at each scale together with the added operations of addition and scalar multiplication and their identity elements form a vector space $V$. We see that the basis vector in each scale is a piecewise constant function which we can call $\varphi$. Analogous to the Haar wavelet, these functions are piecewise constant and each $f^{\mathrm{j}}$ gives the height of the function. In summary if $f^{\mathrm{j}} \in V_{\mathrm{j}}$ then $f^{\mathrm{j}} = \sum_k c_k \, \varphi_{\mathrm{j},k}$.

We can continue at the next scale with

$$\begin{aligned} f^1 &= f^2 + \sum_\ell c_{-J_0+2,\ell} \, \psi_{-J_0+2,\ell} \\ \text{so that } f &= f^2 + \sum_\ell c_{-J_0+1,\ell} \, \psi_{-J_0+1,\ell} + \sum_\ell c_{-J_0+2,\ell} \, \psi_{-J_0+2,\ell} \\ &\vdots \\ \text{until } f &= f^{J_0+J_1} + \sum_{m=-J_0+J_1}^{J_0+J_1} \sum_\ell c_{m,\ell} \, \psi_{m,\ell} \end{aligned} \tag{4.29}$$

The support $[-2^{J_1}, 2^{J_1}]$ of each $f^{\mathrm{j}}$ is the same, but each is piecewise constant on a larger interval $[-2^{-J_0+\mathrm{j}}\ell, 2^{-J_0+\mathrm{j}}(\ell+1)[$ with increasing j. The $f^{J_0+J_1}$ term consists of two constant terms $f^{J_0+J_1}|_{[0,2^{J_1}[} \stackrel{\text{def}}{=} f_0^{J_0+J_1}$ and $f^{J_0+J_1}|_{[-2^{J_1},0[} \stackrel{\text{def}}{=} f_{-1}^{J_0+J_1}$ each spanning half the support of the function $f$ as seen in Fig. 4.9.

At this point we have the most blurred out version of the original function on its support. We see that a lot of the details of the function are stored in the differences $\delta$ and the left over portion is simple. We want to keep all the information in the differences. The rest of the proof is purely mathematical. Because we still have approximations of the function, to continue the blurring we need to increase the support. To increase the support, we notice that we can continue blurring out the function simply by taking averages to the nearest location.

The purpose of this second procedure is to extend the blurring to the full size of the space. In this case, the blurring out of the function does not preserve its support. Again the purpose is to keep all the information about the function in the differences $\delta$ and not the coarse approximation. At every step, the previous support $[-2^{J_1+J_2}, 2^{J_1+J_2}]$ is doubled to

$[-2^{J_1+J_2+1}, 2^{J_1+J_2+1}]$ and the resolution of the function at each scale decreases as original support increases. Since all we are doing is taking averages, we can always start with any function and extend it this way. To cast the support increased blurring succinctly if we let

$$
\begin{aligned}
f^{J_0+J_1+1}|_{[0,2^{J_1+1}[} &\stackrel{\text{def}}{=} \frac{1}{2} f_0^{J_0+J_1} \\
\text{and } f^{J_0+J_1+1}|_{[-2^{J_1+1},0[} &\stackrel{\text{def}}{=} \frac{1}{2} f_{-1}^{J_0+J_1} \\
\text{then the difference } f^{J_0+J_1} - f^{J_0+J_1+1} &= \delta^{J_0+J_1+1} \\
&= \frac{1}{2} f_0^{J_0+J_1} \psi\left(2^{-J_1-1}x\right) - \frac{1}{2} f_{-1}^{J_0+J_1} \psi\left(2^{-J_1-1}x+1\right)
\end{aligned}
$$

is again a linear combination of haar wavelets

(4.30)

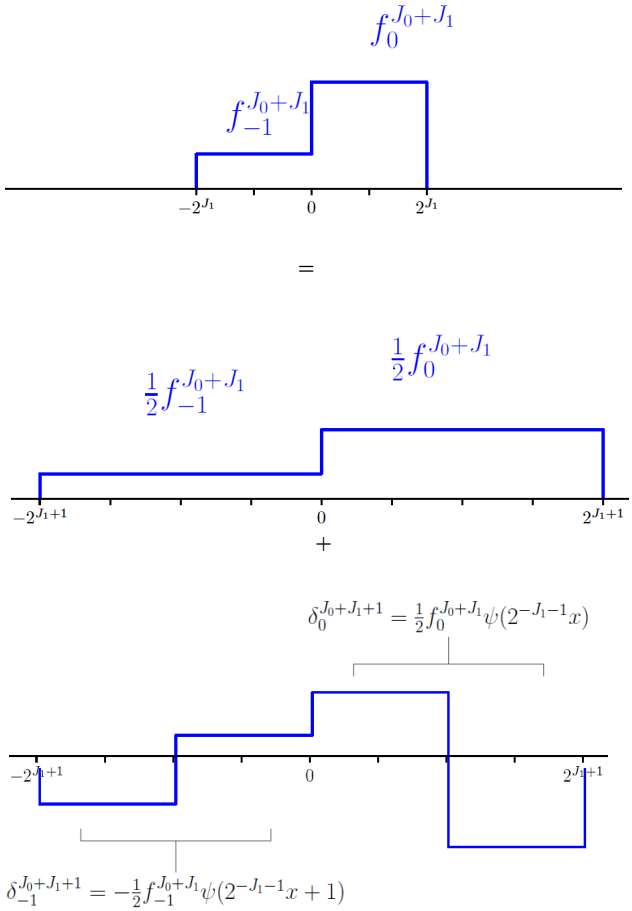


**Figure 4.9. :** $f^{J_0+J_1}$ is blurred to $\frac{1}{2}f^{J_0+J_1}$. The difference is a linear combination of Haar wavelets.

To generalize to functions in $L^2(\mathbb{R})$ on larger intervals, we merely repeat the process above to let

$$f = f^{J_0+J_1+K} + \sum_{m=-J_0+1}^{J_1+K} \sum_{\ell} c_{m,\ell}\, \psi_{m,\ell} \tag{4.31}$$

for $f^{J_0+J_1+K}$ with support $[-2^{J_0+J_1+K}, 2^{J_0+J_1+K}]$. Also similar to eq. 4.30

$$\begin{aligned} f^{J_0+J_1+K}|_{[0,2^{J_1+K}[} &= 2^{-K} f_0^{J_0+J_1+K} \\ \text{and } f^{J_0+J_1+K}|_{[-2^{J_1+K},0[} &= 2^{-K} f_{-1}^{J_0+J_1+K} \end{aligned} \tag{4.32}$$

So that the error

$$\left\| f - \sum_{m=-J_0+1}^{J_1+K} \sum_{\ell} c_{m,\ell}\, \psi_{m,\ell} \right\|_{L^2}^2 = \left\| f^{J_0+J_1+K} \right\|_{L^2}^2 = 2^{-K/2} 2^{-J_1/2} \left[ \left| f^{J_0+J_1} \right|^2 + \left| f^{J_0+J_1} \right|^2 \right]^{0.5} \tag{4.33}$$

can be made arbitrarily small by taking $K$ large enough because of the exponential relation. We can thus start with any function and create a multiresolution analysis within its support or extended to the whole space using wavelets.

In summary we notice that the idea of multiresolution analysis (MRA) is that at each level of a function approximated with piece-wise constant functions, we can write the function as a sum of coarse approximations and that the difference between the approximation at resolution $2^{\mathrm{j}}$ and $2^{\mathrm{j}-1}$ is a linear combination of wavelets $\psi_{\mathrm{j},k}$. These levels form a ladder of contained subspaces $\{V_{\mathrm{j}}\}_{J\in\mathbb{Z}}$

### Properties of MRAs

In the previous subsection 4.3.2, the necessity of an MRA was motivated by the need for nested subspaces $\{V_{\mathrm{j}}\}$ that are independent. We then proved that MRAs satisfy this requirement. The spaces $\{V_{\mathrm{j}}\}_{\mathrm{j}\in\mathbb{Z}}$ have the properties that

Property 4.1

(i) $\forall \mathrm{j} \in \mathbb{Z}, V_{\mathrm{j}+1} \subset V_{\mathrm{j}}$ forming the ladder of nested subspaces

(ii) $\forall \{\mathrm{j}, k\} \in \mathbb{Z}^2, f(x) \in V_{\mathrm{j}} \Leftrightarrow f(2^{-\mathrm{j}}x - k) \in V_{\mathrm{j}+1}$ so that translates of a function stay in the original space

(iii) $\forall \mathrm{j} \in \mathbb{Z}, f(2x) \in V_{\mathrm{j}} \Leftrightarrow f(x) \in V_{\mathrm{j}+1}$ so that dilates of the original function are the only allowed elements in the nested subspaces

(iv) $\cap_{\mathrm{j}\in\mathbb{Z}} V_{\mathrm{j}} = \{0\}$ as the spaces get smaller, the only vector in all subspaces is the zero vector

(v) $\overline{\cup_{\mathrm{j}\in\mathbb{Z}} V_{\mathrm{j}}} = L^2(\mathbb{R})$ the closure of the union of these subspaces is the whole space

Following the development in subsection 4.3.2 we see that a single function is required to generate all properties of the MRA. We saw that the function $\psi$ helps with the projection

$$\mathcal{P}_{V_{\mathrm{j}-1}} f = \mathcal{P}_{V_{\mathrm{j}}} f + \sum_{l\geq \mathrm{j}} \sum_{k\in\mathbb{Z}} \langle f, \psi_{l,k}\rangle \, \psi_{l,k} \tag{4.34}$$

of a function $f$ onto a nested subspace. The $\langle f, \psi_{\mathrm{j},k}\rangle$ on the rhs of eq. 4.34 is the wavelet transform of $f$. This nested projection only happens if in addition to the previous properties,

- $\exists\, \varphi \in V_0$ such that $\{\varphi(x-k)\}_{k\in\mathbb{Z}}$ constitutes an orthonormal or a *Riesz*[1] basis for $V_0$

But these properties are already obvious when we see that the blurred out features of a picture are in the original picture from property 4.1 (i) and property 4.1 (iii). And you **can** obtain the original picture by adding up all the details from property 4.1 (v). Also adding up two blurred pictures does not recreate the original for example from property 4.1 (ii). The unique thing that the MRA reveals is that we are able to carry out this blurring out of the picture by this process of averaging nearby pixels. The MRA tells us that the averaging is a feature of a single function $\varphi$ so that any given function that satisfies the last property will generate a unique series of nested subspaces. Said another way, there are different ways to average nearby pixels in an image, but in all cases the blurred out image is contained in the original.

The function $\varphi$ is called a scaling function. Since the $\{\varphi\}$ constitute a basis for $V_0$ any function $f(x) = \sum a_k \, \varphi(2x-k)$. And since the finer scale $\varphi_{-1,k}(x) = a_k \, \varphi(2x-k)$ with $a_k = \sqrt{2}\langle \varphi, \varphi_{-1,k}\rangle$, it is sufficient to use the scaling function to generate the wavelet by alternating between values in the fine scale.

$$\psi(x) = \sum_k (-1)^k \langle \varphi, \varphi_{-1,-k+1}\rangle \, \varphi(2x-k) \tag{4.35}$$

The unique aspect of the choice of wavelet function is that the scaling function that it is based on can be made to capture most of the features of the function so that the left over portion

[1]↑A sequence $\{q_k\}$ forms a Riesz basis for a Hilbert space $H$ if in addition to an orthonormal basis set $\{\mathrm{e}_k\}$ for $H$ there exists an invertible linear transformation $T$ such that $T\mathrm{e}_k = q_k$ for all k

is small. This choice is formalized by the support of the wavelet and scaling functions. In addition to the ladder of subspaces $\{V\}$, the portion that is left $\{W\}$ out is spanned by the wavelets.

$$V_{\mathrm{j}} = V_{\mathrm{j}+1} \oplus W_{\mathrm{j}+1} \tag{4.36}$$

From here on, the scales are indexed from $-\infty$ to 0 in order of increasing coarseness. This extensive proof applies to discretely sampled data (such as images) as follows: any discrete finite signal can be represented by approximations $a_{C,k} = \mathcal{P}_{V_C} f$ up to the chosen coarsest scale $C$ and details $d_{\mathrm{j},k} = \sum_{k\in\mathbb{Z}} \langle f, \psi_{\mathrm{j},k}\rangle \, \psi_{\mathrm{j},k}$ with

$$\begin{cases} a_{C,k} & C \in [F, 0] \\ d_{\mathrm{j},k} & \mathrm{j} \in [F+1, C] \end{cases} \tag{4.37}$$

A row of pixels across an image, is a sequence of numbers $z[n]$. This sequence is the digital representation of a line sampled discretely at intervals of $2^F$ with $F$ negative. A wavelet decomposition of this sequence, associates it with a function $f(x)$ in $V_F$. The association is carried out at the finest scale F and may be done by [71]

$$\begin{aligned} & f(x) = \sum_{n=0}^{N-1} z[n] \varphi(2^{-F} x - n) \\ & \text{assuming } f \text{ is ``regular''} \\ & z[n] = \sqrt{2^{-F}} a_{F,n} \quad \Longrightarrow \quad a_{F,n} = \frac{1}{\sqrt{2^{-F}}} z[n] \forall n \in \mathbb{Z} \end{aligned} \tag{4.38}$$

Once this function $f$ is obtained, we can approximate the function at any scale using the properties of the MRA. The association follows eq. 4.34 as follows

$$f = \mathcal{P}_{V_{\mathrm{j}}} f + \sum_{l=F+1}^{\mathrm{j}} \sum_{k\in\mathbb{Z}} \langle w, \psi_{l,k}\rangle \, \psi_{l,k} \tag{4.39}$$

The projections

$$\begin{aligned} \mathcal{P}_{V_\mathrm{j}} f &= \sum_k a_{\mathrm{j},k} \varphi_{\mathrm{j},k} \\ \text{and} \quad \sum_{k\in\mathbb{Z}} \langle f, \psi_{\mathrm{j},k}\rangle \psi_{\mathrm{j},k} &= \sum_{k\in\mathbb{Z}} d_{\mathrm{j},k} \psi_{\mathrm{j},k} \end{aligned} \tag{4.40}$$

It is obvious that there are smart ways to carry out this averaging procedure that are beneficial to images, which equals the choice of wavelet functions, to motivate which ones to choose, we start with some properties of wavelets.

### 4.3.3 Vanishing Moments and Regularity

That a wavelet function has $n$ vanishing moments implies (both ways) that

$$\langle \psi, x^p \rangle = \int_{\mathbb{R}} \mathrm{d}x \; x^p \psi(x) = 0, \text{ with } p \in [0, n[ \tag{4.41}$$

which means all polynomials to order $p$ are orthogonal to this function. The number of vanishing moments is related to the smoothness (regularity) of the function. This is not a one to one relationship. Smoother wavelets are better for describing abrupt changes in an image. This means the wavelet coefficients will have small values quickly - in other words, the scaling function captures most of the features of the function. Polynomials of degree less than or equal to $N$ can be generated by linear combinations of the scaling function. An orthonormal basis of wavelets can consist of $C^{N-1}$ wavelets (differentiable $N-1$ times) only if the mother wavelet has $N$ vanishing moments[70]. The number of vanishing moments usually increases with the support of a function. Ingrid Daubechies discovered a series of wavelets (Daubechies wavelets and Coiflets) that have compact support of width $(2N-1)$ so that in addition to having a high number $N$ of vanishing moments, can have low computational cost. The lowest member of these series happens to be the Haar wavelet from the previous section with 1 vanishing moment.

For small $N$, Daubechies wavelets and their scaling functions ${}_N\psi$, ${}_N\varphi$ are differentiable $N-1$ times. For large $N$, Daubechies wavelets are differentiable $\mu(N-1)$ times, with $\mu \simeq 0.2$

so that some zero moments are wasted. A small improvement can be obtained by sacrificing a few vanishing moments for regularity with the same support width. This is the case for Coiflets and introduces the requirements for a biorthogonal MRA. One obvious result of the sacrifice is that for a fixed support width, a number of vanishing moments can be traded for increased regularity. Compression algorithms require a high number of vanishing moments. Image processing however, where few translates are included in the wavelet representation, require higher regularity. In this work, **coiflets** are used which provide the twice the number of vanishing moments, for the wavelets and the highest level of symmetry to the compactly supported wavelets.

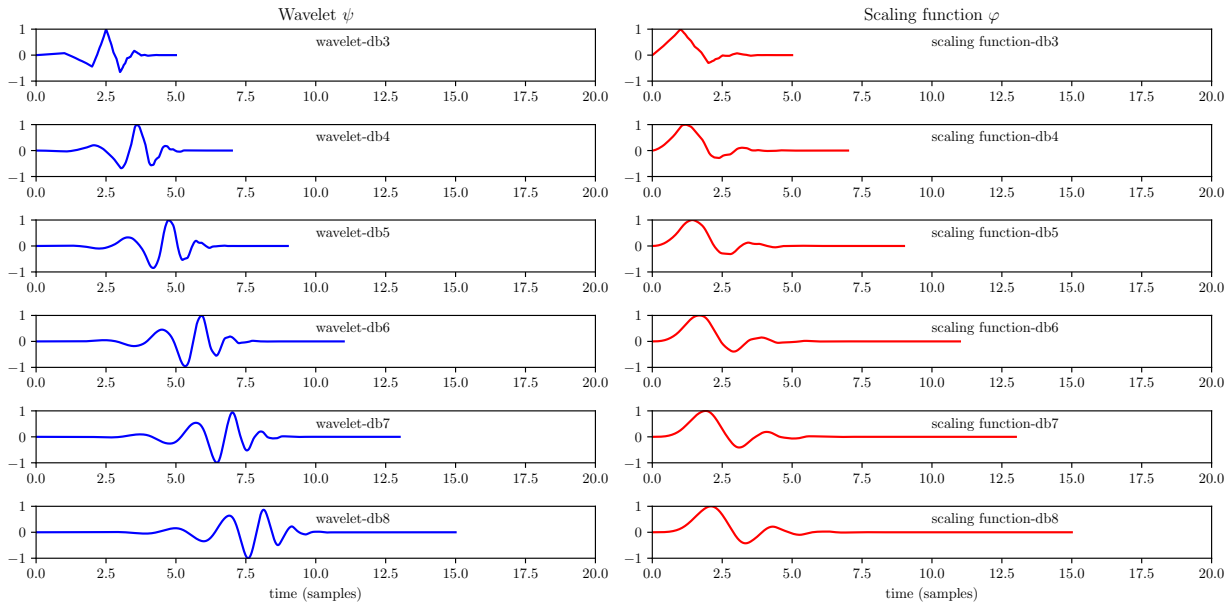


**(a)** Daubechies

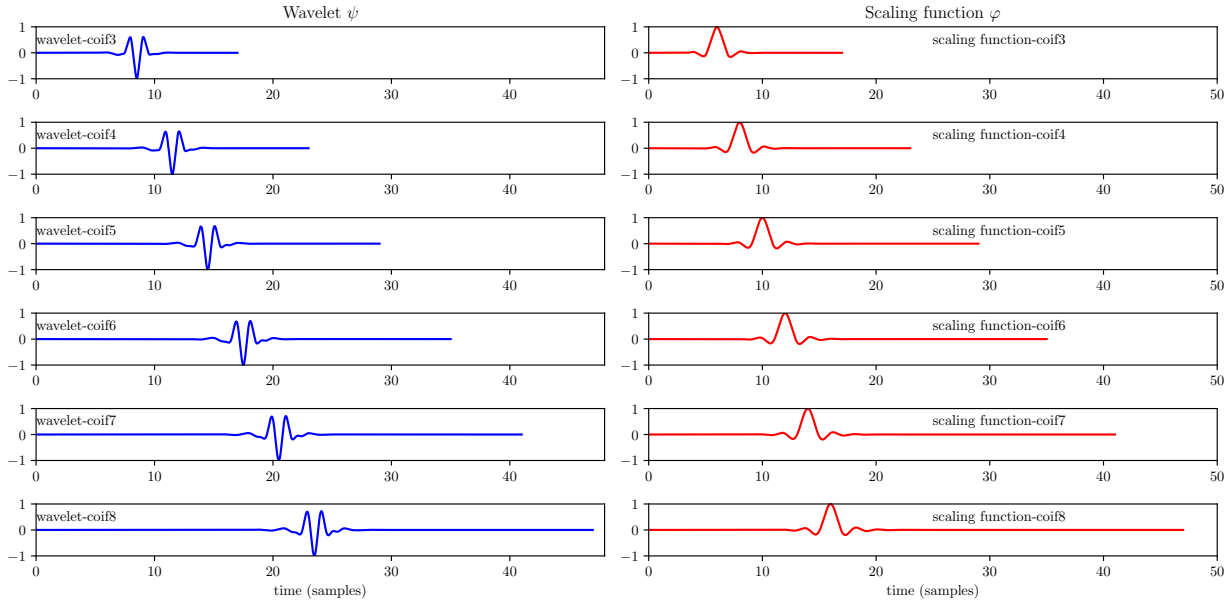


**(b)** Coiflet

**Figure 4.10. :** Daubiechies (dbN) and Coifman (coifN) wavelet and scaling functions, showing increased support width and regularity with N. Daubiechies (dbN) wavelets have $N = m$ vanishing moments while Daubechies scaling functions have ($N = 0$) vanishing moments. Coiflets (Coifman wavelets) have $N = 2m$ vanishing moments and Coiflet scaling functions have $N = 2m - 1$ vanishing moments.

The regularity of a wavelet also describes how fast it decays. A wavelet would gain its regularity from the regularity of the underlying scaling function, so it suffices to measure the regularity of either. Here again we see that the regularity is not identical to the number of vanishing moments as scaling functions do not in general have vanishing moments. There are many measures of regularity, and not one is uniquely tuned to wavelets with compact support because they are not infinitely differentiable. In addition, global estimates of regularity only prove decay of the fourier transform of the scaling function. Local estimates of smoothness or differentiability fluctuate depending on the direction of approach. For the local estimate of regularity, we can obtain a bound

$$|\psi(x) - \psi(x_0)| \leq K' 2^{-\alpha \mathrm{j}} \leq K|x - x_0|^{\alpha} \tag{4.42}$$

for $x - x_0 \in [2^{-(\mathrm{j}+1)}, 2^{-\mathrm{j}}]$. Which proves Hölder continuity with exponent $\alpha$. When a signal $f \in L^2([0,1])$ is projected onto a wavelet basis with $n$ vanishing moments, it is decomposed into approximations and details. If the function is Hölder continuous with exponent $\alpha < n$ then the function can be replaced with its Taylor series with as many terms as are well defined. The integral of the product of the function and the wavelet is zero. On the other hand, if the function is continuous with Hölder exponent $\alpha > n$ then the details at that scale are of amplitude dependent on $\alpha$.

### 4.3.4 Biorthogonal MRAs

The wavelet allows both time-frequency localization and representation of functions in scales. We will use two MRAs $\{V\}$ & $\{\tilde{V}\}$ to carry out the two functions of the wavelet. The second MRA is obtained if we do not assume the wavelet and scale spaces are orthogonal, instead

$$W_{\mathrm{j}+1} = V_{\mathrm{j}} \cap (\tilde{V}_{\mathrm{j}+1})^{\perp} \text{ with } \cdot^{\perp} \text{ the orthogonal complement} \tag{4.43}$$

This is called a biorthogonal MRA (BMRA). The bi-orthogonality comes from enforcing orthogonality between the second wavelet space and the first MRA. To complete the definition

of the two spaces, we let wavelet functions in the first space constitue a *Riesz* basis dual to those in the second. Two sets of *Riesz* basis are dual if

$$\begin{aligned}
&\langle \psi_{\mathrm{j},k}, \tilde{\psi}_{\mathrm{j}',k'} \rangle = \delta_{\mathrm{j},\mathrm{j}'}\delta_{k,k'} \\
&\text{with a non-zero inner product when the scale and location coincide, also} \\
&\langle \varphi_{\mathrm{j},k}, \tilde{\psi}_{\mathrm{j},k'} \rangle = 0 \\
&\text{the dual wavelet is orthogonal to integer translates of the scaling function} \\
&\langle \psi_{\mathrm{j},k}, \tilde{\varphi}_{\mathrm{j},k'} \rangle = 0 \\
&\langle \varphi_{\mathrm{j},k}, \tilde{\varphi}_{\mathrm{j},k'} \rangle = \delta_{k,k'}
\end{aligned} \tag{4.44}$$

The last equality is a consequence of the lack of interchangeability between the two spaces in general. In BMRAs, wavelets $\psi_{\mathrm{j},k} \in W_{\mathrm{j}}$ are dual to $\tilde{\psi}_{\mathrm{j},k} \in \tilde{W}_{\mathrm{j}}$. The wavelets in $W_{\mathrm{j}}$ are not in the orthogonal complement of $\tilde{V}$ in $V_{\mathrm{j}-1}$, so that $\tilde{W}_{\mathrm{j}+1} = \tilde{V}_{\mathrm{j}} \cap (V_{\mathrm{j}+1})^{\perp}$ also. The BMRA allows the analysis and synthesis roles of the wavelet to be split between two wavelets, one for synthesis (time-frequency localization) and the other for analysis. In addition, going between scales we use the following relations

$$\begin{aligned}
\varphi_{1,0}(x) &= \frac{1}{\sqrt{2}}\varphi\left(\frac{x}{2}\right) = \sum_k h\left[k\right]\varphi_{0,k}(x), \text{ with } h\left[k\right] = \langle \varphi_{1,0}, \tilde{\varphi}_{0,k} \rangle \\
\tilde{\varphi}_{1,0}(x) &= \frac{1}{\sqrt{2}}\tilde{\varphi}\left(\frac{x}{2}\right) = \sum_k h\left[k\right]\tilde{\varphi}_{0,k}(x), \text{ with } h\left[k\right] = \langle \tilde{\varphi}_{1,0}, \varphi_{0,k} \rangle \\
\psi_{1,0}(x) &= \frac{1}{\sqrt{2}}\psi\left(\frac{x}{2}\right) = \sum_k g\left[k\right]\psi_{0,k}(x), \text{ with } g\left[k\right] = \langle \psi_{1,0}, \tilde{\psi}_{0,k} \rangle \\
\tilde{\psi}_{1,0}(x) &= \frac{1}{\sqrt{2}}\tilde{\psi}\left(\frac{x}{2}\right) = \sum_k g\left[k\right]\tilde{\psi}_{0,k}(x), \text{ with } g\left[k\right] = \langle \tilde{\psi}_{1,0}, \psi_{0,k} \rangle
\end{aligned} \tag{4.45}$$

The sequences $\{h\left[k\right]\}_{k\in\mathbb{Z}}$, $\{\tilde{h}\left[k\right]\}_{k\in\mathbb{Z}}$, $\{g\left[k\right]\}_{k\in\mathbb{Z}}$ and $\{\tilde{g}\left[k\right]\}_{k\in\mathbb{Z}}$ are called conjugate mirror filters. Discrete wavelets are entirely defined by filter coefficients. The numerical implementation of the wavelet transform is based on these filters since there is no closed form expression for discrete wavelets with compact support. The fact that the coefficients contain only a finite number of terms ensures the wavelets have compact support - shorter computation time. That the signals themselves are also finite means there can be a mismatch of

the size of the wavelet support and the signal support. Boundary conditions are necessary for signal extension. In this work as in the work it is based on, **circular convolutions are used implementing periodic boundary conditions**. This causes artifacts where the boundaries are not periodic. There would otherwise be additional artifacts from using asymmetric wavelets, but the BMRA allows for symmetry. The periodic extensions are carried out over $L^2([0,1])$ by normalizing the length of the signal originally in $\mathbf{L}^2(\mathbb{R})$ to span $\mathbf{L}^2([0,1])$.

### 4.3.5 2-D MRAs and Wavelet Optical Flow

Recall that a 1-D signal $f$ such as an image, supported on $[0, 2^{-F}]$, can be projected onto a wavelet basis and then decomposed into a ladder(s) of subspaces

$$\begin{aligned} V_{\mathrm{j}} &= \mathrm{span}\{\varphi_{\mathrm{j},k} | k \in [0, 2^{-\mathrm{j}} - 1]\} \text{ where} \\ \overline{\cup_{\mathrm{j}\in\mathbb{Z}} V_{\mathrm{j}}} &= L^2([0,1]) \text{ and} \\ \mathcal{P}_{V_F} f &= \mathcal{P}_{V_C} f + \sum_{l=F+1}^{C} \sum_{k\in\mathbb{Z}} \langle f, \psi_{l,k} \rangle \, \psi_{l,k} \end{aligned} \tag{4.46}$$

constituting the MRA. The signal is therefore represented by approximations $a_{C,k_1} = \mathcal{P}_{V_C} f$ up to the chosen coarsest scale $C$ and details $d_{\mathrm{j},k_2} = \langle f, \psi_{\mathrm{j},k} \rangle$ for example, for a 256 x 256 image F=-8, an approximation of the image at coarse scale C=-5 will have details at all scales from F+1=-7 to -5 (see Fig. 4.11).

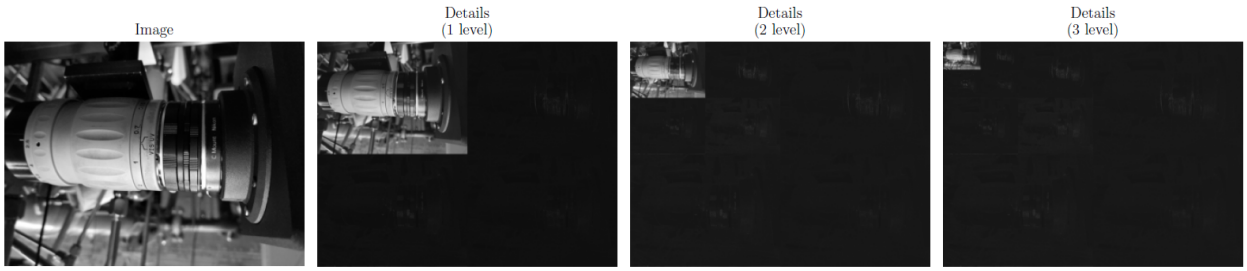


**(a)** Details and approximations on three (3) scales.

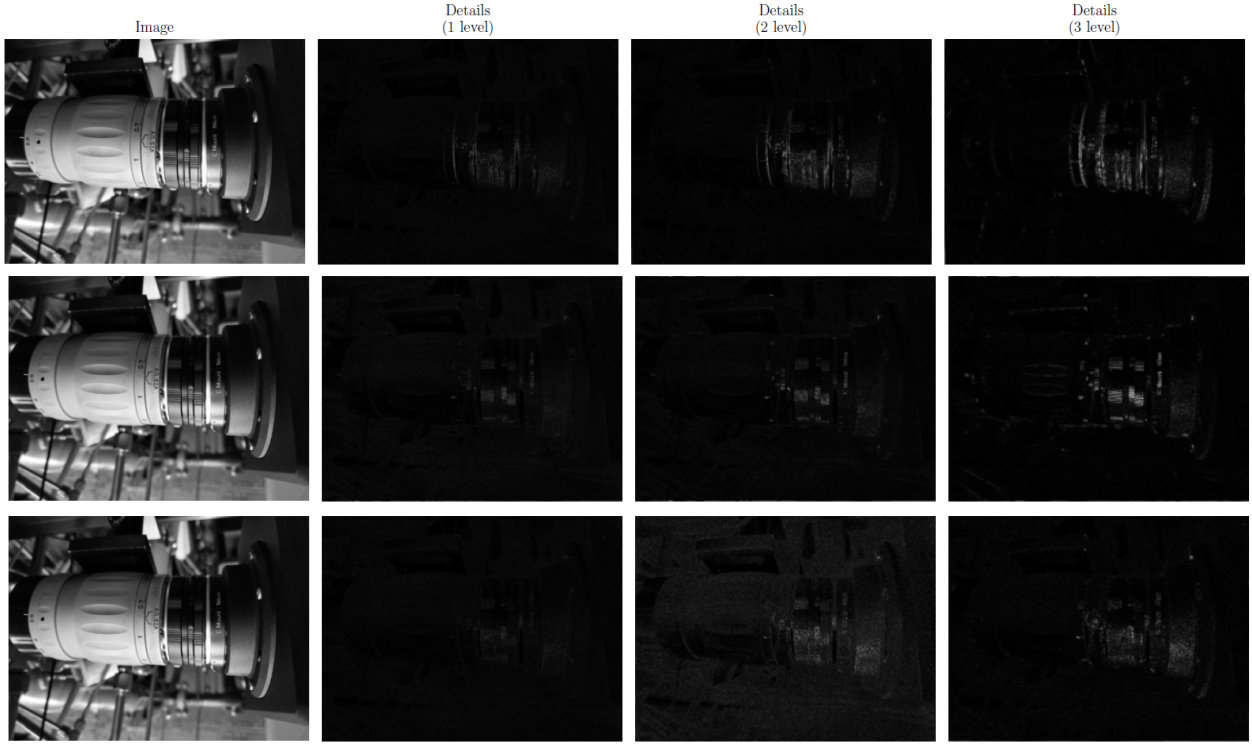


**(b)** Top to bottom: horizontal, vertical and diagonal details

**Figure 4.11. :** 4.11a Horizontal, vertical and diagonal details. 4.11b Details in subsequent scales of a multiresolution analysis: Using a Daubiechies wavelet with 4 vanishing moments computed using PyWavelets[72]

All properties of MRAs and in particular BMRAs are extended to images by taking the outer product of the wavelet basis functions. The new function space is called $\mathbf{L}^2([0,1])^2$

$$V_{\mathrm{j}} \otimes V_{\mathrm{j}} = \mathrm{span}\{\varphi_{\mathrm{j},k_1} \otimes \varphi_{\mathrm{j},k_2} | (k_1, k_2) \in [0; 2^{-\mathrm{j}} - 1]^2\} \tag{4.47}$$

as in Fig. 4.11 with $\otimes$ the outer product.

Images used in this analysis are considered square with $2^{-F}$ x $2^{-F}$ pixels, with necessary padding with zeros if rectangular.

So far we have described the application of MRAs to 1-D and 2-D signals. The unknown of the optical flow problem are the two components of the velocity field

$$\boldsymbol{v} = (v_1, v_2) \in \mathbf{L}^2([0,1])^2 \times \mathbf{L}^2([0,1])^2 \tag{4.48}$$

The $v_{\mathrm{i}}$ are themselves 2-D data. With $\mathbf{V}_F = V_F \otimes V_F$ the 2-D MRAs corresponding to the velocity field,

$$\boldsymbol{v} \in \mathbf{V}_F \times \mathbf{V}_F \subset \mathbf{L}^2([0,1])^2 \times \mathbf{L}^2([0,1])^2 \tag{4.49}$$

We obtain a representation for the three details and approximations

$$\mathbf{V}_F = V_F \otimes V_F = (V_C \otimes V_C) \bigoplus_{F+1 \le \mathrm{j} \le C} (V_{\mathrm{j}} \otimes W_{\mathrm{j}}) \oplus (W_{\mathrm{j}} \otimes V_{\mathrm{j}}) \oplus (W_{\mathrm{j}} \otimes W_{\mathrm{j}}) \tag{4.50}$$

using the isotropic transform.

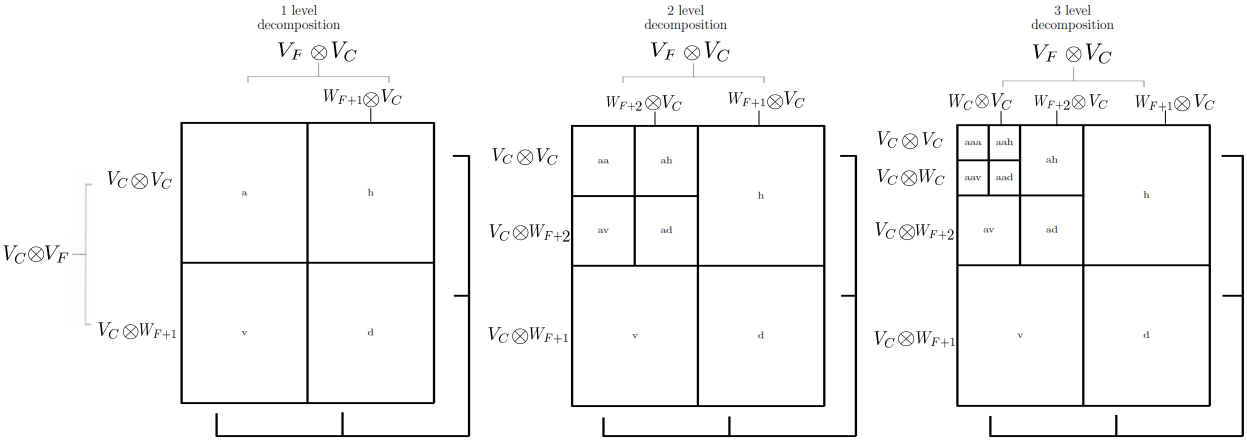


**Figure 4.12. :** Schematic of 2-D wavelet decomposition of a signal. The schematic reveals each set of wavelet coefficients from the wavelet decomposition, one MRA for each dimension. The outer products are replicated at each scale.

The wavelet coefficients $\theta_{\mathrm{i}}$ for each $v_{\mathrm{i}}$, contain the approximations and details. If we define $\boldsymbol{\Theta} = \begin{pmatrix} \Theta_1 \\ \Theta_2 \end{pmatrix}$ as the superset of the coefficients of $\boldsymbol{v}$ such that

$$\begin{aligned} \boldsymbol{v}(\boldsymbol{x}) &= \boldsymbol{\Phi}^T(\boldsymbol{x})\boldsymbol{\Theta} \text{ with} \\ \boldsymbol{\Phi}^T(\boldsymbol{x}) &= \begin{pmatrix} \Phi^T(\boldsymbol{x}) & 0\cdots 0 \\ 0\cdots 0 & \Phi^T(\boldsymbol{x}) \end{pmatrix} \text{ the inverse operator for the wavelet transform} \end{aligned} \tag{4.51}$$

then the optical flow problem is the solution to the simultaneous equations that estimate

$$\begin{aligned} \hat{\boldsymbol{v}}(x) &= \boldsymbol{\Phi}^T(x)\hat{\boldsymbol{\Theta}} \text{ with } \hat{\cdot} \text{ the estimate of } \cdot \text{ and} \\ \hat{\boldsymbol{\Theta}} &= \arg\min_{\boldsymbol{\Theta}} J_{data}(I, \boldsymbol{\Theta}) + \alpha J_{reg}(\boldsymbol{\Theta}) \end{aligned} \tag{4.52}$$

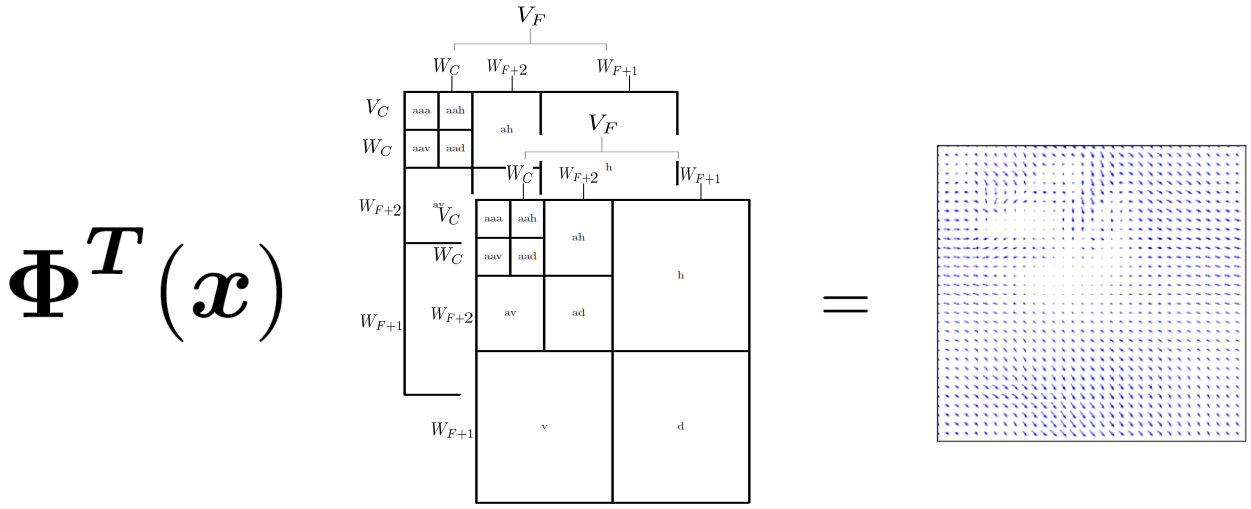


**Figure 4.13. :** Wavelet based optical flow schematic using MRAs for each motion field

### 4.3.6 Implementation

The following includes excerpts from Derian's PhD thesis [68], who is one of the authors of the GPU accelerated C++ code used in computing the wavelet based optical flow. The wavelet based data term for in the displaced frame difference model is

$$J_{data}(I, \boldsymbol{\Theta}) = \frac{1}{2}\int g_L \left(I_0(\boldsymbol{x}) - I_1(\boldsymbol{x} + \boldsymbol{\Phi^T}(\boldsymbol{x})\boldsymbol{\Theta})\right) \mathrm{d}\boldsymbol{x} \tag{4.53}$$

The $p$th coefficient in $\boldsymbol{\Theta}$ corresponding to a wavelet or a scaling function coefficient is obtained from the inner product of the velocity with the basis function

$$\Theta_{\mathrm{i}} = \langle v_{\mathrm{i}}, \phi_p \rangle \text{ where } \phi_p \in V_p \text{ or } W_p \tag{4.54}$$

Estimates of the derivative are used in the minimization algorithm. These estimates involve derivatives

$$\begin{aligned}
\frac{\partial}{\partial \theta_{\mathrm{i},p}} J_{data}(I, \boldsymbol{\Theta}) &= \frac{1}{2} \int \frac{\partial}{\partial \theta_{\mathrm{i},p}} g_L \left( I_0(\boldsymbol{x}) - I_1(\boldsymbol{x} + \boldsymbol{\Phi}^{\boldsymbol{T}}(\boldsymbol{x})\boldsymbol{\Theta}) \right) \mathrm{d}\boldsymbol{x} \\
&= \frac{1}{2} \int \frac{\partial}{\partial \theta_{\mathrm{i},p}} g_L \left( I_0(\boldsymbol{x}) - I_1(\boldsymbol{x} + \boldsymbol{\Phi}^{\boldsymbol{T}}(\boldsymbol{x})\boldsymbol{\Theta}) \right) \cdot \\
&\quad \frac{\partial}{\partial x_{\mathrm{i}}} \left( I_1(\boldsymbol{x} + \boldsymbol{\Phi}^{\boldsymbol{T}}(\boldsymbol{x})\boldsymbol{\Theta}) \right) \frac{\partial}{\partial \theta_{\mathrm{i},p}} \left( x_{\mathrm{i}} + \boldsymbol{\Phi}^{T}(\boldsymbol{x})\Theta_{\mathrm{i}} \right) \mathrm{d}\boldsymbol{x} \\
&= \frac{1}{2} \left\langle \frac{\partial}{\partial \theta_{\mathrm{i},p}} g_L \left( \mathrm{dfd} \right) \frac{\partial}{\partial \theta_{\mathrm{i},p}} \left( I_1(\cdot + \boldsymbol{\Phi}^{\boldsymbol{T}}(\cdot)\boldsymbol{\Theta}) \right), \phi_p \right\rangle_{L^2([0,1]^2)} \\
&\quad \text{with dfd} = I_0(\cdot) - I_1(\cdot + \boldsymbol{\Phi}^{\boldsymbol{T}}(\cdot)\boldsymbol{\Theta})
\end{aligned} \tag{4.55}$$

So that projections of two variables onto the basis functions compose the derivatives of the data term. These two variables are the derivative of the penalty function and the derivative of the motion compensated image. The derivative of the penalty function itself is comprised of the derivatives of the motion compensated image, which is actually computed using the associated optimal weight function that is quadratic in the data term. These variables are also 2-D data.

### Advanced Uses of Wavelets

There are two advanced uses of wavelets namely; computing optical flow using *truncated bases* and computing the regularization which involves autocorrelations. The typical approach to wavelet based image compression proceeds by neglecting the small scale wavelet

coefficients. Choosing to estimate only to scale $L > F$ in the optical flow problem implies that the motion is estimated on a truncated basis.

$$\begin{aligned} \hat{\boldsymbol{v}}(x) &= \boldsymbol{\Phi}^{\boldsymbol{T}}(\boldsymbol{x})\hat{\boldsymbol{\Theta}}|_L \text{ with } L > F \\ \hat{\boldsymbol{\Theta}} &= \underset{\boldsymbol{\Theta}|_L}{\arg\min}\, J_{data}(I, \boldsymbol{\Theta}|_L) \end{aligned} \tag{4.56}$$

This is done in general to reduce the noise from estimation at the fine scales. The noise arises from the loss of contrast at the coarse scales leading to vanishing image gradients. This result coupled with the smaller support width of the wavelets at these scales provides no solution apart from regularization.

The calculations of the regularizer involve derivatives of the motion field. These derivatives are also calculated using wavelet basis functions. The connection coefficients

$$\begin{aligned} J_{\varphi}^{(0)}(x) &= \int \varphi(y)\varphi(y-x)\mathrm{d}y \text{ with } \cdot^{(0)} \text{ the zeroth derivative} \\ &= \int dy \left(\sqrt{2}\sum_m h[m]\varphi(2y-m)\right)\left(\sqrt{2}\sum_n h[n]\varphi(2(y-x)-n)\right) \\ &= \sum_m \sum_n 2h[m]h[n] \int dy\varphi(2y-m)\varphi(2(y-x)-n) \\ &= \sum_k \sum_m h[m]h[m-k] \int dy\varphi(y)\varphi(y-2x+k) \text{ where } y = 2y-m,\ m-n=k \\ &= \sum_k \mathrm{i}[k] J_{\varphi}^{(0)}(2x-k), \text{ with } \mathrm{i}[k] = \sum_m h[m]h[m-k] \end{aligned} \tag{4.57}$$

provide a numerical way to calculate the autocorrelation of a wavelet or scaling function. It is solved using an eigen value approach. The derivative order generalizes, so that $\langle \varphi_{\mathrm{j},k}, \varphi_{\mathrm{j},l} \rangle = J_{\varphi}^{(n)}(q-l)$ and

$$H\ J_{\varphi}^{(n)} = 2^{-n} J_{\varphi}^{(n)} \tag{4.58}$$

It comes in handy since if $f(\boldsymbol{x}) = \sum_{\boldsymbol{k}} a_{F,\boldsymbol{k}} \varphi_{F,k_1}(x_1)\varphi_{F,k_2}(x_2)$ is supported in $[0, 2^F]^2$, the regularizer

$$\begin{aligned}
\left\| \frac{\partial f}{\partial x_1} \right\|_{L^2}^2 &= \int \left( \frac{\partial f(\boldsymbol{x})}{\partial x_1} \right)^2 \mathrm{d}\boldsymbol{x} \\
&= \int \mathrm{d}\boldsymbol{x} \left[ \sum_{\boldsymbol{k}} a_{F,\boldsymbol{k}} \frac{\partial}{\partial x_1} (\varphi_{F,k_1}(x)\varphi_{F,k_2}(x)) \right]^2 \text{ with the } a_{F,\boldsymbol{k}} \\
&= \sum_{\boldsymbol{k},\boldsymbol{k'}} a_{F,\boldsymbol{k}} a_{F,\boldsymbol{k'}} \int \mathrm{d}x \frac{\mathrm{d}}{\mathrm{d}x}(\varphi_{F,k_1}(x)) \frac{\mathrm{d}}{\mathrm{d}x}(\varphi_{F,k_1'}(x)) \int \mathrm{d}x (\varphi_{F,k_2}(x)\varphi_{F,k_2'}(x)) \\
&= \sum_{\boldsymbol{k},\boldsymbol{k'}} a_{F,\boldsymbol{k}} a_{F,\boldsymbol{k'}} \langle \varphi^{(1)}_{F,k_1}, \varphi^{(1)}_{F,k_1'} \rangle_{L^2} \langle \varphi_{F,k_2}, \varphi_{F,k_2'} \rangle_{\mathbf{L}^2}
\end{aligned} \tag{4.59}$$

If we define $M^{(0)}$ and $M^{(1)}$ indexed with $p, q \in [0, 2^{-F} - 1]$ such that

$$\begin{aligned}
\left(M^{(0)}\right)_{p,q} &= \langle \varphi_{F,p}, \varphi_{F,q} \rangle_{L^2} \\
\left(M^{(1)}\right)_{p,q} &= \langle \varphi^{(1)}_{F,p}, \varphi^{(1)}_{F,q} \rangle_{\mathbf{L}^2} = -\langle \varphi_{F,p}, \varphi^{(2)}_{F,q} \rangle_{\mathbf{L}^2} \text{ integration by parts}
\end{aligned} \tag{4.60}$$

then

$$\begin{aligned}
J_{reg}(a_F) &= \frac{1}{2} \sum_{\boldsymbol{k},\boldsymbol{k'}} a_{F,\boldsymbol{k}} a_{F,\boldsymbol{k'}} \left(M^{(2)}\right)_{k_1,k_1'} \left(M^{(0)}\right)_{k_2,k_2'} \\
&= \frac{1}{2} \sum_{\boldsymbol{k}} a_{F,\boldsymbol{k}} \left( M^{(2)} a_F M^{(0)\boldsymbol{T}} \right)_{\boldsymbol{k}} \\
&= \frac{1}{2} a_F : \left( M^{(2)} a_F M^{(0)\boldsymbol{T}} \right) \text{ with } : \text{ the sum of element wise products}
\end{aligned} \tag{4.61}$$

We notice immediately that in calculating approximations and details over multiple scales, the wavelet coefficients of the mass matrices $M^{(0)}$ and $M^{(2)}$ form the connection matrices $N^{(0)}$ and $N^{(2)}$ respectively, which terms are computed for the regularization as follows:

To compute the regularizers

- build the connection matrices $M^{(0)}$ and $M^{(2)}$ at the fine scale $V_F$ at the beginning of the estimation
- from the current motion field, compute $\nabla J_{reg}(a_F) = M^{(2)} a_F M^{(0)\boldsymbol{T}}$ matrix products with $J_{reg}(a_F) = \frac{1}{2} a_F : \nabla J_{reg}(a_F)$

In general, high order regularizers, are composed of terms of the form

$$\pm\Theta_{\mathrm{i}} : \left(N^{(n_1)}\Theta_{\mathrm{j}}N^{(n_1)}\right) \tag{4.62}$$

where the $(\Theta_{\mathrm{i}})$ are the coefficients corresponding to $v_{\mathrm{i}}$ as a matrix. $n_{\mathrm{j}}\forall \mathrm{j} \in 1,2$ is the order of the total derivative wrt $x_{\mathrm{j}}$. The following convention is used to describe the connection matrices $N^{(n)}$.

$$\begin{aligned} &\langle \psi_{\mathrm{i},p}^{n/2}, \psi_{\mathrm{j},q}^{n/2} \rangle_{L^2} \text{ if } n \text{ is even} \\ &\langle \psi_{\mathrm{i},p}^{1}, \psi_{\mathrm{j},q}^{n-1} \rangle_{L^2} \text{ if } n \text{ is odd} \end{aligned} \tag{4.63}$$

In this notation the divergence gradient regularizer is

$$\begin{aligned} J_{reg}(\boldsymbol{\Theta}) = &\frac{1}{2}\Theta_1 : \left(N^{(4)}\Theta_1 N^{(0)} + N^{(2)}\Theta_1 N^{(2)}\right) \\ &+ \frac{1}{2}\Theta_2 : \left(N^{(0)}\Theta_2 N^{(4)} + N^{(2)}\Theta_2 N^{(2)}\right) \\ &+ \Theta_1 : \left(N^{(1)}\Theta_2 N^{(3\boldsymbol{T})}\right) + \Theta_2 : \left(N^{(1)}\Theta_2 N^{(3)\boldsymbol{T}}\right) \end{aligned} \tag{4.64}$$

**Implementation Details and Pseudo Code**

The filterbanks used in computing the wavelet transform consist of the conjugate mirror filters together with downsampling and an upsampling operations. The forward wavelet transform computes from an approximation $\mathcal{P}_{V_{\mathrm{j}+1}}f$ coefficients in a coarser scale $\mathcal{P}_{V_{\mathrm{j}+1}}f$ and the details $\mathcal{P}_{V_{\mathrm{j}}}f - \mathcal{P}_{V_{\mathrm{j}+1}}f$

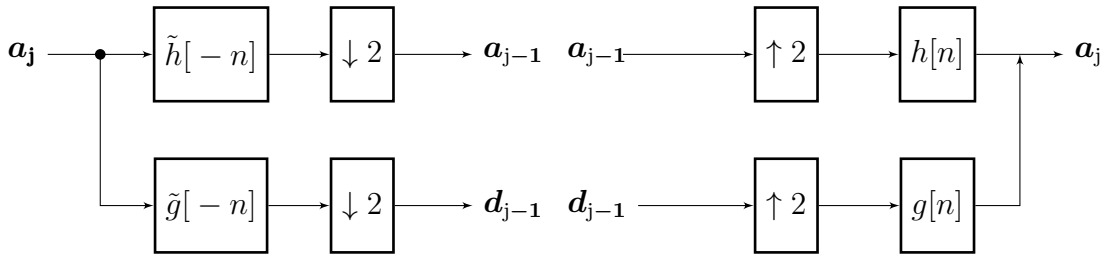


**Figure 4.14. :** Left to right forward and inverse wavelet transform using filterbanks from BMRA showing approximations $\boldsymbol{a}$ and details $\boldsymbol{d}$ at subsequent scales

The smart filterbanks are implemented by

- not computing fine scales $s \in [F, \mathrm{j}[$ during the decomposition of wavelet coefficients
- not adding fine scales $s \in [F, \mathrm{j}[$ during the reconstruction of the $v_{\mathrm{i}}$

The code as supplied was built on a Red Hat Enterprise Linux server with centos7 running CUDA 10.1. The variational optical flow problem has a large number of unknowns. It was minimized using a limited memory BFGS algorithm l-BFGS. This algorithm finds the minimum value $x$ using a current value of the function $f(x)$ and its derivatives. It does this by estimating (building up) the hessian $H$ from multiple iterations of a pseudo gradient descent step in an attempt to find the stationary point of

$$\partial_{1,2} f(\boldsymbol{x}) = \partial_{1,2} f(\boldsymbol{x_n}) + \boldsymbol{H^T}(x - x_n) \tag{4.65}$$

which can be solved exactly by inverting $\boldsymbol{H^T}$

$$x_{n+1} = x_n - \boldsymbol{H^{-T}} \partial_{1,2} f(\boldsymbol{x_n}) \tag{4.66}$$

so the derivatives $\partial_{1,2} f$ of the function as well its value are needed at every step. The Hessian is not obtained from the full history of gradients, but estimated using a few recent iterations of the sort in eq. 4.65, neither is the hessian explicitly stored so as to minimize memory utility.

The estimation of the coefficients is done at each scale j as follows.

- Starting with the coarsest scale $C$, the initial estimate can begin with a zero motion field $\Theta|_C = 0$.
- At each subsequent scale $\mathrm{j} \in [C, F]$, minimize the energy functional with respect to the data term, and its gradient - image like objects. $\hat{\boldsymbol{\Theta}}|_{\mathrm{j}} = \min(I_0, I_1, \boldsymbol{\Theta}|_{\mathrm{j}}, \partial_{1,2}(J_{data}))$
- fill in the entries for the new scale with zeros $\boldsymbol{\Theta}|_{\mathrm{j}+1} = \begin{pmatrix} \Theta_1|_{\mathrm{j}} \\ 0 \\ \Theta_2|_{\mathrm{j}} \\ 0 \end{pmatrix}$ as reinitialization for the next scale.

The calculation of the derivatives of $J_{data}$ using wavelet coefficients proceeds as follows

- Fill in zeroes for all wavelet components not yet estimated $\boldsymbol{\Theta} = \begin{pmatrix} \Theta_1|_{\mathrm{j}} \\ 0 \cdots 0^T \\ \Theta_2|_{\mathrm{j}} \\ 0 \cdots 0^T \end{pmatrix}$
- Use "filterbank" to invert coefficients to motion field $\boldsymbol{v} = \boldsymbol{\Phi}^T(\boldsymbol{x})\boldsymbol{\Theta}$.
- Calculate gradients of warped images. $I_{w,x_{\mathrm{i}}} = \partial_{x_{\mathrm{i}}} \mathrm{warp}(I_1, \boldsymbol{v})$
- Calculate time derivative. $I_t = I_0 - I_w$
- Create the terms for wavelet decomposition. $G_{x_{\mathrm{i}}} = \prod_{\mathrm{i,j}} I_{w,x_{\mathrm{i}}}(\mathrm{i},\mathrm{j}) I_t(\mathrm{i},\mathrm{j})$. Multiplication by entries
- Carry out wavelet decomposition. $\Theta_{\mathrm{i}} = \Phi^{-1} G_{x_{\mathrm{i}}}$. Again with smart *filterbanks*.
- Compute gradients wrt each component direction. $\Theta_{x_{\mathrm{i}}}|_{\mathrm{j}}$ and the data term $J_{data} = 0.5 \sum_{\mathrm{i,j}} I_t(\mathrm{i},\mathrm{j})^2$

# 5. EXPERIMENTAL APPARATUS

## 5.1 Test Rig

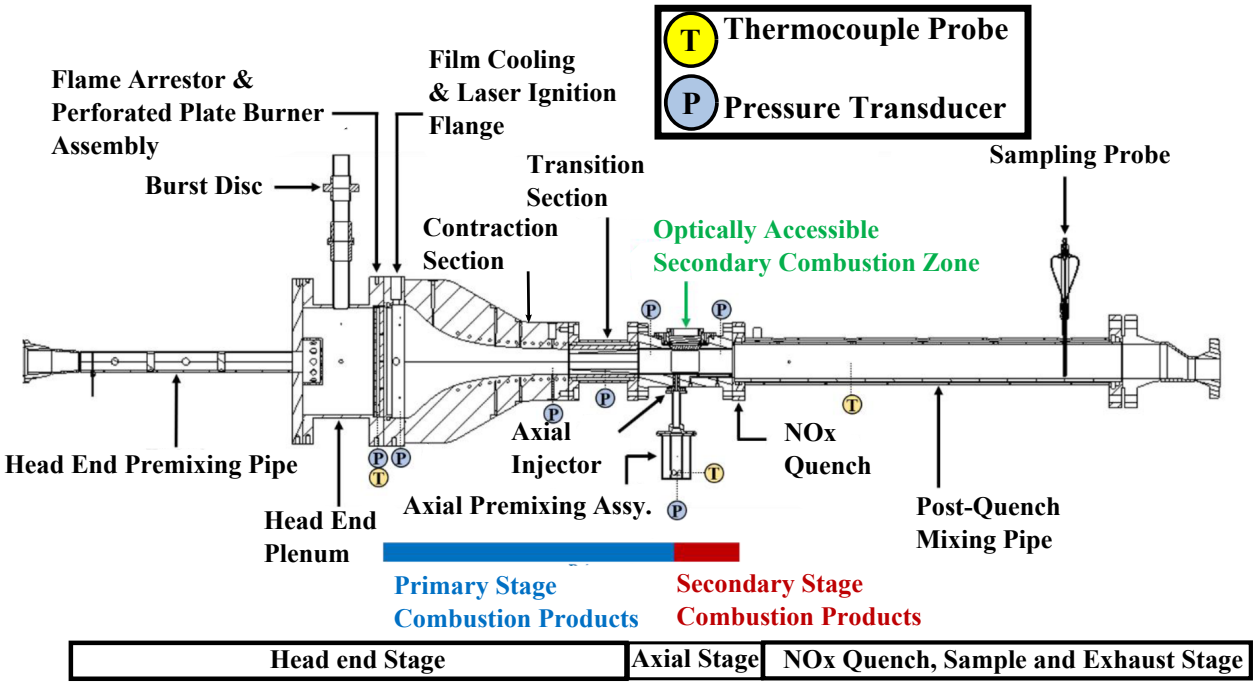


**Figure 5.1. :** Schematic of high pressure test rig reproduced from [9].

The gas turbine combustion rig used for this work is a 4.3 meter long, 0.6 meter wide assembly, comprising two combustion zones, supplied by two fuel/air premixing chambers, and with a high temperature nozzle downstream of the primary combustion zone. The rig is equipped with optical access for primary stage ignition and secondary stage diagnostics described in Rodrigues et al. [9]. The test rig is housed in the gas turbine test cell in the Zucrow high pressure complex [73]–[75]. It was supplied with heated non-vitiated air from a natural gas fired heat exchanger at a simulated nominal compressor discharge temperature of 550 K to both combustion zones. Natural gas was supplied to the test rig from a bulk supply where it was stored at up to 248 bar and metered through independent regulated supply lines to the primary and secondary combustion zones. Hydrogen was also supplied to the test rig from cylinders, where it is stored at up to 138 bar. It was supplied through two independent regulated lines to a pilot flame at the primary stage on one leg and mixed into the axial fuel

supply on the other. Facility water was supplied from two fixed displacement pumps to the test rig and split via separately metered lines to various locations in the test rig. One leg is injected into the post flame gases to freeze post flame NOx formation reactions downstream of the secondary combustion zone. Other legs are used for cooling all hardware that houses post flame gases. Facility nitrogen is supplied to the test rig for purging the fuel run valves and the emissions sampling probe. The probe would otherwise be immersed in the quench water flow prior to ignition.

The flame in the head end combustor is a flat flame stabilized on a perforated plate burner described in Rodrigues et al. [76]. The non-swirling vitiated flow from the head end combustor is accelerated in the downstream flow contraction to arrive at the test section at the jet upstream Mach number. The chamber pressure at the head end, the gas temperature upstream of the head end burner, the vitiated flow Mach number upstream of the jet, and a few other measured and calculated quantities provide feedback to the test conductor that operating conditions decided upon have been reached. Some of these set points are fixed throughout the duration of the test based on the installed hardware. One such set point as the axial stage air split

$$S_{ax} = \frac{\dot{m}_{air,AX}}{\dot{m}_{air,AX} + \dot{m}_{air,HE} + \dot{m}_{air,Film}} \tag{5.1}$$

which was fixed at 1.6% for this test series and the hydrogen mole fraction in the fuel

$$xH_2 = \frac{\dot{n}_{H_2,AX}}{\dot{n}_{H_2,AX} + \dot{n}_{NG,AX}} \tag{5.2}$$

The head end chamber is kept at 5 bar during the experiment by means two ABZ seal series 400 butterfly valves.

The test section with optical access is the chamber for the secondary combustion zone. The details of the test section can be found in Rodrigues et al. [9]. A brief summary is described here. Fluid systems that supply this hardware include natural gas, hydrogen, air, and water. The fuel mixture of natural gas and hydrogen is premixed into the air supply upstream of injection via a flush mounted 5.36 mm ID injector. This injector diameter is

different from the injectors used on previous results from this test rig and was chosen to facilitate optical diagnostics. More details on the test conditions will be given in the test matrix in 6, subsection 6.1 and 6.2.2.

The flow path on the optical section is 90° to the direction of optical access. It has a rectangular cross section of dimensions 40 mm wide x 90 mm high. The optical access covers 80 mm of the full 90 mm of the flow path. This is especially important near the bottom wall of the test section where about 4.65 mm is not available for end on imaging up to the wall with the flush injector. In cases where the wall was viewed, the camera was angled 16° to view past the edge of the optical access see Fig. 5.2c. The window material is fused quartz.

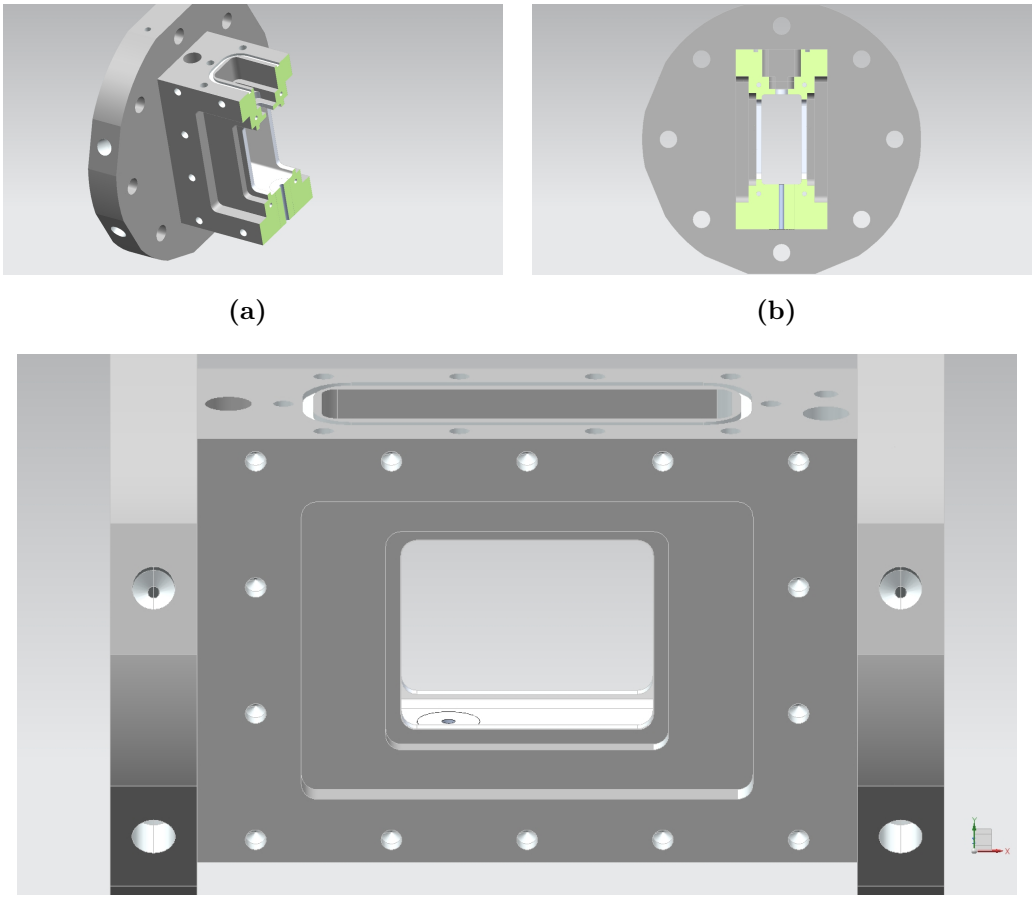

**(a)** **(b)**

**(c)**

**Figure 5.2. :** Perspective views of optical test section schematic showing section through flush injector in (5.2a) trimetric view, (5.2b) looking upstream at injector orifice, and (5.2c) Angled view of injector to view orifice exit.

Condition measurement on the test rig was accomplished by instruments connected to one of three data acquisition systems. Grounded stainless steel sheathed type K- thermocouple probes (Omega GKMQSS), were used for measuring flow temperatures for gas metering. Exposed type K- thermocouple probes were used in wall temperature measurement. Inconel sheathed type K- thermocouple probes (Omega GKMQIN) were used for flow temperatures where the probe was immersed in post combustion gasses. The standard limit of error is either 2.2K or 0.75% for these measurements - the greater of the pair. Low noise pressure transducers (GE Unik 5000) with accuracy of 0.04% were used in measuring flow pressures. They were used with venturis for the live metering of mass flow rates of all gases and water. The two previous transducers are termed the low frequency measuring instruments on the test rig and are sampled at 260 Hz. They are connected to a National Instruments data acquisition device SCXI 1001 chassis. Kulite dynamic pressure transducers are also used in monitoring test rig thermoacoustic pressure oscillations. These transducers are connected to another data acquisition and signal conditioning system (DSP-Con) for lossless high bandwidth measurement sampled at 180 kHz. The third standalone data acquisition and signal conditioning system is the MKS MG2030 FTIR spectrometer for live gas sampling. The measured gases were sampled at 1 Hz. 20 s of data was averaged for the measurement and the standard deviation is the reported uncertainty.

The tests were run remotely via a LabVIEW virtual instrument (VI) for controlling fuel, air and water valves and other devices on the test rig. The LabView VI provided live redline monitoring to shut off fuel run valves in the case of flashbacks or loss of active cooling. Steady state operation is achieved for each test condition before images are acquired.

### 5.1.1 Contraction Section Geometrical Features

As an example of the design procedure that was carried out on individual components that make up the test rig, the design of the contraction section will be reviewed. The combustor was split into a high temperature nozzle followed by three modular test sections to facilitate residence time modularity independent of mass flow rate of the combustion gas. The contraction section is a high temperature subsonic nozzle, it has an area ratio of 41.8

and features active cooling to prevent thermal stress failure. The nozzle receives gas with a velocity distribution that is uniform in the cross sectional plane. The upstream conditions of the gaseous flowfield are controlled by a perforated plate burner [76]. The burner promotes the stabilization of a lean flat natural gas air (NG/air) flame, whose combustion product (vitiated air) is supplied to the inlet of the contraction section. The plate design geometry was controlled by the total mass flow rate of gaseous reactant and the turbulent consumption rate of natural gas at the 5 bar pressure and 500 K upstream temperature. Stabilizing this flame on a plate resulted in the design requirement of about 5000 400µm holes spanning a diameter of about 406mm. This upstream diameter fixed the inlet design of the contraction section. As it was designed to accelerate the gas in the axial direction and exhaust it into a channel where the velocity distribution remains uniform, the wall geometry was chosen to allow a gradual change in Mach number axially. The design flow was path based on vitoshinski nozzle theory [77]

$$y = \frac{y_e}{\sqrt{\left(1 - \left(1 - \left(\frac{y_e}{y_i}\right)^2\right) \frac{\left(1-3\left(\frac{x}{l}\right)^2\right)^2}{\left(1+\left(\frac{x}{l}\right)^2\right)^3}\right)}} \text{ with}$$

$$\begin{aligned} y_i &\quad \text{the inlet radius} \\ y_e &\quad \text{the exit height} \\ y &\quad \text{the local height} \\ x &\quad \text{the current axial distance} \\ l &\quad \text{the length of the nozzle} \end{aligned} \tag{5.3}$$

The downstream channel has a rectangular cross section that provides a high aspect ratio for the jet in crossflow configuration, where the jet issues into the longer dimension. The right angles of the rectangle were chosen to facilitate optical diagnostics of the secondary combustion zone downstream of the contraction section.

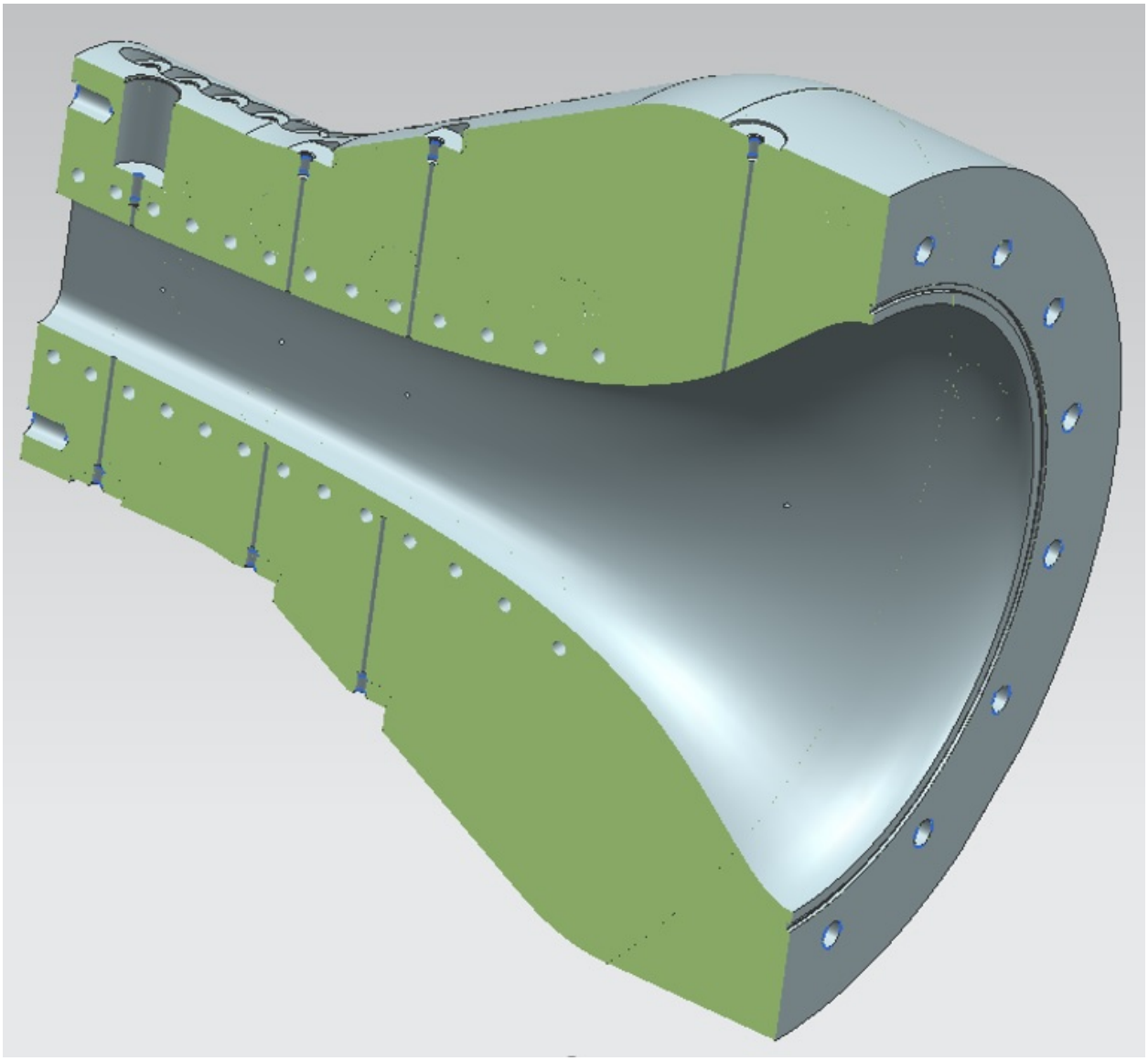

**Figure 5.3. :** Cross section of the contraction section. Temperature and pressure measurement ports are also shown. Flow path highlights transition from round inlet to square outlet. Two vitoshinski transitions are demarcated by two of the four sides of the transition – one transition results in the height of the rectangular exit cross section and the other results in the width of the rectangle

### 5.1.2 Contraction Section Heat Transfer Analysis

The material chosen for nozzle design is stainless steel 347. This particular stainless steel was chosen based on yield strength derating at high temperatures. At the crossflow temperatures and Mach numbers the hardware is designed for, the bare surface of the metal

would fail thermally if uncooled. The cooling scheme employed for the hot wall is regenerative cooling akin to rocket nozzles. The design criteria is to ensure the metal temperature does not exceed 1000K at the highest design Mach number. This temperature was chosen based on the softening temperature of stainless steel 347.

The cooling of the nozzle was done actively using pressurized water. The cooling geometry was novel, uniquely designed to concentrate the cooling at the nozzle exit where the heat fluxes are the highest. The cooling design was called "double-helix" because two circuits designed as helices comprise the cooling channel design.

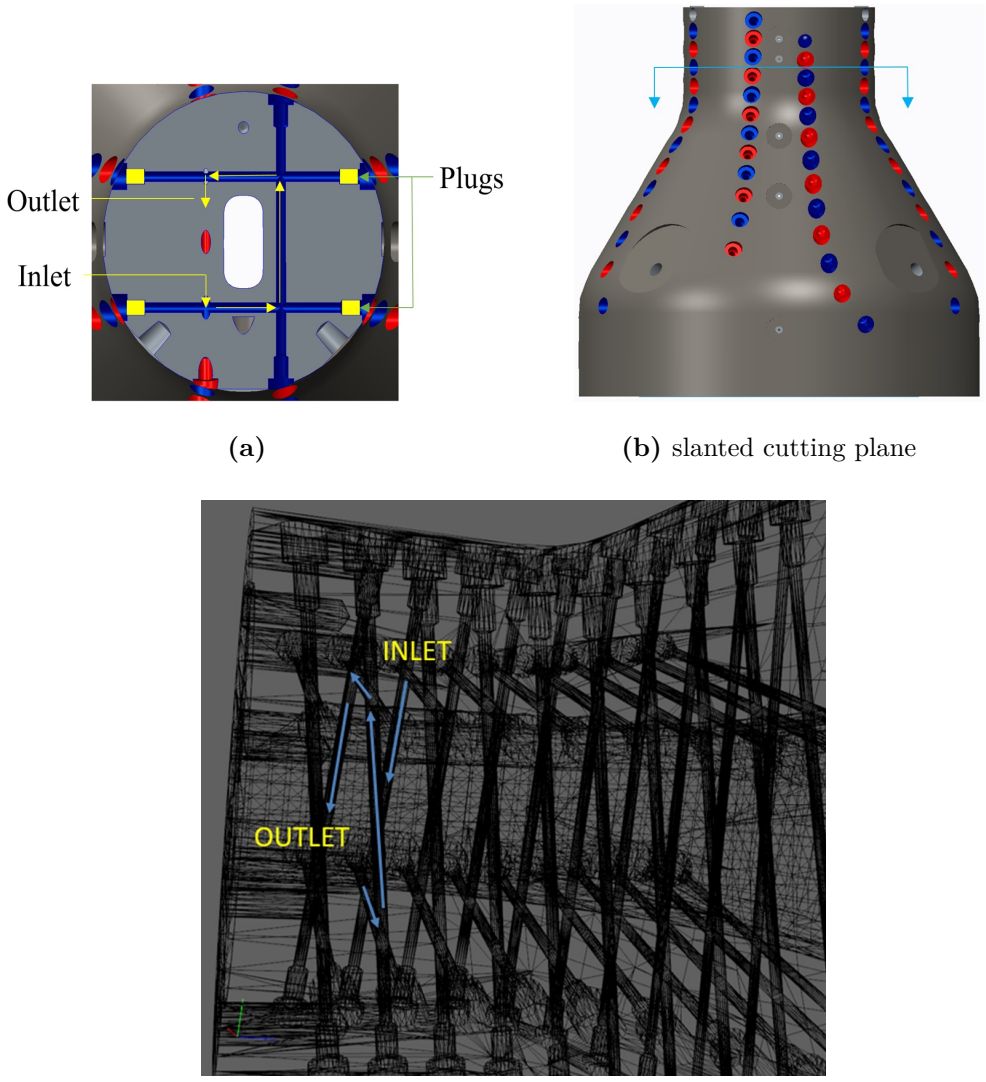


**(a)**

**(b)** slanted cutting plane

**(c)** wireframe view

**Figure 5.4. :** Contraction section helical cooling, with cooling channels are colored for different helices. 5.4a Cross section through flow path showing inlet and helical loop. 5.4b Cutting plane and viewing arrows highlighted. Ports labelled for intersecting regions – blue. 5.4c Wireframe view of nozzle highlighting single loop with upstream fed inlet

The flow path of the coolant around the gas flow path was chosen as a double helix – two independent channels of water highlighted in red and blue in Fig. 5.4. The design of the cooling channels was such that the minimum distance to the nearest hot wall would be kept constant along the combustor length. Each channel would be drilled into the material of the nozzle. The diameter of the coolant flow path was sized small enough to increase velocity

with minimal pressure drop due to the frequent turning of the flow and large enough to aid metering via venturi. At the inlet of the nozzle, due to line contact of the straight cooling channel with the circular hot gas flow path, film cooling was determined necessary to ensure the wall temperature design criteria would be met. The film cooling would issue out of a flange upstream of the nozzle and flow parallel to the wall to keep hot combustion gas away from the wall. Thermal barrier coating of the metal surface was determined necessary to keep the heat content of the hot gas from being conducted out through the walls into the coolant flow, thereby preserving adiabaticity of the combustor. The thermal barrier coating also serves to protect the wall from thermal failure. The calculations for the Mach number through the hardware were performed using Matlab ®with input of flow areas from the CAD model that drives the design. The Bartz one dimensional lumped parameter model was used to calculate the heat transfer coefficient as it was shown to predict the flow properties in nozzle walls better than low Mach number (or Mach number independent) correlations. The modified Bartz equation from [78] was used. It accounts for property variation in the thermal boundary layer and local wall curvature. The heat transfer coefficient was calculated through an iterative scheme that predicts the wall temperature based on input coolant temperature hot gas properties, Mach number and wall material thermal properties.

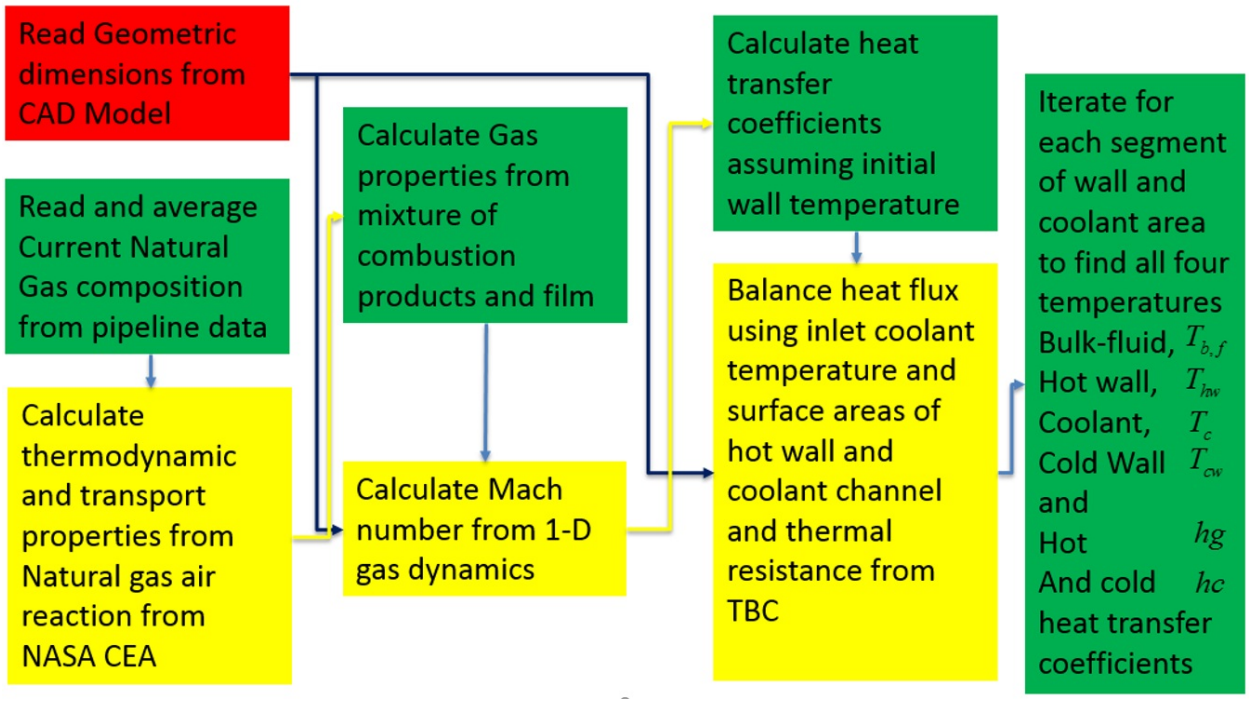


**Figure 5.5. :** Flow diagram for heat transfer calculations

The heat transfer analysis of the contraction section was accomplished as part of the requirements from the critical design of the part. The design criteria was to prevent the wall temperature from exceeding 1000K. The analysis was carried out as a quasi-1D heat flow through the part in the (radial) direction of the distance between the hot wall surface and the coolant channel. Axial heat transfer along the length of the part was ignored. The part was broken up into segments of length over which the hot gas progresses axially and heats up the hot wall via convection. The heat content from that same segment is transfered into the the coolant channel adjascent to that wall segment. The heat is convected to the cooling channel in the next segment increasing the fluid temperature. The coolant runs orthogonal to the flow path. Two coolant channels would be around the wall section since the helical cooling design features rectangular flow path around the walls. The inlet of the contraction section would feature film cooled walls which lowers the gas temperature near the walls. The coolant progressed in the same axial direction as the hot gas to increase the water temperature at the exit and thus decrease the thermal stress due to high heat fluxes.

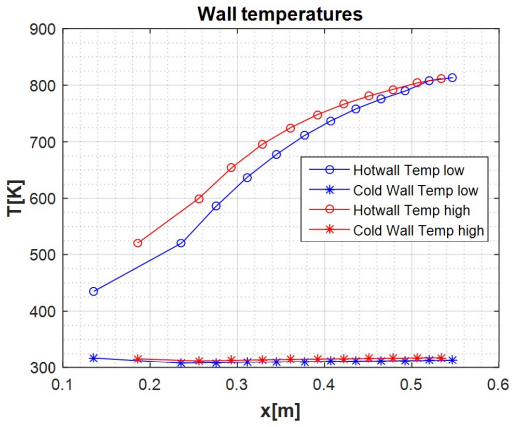


**(a)**

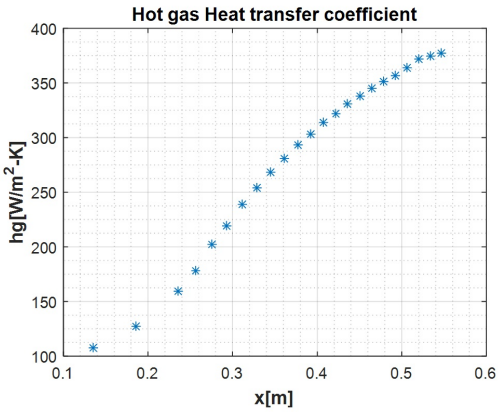


**(b)** hot gas heat transfer coefficient

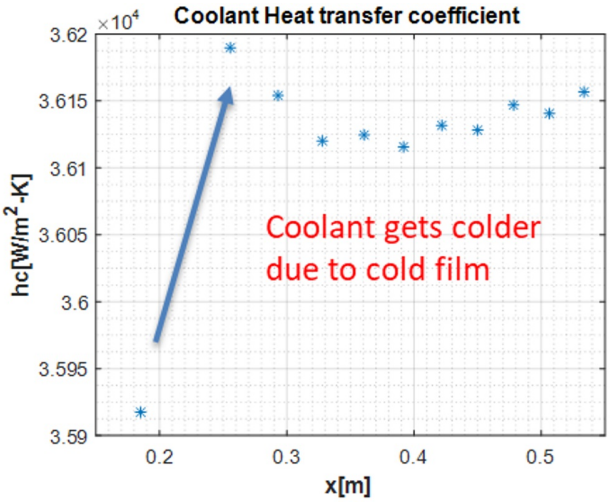


**(c)** coolant heat transfer coefficient

**Figure 5.6. :** Typical 1D heat transfer output which serves as input boundary conditions to the ANSYS 3D solver. 5.6a Wall temperatures for top and side walls of contraction section at water cooling locations along the nozzle. Top walls are hotter on hot gas side and cooler on coolant side due to longer coolant channel length on side wall compared to top and bottom walls. 5.6b heat transfer coefficient to bare metal which is a lumped parameter with contribution from hot gas boundary layer and thermal resistance from thermal barrier coating. 5.6c Coolant heat transfer coefficient which is two orders of magnitude higher than the hot gas heat transfer coefficient to compensate for the smaller surface area of the coolant channel. This was afforded by the mass flux through the coolant channel.

A typical result for the 0.7 contraction section exit Mach number, 22% airsplit at HE equivalence ratio of 0.7 is shown in Fig. 5.6. The TBC coating thermal conductivity was

estimated at 700mW/m/K at 900µm thickness. The film of air is calculated as a fraction of the head end air mass flow rate at 34%.

### 5.1.3 Contraction Section Thermal Stress Analysis

The analysis of thermal stress in the material was performed in ANSYS workbench ©. The software computes the temperature distribution as well as stress distribution in a 3D model given input boundary conditions. The heat transfer input parameters imported to the model as boundary conditions to the thermal solver are the "effective heat transfer coefficient" $1/R_c$ to the bare metal surface of the nozzle as a function of adiabatic wall temperature with the film cooling effectiveness, where

$$
\begin{aligned}
R_c =& \frac{1}{h_g} + \frac{t_{tbc}}{k_{tbc}} \text{ with} \\
h_g \quad & \text{the hot gas heat transfer coefficient} \\
t_{tbc} \quad & \text{the thermal barrier coating (TBC) thickness} \\
k_{tbc} \quad & \text{the thermal conductivity of the TBC}
\end{aligned}
\tag{5.4}
$$

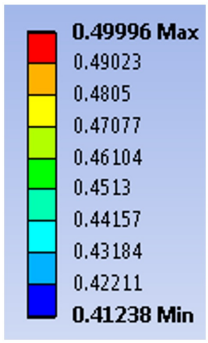


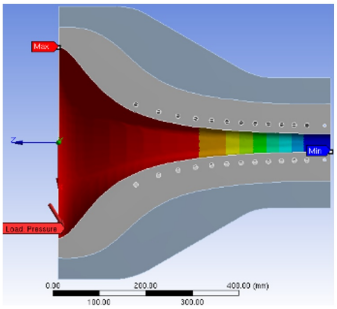


**(a)** Pressure load in MPa

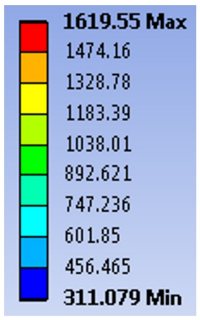


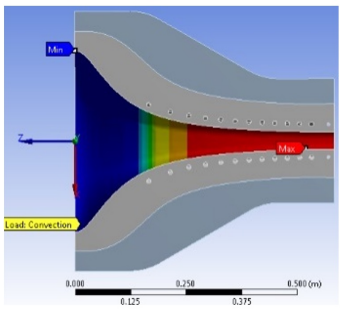


**(b)** Temperature distribution (K) input BC to the SS 347 wall

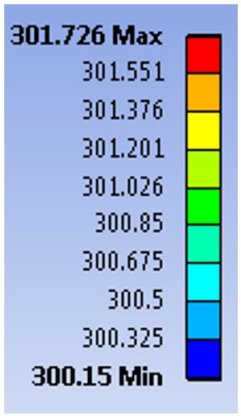


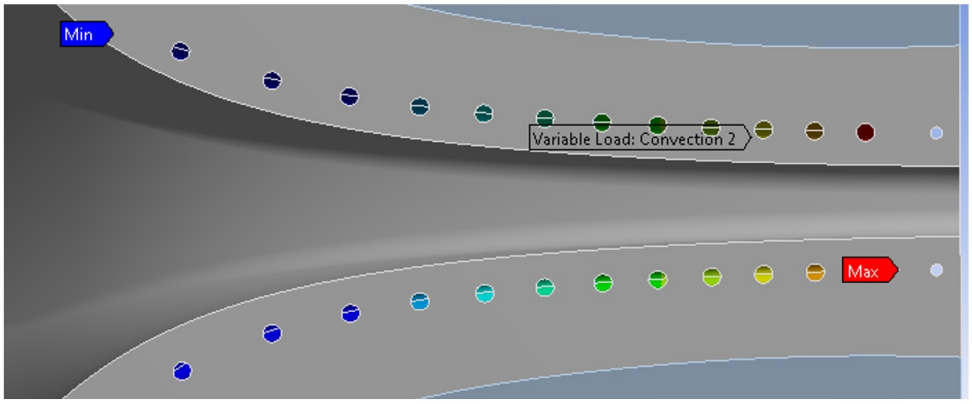


**(c)** Coolant temperatures (K) fed to the heat transfer coefficient

**Figure 5.7. :** Pressure load boundary condition and temperature boundary conditions to the stress solver. 5.7bTemperature distribution input BC for hot gas wall shows effect of film cooling.

The thermal properties of the metal the temperature profile of the coolant and the pressure profile due to gas expansion are also defined as inputs parametrized with distance from the inlet as shown in Fig. 5.7. The ANSYS solver was ANSYS workbench Mechanical ANSYS Parametric Design Language (MAPDL) solving the constitutive and compatibility equations of stress and strain on each node. A half or quarter of the full geometry was imported into the mesher shown in Fig. 5.8. An unstructured mesh was used to capture the physics of heat transfer and structural dynamics following thermal and pressure loads from the heat transfer and the coolant and hot gas pressures respectively. The solver ran cases with linear stress-strain relation in the material as well as bilinear isotropic stress-strain rela-

tion in the material because of the tendency for the inner surfaces to yield due to the thermal loading. The use of the bilinear isotropic model indicates the extent of plastic deformation after one cycle.

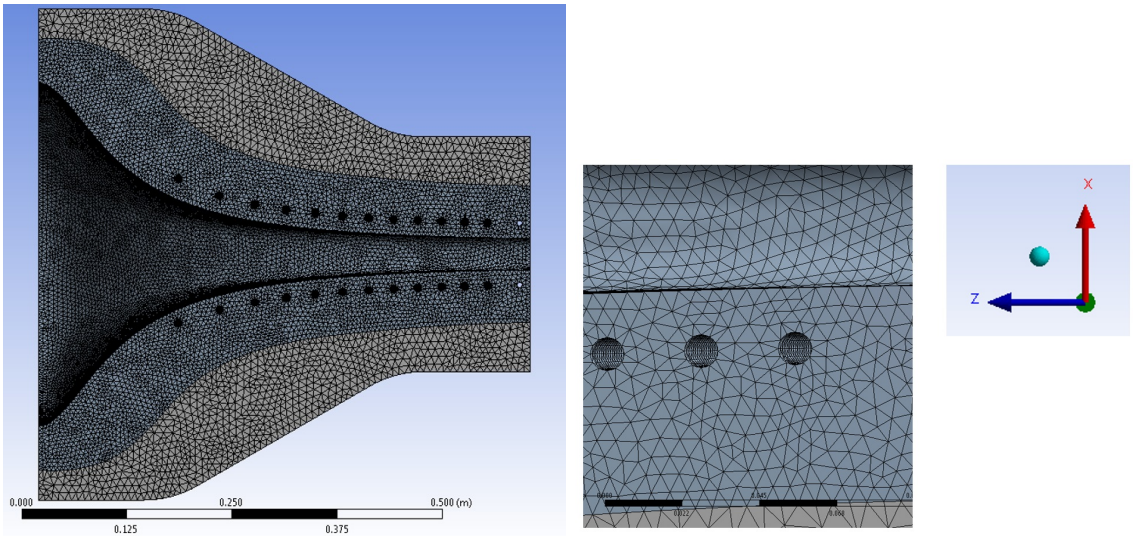


**(a)** **(b)** Temperature load and coolant temperatures

**Figure 5.8. :** 5.8a Half model of nozzle used in some analyses, featuring a total of 2.1 M nodes on an unstructured mesh. Symmetry boundary conditions are employed across the cut faces. 5.8b Zoomed in view of mesh around cooling channels

Von-Mises stresses were used to describe the stressed state of the material given the ductile nature of stainless steel. The linear stress model assumes a linear stress-strain curve even after the material has deformed plastically as shown in Fig. 5.9. This is useful for determining the factor of safety in a linear model. This analysis was to predict the number of cycles the design could handle given the high stressed state of the inner surface of the metal during operation. The bilinear isotropic model reflects the mechanical behavior of the material in reality, and was used to show the realistic stress states in the material following the thermal and pressure loads.

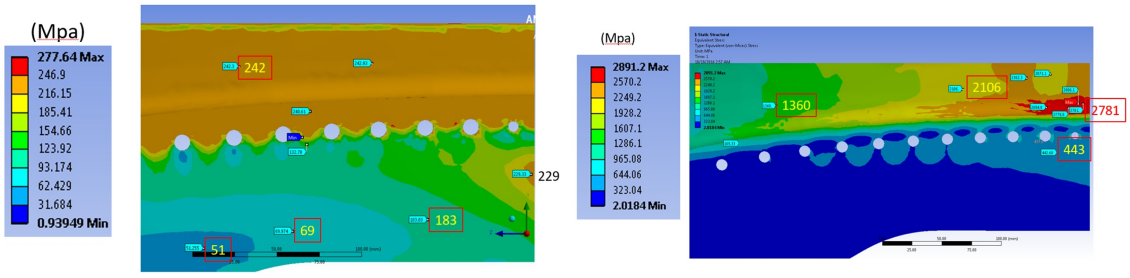


**(a)** bilinear isotopic stress model result

**(b)** linear stress model result

**Figure 5.9. :** 5.9a Quarter model showing equivalent Von-Mises stress results near the nozzle exit plane using a bilinear isotropic stress model. This model bounds the maximum value of stress in the material by using a nearly flat stress strain curve after the yield strength. The brown highlights in the result map represent the regions of plastic deformation due to thermal stress. 5.9b The high equivalent Von-Mises stressed state at the exit of the nozzle in the linear model indicates that the corners of the walls where the flow path is rectangular are not free to expand to relieve stress. The unusually high stress in the material is due to the unrealistic stress model which uses a strictly linear stress strain curve for stainless steel even after the yielding

The Von Mises stresses were linearized to describe the total stress in the part using (constant) membrane and bending stresses varying linearly. The linearization was performed using the line integral method. The bending stresses are calculated such that the neutral axis is at the midpoint of the path. The line that creates the path is usually cut through material between the hot wall and the coolant channel.

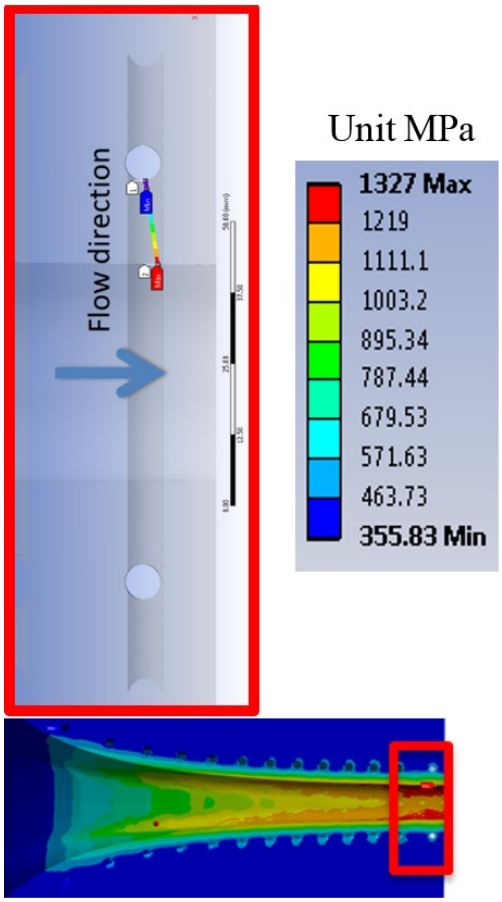


**(a)** locus of points used in stress cut

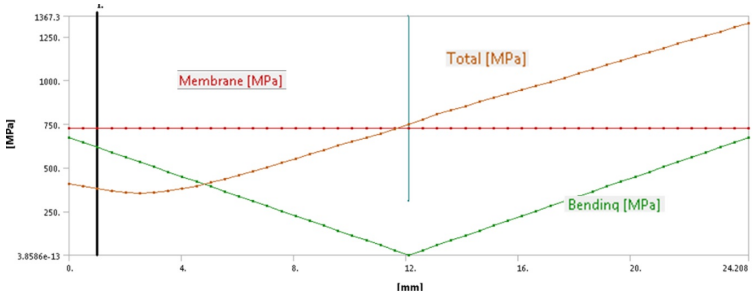


**(b)** linear stress model result

**Figure 5.10. :** 5.10a Cut along the distance between the hot wall and the coolant channel showing distribution and source of stresses. 5.10b Linearized primary stresses (bending and membrane) account for most of the stress to the hot wall. After the neutral axis, the sum of membrane and bending is almost identical to the total stress in the part. The stress in the part does seem to vary linearly along the part for most of the length which might indicate that bending stress accumulates from the rectangular wall attempting to relieve stress by turning circular.

The results indicated in Fig. 5.10 show that the stress in the part is governed by the temperature difference between surfaces and highest where the coldest parts are close to hot surfaces. Stress accumulation at the rounded corners was expected especially at the exit plane. The results provided input to the design by informing the distance between the coolant channel and the hot wall.

### 5.1.4 Contraction Section Design Validation

The contraction section survival was a huge milestone for this project. The in-house codes by Siemens Energy estimated the number of starts and stops for this device - the number of ingitions to be about 200 for the lifetime. It has surpassed this value and has no obvious material faults. This is in addition to the lower film cooling amount that was used in the life of the device from 34% to 5%. This amount was identified as the maximum amount required for the stabilization the axial jet flame during commissioning. One metric that can be used to test the similarity of the design behavior to real data is the coolant temperature rise. The coolant temperature is shown in Fig. 5.11 to stay fairly constant from exit Mach 0.5 to exit Mach 0.7 corresponding to vitiated flow Mach 0.4 to 0.5. The increase in water temperature matches the expected trend and order of magnitude of water temperature rise from the contraction section calculated during the design phase of the project.

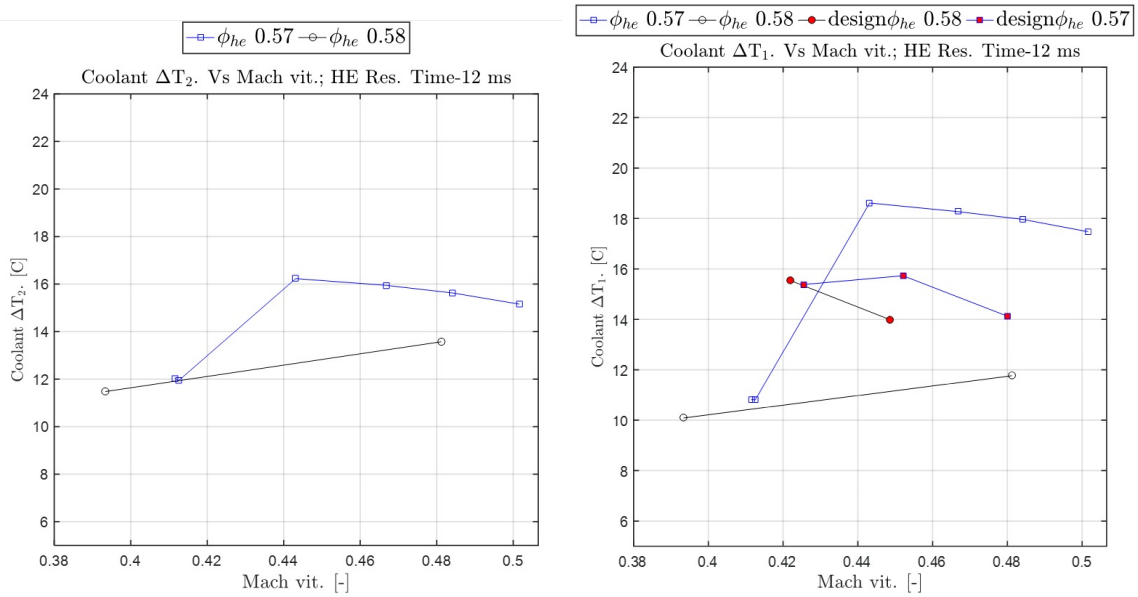


**(a)** Coolant temperature change helix 2 **(b)** Coolant temperature change helix 1

**Figure 5.11. :** Coolant temperature rise in both legs of helical cooling in contraction section at multiple equivalence ratios which compares well with the near 15 °C increase from the design study.

## 5.2 Diagnostic Systems

The optical measurement configuration was designed to obtain data from one or two opposing views of the jet trajectory: The plane of measurement includes the jet normal direction and the direction of the crossflow (see figure 5.12). In this subsection, we shall describe the experimental systems for OH PLIF and $OH^*$ chemiluminescence.

### PLIF Camera and Accompanying Optics

A Photron Fastcam SAZ intensified with a Lavision High Speed UV-IRO was used to capture OH PLIF at 5 kHz using the full 1024 x 1024 pixels. This camera was positioned on the right side of the rig looking downstream see figure 5.12. This camera and intensifier and light collecting optics are assembled on two translation stages Zaber A-LST0250A-E01 for focusing and translating the field of view. A Cerco 2178 100mm f/2.8 UV lens adapted to a 7mm lens tube and coupled to a Semrock $320 \pm 40$nm filter was used for all but one

OH-PLIF measurement. For the highest crossflow Mach number condition, OH PLIF was captured the previous camera system with a Cerco 2073 45mm f/1.8 UV lens with a separate $320 \pm 40$nm filter. This was performed simultaneously with the high repetition rate data system described next.

### Chemiluminescence Cameras and Accompanying Optics

A Phantom v2512 camera coupled to a Lambert Instruments HiCATT 25 intensifier was used for capturing $OH^*$ chemiluminescence images. This is hereafter called the high repetition rate camera system. Two image framing rates described in this paper for the high repetition rate camera system, imaging at 150 kHz using 384 x 288 pixels the field of view is shown in 5.13. The other was imaging at 100 kHz using 384 x 192 pixels for the unattached flames. These measurements were captured on the left side of the rig looking downstream see figure 5.12. The mean flame position was obtained via the high repetition rate camera system imaging the $OH^*$ chemiluminescence using the Cerco 2178 100mm f/2.8 UV lens coupled to a Semrock $320 \pm 40$nm filter. Simultaneous measurements were obtained to compare against OH PLIF. The faster camera timing was provided by a burst following the slower laser pulse, with 19 burst pulses between the 5 kHz laser shots for the 100 kHz measurements for example. The pulses were generated using a quantum composer 9520 pulse generator.

A Phantom v7.3 camera intensified with a Lavision High Speed UV-IRO was also used on one test day at 10 kHz using 152 x 512 pixels for imaging the unattached flames. This was used on the single crossflow Mach number 0.41 condition.

The geometry of the optical access on both sides of the windowed combustor prevents direct measurement up to the wall of the combustor as shown in figure 5.2. To establish the location of the attached jet, in one test case, the camera is angled at 16° to view the injector orifice past the edge of the optical access. These measurements will be designated angled camera see figure 5.2c.

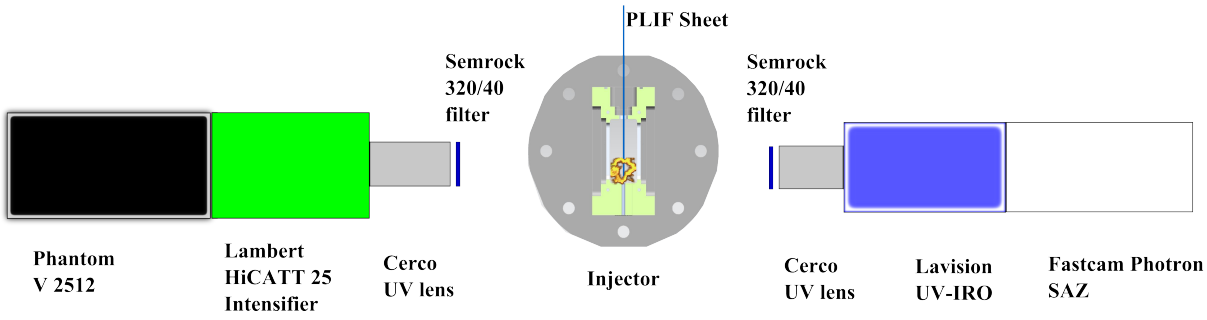


**Figure 5.12. :** Camera setup for simultaneous measurements, flow out of the page.

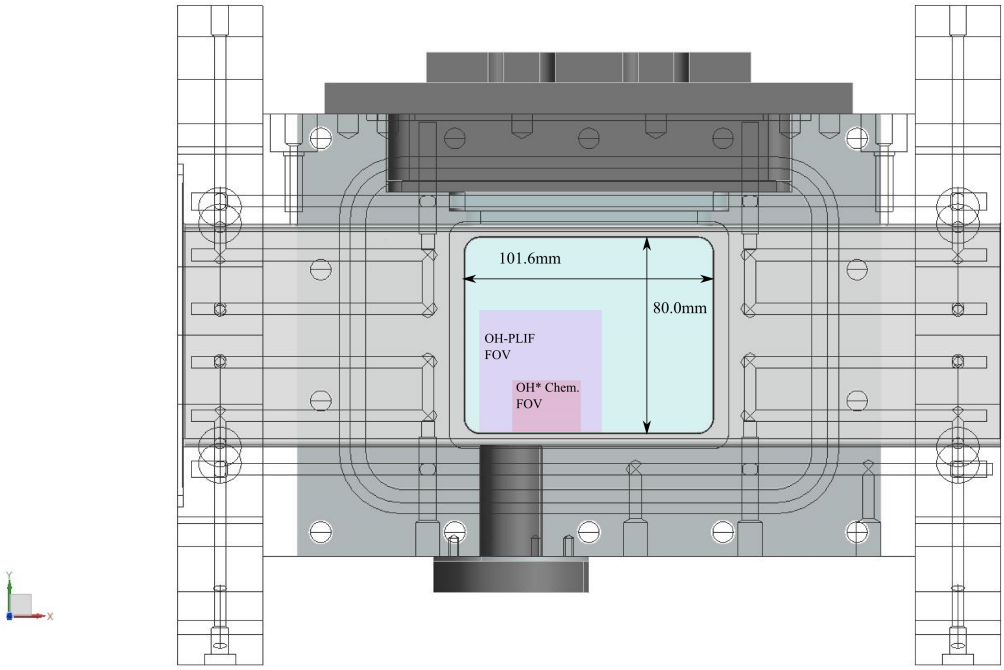


**Figure 5.13. :** Field of View for OH PLIF and close up OH* Chemiluminescence. The optical ingres measures 101.6 mm x 80 mm

## 5.3 Experimental Uncertainty

The mass flow measurements were carried out using sonic venturis for gaseous flows and cavitating venturis for water. For either case the low frequency pressure transducers were used to measure the upstream flow pressure. The omega thermocouples were used to measure temperature for the sonic venturi measurements. Uncertainties for air, natural gas and

hydrogen measurements are 1.4% of the calculated quantities accounting for temperature, pressure and uncertainties of throat area (at the flow temperature). The Mach number uncertainties are also 1.4% propagated from the uncertainties of the mass flows, pressures, and areas. Thermodynamic and transport properties were computed using Refprop. In the case where the water content of the flow resulted in compositions outside the valid range of the Refprop software [79], an equation by Davidson [80] was used.

# 6. FLAME ATTACHMENT BY HYDROGEN ADDITION EVIDENCED BY OH* CHEMILUMINESCENCE

The spatial and temporal behavior of hydrocarbon flame chemiluminescence can evince the nature of the underlying flowfield. Typically the imaging is spectrally isolated and time resolved to interpret changes in the luminescence from the flame brush. In this section some flame theory will be used to describe the results from 150 kHz repetition rate $OH \cdot$ chemiluminescence imaging of flames using the configuration described in 5.2.

## 6.1 Effect of Natural Gas Equivalence Ratio on the Average Attached Flame Behavior

### Test Conditions

The following tables describe the test conditions that were used to investigate favorable stabilization conditions for the JICF flame. Tables 6.1 and 6.2 capture the intent to understand the effect of crossflow Mach number on the behavior of the flame. The highest crossflow Mach number condition in the test series was 0.68, one of two conditions which OH-PLIF measurements were made. This will be discussed in the next chapter. The hydrogen content $xH_2$

$$xH_2 = \frac{\dot{n}_{H_2}}{\dot{n}_{H_2} + \dot{n}_{NG}} \tag{6.1}$$

is reported as a fraction of the total moles of fuel injected into the axial stage.

**Table 6.1. :** Attached Flame Test Conditions

| Upstream conditions | | | | Jet conditions | | | |
|---|---|---|---|---|---|---|---|
| Mach # | $Re_{Dh}$ | $T_0$ | $T$ | $\phi_{AX,NG}$ | Min. $xH_2$ | J | $Re_D$ |
| 0.31 | 53080 | 1670 | 1647 | 0.71 | 0.63 | 1.9 | 126900 |
| 0.31 | 52900 | 1676 | 1654 | 1.45 | 0.46 | 2.1 | 140800 |
| 0.31 | 52670 | 1681 | 1658 | 2.0 | 0.59 | 2.4 | 134400 |

**Table 6.2. :** Attached Flame Test Conditions

| Upstream conditions | | | | Jet conditions | | | |
|---|---|---|---|---|---|---|---|
| Mach # | $Re_{Dh}$ | $T_0$ | $T$ | $\phi_{AX,NG}$ | Min. $xH_2$ | J | $Re_D$ |
| 0.63 | 87540 | 1776 | 1680 | 0.71 | 0.79 | 1.5 | 196400 |
| 0.63 | 84300 | 1811 | 1716 | 1.41 | 0.71 | 1.6 | 249400 |
| 0.63 | 84440 | 1825 | 1730 | 2.0 | 0.71 | 1.8 | 249600 |

The description of conditions reported in this paper were motivated by the process of flame attachment which begins with a premixed natural gas jet which is enriched with hydrogen. The amount of hydrogen $xH_2$ is reported as a fraction of the total fuel injected into the axial stage. The natural gas concentration is reported as the equivalence ratio $\phi_{AX,NG}$ prior to the injection of hydrogen for flame attachment. The averages are from the total of 6000 images, 40 ms of flow time. The term flame brush is used for the average image. Figure 6.2 shows the effect of the baseline natural gas concentration of the transverse jet on the flame attachment. The image shows in addition to the $OH^*$ distribution, the location of the injector - black rectangle - relative to the bottom wall of the combustor - Y/D = 0 and the 4.65mm portion without optical access - white rectangle. The steps towards attachment in the test procedure were (1) to inject the mixture of natural gas and air into the combustor, (2) hydrogen was then added to the premixed fuel until attachment occurred as shown in Fig 6.1.

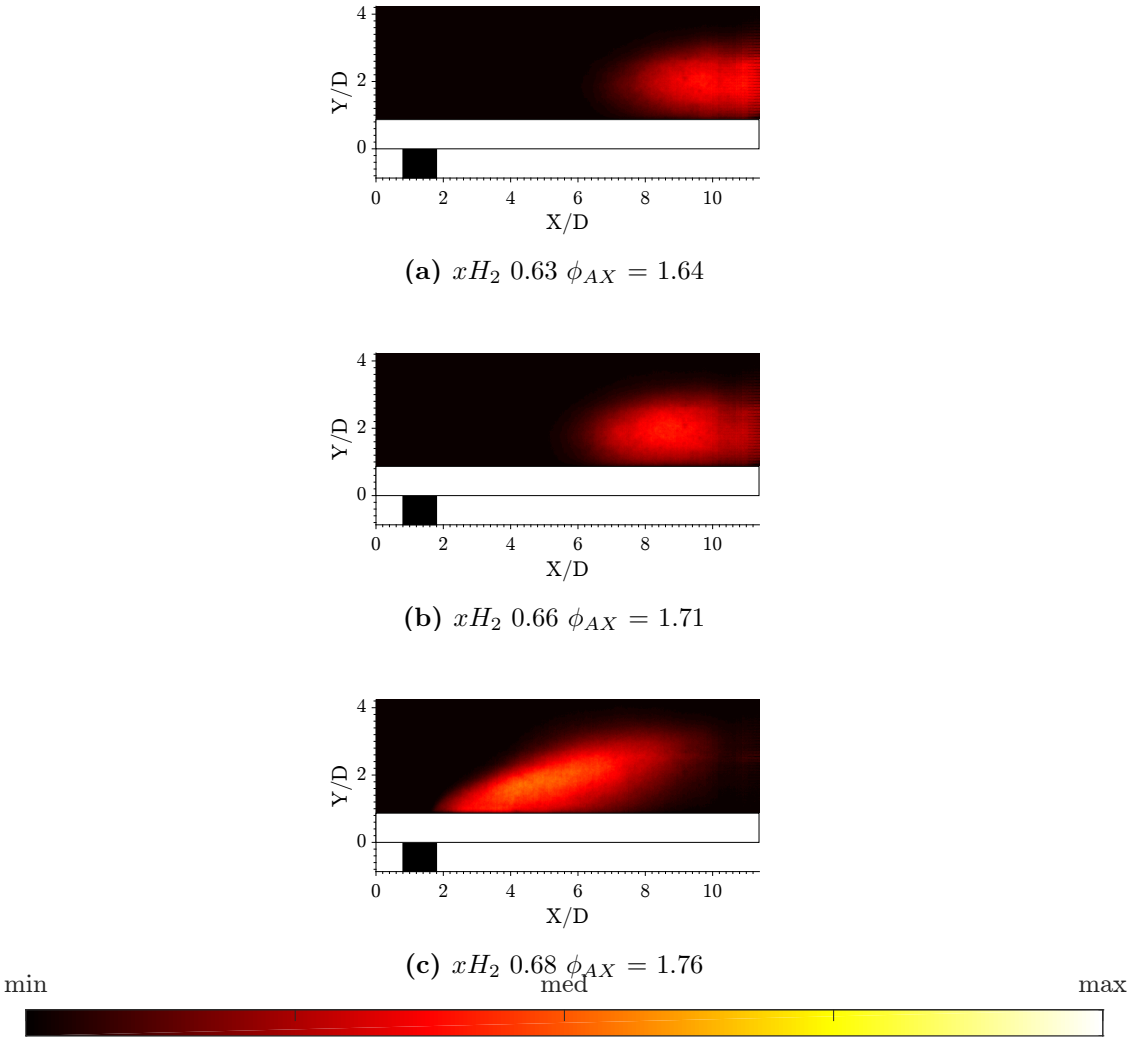


**(a)** $xH_2$ 0.63 $\phi_{AX} = 1.64$

**(b)** $xH_2$ 0.66 $\phi_{AX} = 1.71$

**(c)** $xH_2$ 0.68 $\phi_{AX} = 1.76$

**Figure 6.1. :** Average images of unattached to attached flames at increasing hydrogen content on a premixed fuel jet at $\phi_{AX,NG} = 1.18$ and crossflow Mach number of 0.41. 6.10f $xH_2$ 0.63 $\phi_{AX} = 1.64$, 6.10h $xH_2$ 0.65 $\phi_{AX} = 1.71$, 6.10j $xH_2$ 0.68 $\phi_{AX} = 1.76$.

The series of images in Fig. 6.2 (which are split across two pages) show the behavior of the jet under three natural gas equivalence ratios. The behavior of the jet can be summarized as such: as the jet natural gas equivalence ratio increases, the fraction of hydrogen in the total fuel required to keep the flame attached to the injector decreases. This trend is not monotonic in either the 0.31 or the 0.63 crossflow Mach numbers.

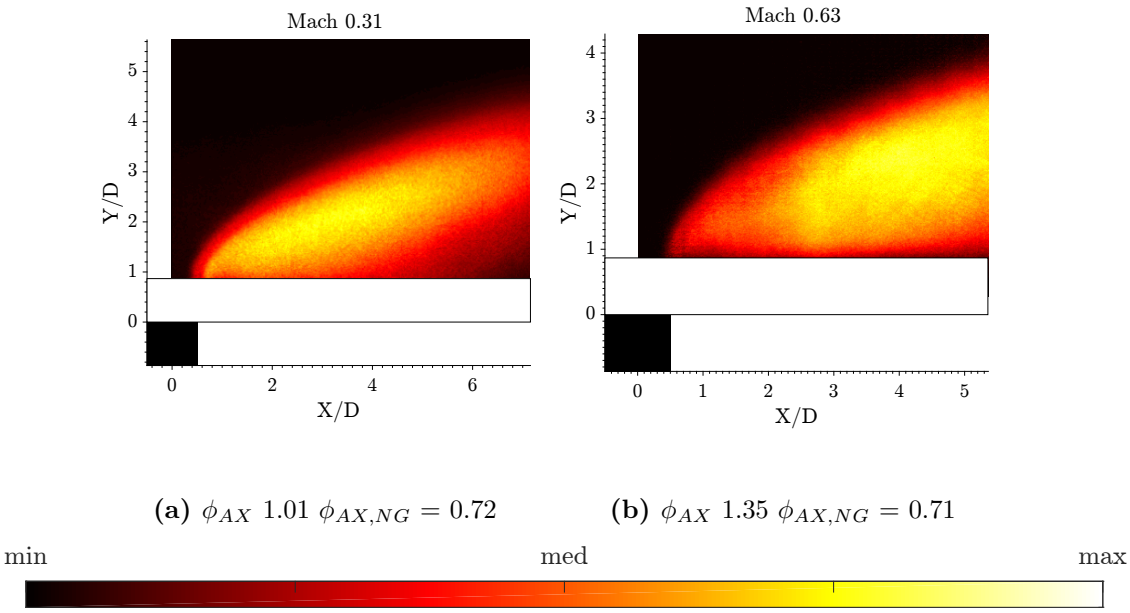


**(a)** $\phi_{AX}$ 1.01 $\phi_{AX,NG} = 0.72$ **(b)** $\phi_{AX}$ 1.35 $\phi_{AX,NG} = 0.71$

**Figure 6.2. :** Average images at Mach 0.31 (left) and Mach 0.63 (right).
6.2a $xH_2$ 0.63 6.2b $xH_2$ 0.79

The flame attachment behavior for different natural gas equivalence ratios at the 0.31 crossflow Mach number is also shown in Fig. 6.2. The flame attachment point recedes from the injector face similar to the $CH_4$ doped $C_2H_6$ flames in the RJICF experiment by Sirignano et al. [37]. The attachment at the $\phi_{AX,NG}$ 0.71 condition requires the highest hydrogen content where what is observed is a cusp at the edge of the attached flame, perhaps an average of leading points in this flame. It is easier to distinguish the bottom edge of the flame brush from the bottom edge of the image providing a clear indication of the flame brush thickness. This trend is shown in Fig. 6.4a. As indicated in table 6.2 addition of natural gas reduces the required hydrogen for attachment at the $\phi_{AX,NG}$ 1.4 condition - the minimum at this Mach number. It is also clearer from the $\phi_{AX,NG}$ 1.4 condition that the flame attachment increasingly follows the bottom wall of the combustor as the natural gas equivalence ratio increases. The vertical extent of the flame brush at the $\phi_{AX,NG}$ 2.0 condition is larger because of the total fuel equivalence ratio, lower reactivity of the fuel and buoyancy following heat release in the jet DSL. This behavior was captured by extracting

the peak flame brush intensity in Fig. 6.3i. It is also possible that differential diffusion is responsible for the attachment of the flames at the different natural gas contents [81].

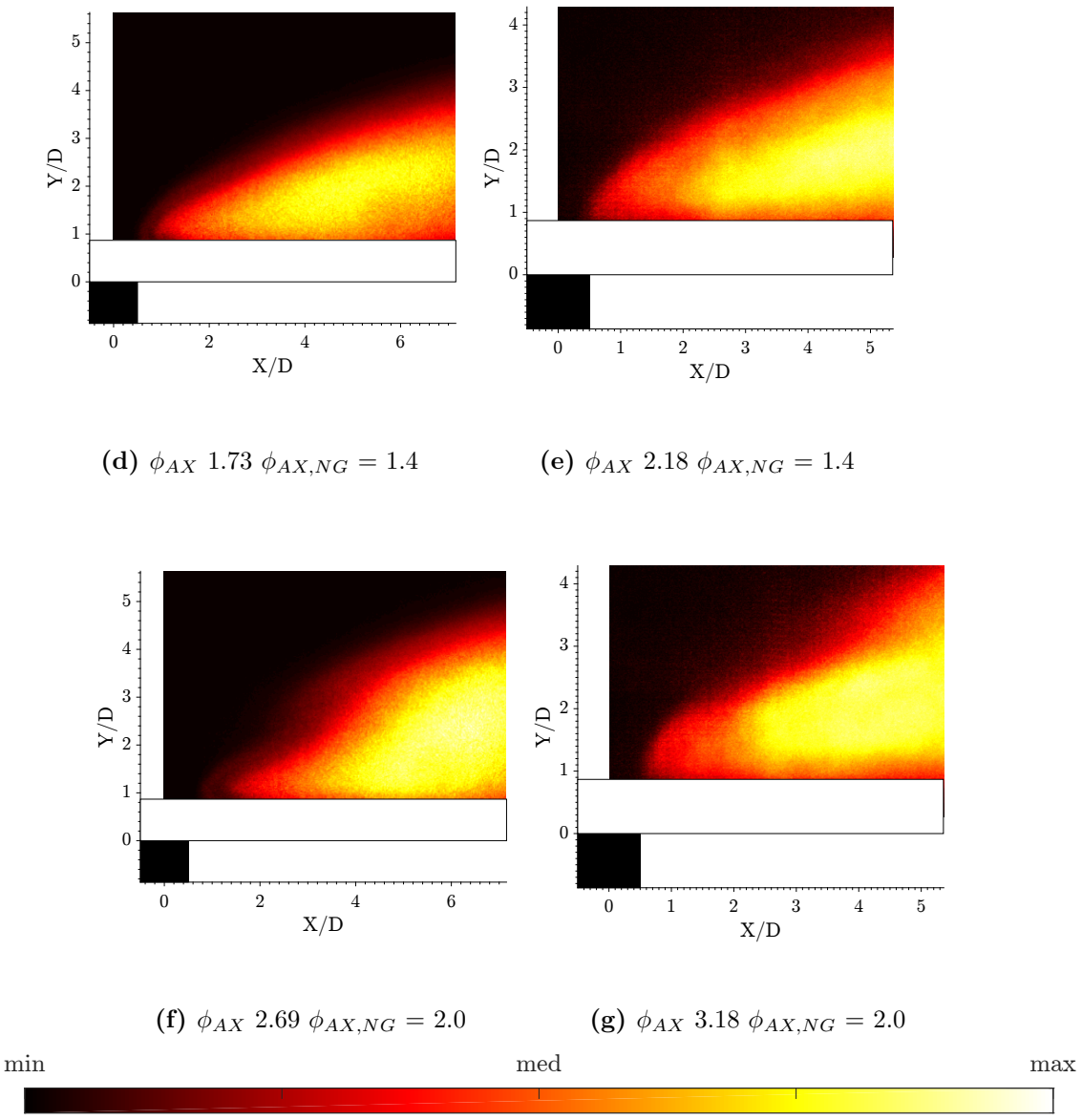


**(d)** $\phi_{AX}$ 1.73 $\phi_{AX,NG} = 1.4$ **(e)** $\phi_{AX}$ 2.18 $\phi_{AX,NG} = 1.4$

**(f)** $\phi_{AX}$ 2.69 $\phi_{AX,NG} = 2.0$ **(g)** $\phi_{AX}$ 3.18 $\phi_{AX,NG} = 2.0$

**Figure 6.2. :** ...contd average OH* chemiluminescence images at Mach 0.31 (left) and Mach 0.63 (right).
6.2d $xH_2$ 0.46 6.2e $xH_2$ 0.71
6.2f $xH_2$ 0.59. 6.2g $xH_2$ 0.71.

For the 0.63 crossflow Mach number case, the hydrogen mole fraction decreases from the $\phi_{AX,NG}$ 0.71 case where the flame is attached the most robustly. The amount of hydrogen required for attachment is almost 80% by mole. It is also the highest at this crossflow Mach number. Also the point of maximum intensity in the flame brush moves toward the bottom wall initially before expanding due to the high heat release as seen in Fig. 6.3j. This may be attributed to the change in the mode of flame attachment from a shear layer stabilized flame to a boundary layer stabilized flame. This hypothesis will be tested further using instantaneous chemiluminescence images. Because of the high $OH^*$ chemiluminescence luminosity of the high hydrogen content fuels, it is difficult to distinguish the effect of the natural gas content on the flame brush thickness shown in Figs. 6.2b and 6.2e which is further highlighted in Fig. 6.4b. Another distinguishing effect overall is highlighted in the highest natural gas equivalence ratio where the flame brush increases in height and recedes from the injector face. This is highlighted in the rounded front of the flame brush.

Leading point theory described in Lipatnikov et al. [56] can help describe the curved front of propagation of the instantaneous flame in near the wall of the combustor as critically curved for this $Le > 1$ flame at this condition. This accounting of the flame Lewis number is understood because the flame brush is stabilized on the leeward side of the jet exclusively, where significant entrainment of combustion products and crossflow vitiated air occurs. This entrainment is responsible for diluting the jet downstream shear layer pre-ignition though the entrainment of hot crossflow or combustion products necessary for ignition of the warm jet. This occurs at the jet exit and the flame propagates with the jet and any wake coherent structures downstream. Should the coherent structures produce bulges that push into the jet core, these bulges are filled with more oxidizer than fuel relative to the jet core hence the reacting bulges are of $Le > 1$. It is possible that the jet core fuel also produces bulges into the crossflow, but this was not a predominant feature of the jet, consistent with other numerical efforts for hydrogen enriched methane flames by Hawkes and Chen [57]. Using this definition, it is clear that any propagating bulges from the oxidizer into the fuel would be critically strained 'superflamelets' that have to both contend against high strain rates in the jet wake of the RJICF but also have the right surface area to volume ratio to compete against the diffusive-thermal instability.

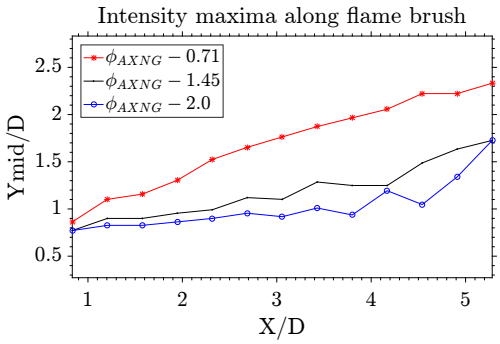


**(i)** Mach 0.31

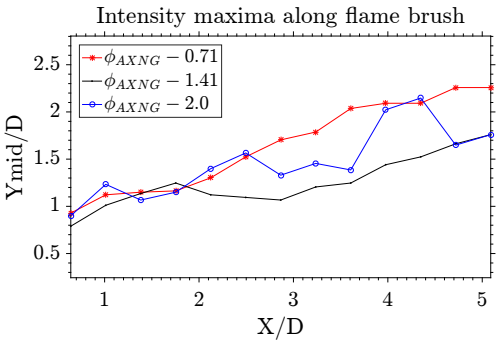


**(j)** Mach 0.63

**Figure 6.3. :** Flame brush peak intensity (FWHM) from Average images at Mach 0.31 6.3i and Mach 0.63 6.3j

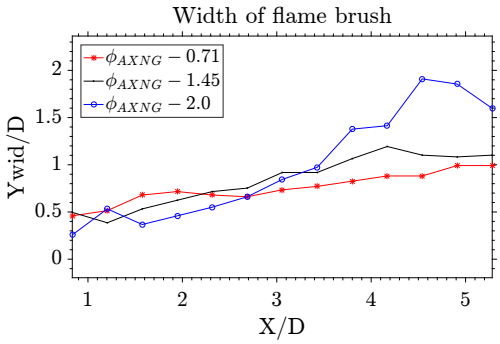


**(a)** Mach 0.31

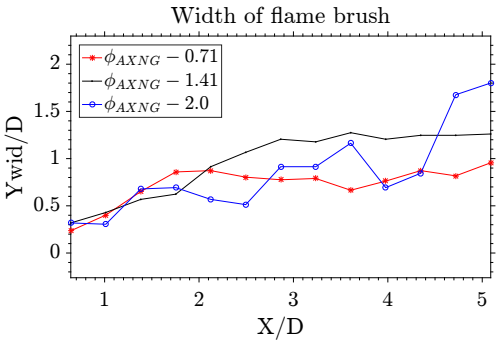


**(b)** Mach 0.63

**Figure 6.4. :** Flame brush width (FWHM) from Average images at Mach 0.31 6.4a and Mach 0.63 6.4b

The instantaneous images in Fig. 6.5 correspond to 53 µs of flow time with the combustor operating at crossflow Mach 0.31 and jet conditions $\phi_{AX,NG}$ 2.0, $\phi_{AX}$ 2.69 ,$xH_2$ 0.59. Here the images have been processed with a sliding Gaussian filter with a kernel of 2 pixels in diameter. The edges were marked using a canny edge detection algorithm. The large coherent structure labeled 'B' that is convected in the images is fluid in the jet wake that is observed during one phase of the flow time - the time required for repeating of coherent structures at any one location. In this duration, the fluid undergoes ignition, subsequent heat release and convection out of the image frame. The reignition kernels labeled 'A' were formed near the injector at t = 0 µs and are assumed to be located at a leading point in the jet wake. They reconnect with the convected coherent structure due to the reactivity of the fuel. It has been surmised that autoignition occured where high temperature and very rich fuel concentrations were found [82]. These images with ignition kernels appearing at the injector separate from the convected body of fluid undergoing heat release suggest otherwise. This implies that they are at a location of high strain rate. At the beginning of the phase duration, the time scale of igniting the fluid parcel is similar to the flow time scale in the jet wake, so that the ignited fluid proceeds upstream and attaches the flame to the injector face, reigniting the entrant fuel. As the fluid parcel runs out of fuel, it undergoes convection out of the frame, and top edges of the fluid become entrained vertically into the jet, igniting fluid that escaped the injector resulting in the large heat release - the brighter region at 'B'. The comparatively lower strain rates associated with this crossflow Mach number allow the flame labeled 'B' - corresponding to fluid undergoing heat release - to remain largely undeformed as it is convected. The shape of the extended ignition kernel at the injector face seems to follow the jet trajectory. In summary it was observed that often the fluid undergoing heat release detaches from the ignition kernel at the injector face, and may reattach through boundary layer fluid at the bottom wall of the combustor. That the flame is reignited means the ignition kernels at the injector face are traveling at or above the flow time scales despite the convection of other fluid undergoing heat release further downstream of the injector face.

## 6.2 Instantaneous Attached Flame Behavior

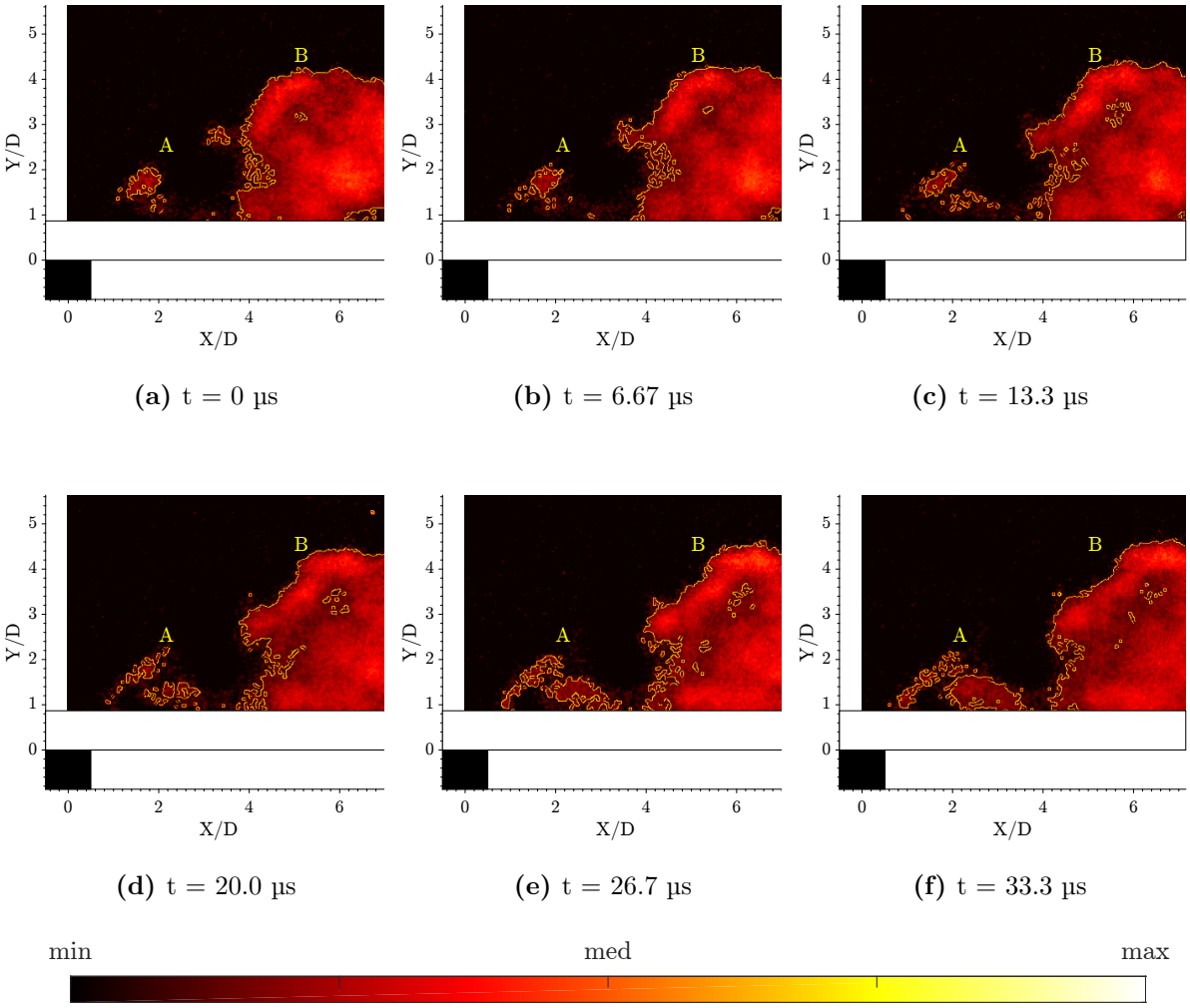


**(a)** t = 0 µs **(b)** t = 6.67 µs **(c)** t = 13.3 µs

**(d)** t = 20.0 µs **(e)** t = 26.7 µs **(f)** t = 33.3 µs

**Figure 6.5. :** Instantaneous images at crossflow Mach 0.31. Conditions are $\phi_{AX,NG}$ 2.0, $\phi_{AX}$ 2.69 ,$xH_2$ 0.59 captured at 150kHz

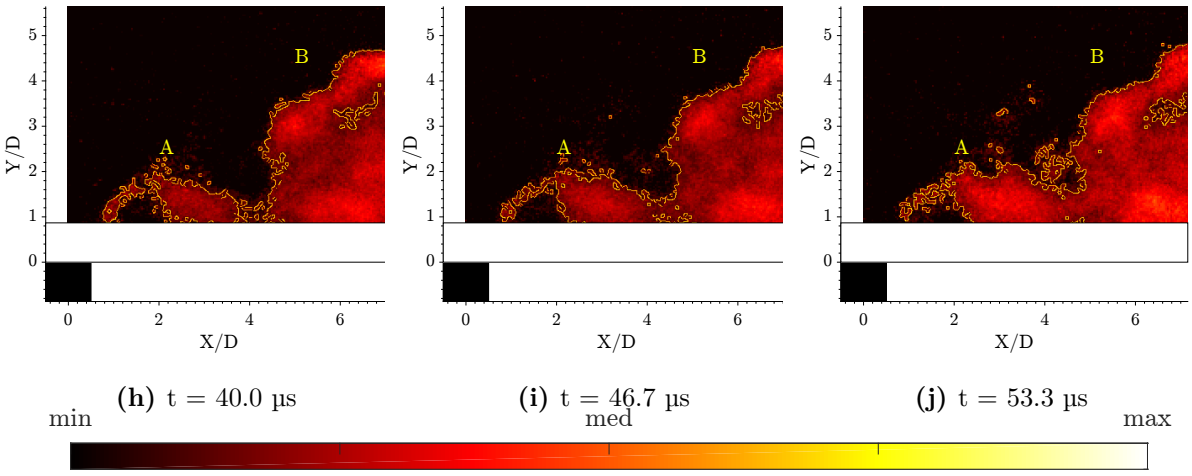


**(h)** t = 40.0 µs **(i)** t = 46.7 µs **(j)** t = 53.3 µs

**Figure 6.5. :** ... contd. instantaneous images at crossflow Mach 0.31. Conditions are $\phi_{AX,NG}$ 2.0, $\phi_{AX}$ 2.69 ,$xH_2$ 0.59 captured at 150kHz

At the higher crossflow Mach number of 0.63, the $\phi_{AX,NG}$ 2.0, $\phi_{AX}$ 3.18, $xH_2$ 0.71 jet in figure 6.6 undergoes similar events as discussed at the lower Mach number. Here again the images have been processed with a sliding Gaussian filter with a kernel of 2 pixels in diameter. The edges are marked using a canny edge detection algorithm. The shorter timescales and higher strain rates are evident in the deformation of the fluid parcels undergoing heat release and the faster turnover. The large quantity of OH* labeled 'B' in Fig. 6.5 is replaced with a much smaller quantity of OH* also labeled 'B' in Fig. 6.6 at crossflow Mach number 0.63. Because of the shorter flow timescales at Mach 0.63, a higher hydrogen content was required to attach the flames in Fig. 6.6, which corroborates the higher quantity of OH*. That the jet has a lower hydrogen content (minimum required for attachment at the 0.63 Mach number) is also evident in that the edge of the leading point from the injector face recedes. It is evident in these images that the flame proceeds to the injector along the bottom wall of the combustor and only after the leading point consumes fuel along the wall is the top edge of the fluid entrained vertically into the unburned mixture closer to the jet core. Vertical entrainment is seen in the sequence of images from 33 µs - 53 µs along with the marker labeled 'A'. Reignition of the jet fluid is dependent on flame propagation to the jet injector through the low pressure wake. The ignition kernel observed here is more broken showing more dependence on autoignition at higher crossflow Mach number. The transverse jet flame has a quicker convection of the coherent structure out of the frame at this crossflow Mach

number - one phase of flow time. This is in response to the shorter flow timescales and higher turbulence.

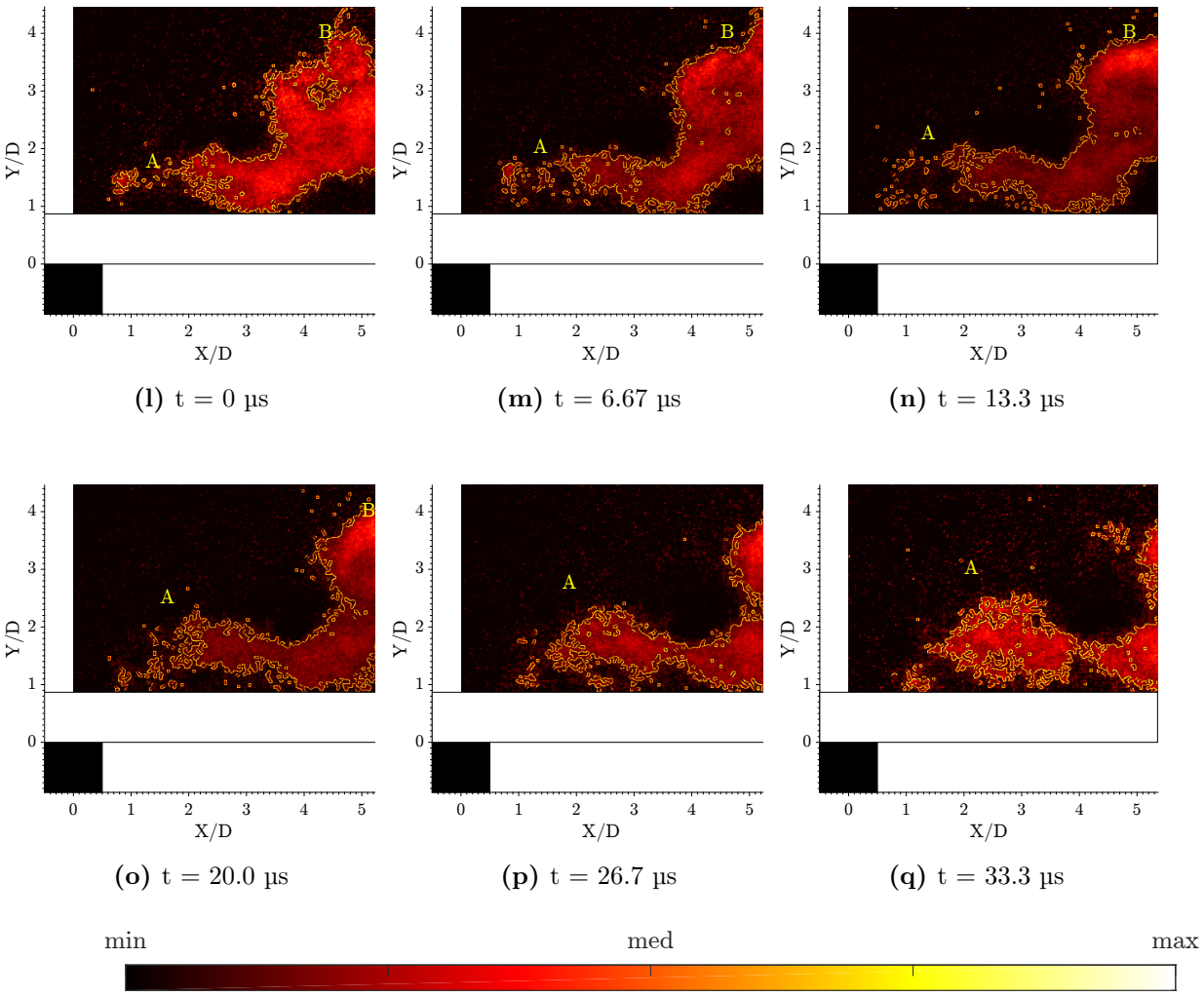


**(l)** t = 0 µs **(m)** t = 6.67 µs **(n)** t = 13.3 µs

**(o)** t = 20.0 µs **(p)** t = 26.7 µs **(q)** t = 33.3 µs

**Figure 6.6. :** Instantaneous images at crossflow Mach 0.63. The jet conditions are $\phi_{AX,NG}$ 2.0, $\phi_{AX}$ 3.18, $xH_2$ 0.71 captured at 150kHz

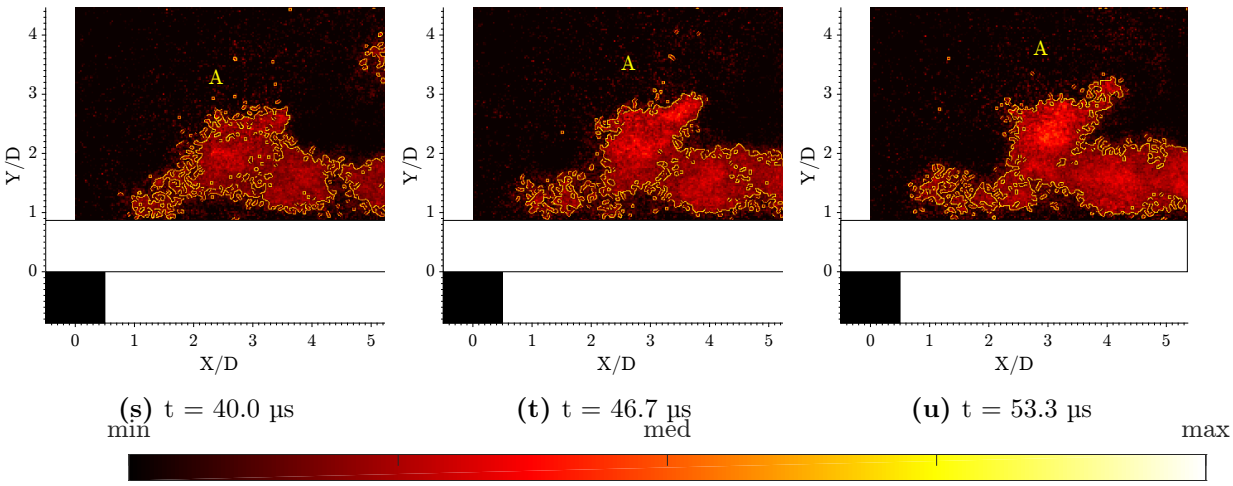


**Figure 6.6. :** ... contd. instantaneous images at crossflow Mach 0.63. The jet conditions are $\phi_{AX,NG}$ 2.0, $\phi_{AX}$ 3.18, $xH_2$ 0.71 captured at 150kHz

### 6.2.1 Attached Flame Intensity PDFs

The histogram of intensity captured at the injector in figures 6.8 and 6.9 were captured as follows. The intensity values of a square region of pixels with each side matching the diameter of the injector, as shown for example in Fig. 6.7,

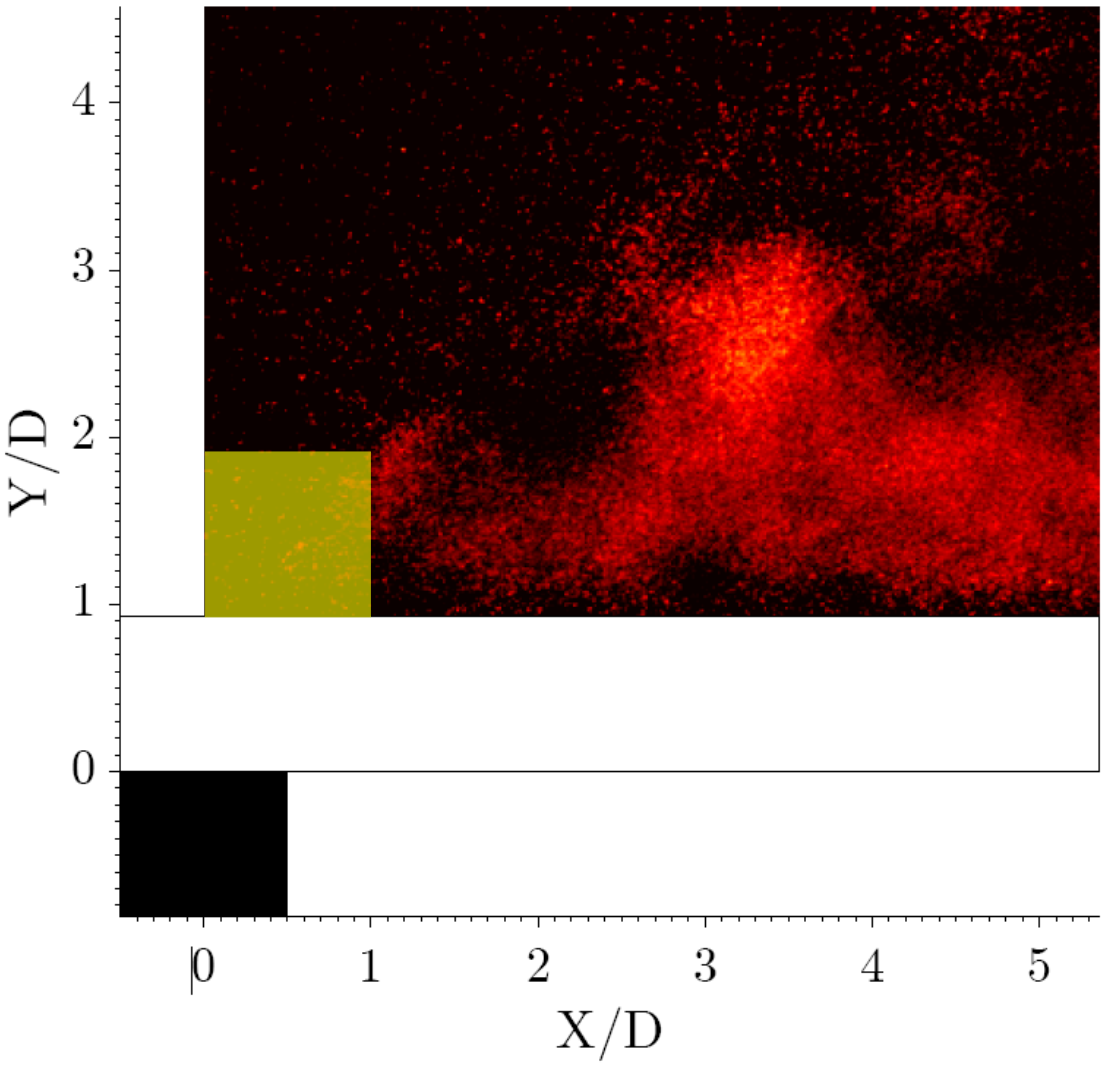


**Figure 6.7. :** Green square is a superpixel - an area over which the intensity is summed up

were summed up in each image to produce a pseudo-scalar quantity. This scalar was then binned into an ensuing histogram to show which jet conditions produce flames closest to the attachment point. For the lower Mach number cases, the histograms were binned with 200 bins. The higher Mach number cases had 20 bins due to fewer intermediate counts encountered in the binning for these images. Furthermore to remove the DC component at the injector, the bin corresponding to the zero count is not shown, the x-axis has been reinitialized count 10. The histogram reveals the drift away from attachment associated with the increase in the proportion of natural gas in the premixed fuel. The more drastic effect

shown in the images in Fig. 6.5 is also captured in the corresponding intensity histograms. It is more difficult to identify the reduction in intensity at the injector face at the crossflow Mach 0.63 case because of the higher luminosity associated with the higher hydrogen content.

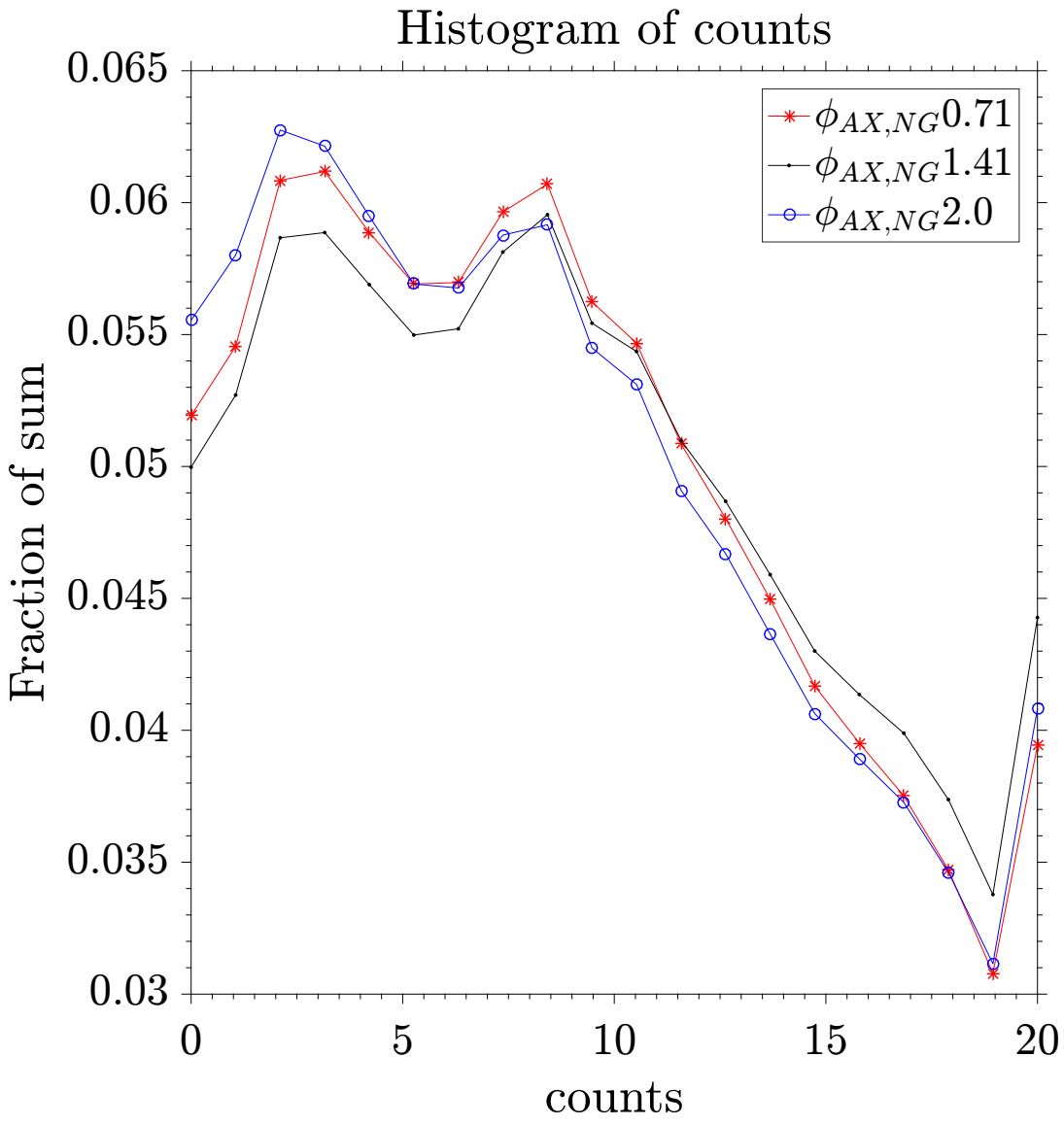


**Figure 6.8. :** PDFs of intensity of attached flames captured at 1 jet diameter after the injector at crossflow Mach 0.63.

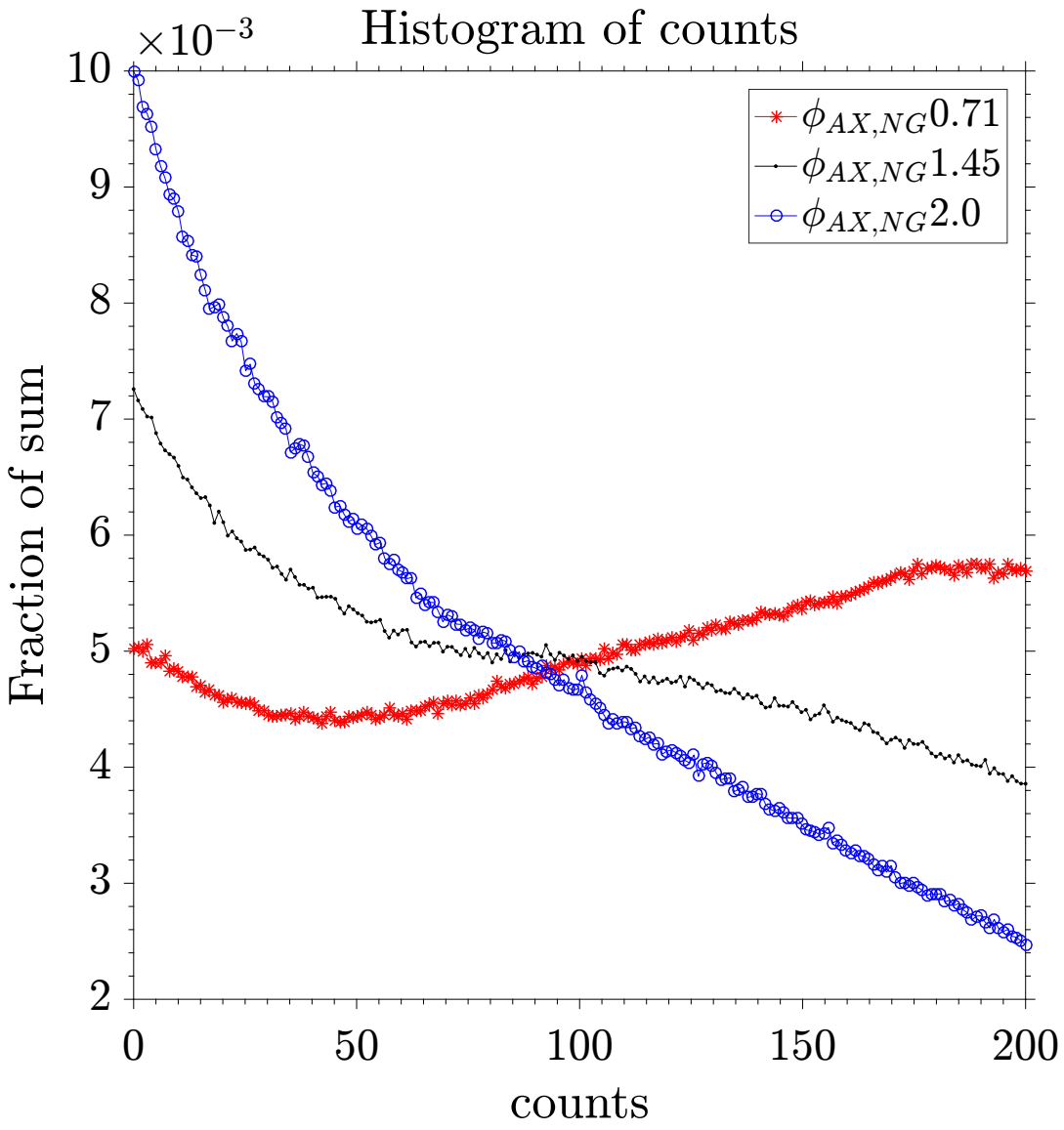


**Figure 6.9. :** PDFs of intensity of attached flames captured at 1 jet diameter after the injector for crossflow Mach 0.31.

### 6.2.2 Unattached Flame Behavior

The objective of capturing images of unattached flames at different crossflow Mach numbers were threefold. The first is to establish the range of hydrogen content necessary for the flame to stay attached robustly at the injector face. For this part the premixed natural

gas jet was enriched with hydrogen until attachment and then the hydrogen content was decreased even after detachment to observe the possibility of hysteresis. The hysteresis of hydrogen content for attachment was not observed. In addition, the hysteresis of unattached positions was not observed to within experimental accuracy. The second goal was to look for different mechanisms of flame stabilization between the unattached and attached locations. The measurements used to inform this result would be NOx, CO and UHC emissions and instantaneous PLIF measurements of the flames which will be shown in the next chapter. The measured emissions were in within the accuracy of the instrument due to the low increase in temperature following heat release at the axial stage mass flow rate. Finally the increase in crossflow Mach number is expected to increase the local strain rate at the flame attachment location, and hence the amount of hydrogen required for stabilization and attachment would provide some quantifier for correlating the extinction strain rate to the crossflow Mach number.

### Test Conditions

The interaction of the unattached flame through the wake of the jet was captured on two test days to reveal the behavior of the jet flame under unattached conditions at different jet and corresponding crossflow Mach numbers. For each crossflow Mach number, the jet natural gas composition was fixed and the hydrogen mole fraction was increased in increments until attachment with images captured in between.

Tables 6.3,6.4, 6.5 and 6.6 reflect the intent to understand the effect of upstream Mach number on the amount of hydrogen required to attach an unattached hydrogen enriched premixed natural gas flame at the injector face. These tables correspond to data obtained at a fixed natural gas equivalence ratio increasing hydrogen up to the point of attachment. The average flame position is defined as the distance of the flame leading edge from the downstream edge of the injector orifice.

**Table 6.3. :** Fixed Natural Gas (FNG) Test Conditions

| Upstream conditions | | | | Jet conditions | | | |
|---|---|---|---|---|---|---|---|
| Mach # | $Re_{Dh}$ | $T_0$ | $T$ | $\phi_{AX,NG}$ | Min. $xH_2$ | J | $Re_D$ |
| 0.27 | 49310 | 1617 | 1600 | 1.17 | 0.59 | 2.0 | 130000 |
| 0.41 | 72100 | 1596 | 1559 | 1.18 | 0.68 | 2.0 | 138300 |
| 0.68 | 86200 | 1839 | 1730 | 0.8 | 0.85 | 1.4 | 236700 |

**Table 6.4. :** Flame progression for Mach 0.27 FNG condition

| Flame ID | Average Flame Position | Hydrogen in fuel blend | | |
|---|---|---|---|---|
| $\phi_{AX,NG}$ 1.17 | mm | $xH_2$ | $\dot{m}H_2$[g/s] | $\phi_{ax}$ |
| 2A | 30 | 0.48 | 0.09 | 1.42 |
| 2B | 23 | 0.52 | 0.10 | 1.47 |
| 2C | 18 | 0.55 | 0.12 | 1.53 |
| 2D | 15 | 0.58 | 0.13 | 1.56 |
| 2E | 0 | 0.59 | 0.14 | 1.57 |

**Table 6.5. :** Flame progression for Mach 0.41 FNG condition

| Flame ID | Average Flame Position | Hydrogen content | | |
|---|---|---|---|---|
| $\phi_{AX,NG}$ 1.18 | mm | $xH_2$ | $\dot{m}H_2$[g/s] | $\phi_{ax}$ |
| 4A | 35 | 0.55 | 0.17 | 1.53 |
| 4B | 29 | 0.59 | 0.20 | 1.59 |
| 4C | 25 | 0.62 | 0.22 | 1.64 |
| 4D | 20 | 0.65 | 0.26 | 1.71 |
| 4E | 0 | 0.67 | 0.28 | 1.76 |

**Table 6.6. :** Flame progression for Mach 0.68 FNG condition

| Flame ID | Average Flame Position | Hydrogen content | | |
|---|---|---|---|---|
| $\phi_{AX,NG}$ 0.8 | mm | x$H_2$ | $\dot{m}H_2$[g/s] | $\phi_{ax}$ |
| 6A | 56 | 0.75 | 0.38 | 1.39 |
| 6B | 40 | 0.77 | 0.42 | 1.48 |
| 6C | 29 | 0.80 | 0.51 | 1.63 |
| 6D | 19 | 0.83 | 0.62 | 1.78 |
| 6E | 0 | 0.85 | 0.71 | 1.94 |

A total of 9 hydrogen addition sweeps at a fixed natural gas equivalence ratio were imaged. 3 of those 9 are listed in tables 6.3, 6.4, 6.5 and 6.6. Average unattached flames are shown in the following images in figures 6.10. The flame shapes are similar in that the upstream portion of the average unattached images are rounded at the leading edge. The vertical extent of the flame brush is consistent between the flame positions, the only difference is the location of the leading edge. The vertical extent of the flame brush is about 3.5 jet diameters for the attached flame in the 0.41 crossflow Mach number condition, compared to about 5.5 jet diameters for the attached flame in the 0.68 crossflow Mach number condition. The increase in the vertical extent of the flame brush is due to the increase in the total amount of fuel being burned.

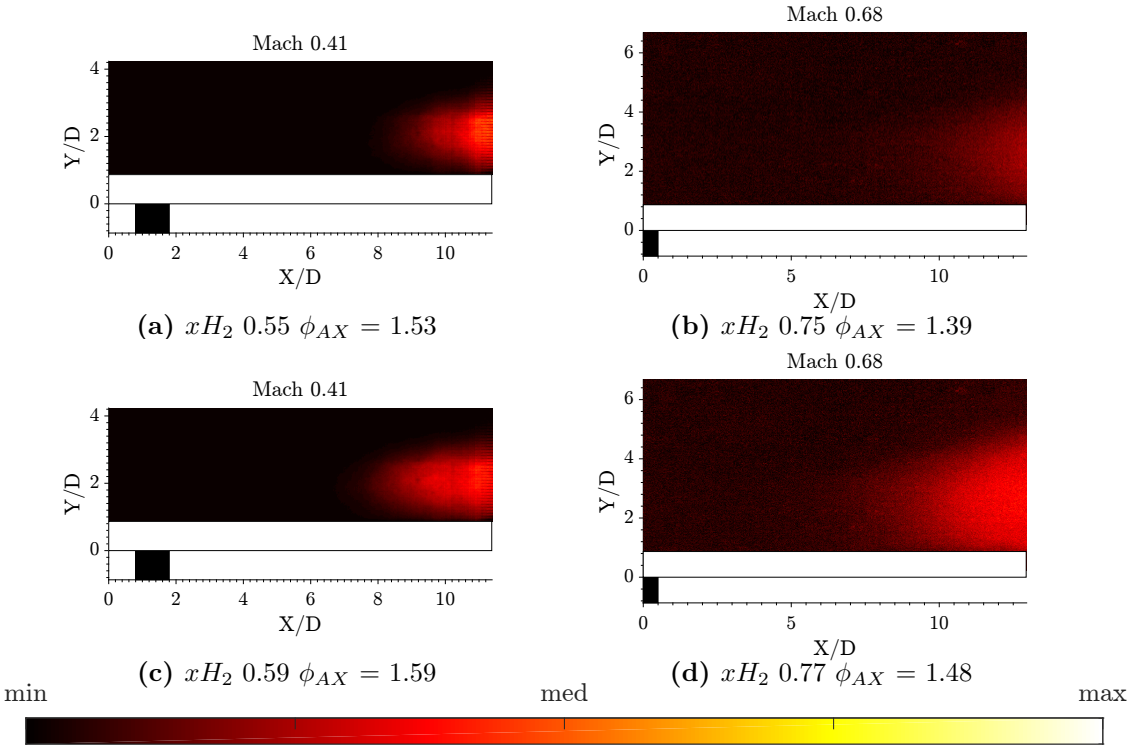


**(a)** $xH_2$ 0.55 $\phi_{AX} = 1.53$ **(b)** $xH_2$ 0.75 $\phi_{AX} = 1.39$

**(c)** $xH_2$ 0.59 $\phi_{AX} = 1.59$ **(d)** $xH_2$ 0.77 $\phi_{AX} = 1.48$

**Figure 6.10. :** Average images of unattached to attached flames at increasing hydrogen content on a premixed fuel jet at two equivalence ratios and crossflow Mach numbers. Right $\phi_{AX,NG} = 0.8$ and crossflow Mach number of 0.68. Left $\phi_{AX,NG} = 1.18$ and crossflow Mach number of 0.41. 6.10a $xH_2$ 0.55 $\phi_{AX} = 1.53$, 6.10b $xH_2$ 0.75 $\phi_{AX} = 1.39$, 6.10c $xH_2$ 0.59 $\phi_{AX} = 1.59$, 6.10d $xH_2$ 0.77 $\phi_{AX} = 1.48$,

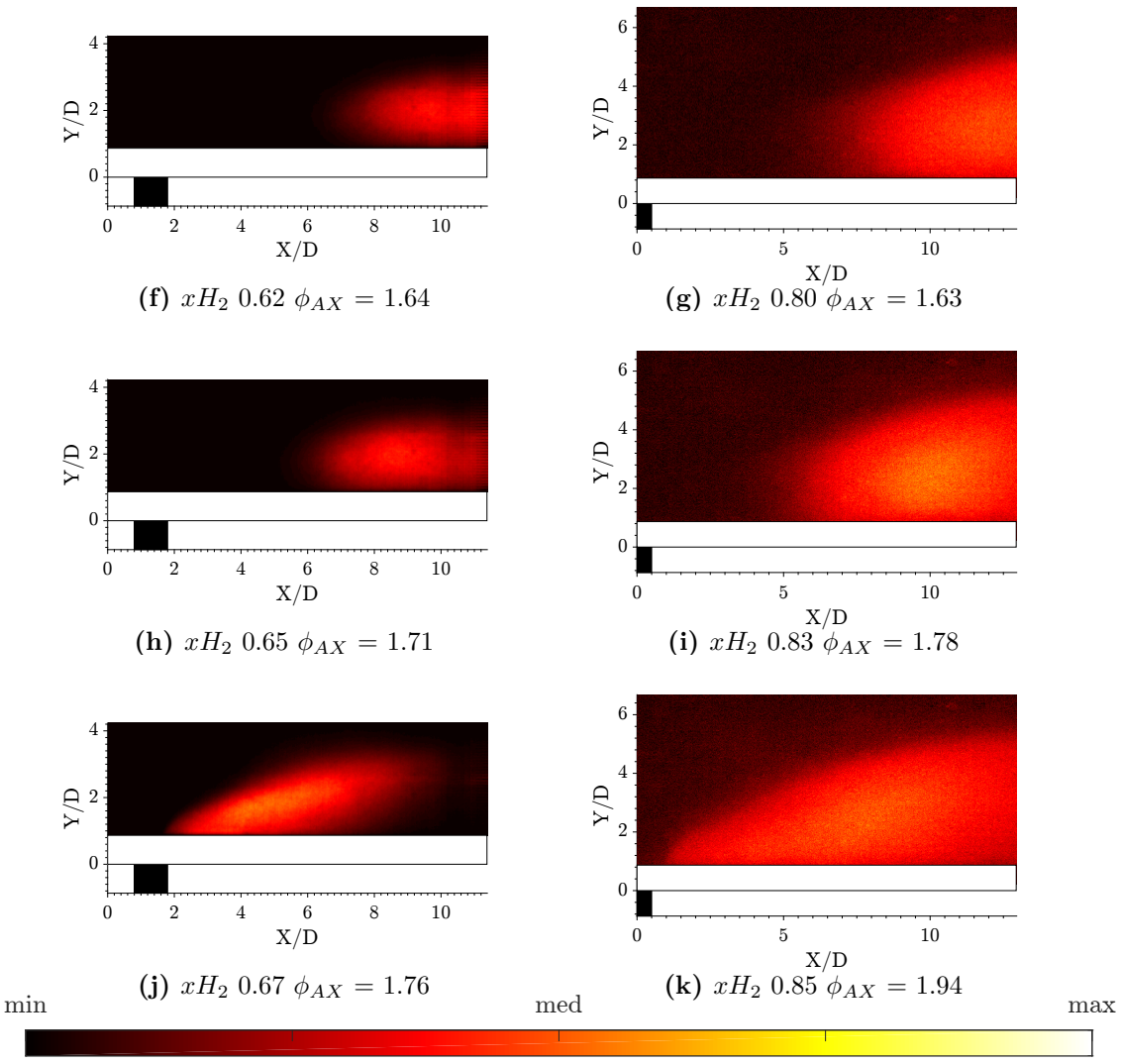


**Figure 6.10. :** ...contd average images of unattached to attached flames at increasing hydrogen content on a premixed fuel jet at two equivalence ratios and crossflow Mach numbers. Right $\phi_{AX,NG}$ = 0.8 and crossflow Mach number of 0.68. Left $\phi_{AX,NG}$ = 1.18 and crossflow Mach number of 0.41. 6.10f $xH_2$ 0.62 $\phi_{AX}$ = 1.64, 6.10g $xH_2$ 0.80 $\phi_{AX}$ = 1.63, 6.10h $xH_2$ 0.65 $\phi_{AX}$ = 1.71, 6.10i $xH_2$ 0.83 $\phi_{AX}$ = 1.78, 6.10j $xH_2$ 0.67 $\phi_{AX}$ = 1.76. 6.10k $xH_2$ 0.85 $\phi_{AX}$ = 1.91.

The average flame brush leading edge in figure 6.11 shows the required hydrogen content increases significantly at higher crossflow Mach number. The amount of hydrogen starts high and stays high ($xH_2 \geq 0.7$), and the slope is low from the closest unattached point to the attachment point.

The mole fraction of hydrogen required to attach an initially unattached flame in the crossflow with Mach number 0.41 was 68% and increased to 85% in the crossflow with Mach number 0.68. The shapes of the attached flames indicate that the flames exhibit downstream shear layer (DSL) flame behavior at these natural gas contents. It is consistent with the natural gas equivalence ratio for the 0.68 crossflow Mach RJICF. The unattached RJICF stays close to bottom wall of the combustor at every point as it progresses toward the injector. At both Mach numbers, the final jump from unattached to attached flame was abrupt as shown in the slope of the flame leading edge position vs hydrogen mole fraction plot (see Fig. 6.11). The higher crossflow Mach number case shows that the unattached flame progresses further into the unburned fluid before final attachment. This abrupt attachment shows that the far wake of the jet is more uniformly mixed than closer to the injector face so that unattached flame stabilization is similar between positions. The slope of the plot at the higher crossflow Mach number case is similar before and after the flame is attached, showing the slower mixing of a jet flame in a crossflow with a higher Mach number. Here the progress of the unattached flame is more constrained by the high strain rate region the flame is progressing into than on the mixedness of the fuel.

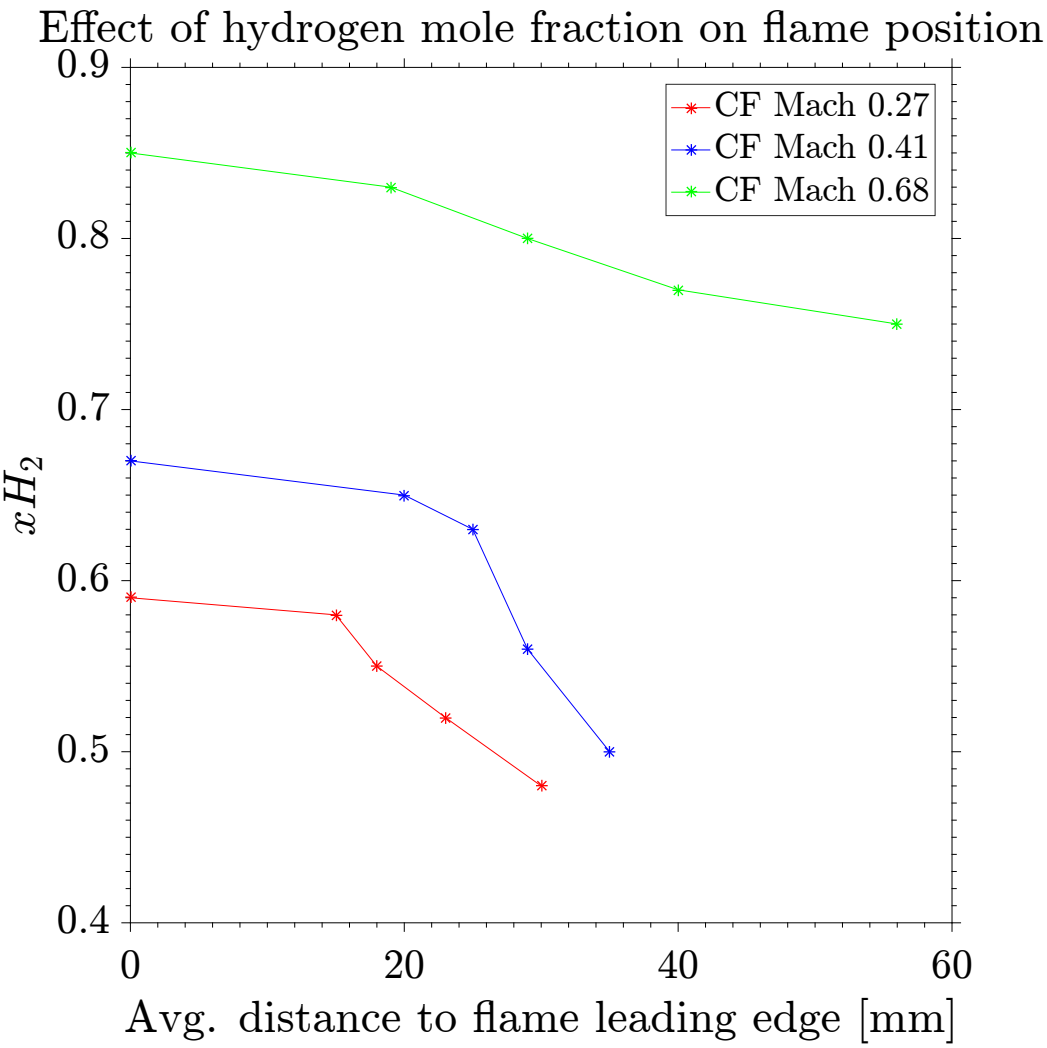


**Figure 6.11. :** Flame brush leading edge.

The average flame brush leading edge in Fig. 6.11 shows the required hydrogen content increases significantly at higher crossflow Mach number. The amount of hydrogen starts high ($\geq$70%) and stays high, and the slope as plotted is low from the closest unattached point to the attachment point.

# 7. OH PLIF MEEASUREMENTS

The OH PLIF measurements were captured using the configuration described in section 5.2. The detection limits from the linear OH LIF are well within the expected superequilibrium OH from a flame featuring the fuels and oxidizer. The test conditions where OH PLIF are obtained include the 0.31, 0.45 and 0.68 crossflow Mach conditions. Both attached and unattached OH PLIF measurements were made for the 0.31 and 0.45 crossflow Mach cases.

## 7.1 OH Transition

For OH PLIF, the laser was tuned to the absorption line of OH near 283 nm corresponding to the $Q_1(6)$ (1,0) vibrational band of the $A^2\Sigma^+ \leftarrow X^2\Pi$ system. Fluorescence was captured from the $A^2\Sigma^+ \rightarrow X^2\Pi$ (0,0) and (1,1) bands around 308nm. A diode pumped solid state laser (Edgewave Innoslab IS 200-2-L) lasing at 532nm at 5 kHz, was used to pump a dye laser (Sirah Credo) with output wavelength near 566nm. The dye laser output was frequency doubled to the absorption line near 283nm and expanded using a cylindrical and a spherical lens system to the sheet width of about 25mm and thickness of about 300µm. The maximum ultraviolet pulse energies from the dye laser were about 50µJper pulse. The laser power was much lower than in previous measurements. Both the pump and dye lasers needed repair but the funds were not available.

## 7.2 OH PLIF Sheet

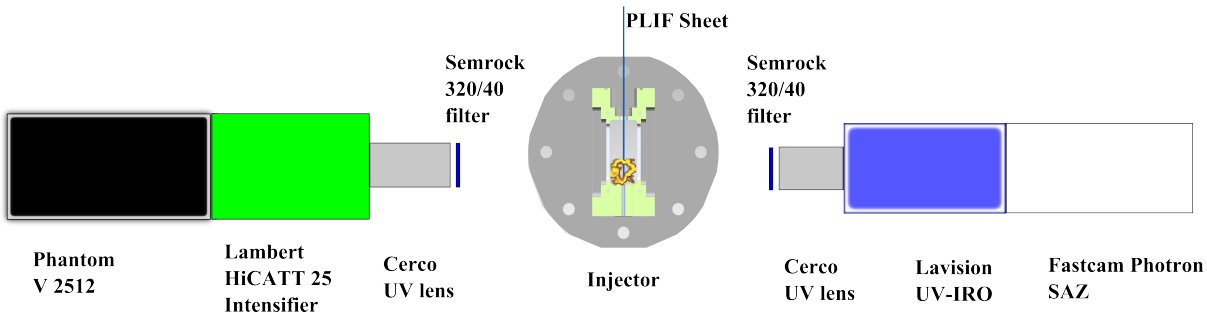


**Figure 7.1. :** Camera setup for simultaneous measurements, flow out of the page.

Figure 7.1 shows the laser sheet as positioned during the experiment at the center of the jet orifice. It was positioned so as to span a region upstream and downstream of the injector with imaging normal to this plane. Since the OH PLIF camera and the final sheet forming optics are assembled on translation stages, images captured from different portions of the flame can be compared for intensity, with the same collection efficiency. The intensifier gate was open for as long as 200ns or as short as 60 ns. The longer gate measurements were post processed by subtracting out the average non-resonant background (mostly chemiluminescence) which is largely absent at lower gate periods.

The images from the OH-PLIF measurements are corrected for pixel non-uniformity artifacts. Post processing for the images involves correction of pixel to real world units and in the case of OH PLIF images, cropping to focus on the portion of the image with relevant data.

## 7.3 Laser Sheet Correction

Some lasers propagate as Gaussian beams out of the output coupler, however propagation through or reflection from imperfect optics mixes the rays such that the beam profile is modified. The solid state laser used in this experiment has a top-hat profile prior to frequency doubling in the dye laser. Although the profile is not measured after each lens in the beam

path, it is expected that some modification of the beam profile occurs, especially from the sheet forming optics that concentrate the light into the center of the beam. To present the PLIF data in a way that enables quantitative comparison within each image, such that the pixel intensity is uniquely due to the quantity of OH in the flame and not due to laser profile, the laser sheet profile was obtained from the average flame image.

As the laser was operating at a peak pulse power of 50 µJ, the maximum sheet width capable of producing high contrast images was limited to about 25 mm. The flame was often however as long as 70 mm. The final turning mirror and the sheet forming optics were mounted on a translation stage to enable axial translation of the laser through the flame, with the lateral position of the laser aligned parallel to the vertical walls of the combustor and at the center of the bottom wall of the combustor, shown schematically in Fig. 7.1. The camera, intensifier and the 340 nm band pass filter were also installed on a translation stage. The difference in length of the laser sheet and the flame requires the laser sheet to be translated through the flame to obtain PLIF measurements of each part of the flame. The laser and the camera were translated the same amount between frame captures with the laser sheet centered on the image domain. This was done to ensure the image captures LIF at the same angle to the camera.

As an example of the laser profile procedure, a laser profile was extracted from the average of 1037 OH PLIF images spanning a period of 207 milliseconds at the conditions $\phi_{AX,NG}$ 0.8, and crossflow Mach number of 0.68. The image formed from these time average images is determined by LIF and the laser sheet profile. PLIF images from overlapping sections of the flame were obtained so as to capture LIF from the same portion of the flame modified by different portions of the laser. Some portions of the two images that contain overlapping portions are then reduced to line plots by averaging over a chosen vertical band of pixels to obtain intensity plots spanning a horizontal distance. The chosen vertical band is inspected to ensure it is far from flame edges where spatial nonuniformitites are expected. These intensity profiles themselves are not the laser profile since there could be flame nonuniformities in both vertical and horizontal directions that contribute to the acquired profile. To test this, profiles from multiple overlapping portions are compared. Figure 7.2 gives a comparison for the laser profile from six portions of the flame. The lower intensity of the laser profile at the 0 mm

mark is due to the attachment of the flame at the injector face providing no OH upstream of the attachment point. The similarity between the profiles gives the author confidence to correct the images using the similar intensity profiles. Finally a threshold is applied to the laser profile, so that the portions of the image that give less than 5% of the maximum signal are not used.

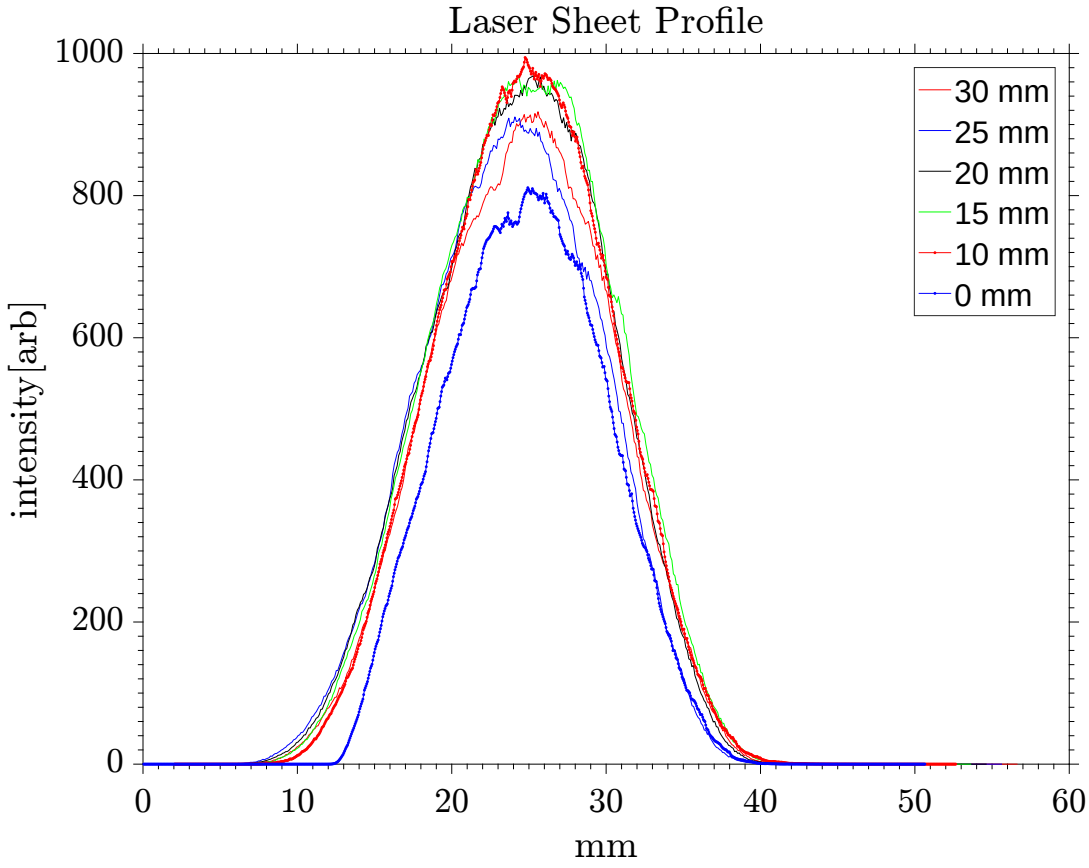


**Figure 7.2. :** Laser sheet profile as evidenced by similarity of average OH PLIF images over different portions of the flame. The legend shows illumination from different locations of the laser sheet along the length of the flame.

Ideally, correction of images would proceed with division by the laser profile, however this will amplify noise in the image where the profile nears zero. The profile is therefore modified by increasing the floor by a margin representative of the noise floor in each image. This allows division of image pixels with small intensity by a value in the profile not too small as

to amplify them significantly. Final correction of the instantaneous images is obtained by extending this profile to two dimensions by repetition, subsequent division of the image by the profile is carried out pixel by pixel.

An example of an image after correction is shown in figure 7.3. These PLIF images and subsequent figures are obtained with the laser sheet at the centerplane of the jet ((X,Y) plane, Z=0).

To reintroduce the schematic around the images, the dark rectangle beneath the image frame (in images near $X/D = 0$) signifies half of the injector ID, with the injector centerline at $\mathbf{X/D} = 0$. The white rectangle from $\mathbf{Y/D}$ 0-0.87 is the portion of the combustor that prevents optical access previously called the "lip". Crossflow direction is left to right (positive $\mathbf{X/D}$), and the jet issues into the positive Y/D direction.

The description of conditions reported in this chapter were motivated by the process of flame attachment which begins with a premixed natural gas jet which is enriched with hydrogen. The amount of hydrogen $xH_2$ is reported as a fraction of the total fuel injected into the axial stage. The natural gas content is reported as the equivalence ratio prior to the injection of hydrogen for flame attachment. The conditions of this jet are $xH_2$ of 87% in the total fuel, and a natural gas equivalence ratio $\phi_{AX,NG}$ of 0.82 in the premixed jet, with the jet Mach number of 0.59, crossflow Mach number of 0.68 and jet to crossflow momentum flux ratio of 1.4.

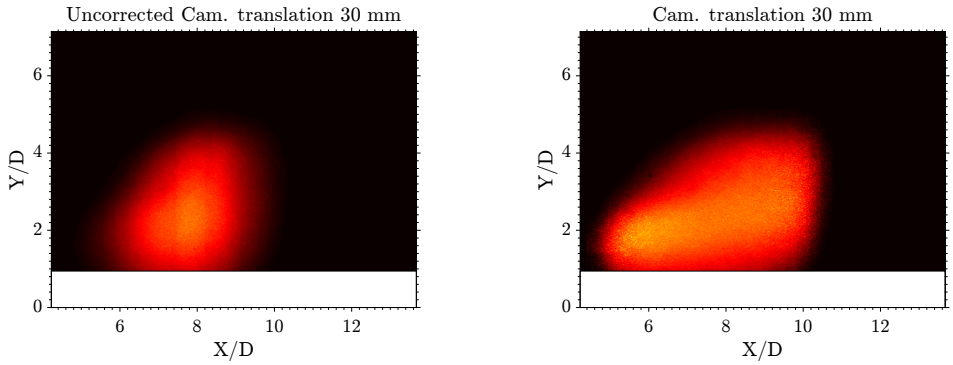


**(a)** Raw image.

**(b)** Processed image.

**Figure 7.3. :** Average of 1037 instantaneous OH PLIF images obtained with the camera (and laser sheet) positioned 30mm from the default position (capturing the injector). 7.3a The average of the images. 7.3b The average after laser sheet correction.

Post processing for the images involves correction from pixel to real world units using a dot target. For the highest Mach number condition OH PLIF was captured synchronized with the high repetition rate data system.

## 7.4 Attached Jet Flame

### 7.4.1 Flame Attachment Location

The flame attachment point was captured in Fig. 7.4 showing the flame is attached entirely on the leeward side of the jet injector. The images were obtained with the camera angled at 16°. The injector profile was straight and flush which would contribute to the jet profile at the injector face. The behavior of different injectors has been discussed in previous publications with the immediate effect of changing the strouhal number of the jet. Fully developed flow as is the nature of jets issuing from straight flush injectors have a lower strouhal number leading to later onset of vortex shedding and the associated instabilities responsible for mixing to initiate and or extinguish a flame [35]. This could contribute to the observed downstream shear layer burning.

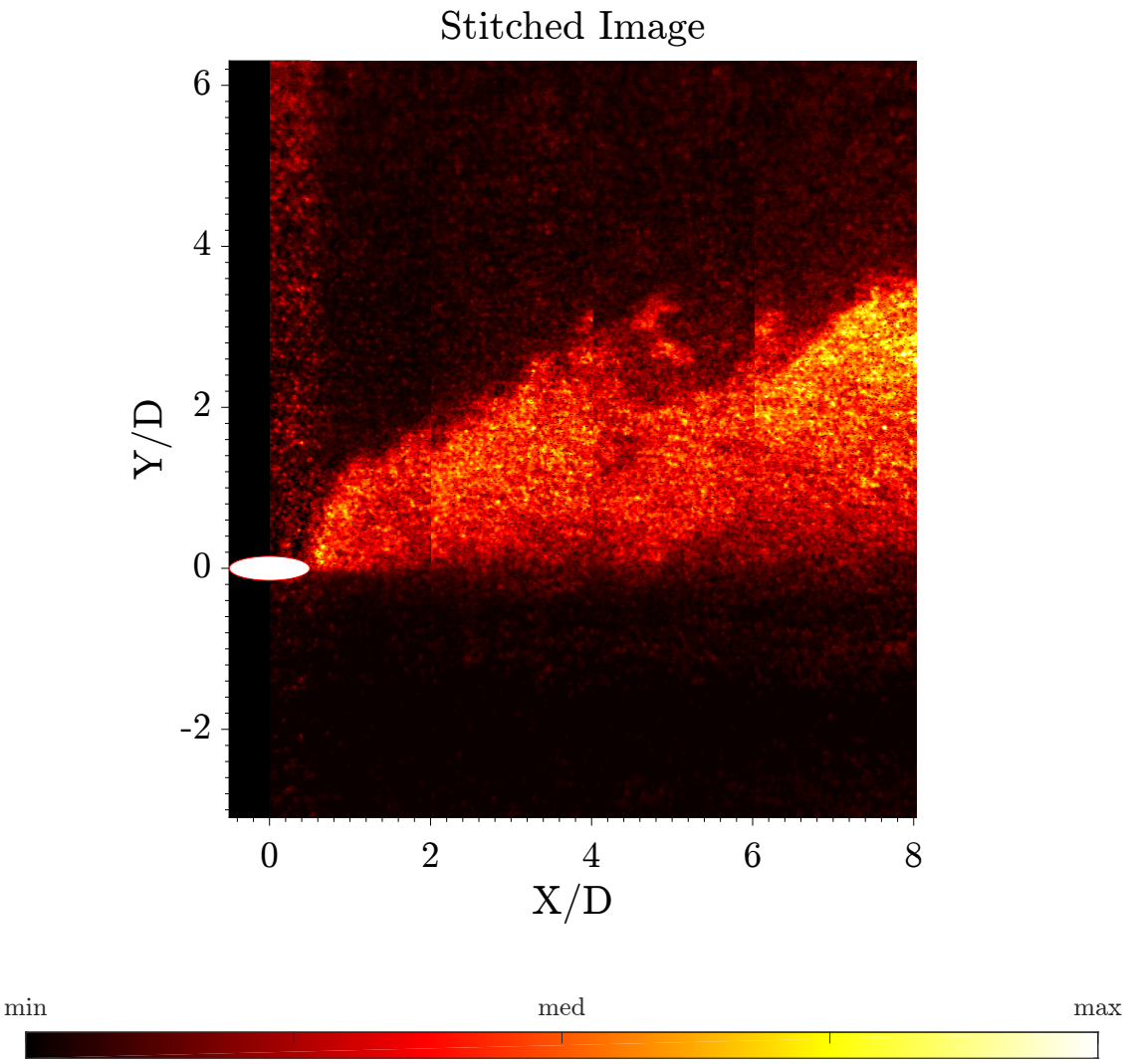


**Figure 7.4. :** Stitched instantaneous OH PLIF images, 10.7 mm apart, of a $\phi_{AX,NG}$ 1.45 jet with upstream condition of Mach 0.31 and $xH_2$ 53% at attachment with total $\phi$ 1.74 viewing the injector orifice at 16°.

From Fig. 7.4 it is clear that the flame is anchored at the bottom wall of the combustor and OH fills the distance from the wall to the top edge of the flame brush somewhat uniformly. For these low Mach crossflow cases, in addition to camera removal of camera artifacts in the stitched images, periodic artifacts were removed by spectral filtering.

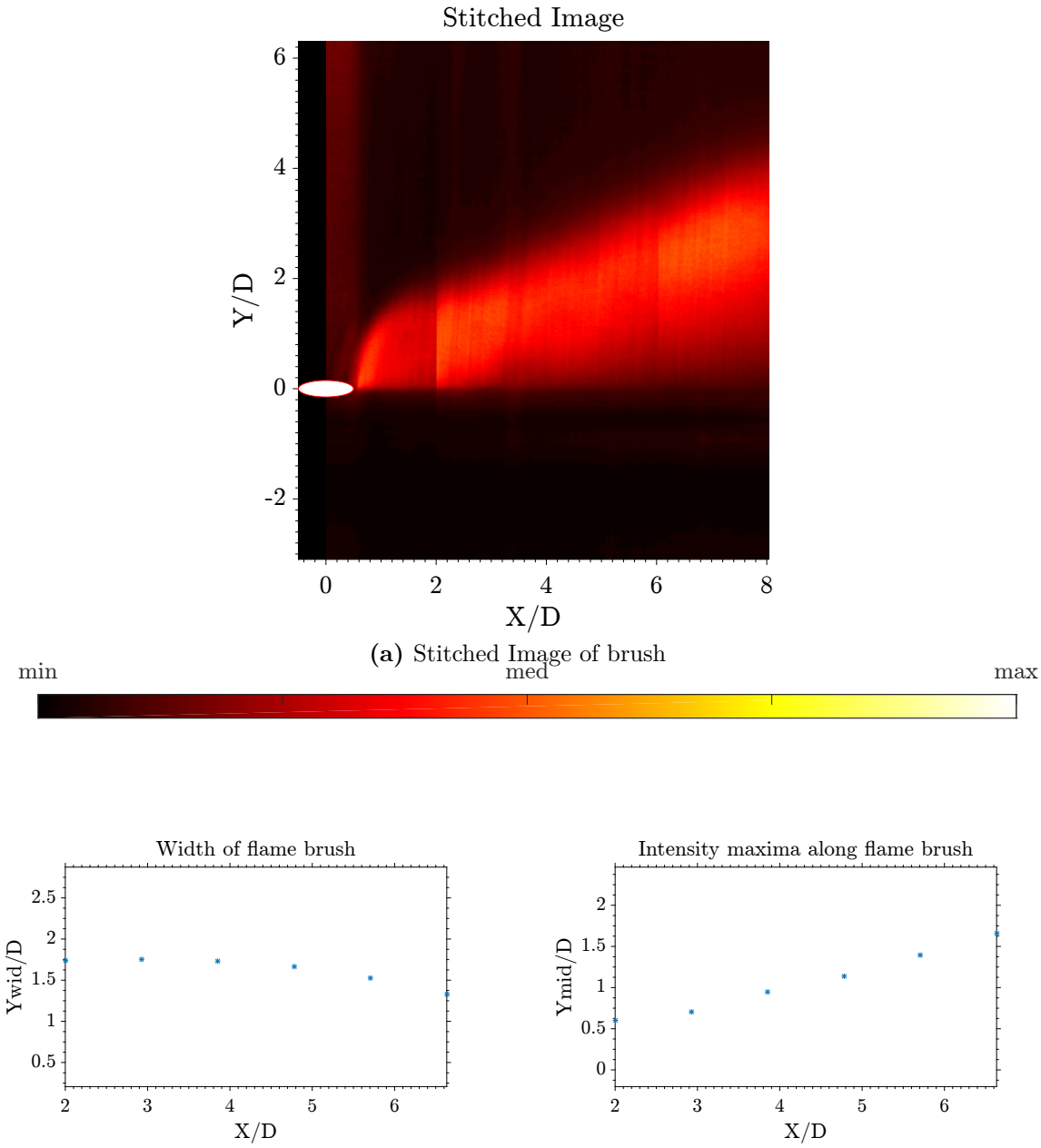


**(a)** Stitched Image of brush

**(c)** Brush width

**(d)** Brush height

**Figure 7.5. :** Statistics along flame brush. 7.5c The width of the intensity plot using the portion above the maximum.7.5d The trace of maxima of intensity as an estimate of the brush location above the bottom wall of the combustor. Same conditions as Fig. 7.4.

### 7.4.2 Jet Flapping

OH-PLIF measurements were performed on flame 6E (Fig. 6.10k) with the highest hydrogen content ($xH_2$ 0.85 $\phi_{AX} = 1.94$). Because the laser sheet was moved to sequentially cover overlapping regions of the flame, a stitched image shown in Fig. 7.6 covers the observed length of the flame. These images are obtained with the camera normal to the test section window.

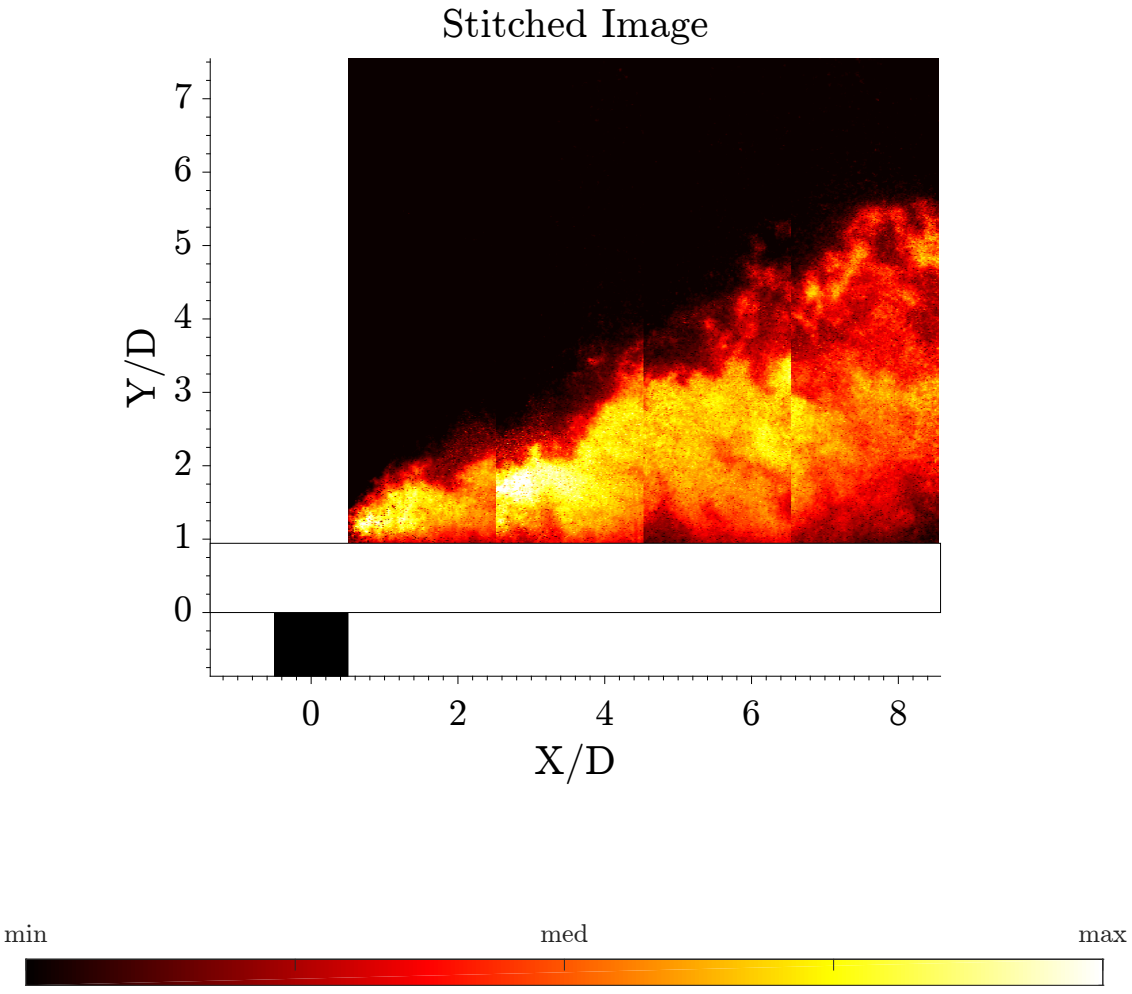


**Figure 7.6. :** Stitched instantaneous OH PLIF images at four locations 10.7 mm apart of a $\phi_{AX,NG}$ 0.8 jet with upstream condition of Mach 0.68 minimum $xH_2$ 85% for attachment with total $\phi$ 1.33.

These images are time resolved from the 10ns UV laser pulse, but there was no correlation between the images.

Jet flapping in the vertical direction is also observed in figures 7.7c and 7.7d where between the 4-6 jet diameter locations, the slope of the OH distribution is negative unlike the other images. It is not obvious how much the OH distribution may lift off the bottom wall due to the smaller vertical span of the OH distribution near the injector and the occlusion from the portion of the flow hidden behind the lip of optical access (between Y/D of 0 and 1). The vertical extent of the flame at this location reaches up to 4 jet diameters. The relative stability of the flame attachment is estimated with these images, perhaps up to the limit of the repetition rate.

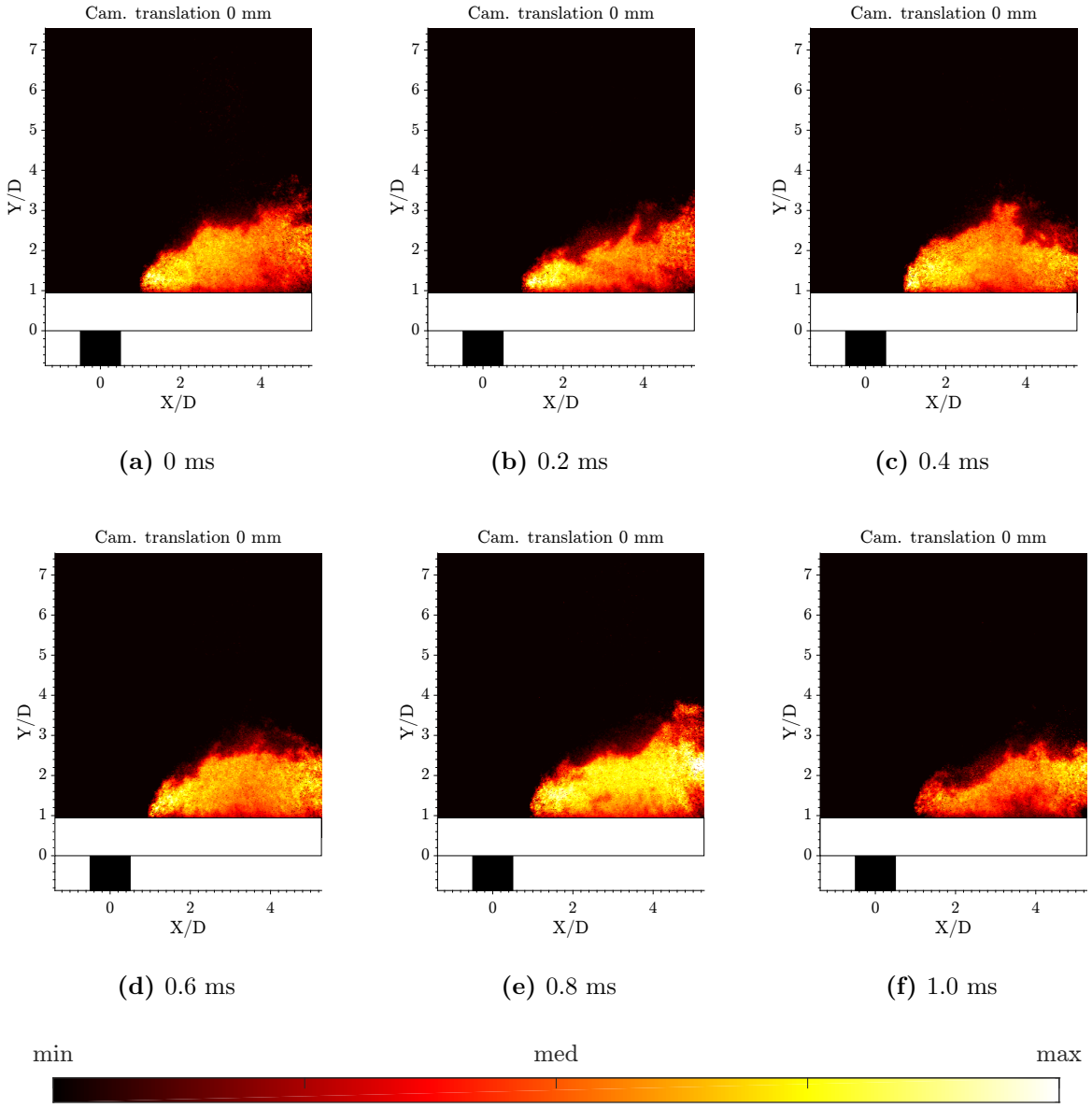


**(a)** 0 ms **(b)** 0.2 ms **(c)** 0.4 ms

**(d)** 0.6 ms **(e)** 0.8 ms **(f)** 1.0 ms

**Figure 7.7. :** Instantaneous PLIF images obtained with the camera (and laser sheet) positioned at the default position (capturing the injector). 7.7a The first of the series showing large OH at the left bottom. 7.7f Like the other five images shows structure in the OH distribution from interraction of the OH with flow turbulence.Same conditions as Fig. 7.6.

The images in Fig. 7.7 show the OH distribution near the injector. There is no observed OH upstream of the injector. To check this rigorously, the bit shift operator was used on the intensity of these images. The crossflow OH is visible in these bit shifted images above the jet OH in the region of the laser sheet, but no OH is observed upstream of the jet near the

injector. The authors estimate that this may be due to the high strain rates at this location. In an experiment with a laterally confined jet at a much lower crossflow Mach number, Sirignano et al. [37],[30] described their JICF flames as having no observed luminescence near the upstream injector location. This finding that there is no OH upstream of the jet, (nor is there any to be expected within the jet fluid) together with the OH distribution downstream of the injector, suggests that the OH distribution follows the downstream curve of the jet shear layer trajectory. The OH distribution fills the region between the shear layer and some region close to the bottom wall of the combustor.

The intensity of the OH distribution is also nearly uniform in these images. It will be contrasted in the next section with unattached flames. In those images, the high OH was localized to the upstream portions of the image. This OH quantity could possibly demarcate the portions of the flow that are generating OH from those where OH is being convected. A few other cases where boundary layer burning was also observed in literature is experiments by Solana-Perez et al. [33] Gamba and Mungal [83] under supersonic crossflow conditions. The images showed their unconfined hydrogen RJICF to generate OH near the bottom wall of the combustor, in the subsonic boundary layer. The bow shock-boundary layer interaction created new vortex systems in the crossflow boundary layer that wrapped around the jet tube. Combustion identified in the jet upstream shear layer (USL), observed via OH PLIF, was shown to occur with less probability than the subsonic boundary layer, with the OH illuminating a thin line in the shear layer. Jet upstream shear layer (USL) ignition was also shown to occur with higher probability in the center plane than off center. Finally, in the off centerplane measurements, the OH filled the region between the OH boundary and the bottom wall similar to these measurements. The off centerplane OH distribution was however not attached to a fixed point. It was shown to progress upstream with higher J values and only reached the injector when the upstream shear layer also ignited. The point being that these wall bound vortex systems assist in ignition in a confined jet by mixing boundary layer fluid with the jet fluid. The previous analysis of the time resolved chemiluminescence images revealed the role of the low speed boundary layer in the formation of these leeward stabilized flames. If we identify the high intensity OH with the flame, we can further infer that the location of the flame attachment point is near the downstream end of the injector. This is

consistent with other experiments that have shown the leeward side of the jet to be more conducive to flame attachment. That the top portion of the OH distribution is wrinkled could indicate some strain creating eddies associated with the jet core. It is known that the leeward side of the JICF flowfield sees more organized coherent structures [21].

### 7.4.3 Flame Brush Statistics

We use the term flame brush to describe the average PLIF image. The vertical extent of the flame brush gives an indication of the vertical height of the jet cross section in this way. The vertical height of the jet is likely dominated by the initial bending from the crossflow near the injector, and the buoyancy from heat release downstream. If the jet core is understood to provide the fuel responsible for the jet OH, then as the jet core increases in height with downstream distance, the edge of the shear layer increases in height consistent with the increase in vertical distance covered by the OH distribution. This increase in vertical distance could also be due to the shear layer thickening due to mass diffusion. To provide an order of magnitude estimate for this, we use a compressible shear flow. The shear layer thickness in spatially developing mixing layer scales linearly with distance. The convective mach number at this condition is 0.18 so little adjustment should be made for compressibility effects. The momentum thickness starting at the injector up to 6 jet diameters downstream is estimated to be 0.06 jet diameters via scaling arguments, two orders of magnitude smaller than the increase observed. To quantify the vertical extent of the jet, line plots through the average images have been created in a similar fashion to the laser sheet profile. The location of the line plot was chosen so as to capture the latter part of the brush. The line plots generated show the PDF of the flame brush. These have a particular width and center. There is also some asymmetry in the OH distribution when the camera is closer to the injector as can be seen in Fig. 7.8. This is again due to the lip of optical access.

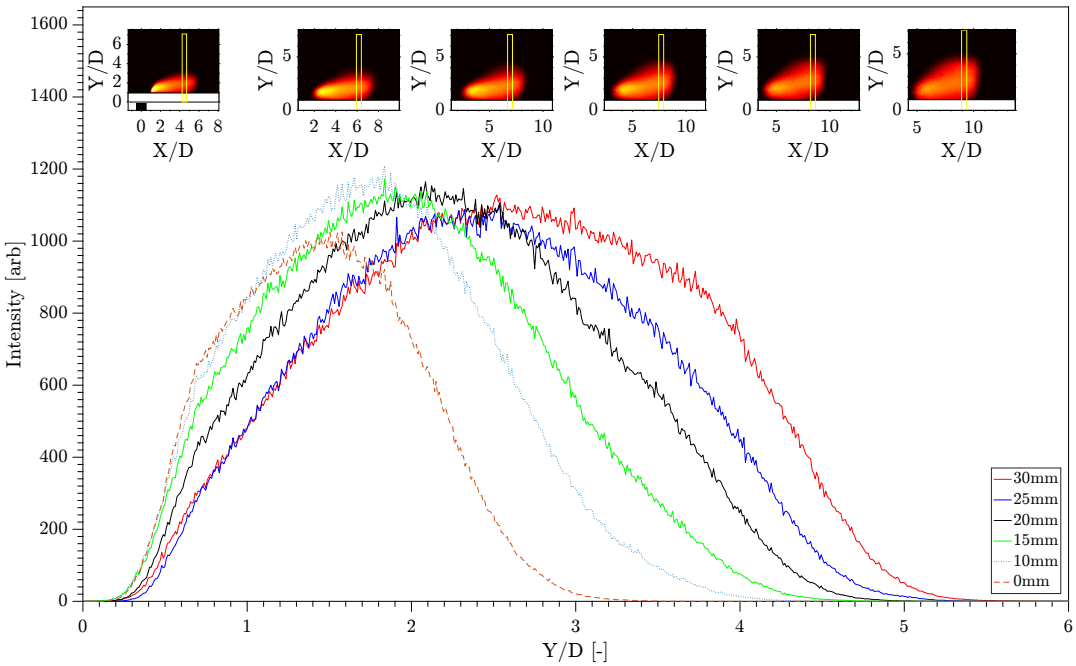


**Figure 7.8. :** Flame brush Intensity distribution downstream of the injector and subsequent downstream positions.

The left portion of the plots in Fig. 7.8 shows the cut off due to the lip of optical access. The width and centers of the flame brush profiles indicate the amount of buoyancy induced vertical trajectory of the jet.

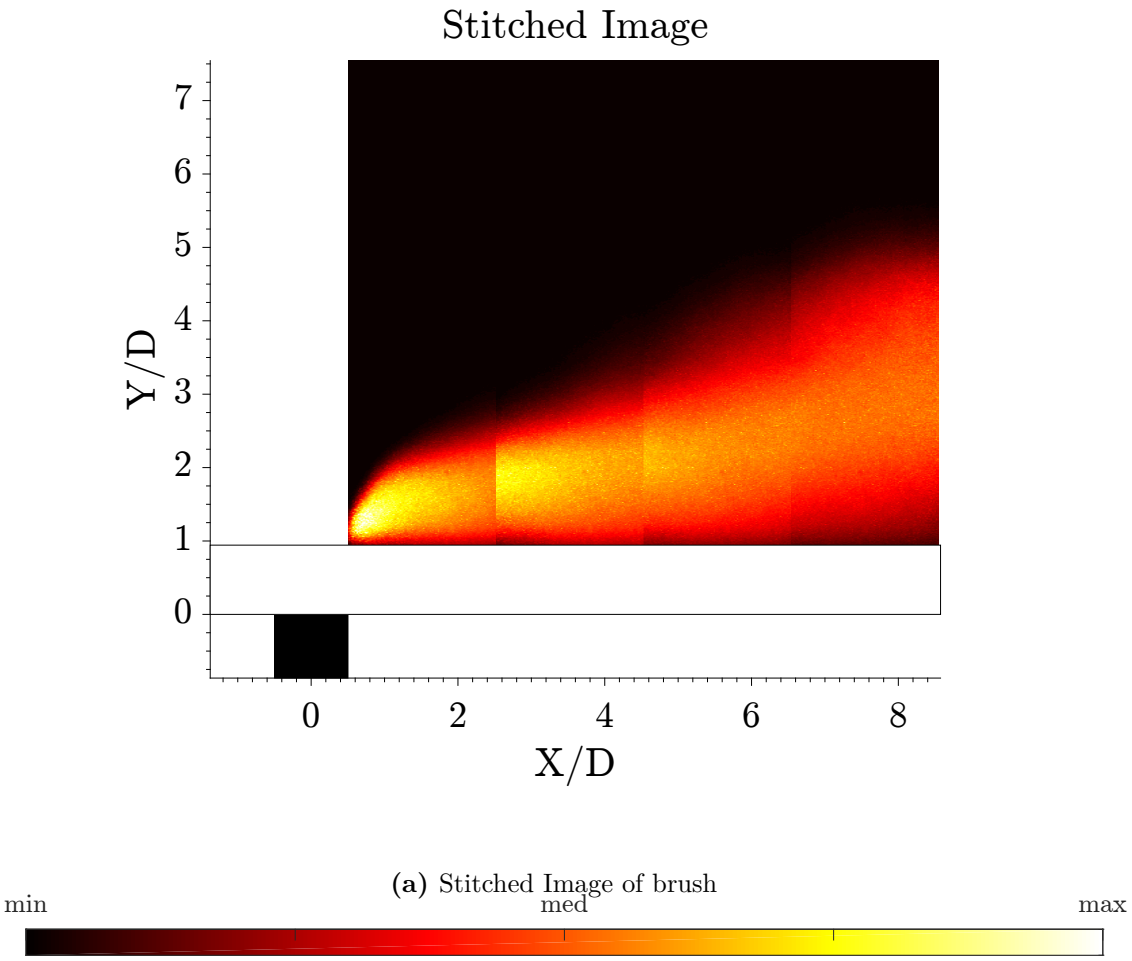


**(a)** Stitched Image of brush

**Figure 7.9. :** Flame brush. Same conditions as Fig. 7.6.

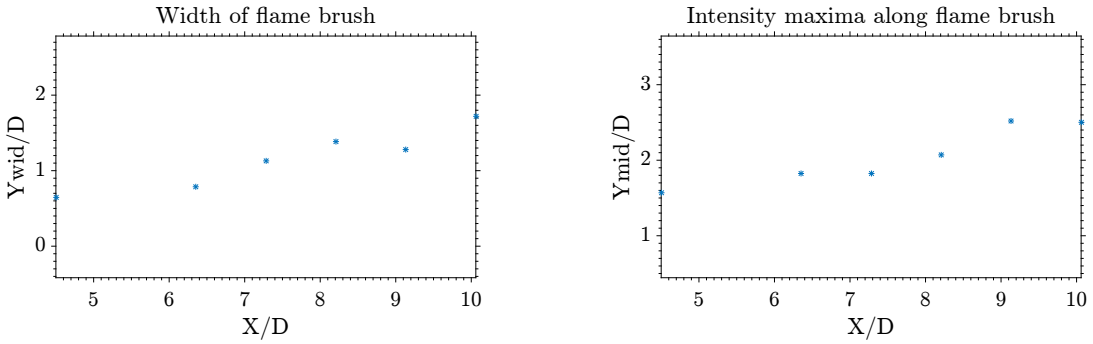


**(c)** Brush width

**(d)** Brush height

**Figure 7.9. :** ...contd. Statistics along flame brush. 7.9c The width (HWHM) of the intensity plot using the portion above the maximum.7.9d The trace of maxima of intensity as an estimate of the brush location above the bottom wall of the combustor. Same conditions as Fig. 7.6.

Although it is not straight forward to compare the vertical dimension of these images with those of the low Mach crossflow images due to the camera angle, some qualitative statements will be made. The flame increases in vertical extent similarly to the low Mach number crossflow flame. The rate of increase of the maximum intense portion of the brush is linear similar to the low crossflow Mach number case. The flame brush width is however similar from injector to brush end for the low crossflow Mach number case.

### 7.4.4 Flame Attachment Angle

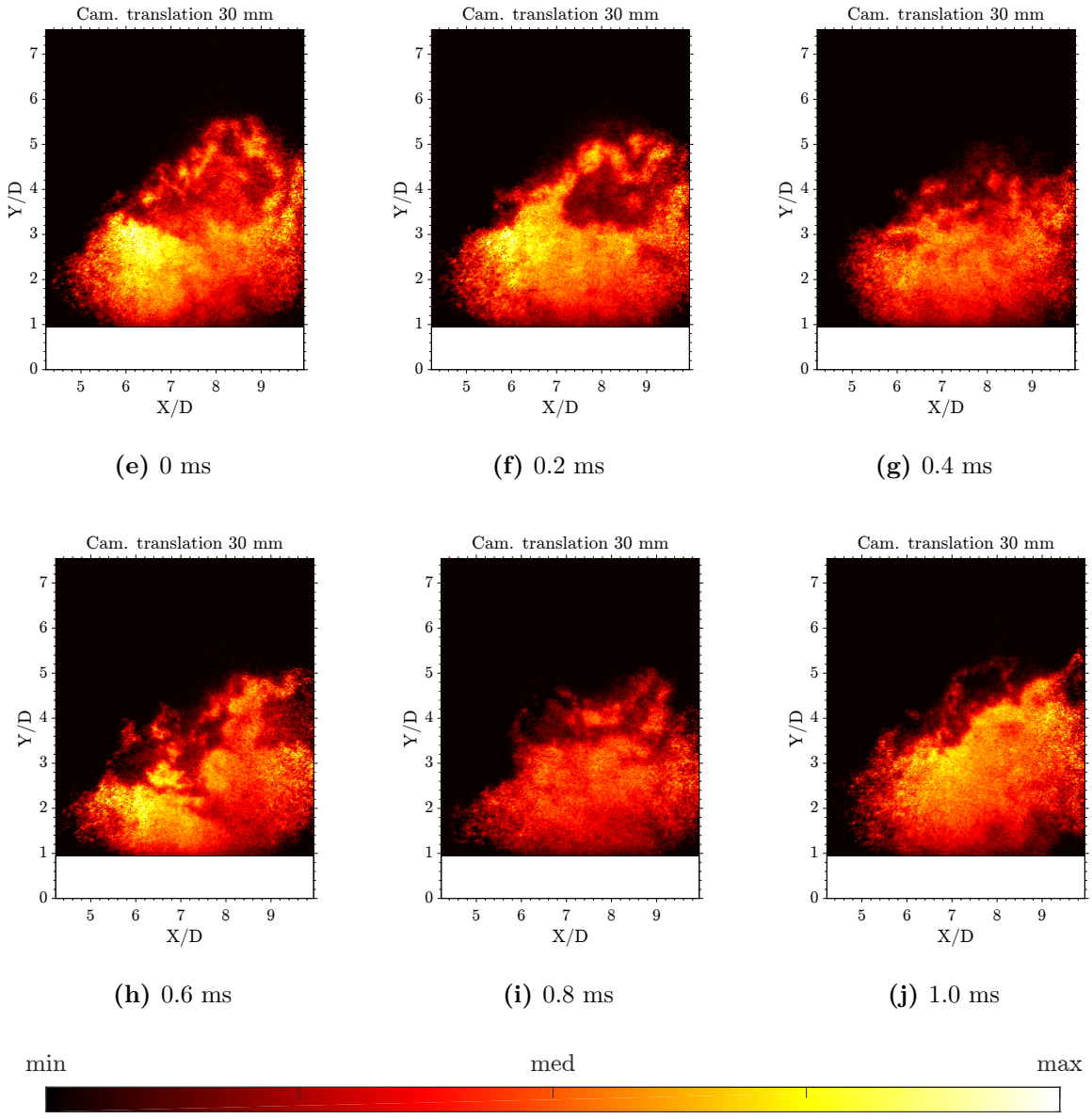


**(e)** 0 ms **(f)** 0.2 ms **(g)** 0.4 ms

**(h)** 0.6 ms **(i)** 0.8 ms **(j)** 1.0 ms

**Figure 7.10. :** Instantaneous PLIF images obtained with the camera (and laser sheet) positioned 30 mm from the default position (capturing the injector). 7.10e for example shows large OH at the left bottom. 7.10f and 7.10h show structure in the OH distribution at the top portions from interaction of the OH with flow turbulence. Same conditions as Fig. 7.6.

The series of images in Fig. 7.10 show the intensity distribution of OH LIF near the bottom wall of the combustor. This observed OH was generated from the JICF flame, which shows that the post flame brush reaches up to six (6) jet diameters vertically at the 6 to 10 jet diameter region downstream of the jet injector. The upstream portions of the OH field are aligned at a positive angle to the bottom wall of the combustor measuring counterclockwise, and the downstream portions of the field shows the OH lifting vertically from the bottom wall consistent with the downstream portions also aligned at a positive angle to the bottom wall. This could be due to buoyancy and reaction propagation into the jet core as will be contrasted with regions near the injector which may be momentum driven. Figures 7.10e,7.10f,7.10h and 7.10j where high localized OH was observed in the distribution show the OH to occur near the upstream side of the flow. This behavior will be compared to OH distribution in locations near the injector to estimate whether the OH was being generated or merely convected. The crossflow OH was not evident in these images due to the comparatively high amount of OH from the jet. To observe the crossflow OH, the bit shift operator was used on the intensity of these images; this places a cutoff after a certain chosen bit shift. In a 255 bit image with a maximum bit shift of 8, if the maximum bit shift is artificially set at 3, every pixel with intensity above $2^3 - 1 = 7$ is set to $2^8 - 1 = 255$. The crossflow OH was visible in these bit shifted images above the jet OH in the laser sheet illuminated portion of it. We expect that the interaction between the jet and the crossflow at the windward side was highly strained.

## 7.5 Unttached Flames

The schematic in Fig.7.11 reveals a typical unattached flame PLIF with respect to the bottom wall of the optical section.

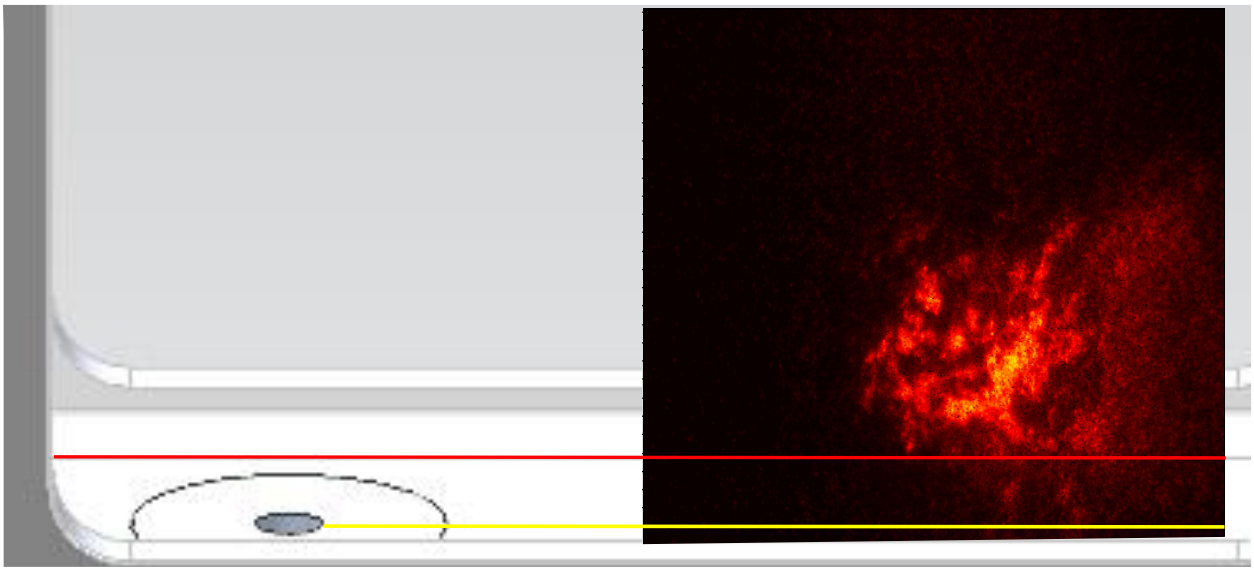

**Figure 7.11. :** Schematic of unattached flame showing the line where the laser sheet meets the bottom wall in yellow. As the camera is angled, one edge of the bottom wall of the combustor is shown in red.

When the flame was observed as unattached, the instantaneous PLIF images show the flame to be composed of broken flamelets instead of a uniform burning or a continuous PLIF image typical of diffusion flames as seen in the OH PLIF images of the attached flame see Fig. 7.12f. The broken flamelets surround coherent structures that they illuminate via PLIF. That they occur predominantly in the downstream region of the jet coherent structures indicates that mixing in the shear layer is responsible for the OH formation for these unattached flames. There is also very little contribution of the bottom wall to the stabilization of the unattached flame, observed in these images which are also obtained from a tilted camera view. Images of chemiluminescence at higher repetition rate which reveal the formation and convection of these heat release pockets show that for the unattached flame, the location of flame stabilization is very dynamic and the formation of $OH^*$ is succeeded quickly by quenching during which new $OH^*$ is formed in the shear layer. The instantaneous behavior of the flush unattached jet is quite unlike the attached jet even though the emissions result indicate no significant difference before and after attachment. Experiments by Micka and Driscoll [31] under high subsonic crossflow conditions showed their confined hydrogen RJICF to generate $OH^*$ near the bottom wall of the combustor, in the subsonic boundary

layer with no evidence of upstream shear layer burning. With a less reactive 50/50 $H_2-C_2H_4$ fuel, instantaneous OH and mean $CH^*$ were displaced from the injector face similar to the results in this report. Like their measurements the instantaneous OH PLIF shows broken flamelets. Unlike their measurements, the OH PLIF of the broken flamelets in the wake burning transverse jet in this report are not likely to be connected to the bottom wall and may be connected through the shear layer to the crossflow, showing more non-uniform burning than at the attachment point.

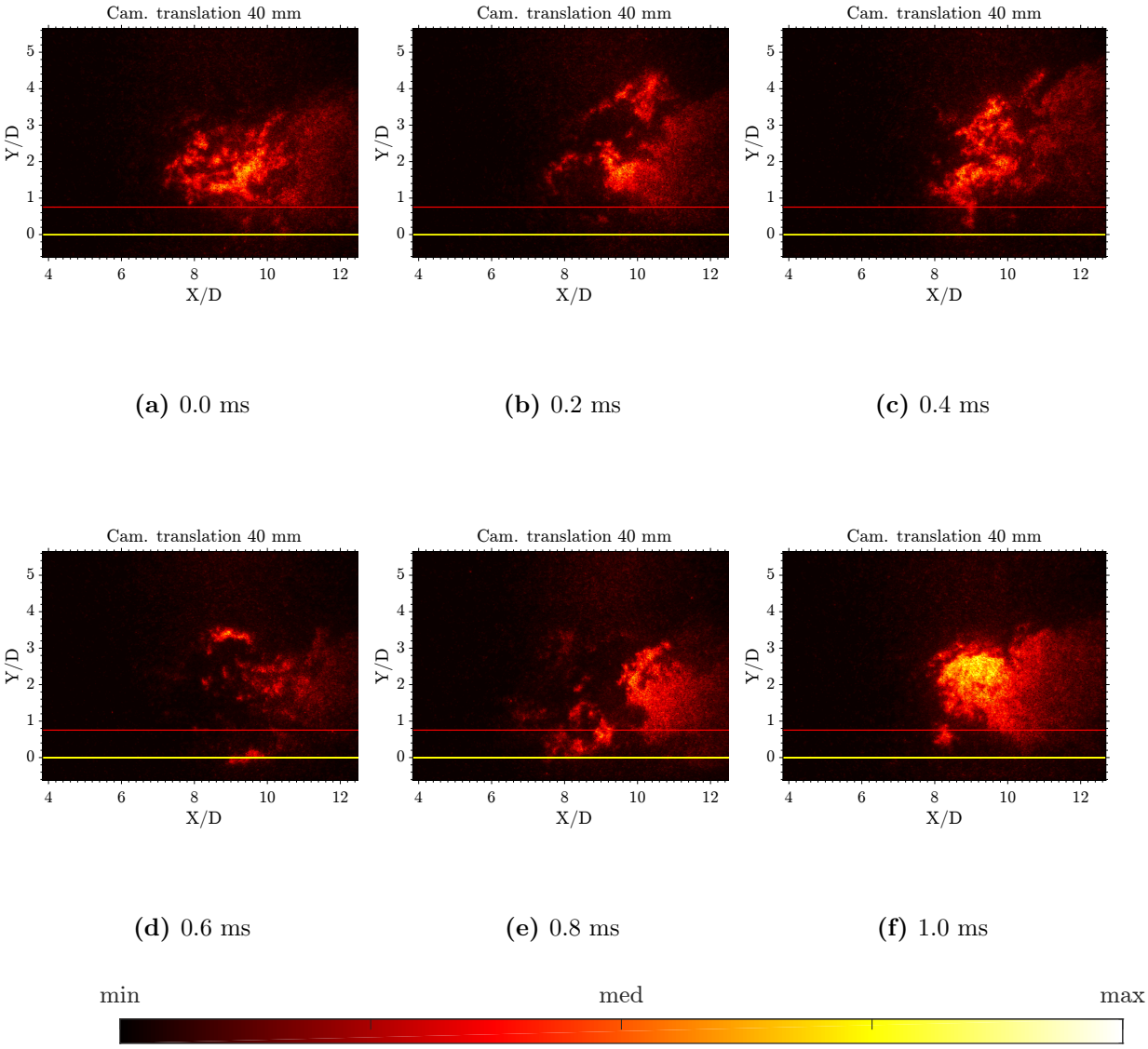


**(a)** 0.0 ms **(b)** 0.2 ms **(c)** 0.4 ms

**(d)** 0.6 ms **(e)** 0.8 ms **(f)** 1.0 ms

**Figure 7.12. :** Instantaneous PLIF images of unattached flame obtained with the camera (and laser sheet) positioned 40mm downstream of the injector. 7.12a The first of the series shows disconnected broken OH. Like the other five images, it shows structure in the OH distribution occurring downstream of a coherent structure. Same crossflow conditions and camera angle as Fig. 7.4 with 44% $xH_2$. Crossflow direction is left to right as in all other images and the jet issues vertically up.

# 8. OPTICAL FLOW RESULTS

The objective of this chapter is to discuss the results of optical flow velocimetry on the chemiluminescence measurements of the transverse reacting jet captured at 150 kHz. I aim to describe the reaction propagation in the flowfield. Because the emission is from reacting jet chemiluminescence, brief comments will be made throughout the discussion on this particular subject. The contributions from this chapter are being developed to be published in a paper to be submitted to the Combustion and Flame journal.

## 8.1 Nature of the Scalar

### 8.1.1 Tracking Instances of OH* Chemiluminescence Between Images

First I set out to describe the nature of the reactive scalar that is being used to generate the optical flow velocity vectors. $OH^*$ chemiluminescence arises in hydrogen and hydrocarbon flames as a result of chemical excitation of a small population of ground state intermediates, which are short lived. The formation of these excited species follows a few reactions. In the presence of hydrocarbons, the following reaction is shown in literature by flame [84], shock tube and mass spectroscopy of chemiluminescence to dominate the formation of $OH^*$

$$CH + O_2 \rightarrow CO + OH^* \tag{R 8.1}$$

with the addition of hydrogen, hydrogen/methane flames see additional $OH^*$ from

$$H + O + M \rightarrow M + OH^* \tag{R 8.2}$$

The quenching of $OH^*$ occurs via one of two channels; radiative decay

$$OH^* \rightarrow OH + h\nu \tag{R 8.3}$$

and non-radiative decay [85],[86],[87]

$$OH^* + M \rightarrow OH + M \tag{R 8.4}$$

via collision partners M. The lifetimes of excited states before quenching at atmospheric pressure are in the nanosecond range Tamura et al. [88] detail a list of collision partners for OH at various temperatures (including flame temperatures) from ground state populations and show that these values could be used to predict the collisional quenching in flames. So the scalars that are being imaged are short lifetime scalars that are generated in the flame and could be tracked before they are extinguished. Chemiluminescence is also nonuniform in the flame, creating higher intensity images at locations of high heat release and dissipating due to collision partners. This creates a rich textured scalar image that could benefit from tracking techniques. Quenching of the chemiluminescent species by collisions are correctly interpreted as slowing down of the reaction propagation. Increase in intensity is also rightly interpreted as increase in reaction propagation speed. Some work has been done to establish this method of quantifying motion of potentially "quenched" scalars by Derian et al. [89] using lidar images of atmospheric aerosol particles. In that article, they used aerosol backscatter images from lidar measurement. The behavior of aerosol in the atmosphere is similar to the nature of chemiluminescence albeit in largely different orders of magnitude. In lidar images, out-of-plane motion and turbulent diffusion cause changes in signal intensity which was minimized in their case for more reliable data.

### 8.1.2 Contribution of Out of Plane Motion to the Velocity Estimate

To obtain from path averaged measurements spatially resolved measurements in the depth of the material, deconvolution tomography is usually applied if many focus planes in the thickness of the object [90] or at different angles to the object [91] can be acquired. Deconvolution with a point spread function (PSF) is another method to remove out of focus planes from an image if the PSF is known or can be measured [92]. A Radon or Abel transform can also be used if axisymmetry is expected [93][19] with some measure of success. None of these features are applicable to the flames in this chapter which are embedded in the high Mach number flowfield with a short timescale. Instead comparisons are made by virtue of simultaneous measurements of OH-PLIF to the path averaged $OH^*$ chemiluminescence to identify possible out-of-plane contributions to the low depth of field images.

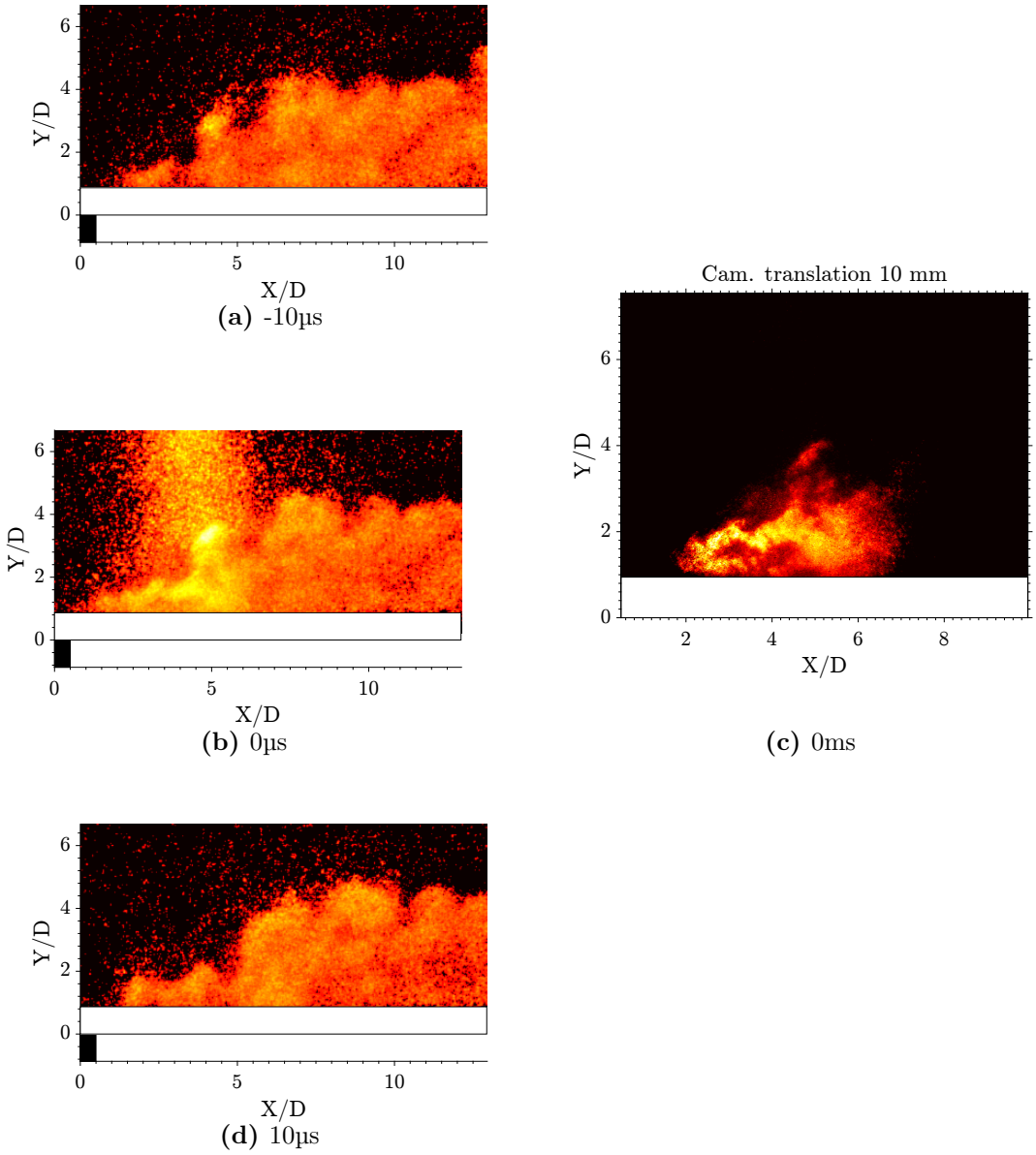


**(a)** -10µs **(b)** 0µs **(c)** 0ms **(d)** 10µs

**Figure 8.1. :** Comparison of OH-PLIF obtained from the PLIF camera system(8.1c) with a 10ns integration time and the chemiluminescence camera system(8.1b), with a 2µs integration time, and sequential OH*-Chemiluminescence images 10µs before (8.1a) and 10µs after the PLIF images, (8.1d) compared for out of focus plane contribution

Two conclusions can be reached from images in Fig. 8.1: regarding the sharpness of the flame features, OH-PLIF images are better for optical flow. The texture of these chemiluminescence images is however sufficient to test with a given algorithm to track these features. Regarding out of focus plane contribution to the image, the features being tracked in the

chemiluminescence images before and after the OH-PLIF image, are similar to the features in the OH-PLIF image. This argument is qualitative. This similarity between OH-PLIF and OH* chemiluminescence where available, was consistent in all cases observed.

## 8.2 Wavelet Optical Flow Theory

This section contains a summary of the optical flow algorithm and in it I describe how it was adapted to the chemiluminescence images. This optical flow algorithm provides a motion estimate that obtains velocity vectors. For accurate results, the user must take into account the nature of the scalar and its response to the underlying flowfield. The algorithm **Typhoon** by Derian [68], which is used in this chapter, implements a wavelet based optical flow estimation generating a displacement field $v_{\mathrm{i}}; \mathrm{i} = 1, 2$ from a pair of images. The data term is the term that connects the images to the velocity field. The regularization term is responsible for filling in the solutions where the data term fails. In the following $\hat{x} = \arg\min_x f(x)$ is the value $x$ that obtains a minimum for a function $f(x)$.

$$\begin{aligned} \hat{\boldsymbol{v}} &= \arg\min_{\boldsymbol{v}} J_{data}(I(\boldsymbol{x}), \boldsymbol{v}(\boldsymbol{x})) + \alpha J_{reg}(\boldsymbol{v}(\boldsymbol{x})) \\ &= \arg\min_{\boldsymbol{v}} \frac{1}{2} \int \rho\left[f_{data}(I(\boldsymbol{x}), \boldsymbol{v}(\boldsymbol{x}))\right] \mathrm{d}\boldsymbol{x} + \alpha \left[f_{reg}(\boldsymbol{v}(\boldsymbol{x}))\right]^2 \mathrm{d}\boldsymbol{x} \end{aligned} \tag{8.1}$$

The use of wavelets mirrors the classical multiresolution approach which deals with large displacements by filtering and subsampling to bring patterns which were originally far apart closer together. Wavelets deal with large displacements by decomposing the velocity field at scales in orthogonal spaces such that the optical flow problem is solved in each scale, and the results from each scale is "summed" up to make the whole. In addition this motion estimate benefits from the statistical nature of velocity fields: in the frequency domain the transfer of energy in the inertial subrange reveals an equilibrium that shows the lossless transfer of energy between scales. This is a qualitative statement as the reader is reminded of the high dimensionality of turbulence compared to the available scales in an image. The way the optical flow estimate is adapted to these images is as follows. First the pair of images is entered into a model that if solved obtains a velocity field responsible for the motion of

patterns in the image. The model is called the data term. The data term is penalized when it is not satisfied in a minimization algorithm. That penalty function should be robust to outliers. In addition to a data term, there is a regularization term that accounts for the aperture problem, where multiple solutions or no solutions can be obtained from the data term. Regularization imposes assumptions on the nature of the flowfield to be computed. Wavelets are used in the process for computing motions independently at separate scales so that the problem is solved in the wavelet space and only finally converted to velocities at the end.

$$\begin{aligned} \hat{\boldsymbol{v}}(x) &= \boldsymbol{\Phi}^T(x)\hat{\boldsymbol{\Theta}} \text{ with } \hat{\cdot} \text{ the estimate of } \cdot \text{ and} \\ \hat{\boldsymbol{\Theta}} &= \arg\min_{\boldsymbol{\Theta}} J_{data}(I, \boldsymbol{\Theta}) + \alpha J_{reg}(\boldsymbol{\Theta}) \end{aligned} \tag{8.2}$$

The regularization imposed on the optical flow velocities is that of Horn and Schunk.

$$f_{reg}(v_{\mathrm{i}}) = \sqrt{\left[\frac{\partial v_{\mathrm{i}}}{\partial x_1}\right]^2 + \left[\frac{\partial v_{\mathrm{i}}}{\partial x_2}\right]^2} \tag{8.3}$$

with the square root cancelling the square in eq. 8.1. This regularization penalizes large gradients in each component of velocity without enforcing a sourceless continuity $\nabla \cdot \boldsymbol{v} \neq 0$.

### 8.2.1 Quantifying Accuracy

The aliasing problem in Fig. 8.2

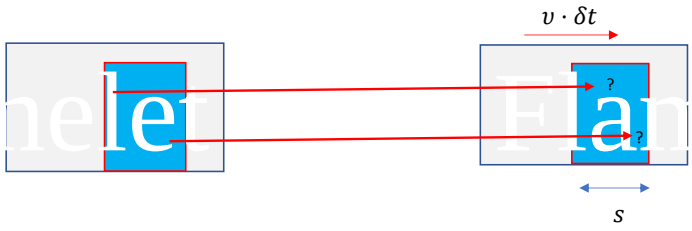


**Figure 8.2. :** The aliasing problem; the word Flamelet is transported between frames too fast to be captured by the code. If only portions of the frame of size s are considered, the displacements $|v| > s$ are not allowed since the portions of the image being considered are not correlated. [94].

is mostly evident at the edges of the images. Aliasing arises along the edges of the image where objects vanish. The algorithm seeks to identify with each pixel a displacement vector within the frame. This results in portions of the image that disappear assigned (displaced) to other portions of the image still within the frame, causing erroneous velocities near the edges. It also arises when new objects enter the frame as the old objects nearest to the new objects are assigned displacement vectors indicating expansion into the shape of the combined objects. This causes large expansions near the injector area. The velocity vectors at the edges of the image were removed for the 0.63 crossflow Mach number case. In practice the algorithm merely produces the displacement vectors in terms of pixels, conversion to velocity is done using a pixel-to-real-units calibration and the time between frames. The kinds of errors from the estimator include discretization errors, and errors associated with the capacity to capture motion at different scales. The penalty function by Leclerc [65] which is very robust, was shown to have similar cumulative error to the that suggested by Geman and Reynolds [63] as well as that suggested by Geman and McClure [64]. Discretization errors are present in all estimators, due to the finite sampling of the data term. Systematic error is reduced below the $\pm 0.5$ pixel limit using interpolation by wavelets. To reduce the error further requires higher pixel density (the camera is closer to the object) or longer time between frames. Both of which decrease the accuracy in practice due to larger apparent displacements for larger pixel densities or the degradation of the stationary assumption

between frames with longer wait times. In this report, the pixel densities were about 10 - 13 pixel/mm with 150 frames/s.

In computing the velocity vectors, the algorithm uses the regularization to fill in vectors where the gradient in intensity is zero, such as in the areas outside the flame brush. Those vectors are uniform in magnitude and direction and take the value of the nearest flame vector. Those vectors do not contribute information to the vector field, and so were masked out based on an intensity threshold representing the flame brush for the first image of the pair used in the computation. The calculation of the velocity gradients was carried out using the unmasked velocity field to prevent edge effects, the computed velocity gradients were thereafter masked using the same intensity threshold.

### 8.3 Tracking Features: Flowfield vs Flame

It is important at the outset to distinguish the motion of fluid elements from the propagation of reactions within them. This is analogous to diffusion of color into a moving stream. In turbulent combustion, the macroscopic description of heat release follows exothermic chemical reactions which occur as propagating fronts within the bulk fluid. Measurements of velocity using light emission (from heat release) must then isolate the role of fluid motion from that of reaction propagation. Femtosecond laser electronic excitation tagging (FLEET) for example, produces fluorescence for motion tracking shortly after electronic excitation, but fluorescence from rotationally populated nearby lines [95] could increase the fluorescence intensity so that uncertainties in the quantification of the center of the fluorescence probe volume arise from the choice of delay [96]. Seeded laser velocimetry on the other hand follows the motion of marked particles that faithfully follow the fluid elements. Here the heat release marker is used to trace reaction propagation in this turbulent reacting flow. When obvious, I will identify in relevant locations the advection of the flame by the flowfield.

#### Uncertainty Estimates

To reduce the uncertainty in planar velocity measurements from digital images, the algorithm must account for noise, large displacements, multiple motions in a small neighborhood,

temporal aliasing (wagon wheel effect) and the issues associated with projection of a 3D scene to a 2D image [97], [98]. Noise in the images can be prefiltered. Prefiltering using a low pass filter serves two additional purposes: it reduces the amplitude of higher order terms in the image prior to derivative operations. It also reduces temporal aliasing. Temporal aliasing occurs due to the discrete sampling of a continous variable such as is done with images. In the time-frequency spectrum, replicas of the original image are generated at the sampling frequency $2\pi/T$ (where $T$ is the image repetition rate) due to this discrete sampling. The derivative operators used in optical flow algorithms treat these replicas similarly to the original. Prefiltering, especially at the coarse scales, avoids these replicas. The wavelet approach addresses motions at different scales.

Similar wavelet-optical flow algorithms have been designed to quantify uncertainty within the scope of the algorithm, where the velocity field is composed of separate large and small scale components also known as subgrid scale velocity in the large eddy simulation literature [99]. This decomposition highlights the *dense* property of optical flow, that it allows the computation of velocities down to very small scales - a property that is employed in these computations - however the largest sources of uncertainty in this adaptation lie in the interpretation of the images and not in the smallest scales to be resolved.

The following uncertainty analysis applies only to the chemiluminescence measurement. To quantify the departure from the true velocity, I first identify what the technique should encounter in generating the measured velocities. Since the chemiluminescence is path averaged, the image plane will contain light from the flame within the depth of field of the lens. Light from outside the depth of field will arrive at the camera sensor, however, it is expected that the intensities will be much lower. This was corroborated with comparisons of OH-PLIF measurements with chemiluminescence measurements, with both measurements captured with the camera angled to view the combustor bottom wall. The results showed that despite the three dimensionality of the flame, the OH-PLIF images aligned with the chemiluminescence images, which were constrained only by the depth of field of the lens. The out of focus images behave similar to a transparency problem (optical flow for motion behind a translucent object-cite transparency) and is readily handled by the algorithm. The

true velocity is thus estimated as the velocity that captures the 2D motion parallel to the image plane. Departures from this are the largest source of uncertainty in the measurement.

The 2mm depth of field of the lens contains sufficient out-of-plane motion to decrease the measured velocities in all directions. This can be quantified by the number of crossings of the spanwise fluctuating velocity through the midplane of the depth of field of the lens as follows: Following [100] Let $L$ be the image distance, $Z$ the object distance and $(X, Y)$ the position of the object in the object plane. The position of the image in the image plane is $(x_s(Z), y_s(Z))$ can be obtained by the simple lens formula

$$\begin{aligned} x_s(Z) &= \frac{L}{Z}X = M \cdot X \\ y_s(Z) &= \frac{L}{Z}Y = M \cdot Y \end{aligned} \tag{8.4}$$

where $M = L/Z$ is the image magnification. In the following, I use small angle approximations to estimate the motion of an image due to out-of-plane translations and rotations. The out-of-plane translation or rotation of the object by $\Delta Z$ - defined as positive away from the image - places the image at $(x_s(Z + \Delta Z), y_s(Z + \Delta Z))$

$$\begin{aligned} &x_s(Z + \Delta Z) = \frac{L}{Z + \Delta Z}X = \frac{L}{Z(1 + \frac{\Delta Z}{Z})}X \approx \frac{L}{Z}(1 - \frac{\Delta Z}{Z})X \text{ to first order, similarly} \\ &y_s(Z + \Delta Z) \approx \frac{L}{Z}(1 - \frac{\Delta Z}{Z})Y \end{aligned} \tag{8.5}$$

so that

$$\begin{aligned} u(\Delta Z) &= \left(x_s(Z + \Delta Z) - x_s(Z)\right)/\Delta t \approx \frac{x_s(-\frac{\Delta Z}{Z})}{\Delta t} \\ v(\Delta Z) &\approx \frac{y_s(-\frac{\Delta Z}{Z})}{\Delta t} \end{aligned} \tag{8.6}$$

It is understood that the size of the smallest chemiluminescence scalar is much less than the pixel size of the image and hence the effect of the out-of-plane translation or rotation is to change the relative position, implying an additional displacement to that from the optical flow motion. The difference between the measured velocity and the true measurement is

composed of this quantity $(u(\Delta Z), v(\Delta Z))$, the number of out-of-plane motion vectors and the size of the interrogation volume - the depth of field of the lens.

The definition of zero crossings is useful to quantify the out-of-plane motion vectors. Zero crossings applies to random walkers crossing the initial point. It is generalized to level crossings. The (spatial) frequency $f$ of zero crossings for a random walker is proportional to the product of the probability of reaching the initial point and the conditioned expectation value of reaching the initial point which holds for a turbulent velocity fluctuation. The spanwise velocity fluctuation $w = \ell \cdot \sigma_w$ is defined in terms of the level crossing $\ell$ to be within the interrogation volume and the spanwise turbulent intensity $\sqrt{\overline{w'w'}}$, and assuming the fluctuation is gaussian,

$$\begin{aligned} f_{\ell,w} &= \frac{1}{\pi\lambda_w} \mathrm{e}^{-\frac{\ell^2}{2}} \text{ where} \\ \lambda_w &= \sqrt{\sigma_w^2 / \overline{(\partial w/\partial z)^2}} \end{aligned} \tag{8.7}$$

In general the spanwise velocity fluctuation is not gaussian, however it is noted that the frequency $f$ is still inversely proportional to the spanwise intensity Taylor microscale $\lambda_w$ [101] . The uncertainty in the horizontal measured velocity is estimated as $\Delta u = u(\Delta Z) \cdot \mathcal{V}/\lambda_w$, which is statistically equal to $\Delta v$ the vertical component. Here $\mathcal{V}$ is the volume of the interrogation region. An estimate is presented for the following results using the spanwise intensity Taylor microscale from Ruiz et al.'s analysis following Su and Mungal [102]. Their spanwise intensity Taylor microscale of 0.25 $\mathrm{D_j}$ gives an uncertainty bound of $\pm 0.13 \mathrm{m\,s^{-1}}$ for these measurements.

The largest contributor to the uncertainty in the $u$ and $v$ velocities arises due to the insufficient texturing of the image. This gradient based optical flow algorithm benefits from features with sharper edges, to enable accurate tracking of the spatial intensity profile in an image. Images of an untextured marble ball rotating would generate a zero velocity flowfield for example. To test whether the chemiluminescence image is sufficiently textured for this wavelet optical flow algorithm, a single frame of the chemiluminescence data was rotated through a finite angle with a solenoidal vortex of vorticity $74\mathrm{s}^{-1}$. This generated a second image from which the vorticity and divergence were computed. The statistics of

the computed vorticity and divergence are shown in Figs. 8.3 and 8.4. In this and similar figures, the vorticity is defined as the negative of the typical value. The portion of the image being tracked contains 25353 pixels. The parameters of the algorithm used to generate these plots are described in the results section.

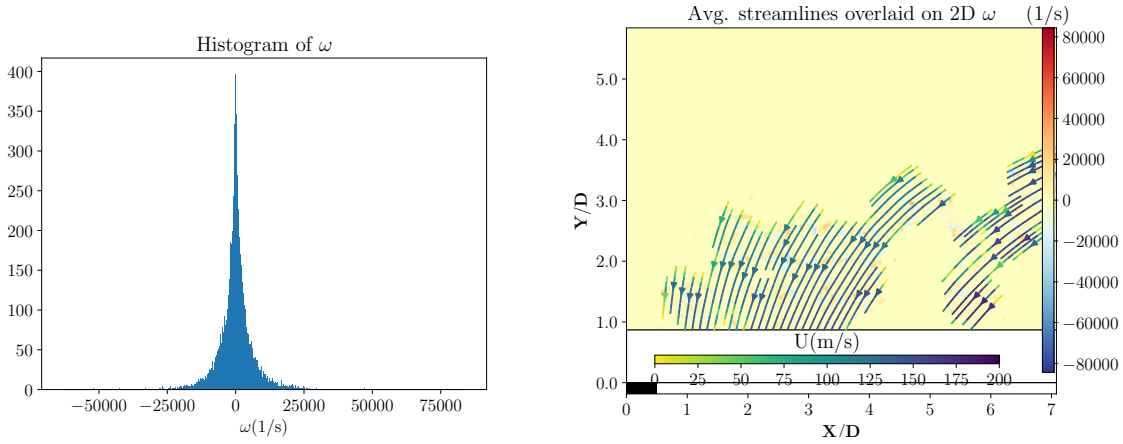


**(a)** Histogram of measured vorticity - $\omega$ **(b)** Streamlines and vorticity from a rotated image

**Figure 8.3. :** Test of the reproduction of a solenoidal vortex using the texture of a chemiluminescence image. 8.3a shows the count of all calculated vorticities. The spread of the result around the ground truth value of 74 $s^{-1}$ although sharply peaked, includes a large weight of values in the wings of the distribution. The measured average was 68 $s^{-1}$

It is clear that the peak is not sufficiently narrow. Of the 25353 pixels which were rotated 396 are along the peak and the wings are heavily weighted. The divergence of the velocity field was computed to quantify the local accuracy of the result to see if the vortex stays solenoical locally. The vortex being solenoidal, should obtain a divergence free flowfield everywhere.

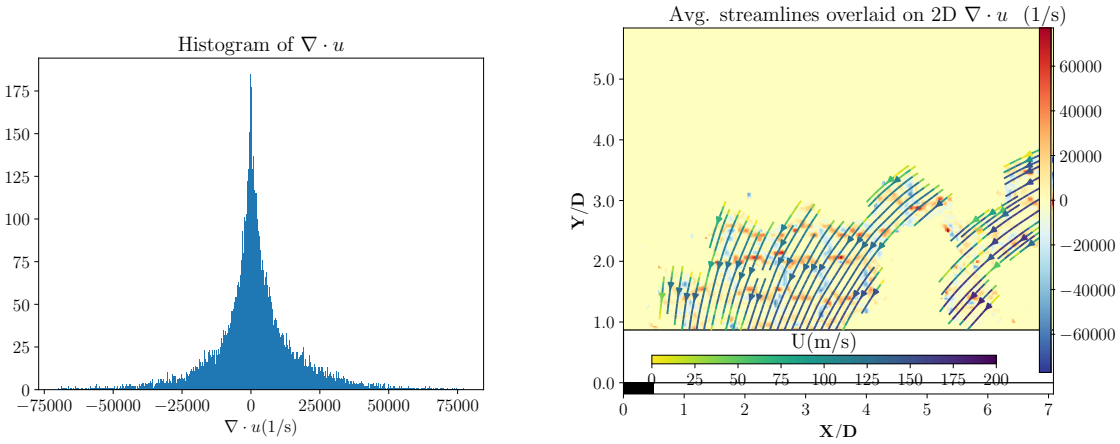


**(a)** Histogram of measured divergence - $\omega$

**(b)** Streamlines and divergence from the same rotated image

**Figure 8.4. :** Testing the accuracy of preserving the solenoidal nature of a vortex using the texture of the chemiluminescence image in 8.3. 8.4a shows the count of all calculated divergences. This histogram is less sharply peaked than that of the vorticity. The spread of the result around the ground truth value of 0 $s^{-1}$ shows the difficulty of the code to track the local patterns in this textured image. The measured average was 1141 $s^{-1}$

Both images from Figs. 8.4b and 8.3b show the local features that are being poorly interpreted due to the texture of the images. Improvement can be obtained by capturing sharper images, which do not require much preprocessing as were in the current dataset. Many parameters were varied to obtain these results, which are the best of the study.

## 8.4 Testing Wavelet Optical Flow

### 8.4.1 Particles in Non-Reacting Flow

**Typhoon** has been tested and reported on largely already in literature [103],[104],[89]. The current implementation was built it on a Red Hat Enterprise Linux centos7 operating system, with Tesla P-100 running CUDA 10.1. To test the build against well known velocimetry algorithms, image pairs from a seeded particles from a planar laser mie scattering (PIV) experiment were obtained to compare the accuracy of the spatial resolution especially with computing the topology of the velocity vector which requires spatial derivatives. The PIV data used for this test was captured from a non reacting jet in crossflow experiment at

low subsonic conditions. The time spacing between the laser shots was 10µs. The resolution of the image was 6.84$\boxed{\text{pixel}}$/mm. The image was cropped to 256x256. The jet and crossflow are both air. Titanium dioxide nanoparticles were used to seed the jet. Measurements were made 10mm from the injector face in the jet normal direction. The jet to crossflow momentum flux ratio was 6.

**Figure 8.5. :** Normal view of 5mm ID Injector, with the full image extents measuring 65mm across and 58mm down.

The correlation algorithm on LaVision Davis® implements a minimization algorithm

$$\forall \boldsymbol{x} \in \Omega_D,\ \hat{\boldsymbol{v}}(\boldsymbol{x}) = \arg\min_{\boldsymbol{v}} \sum_{\boldsymbol{y}\in W(\boldsymbol{x})} -\frac{\left(I_1(\boldsymbol{y}+\boldsymbol{v}) - \mu_1(\boldsymbol{x}+\boldsymbol{v})\right)\left(I_0(\boldsymbol{y}) - \mu_0(\boldsymbol{x})\right)}{\sigma_1^2(\boldsymbol{x}+\boldsymbol{v})\sigma_0^2(\boldsymbol{x})} \tag{8.8}$$

($\sigma^2$ is the variance and $\mu$ is the mean)

on rectangular windows $W(\boldsymbol{x})$ centered on a coarse grid $\Omega_D$. The algorithm solves for the velocity $\boldsymbol{v}$ that recovers the smallest value of the function in eq. 8.8 with displaced partly overlapping windows $W(\boldsymbol{x}+\boldsymbol{v})$ see Fig. 8.6.

For these measurements the windows were started coarse and progressively reduced in a pyramidesque way from 16x16 to 4x4 with 5 passes, with 50 % overlap. Post processing involved removing vectors with $Q < 1.5$ a measure of correlation strength. Groups of vectors less than 5 were also removed. Vectors that failed the median filter based on twice the local standard deviation were also removed. Vectors were also added in by interpolation.

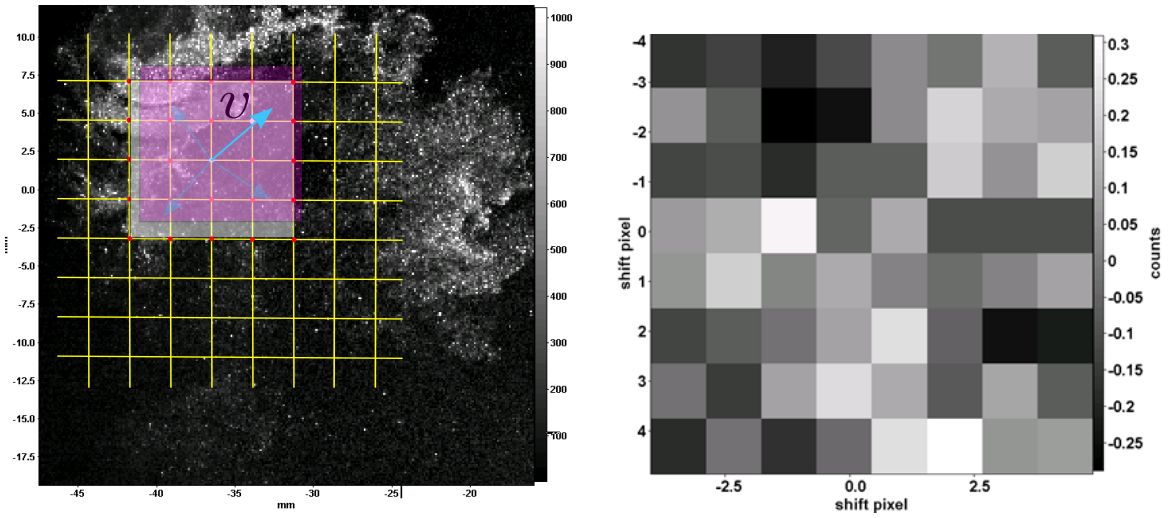


**(a)** Overlaid 4 x 4 windows one for each red dot - $\Omega_D$

**(b)** Optimal pixel shift maximizing cross correlation

**Figure 8.6. :** Schematic of cross correlation algorithm. 8.6a shows one point $\boldsymbol{x}$ with the original window $W(\boldsymbol{x})$ in yellow, three test vectors and one optimal vector $\boldsymbol{v}$ obtained from the maximized correlation at the displaced window $W(\boldsymbol{x}+\boldsymbol{v})$

For the optical flow calculations, the minimization algorithm finds wavelet coefficients that satisfy

$$\begin{aligned}
\hat{\boldsymbol{\Theta}} &= \arg\min_{\boldsymbol{\Theta}} J_{data}(I, \boldsymbol{\Theta}) + \alpha J_{reg}(\boldsymbol{\Theta}) \text{ with the energy functionals} \\
J_{data}(I, \boldsymbol{\Theta}) &= \frac{1}{2} \int g_{gm} \left( I_0(\boldsymbol{x}) - I_1(\boldsymbol{x} + \boldsymbol{\Phi}^{\boldsymbol{T}} \boldsymbol{\Theta}) \right) \mathrm{d}\boldsymbol{x} \text{ and} \\
J_{reg}(\boldsymbol{\Theta}) &= \frac{1}{2} \int \left( \nabla\nabla \cdot \boldsymbol{\Phi}^{\boldsymbol{T}} \boldsymbol{\Theta} \right)^2 \mathrm{d}\boldsymbol{x} \text{ and } \text{ where} \\
\hat{\boldsymbol{v}}(x) &= \boldsymbol{\Phi}^{\boldsymbol{T}} \hat{\boldsymbol{\Theta}}
\end{aligned} \tag{8.9}$$

For this test, since the flow was non-reacting, the regularization was done with the gradient divergence function. To reduce the noise associated with estimating the velocity with at scales, 6 of the 8 scales were estimated. The penalty function for the data term was that suggested by Geman and McClure [64]

$$g_{gm}(f_{data}, \sigma) = \frac{f_{data}^2}{f_{data}^2 + \sigma^2} \tag{8.10}$$

which is actually computed using the associated optimal weight function. Compensation between the data term and the regularization was done by setting the $\alpha$ parameter to a value of $10^{-8}$. The $\sigma$ parameter in the penalty function was set to $10^{-8}$. The wavelet used was the coiflet with 6 vanishing moments.

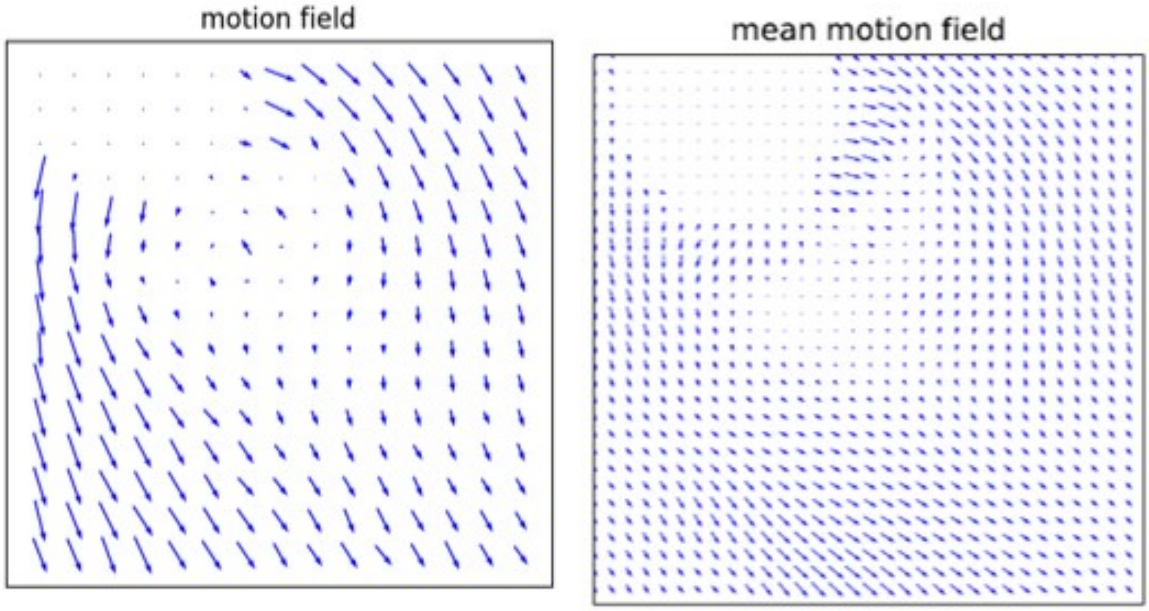


**(a)** Correlation vectors decimated x8

**(b)** OF vectors decimated x8

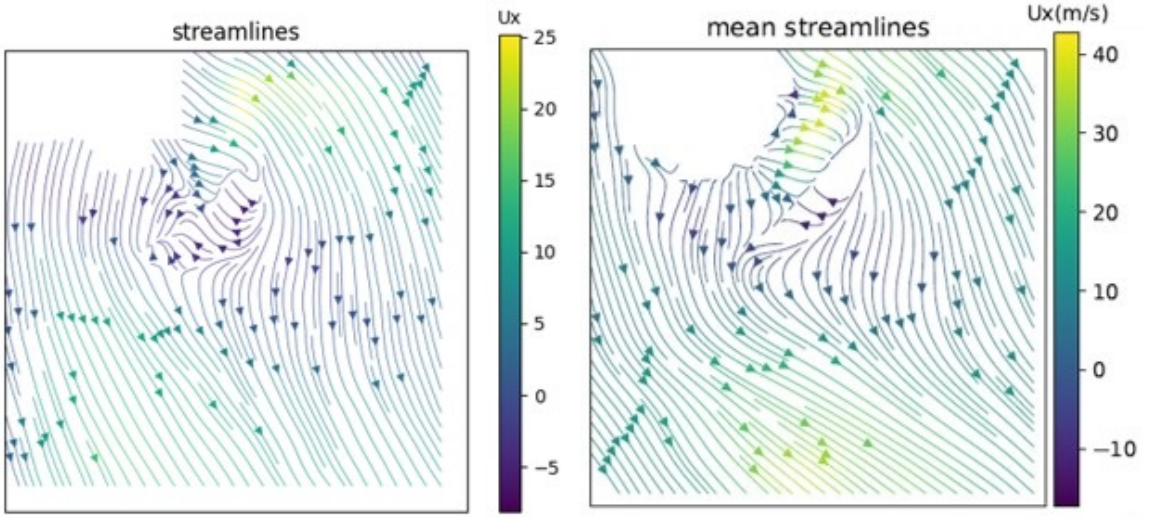


**(c)** Correlation streamlines

**(d)** OF streamlines

**Figure 8.7. :** Comparison of resolution of mean velocity fields computed using the 8.7a,8.7c correlation algorithm and 8.7b,8.7d OF algorithm. The size of the vectors are not to the same scale

The areas around the injector have been cropped out of the computation due to the high reflection of the laser sheet around this region causing artifacts in the PLMS image pair. The resolution of the two results in Fig. 8.7 has been decimated (sub-sampled) by 8, so 1

in every 8 vectors is shown for improved visuals. The lower resolution is one issue that is immediately observed. In addition due to the lower resolution, the velocity vectors are less likely to be represented by the single vector in the 4 pixel window especially where the flow is turning a lot and the streamlines are spread out.

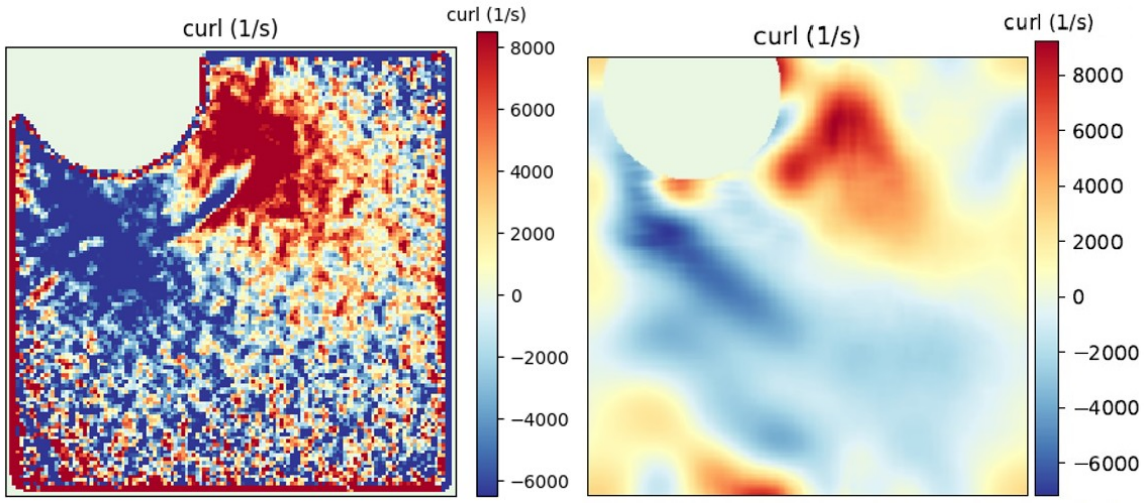


**(a)** Curl computed with correlation algorithm PIV **(b)** Curl computed with OF algorithm

**Figure 8.8. :** Curl of velocity field (vorticity) showing degradation of the topology using the low resolution 8.8a correlation algorithm and the improved result using the 8.8b OF algorithm.

The large gradients at the edges in the curl result from the correlation algorithm arise from the windowing and the lack of resolution for those one-sided gradients.

### 8.4.2 Reacting Scalars

The lack of a genuinely unique method of comparison to test the reaction propagation velocity measurements generated using reactive scalars highlights the novelty and difficulty of this method. A non-rigorous way to do this follows the direction of Son et al. [105] in their recent paper on the use of correlation velocimetry for oxygen chemiluminescence near the injector face of a rocket combustor. The following describes my effort to track motion between reconstructed DMD modes of a more repeatable flame. DMD is a *modal decomposition* technique that interpreted one way decomposes observables in a dynamical system using

a linear infinite dimensional **Koopman** operator whose characteristic values capture the evolution of those observables [106]. The development of correspondence between DMD and the Koopman operator was carried out historically using the Arnoldi algorithm, which reveals the linearity of the operator and its tendency to recreate from a complete basis set the low dimensional representation of a flowfield [13]. It was using two of those projected modes that the dynamics of vortex shedding was captured as imaged via $OH^*$ chemiluminescence. The "periodicity" of the flame is a measure that was heuristically determined by evaluating the tendency for a single DMD mode to reproduce dominant features in the image sequence. It was concluded using this heuristic, that the $OH^*$ chemiluminescence image sequences from transverse jet flames with higher natural gas concentrations were less likely to evolve with repeatable behavior.

For this test of the optical flow velocity measurements, $OH^*$ chemiluminescence images from the 0.31 crossflow Mach number flowfield was used at the condition with the highest hydrogen content - $\phi_{AX,NG} = 0.72$, $\phi = 1.01$, $xH2 = 0.63$. Recall that the amount of hydrogen $xH_2$ is reported as a fraction of the total fuel injected into the axial stage. The natural gas content is reported as the equivalence ratio prior to the injection of hydrogen for flame attachment. We carried out the DMD on 1000 frames of $OH^*$ chemiluminescence of the described transverse jet flame. Mean subtracted images were used to generate the basis vectors, the modes of the decomposition. Reconstruction of the mean subtracted images was carried out using two modes at non-aliased frequencies near 15750Hz and 20250Hz - see Fig. 8.9. The images were captured at 150 kHz.

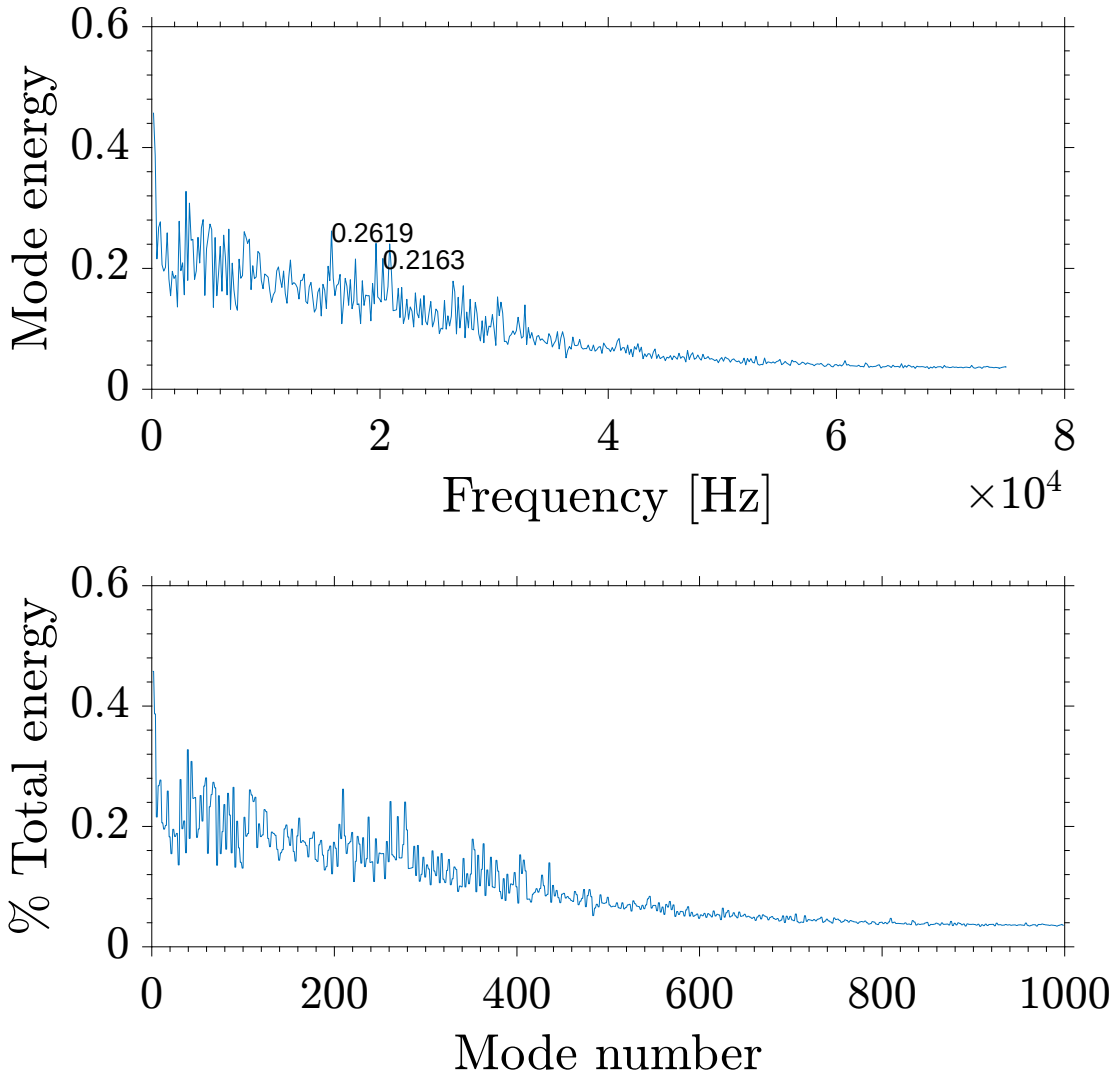


**Figure 8.9. :** Frequencies and mode energies of the two modes (15750Hz and 20250Hz) used in the reconstruction of the spatial modes that generate the coherent structured identified as vortex shedding in comparison to the raw images.

The reconstruction using the two modes at these frequencies generated an observed vortex shedding pattern (apart from vortex pairing and other stochastic features). A single frame comparison of the reconstruction based on these images and the (mean subtracted) raw images is also shown in Fig. 8.10.

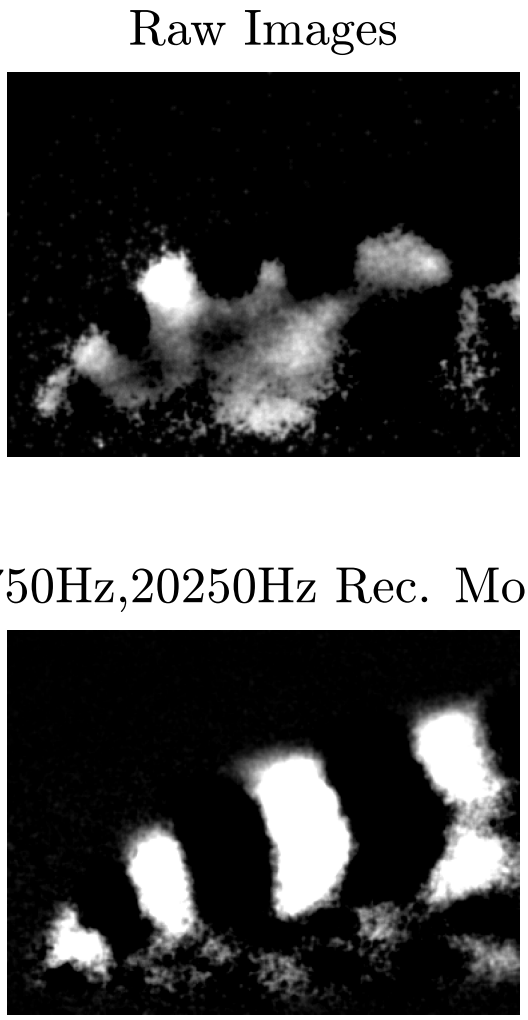


**Figure 8.10. :** Visual comparison of the vortex shedding modes and the raw mean subtracted image.

To capture velocity for comparison against the optical flow results, chemiluminescence intensity from a horizontal band of pixels at Y/D = 3.16 was extracted at 0 and pi/2 relative to the full period. The period spanned 60 µs, near the 15.75kHz mode. The lineplots extracted from the pair of images is shown in Fig. 8.11.

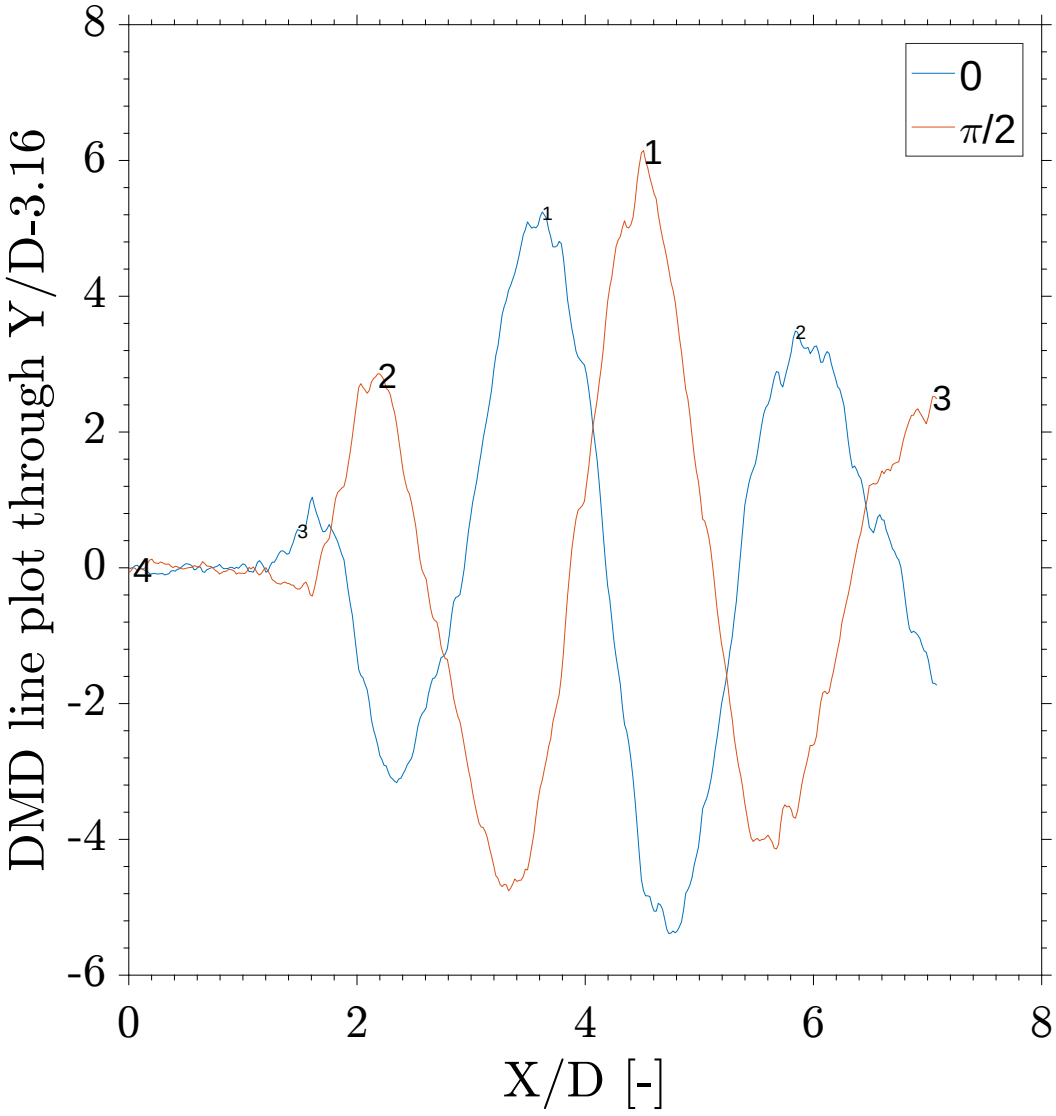


**Figure 8.11. :** Intensity lineplots extracted from the DMD reconstructions at Y/D = 3.16 for tracking features in the flame. Horizontal differences in intensity location using the first of the three identified peaks is continued through the lineplots to obtain locus of displacements at that height.

The difference was computed between the first identified peaks and the lines were thereafter followed. The plot of displacement was used to obtain velocity using the time duration of half the period of the cycle. In fact whether the measurement was carried out using the displacement at the half period or a few instances around this period, the velocity estimate

did not differ by more than 20 m/s. That estimate quickly drops to zero near the cycle origin. The technique of the pattern tracking in this estimate is Lagrangian, which is how the optical flow algorithm works. To take advantage of this, data was collected following the convection of the first point. A comparison to the optical flow results at that height is shown in Fig. 8.12.

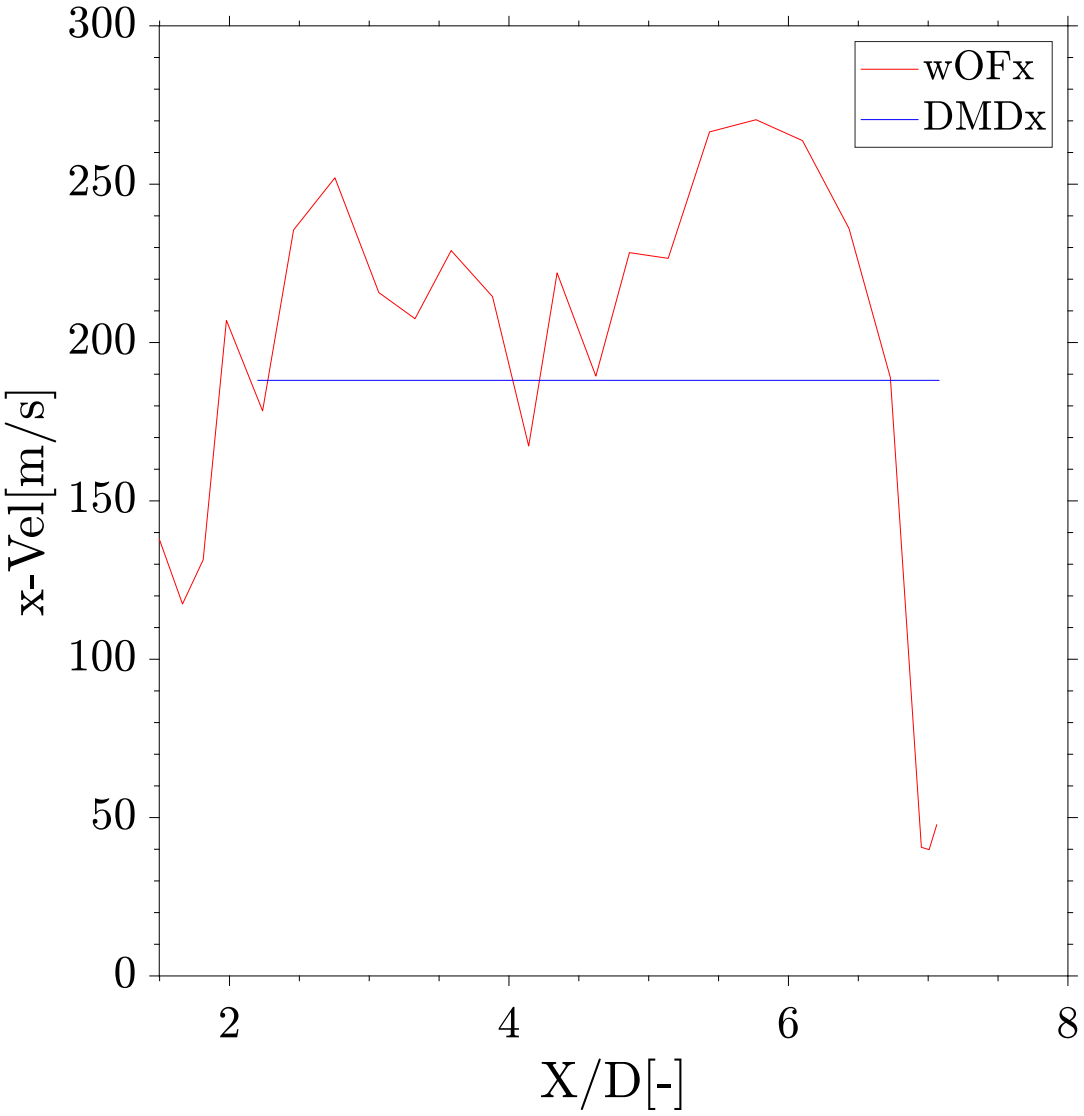


**Figure 8.12. :** Comparison of velocity measurement using feature tracking from DMD reconstruction and OF vectors at Y/D = 3.16.

In contrast to the optical flow and perhaps the raw images, the velocity measured was consistent through the length of the image at that height. It is clear from the featureless line that makes up the pattern tracking estimate of the velocity, that the fluctuations about this estimate are carried by other modes of the decomposition. The order of magnitude comparison is likely the best comparison. It reveals that instantaneous measurements of the velocity field are similar in magnitude to the any displacement of the vortices during the cycle. Perhaps not as a comparison but as an observation, it is noted that there is a large acceleration at the inlet and at the frame exit for the optical flow measurements. It is understood that the deceleration at the frame exit is artificial and due to the aliasing problem.

## 8.5 Results Using Chemiluminescence

The wavelet optical flow parameters used to generate the velocity fields for the results discussed next are as follows. The wavelet and scaling functions used for this analysis are those by Ingrid Daubechies and Ronald Coifman - coiflets [70],[107], with 5 vanishing moments. This wavelet was chosen for its compact support and the number of vanishing moments was chosen to minimize the number of wavelet coefficients at each scale. It was also chosen for a lower accuracy result near the edges of the image where the aliasing problem was noticeable. The data term was the displaced frame difference applied in the variational optical flow estimation, with the robust penalty function suggested by Leclerc chosen due by virtue of its low outlier sensitivity. Of the 8 detail scales in the 288 x 384 pixel image, 6 were used in the estimate. The Horn and Schunk regularization was used to avoid the aperture problem. All pre-smoothing of the $OH^*$ chemiluminescence data was performed using a sliding average Gaussian kernel of width 2.5 pixels. The pre-smoothing aligns with trade secrets in the computer vision open literature as discussed in a recent paper by Sun et al. formalizing why this improves the results [67]. Prior to the pre-smoothing, an image an intensity threshold was applied to the image to remove intensifier noise (see Fig. 8.13).

From the knowledge of the portions of the image containing $OH^*$ chemiluminescence, a valid data domain was selected for the computation. The definition was based on the image

SNR to exclude portions without high intensity patterns which would otherwise be filled with regularization vectors. The velocity fields in the subsequent subsection were selected from the image based on the valid data domain, the pockets of high intensity OH* chemiluminescence.

To reintroduce the schematic around the images, the dark rectangle beneath the image frame signifies half of the injector ID, with the injector centerline at $\mathbf{X/D} = 0$. The white rectangle from $\mathbf{Y/D}$ 0-0.87 is the portion of the combustor that prevents optical access previously called the "lip". Crossflow direction is left to right (positive $\mathbf{X/D}$), and the jet issues into the positive Y/D direction, for example in Fig. 8.14.

We focus attention in this chapter on the first few jet diameters in the flow downstream of the injector, with conditions corresponding to tables 8.1 and 8.2. The leading points of the flame are located in this region as identified in previous chapters. In subsequent sections, the terms leading point and flame (stabilization) front are used interchangeably.

**Table 8.1. :** Attached Flame Test Conditions

| Upstream conditions | | | | Jet conditions | | | |
|---|---|---|---|---|---|---|---|
| Mach # | $Re_{Dh}$ | $T_0$ | $T$ | $\phi_{AX,NG}$ | Min. $xH_2$ | J | $Re_D$ |
| 0.31 | 53080 | 1670 | 1647 | 0.71 | 0.63 | 1.9 | 126900 |
| 0.31 | 52890 | 1676 | 1654 | 1.45 | 0.46 | 2.1 | 140800 |
| 0.31 | 52670 | 1681 | 1658 | 2.0 | 0.59 | 2.4 | 134400 |

**Table 8.2. :** Attached Flame Test Conditions

| Upstream conditions | | | | Jet conditions | | | |
|---|---|---|---|---|---|---|---|
| Mach # | $Re_{Dh}$ | $T_0$ | $T$ | $\phi_{AX,NG}$ | Min. $xH_2$ | J | $Re_D$ |
| 0.63 | 87540 | 1776 | 1680 | 0.71 | 0.79 | 1.5 | 196400 |
| 0.63 | 84300 | 1811 | 1716 | 1.41 | 0.71 | 1.6 | 249400 |
| 0.63 | 84440 | 1825 | 1730 | 2.0 | 0.71 | 1.8 | 249600 |

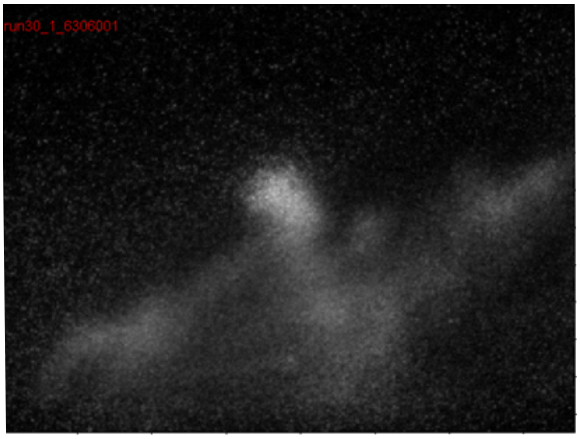


**(a)** Raw image

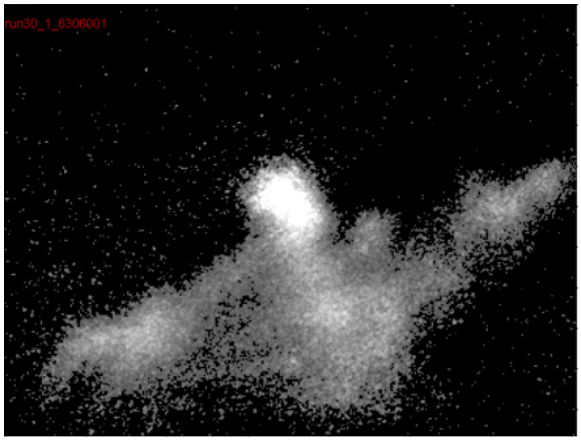


**(b)** Intensity thresholded image


**(c)** Prefiltered image

**Figure 8.13. :** Preprocessing applied to each chemiluminescence image.

### 8.5.1 Average Velocity Topology at Low Equivalence Ratios

In this section the velocity field and topology, the various gradients of the velocity field $\nabla \boldsymbol{v}(\boldsymbol{x})$ and some useful combinations will be reported for the low natural gas equivalence ratio $\phi_{AX,NG} = 0.71$ transverse jet flame. Some post processing has been done to the data at 0.63 Mach number to remove the majority of the velocity field that suffers from the aliasing problem. Some artifacts are still present in the results due to the stochastic nature of the flame. The average and instantaneous topological features are presented as 2-D data since little meaning can be obtained from point probing of the data over time. This is because the domain is not uniformly "seeded" with the tracer. The velocity fields reported next has been decimated (subsampled) by a factor of 8.

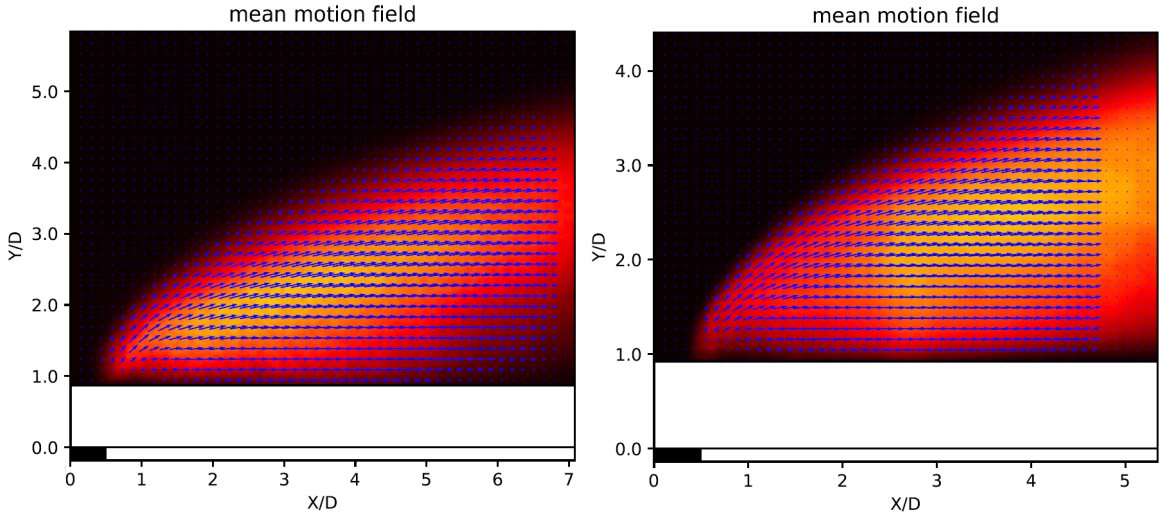


**(a)** $\phi_{AX,NG}$ 0.71, $\phi_{AX}$ 1.01 and $xH_2$ 0.63, Mach 0.31

**(b)** $\phi_{AX,NG}$ 0.71, $\phi_{AX}$ 1.35, $xH_2$ 0.79, Mach 0.63

**Figure 8.14. :** Average velocity field for transverse jet flames for the lowest natural gas equivalence ratio at 8.14a Mach 0.31 and 8.14b Mach 0.63.

The mean velocity field for both crossflow Mach numbers reveals the flame luminosity aligning with the location for which the majority of the vectors were computed. It also shows the near wall velocities to be aligned in the direction of the crossflow, compared to the location near the downstream shear layer which stays at a positive angle to the bottom

wall of the combustor for both crossflow Mach numbers. The flame is more luminous for the higher crossflow Mach number case. This only affects the location of the high average velocity vectors.

The partial picture obtained from the mean velocity field is corroborated by the streamlines colored by the velocity magnitude.

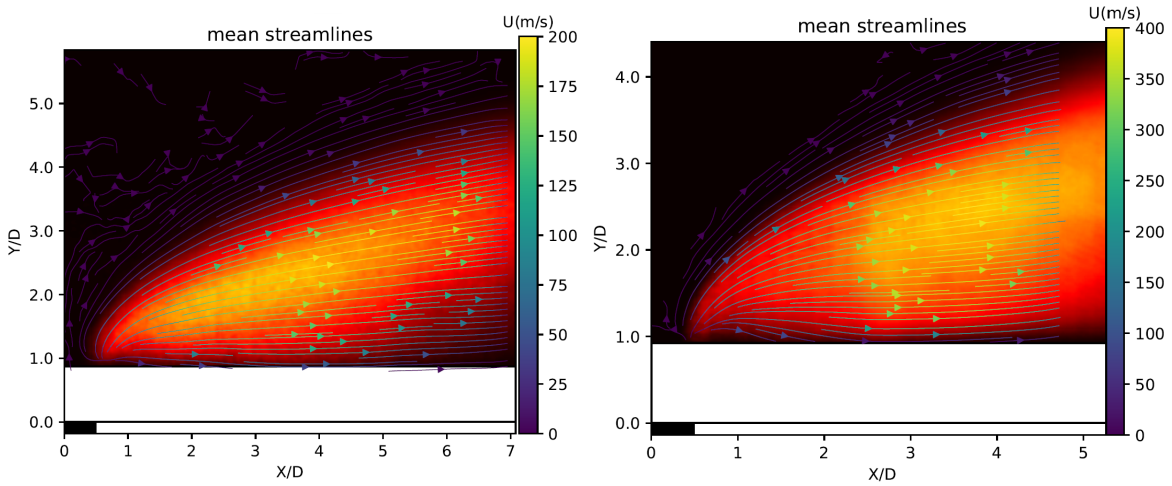


**(a)** $\phi_{AX,NG}$ 0.71, $\phi_{AX}$ 1.01 and $xH_2$ 0.63, Mach 0.31 **(b)** $\phi_{AX,NG}$ 0.71, $\phi_{AX}$ 1.35, $xH_2$ 0.79, Mach 0.63

**Figure 8.15. :** Streamlines from the jet flames same conditions as Fig. 8.14.

A source node similar to those identified in reacting and non-reacting jet fluid trajectories [41] in the downstream region of the jet is also noticed here, although at this point it is not clear that the flame follows the fluid motion. The luminosity in the average image is hence given another interpretation: it indicates locations where the flame is likely to travel through. The high average velocity in the luminous part of the flame is not to be interpreted as flame propagation occurring at higher speeds at that location, in fact as the instantaneous pictures reveal, the whole flame sheet is convected downstream at near similar speeds, apart from high heat release locations near the downstream shear layer (top of the flame brush) where the flame encounters unburned fluid. The averaging of different frames however, picks out the vectors near the brighter portion. It shows that the lower velocity streamlines outside of the luminous portion occur due to the propagation of the reaction fronts through those

locations. The peak mean velocities measured for the high crossflow Mach number case are about twice that of the lower crossflow Mach number case. There are also spontaneous autoignition kernels in the instantaneous picture in Fig. 8.16 that reveal the source of the far out streamlines that persist a few jet diameters before getting entrained into the jet core.

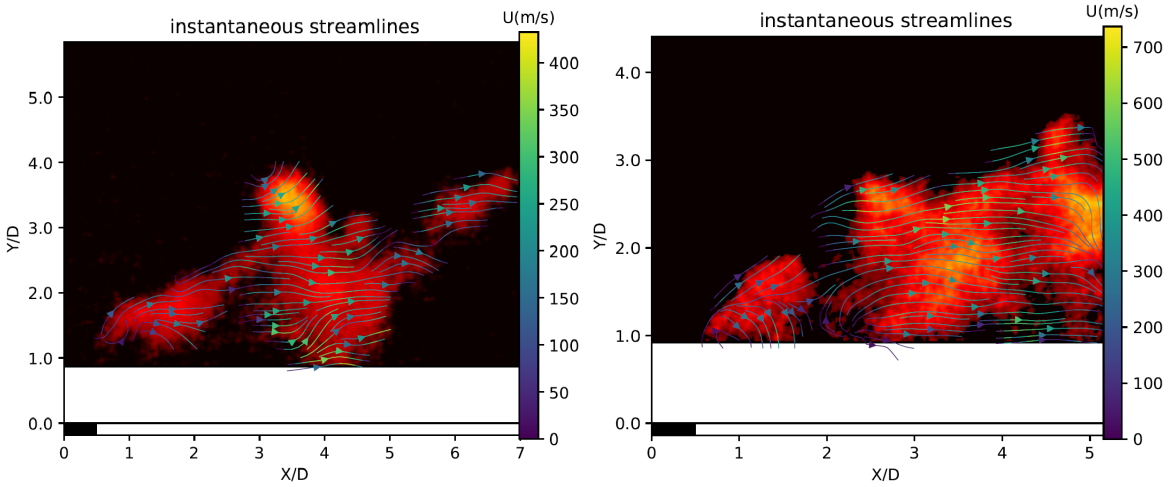


**(a)** $\phi_{AX,NG}$ 0.71, $\phi_{AX}$ 1.01 and $xH_2$ 0.63, Mach 0.31 **(b)** $\phi_{AX,NG}$ 0.71, $\phi_{AX}$ 1.35, $xH_2$ 0.79, Mach 0.63

**Figure 8.16. :** Instantaneous streamlines for transverse jet flames same conditions as Fig. 8.14.

Instantaneous images will also be used to describe the behavior of the transverse jet flame. It was shown in the uncertainty quantification process that the instantaneous images may not reveal the true nature of the flame surface. Corroboration with other 2D images (instantaneous or average) may provide assurance of the accuracy of the results. The instantaneous picture also shows that near the wall at the attachment point, are locations of flame propagation that turn towards the bottom wall between X/D of 1 and 2. The low Mach number image shows the flame turning upwards as it encounters some unburned fluid near X/D=3.5, Y/D=3.5. The flame is also absent near the wall after X/D=5 leading to the lower luminosity in the average images. For both Mach numbers, the flame is generally traveling in the direction of the crossflow.

The rotation rate of the propagating reaction layer was captured using the rotation rate tensor $\Omega_{xy}$ whose singular nonzero component defined as

$$\omega = -\frac{1}{2}\left(\frac{\partial v}{\partial x} - \frac{\partial u}{\partial y}\right) \tag{8.11}$$

is available for this 2D flowfield. It is large negative for positive horizontal gradients in the vertical velocity $\frac{\partial v}{\partial x}$ - counterclockwise rotation - if the magnitudes are larger than the vertical gradients in the horizontal velocity $\frac{\partial u}{\partial y}$ - clockwise rotation. The physics of the clockwise rotation of the propagating flamefront at the injector for the low Mach number flame in Fig. 8.17a is understood to result largely from the high shear from flame expansion and turbulent shear near the jet exit which drags the reacting fluid along with it. When the fluid starts to travel in the direction of the crossflow near the top of the flame brush, "tongues" of instability protrude into the jet core, releasing heat as the reactions proceed. This is corroborated with the change in sign of the vorticity near to top of the flame brush to counterclockwise rotation. This is understood to be in part caused by buoyancy and reaction propagation. In terms of the velocity topology, the change is captured by the vertical gradient of the horizontal velocity. The large value of $\frac{\partial v}{\partial x}$ results in transfer of mass and momentum away from the wall into the flame brush which also explains why the flame brush has a positive slope at its trailing edge between X/D of 6 and 7.

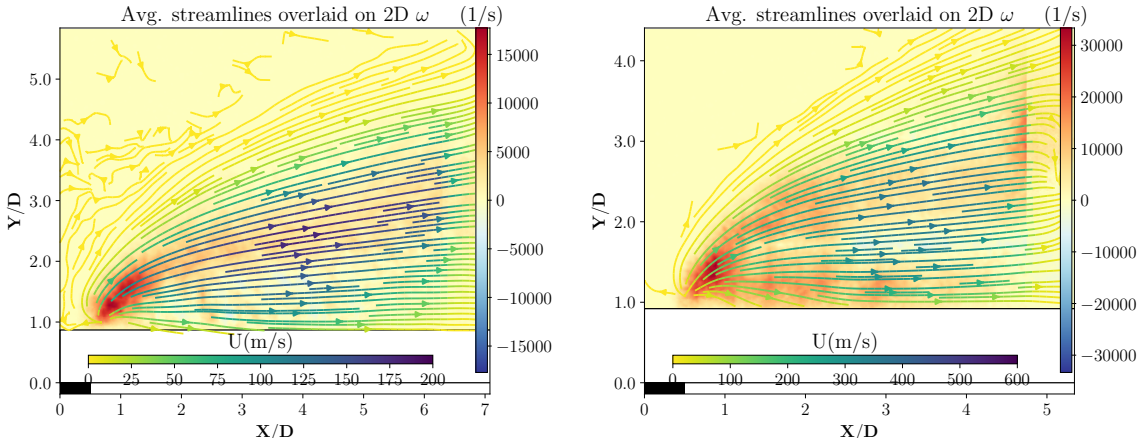


**(a)** $\phi_{AX,NG}$ 0.71, $\phi_{AX}$ 1.01 and $xH_2$ 0.63, Mach 0.31 **(b)** $\phi_{AX,NG}$ 0.71, $\phi_{AX}$ 1.35, $xH_2$ 0.79, Mach 0.63

**Figure 8.17. :** Average vorticity for transverse jet flames same conditions as Fig. 8.14.

The vorticity at the higher Mach number shows the reaction intermediates returning to the wall near the injector, indicated by clockwise rotation. This also follows from the higher shear at the jet exit, which pulls the fluid undergoing heat release further along the downstream shear layer trajectory before it can turn towards the near wall where some fluid at stoichiometric proportions are available to burn. So far the reaction propagation has been suggested to be influential near the top of the flame brush and in part near the jet exit where the flame returns to the wall. The contribution of advection to this velocity field is perhaps through the bulk of the jet wake in the flame brush downstream of the flame stabilization location.

The picture of high shear as discussed previously is seen in Fig. 8.18 and is captured by the x-y entry in strain rate tensor defined as

$$S_{xy} = -\frac{1}{2}\left(\frac{\partial v}{\partial x} + \frac{\partial u}{\partial y}\right) \tag{8.12}$$

the 2D shear, which features a sum of the previous two terms encountered in the definition of the vorticity. In similar manner to the accounting of terms in the vorticity image, notice that where large negative vorticity aligns with large positive shear, indicates locations of large vertical gradient in the horizontal velocity $\frac{\partial u}{\partial y}$. At the jet exit however, at both Mach

number conditions, the vorticity and shear are high positive indicating contributions from the horizontal gradient in the vertical velocity $\frac{\partial v}{\partial x}$ this confirms the role of the jet shear layer in creating a high shear location near the jet column. There the fluid releasing heat is accelerated in the horizontal direction following the bending of the jet by the crossflow. In contrast to that, downstream of the jet exit and near the bottom wall of the combustor for both images the signs of $S_{xy}$ and $\omega_{xy}$ are opposite showing fluid exiting the wall as it gets entrained into the flame brush for the low Mach number flame and turn towards the wall to consume more fuel for the high Mach number flame.

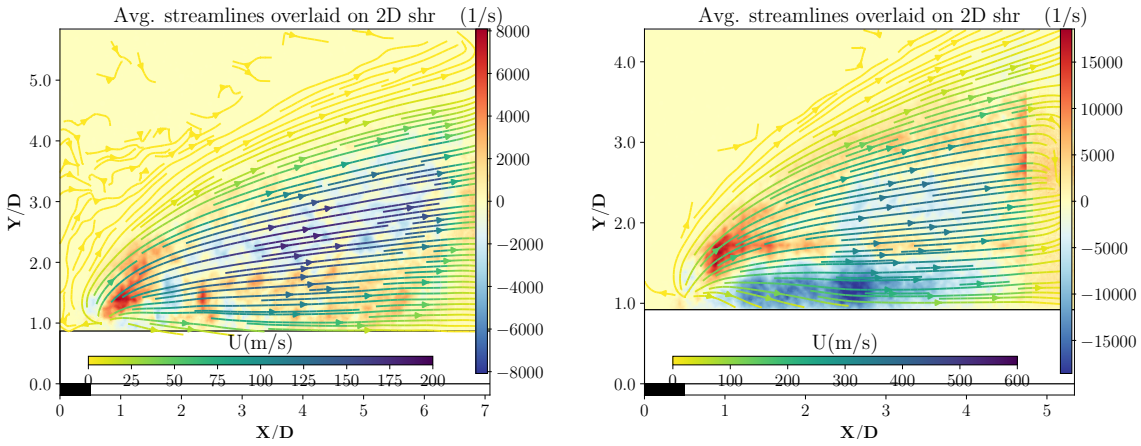


**(a)** $\phi_{AX,NG}$ 0.71, $\phi_{AX}$ 1.01 and $xH_2$ 0.63, Mach 0.31 **(b)** $\phi_{AX,NG}$ 0.71, $\phi_{AX}$ 1.35, $xH_2$ 0.79, Mach 0.63

**Figure 8.18. :** Average in plane shear rate same conditions as Fig. 8.14.

It is likely following the formation of autoignition kernels that the instantaneous location of the partially premixed flame progresses upstream because of thermal runaway causing a fluctuation around the mean flame position. Su et al. [108] hypothesized a complementary mechanism for fluctuations in partially premixed unattached reacting jet leading points as follows: They claim the leading points are likely to ignite at outer shear layer regions which have low axial velocity and are thus able to travel upstream and inwards within a coherent structure. The leading point encounters a step increase in mixture fraction as it travels upstream into smaller coherent structures. As the leading point has consumed fluid with stoichiometric mixture fraction up to this location, it can only travel outwards and downstream,

being convected with the coherent structure and the cycle repeats. A similar behavior was observed in Yoo et al.'s 2011 [109] paper featuring DNS of a coflowing 18/82 $C_2H_4-N_2$ jet where the leading point was established in a low velocity region in which the radical pool builds up given that the convective velocity in this experiment was higher than the average flame displacement speed. The jet velocity was 204m/s and the coflow velocity was 20m/s. The leading point was first gradually advected downstream by the high convective velocity and then suddenly moved upstream due to the autoignition and expansion of a kernel further upstream of the flame base, and the process repeated. Dissipative effects like molecular transport were not dominant since the fuel jet was heavily diluted forcing the stoichiometric mixture fraction to lie closer to the faster moving stream. The plot of flame lift off against time showed sawtooth like features, with the steep velocities (many times in excess of the laminar flame speed) indicative of the autoignition events. Similar liftoff behavior had been observed in coflowing lifted diesel jet flames [110]. Autoignition was also verified in Yoo et al. by rendering the computed hydroperoxy $HO_2$ radicals which occurred upstream of the OH radical used to identify the flame. A comparison could be made to the reacting transverse jet flames since the flame propagation direction is aligned with and opposing the crossflow direction. Also since the description of the transverse jet flames in Micka and Driscoll's [31] paper feature partially-premixed triple flames similar to those observed in co-flowing flames.

The analysis in the previous section carries over to these transverse jet flames which feature reaction propagation in the leeward side of the jet. In this case as in the previous analysis, the more dilute jet ensures that the stoichiometric mixture surface stays near the jet core which is faster moving. In this case however the flame is attached to the injector orifice in the mean field. For the flame to stay attached to the injector, a more dilute jet flame would require lower natural gas equivalence ratio, since only then will the relatively higher reactivity fuel require less hydrogen for attachment. The dilution is carried out by reducing the fuel overall equivalence ratio. The reasoning suggests that the low natural gas equivalence ratio flames do not benefit from near wall burning with the associated rich vortex systems that transfer momentum from the wall since the flames can be closer to the jet column, as was observed.

The difference in part between Yoo et al.'s simulation and these transverse jet flames lies in the reactivity of the dilute jet. If the dilution was carried out with the same fuel - either by adding oxidizer or reducing fuel content - the stoichiometric mixture surface would indeed move inwards towards the jet, allowing advection to push the flame base downstream with longer cycle times. The less dilute transverse jet flames however are less reactive and so I expect this long cycle flame base dynamics to be the observed at the conditions with higher natural gas equivalence ratio. In fact since the balance between reactivity and advection determines the flame stabilization mechanism, I predict those flames will be more likely autoignition stabilized.

### 8.5.2 Stabilization Front Dynamics

The 2D data in Fig. 8.19 reveal the short timescales associated with the $OH^*$ chemiluminescence measurement. In these and subsequent images the contribution of leading point progress towards the injector and flame expansion into the jet core is dominant, more so than the quenching of the generated $OH^*$ radical.

The leading point may follow the bottom wall of the combustor in approaching the jet orifice. A radical pool is established in the near wake of the jet which coincides with the low velocity regions adequate for flame stabilization. The leading points in the reacting transverse jet flame would experience fluctuations due to turbulence inducing two seemingly opposing effects: spatial gradients in ignition delay leading to autoignition events accelerating the flame speed, and advection from the high flow velocity pushing the flame base downstream. These measurements of the flame displacement velocity help compare the effects.

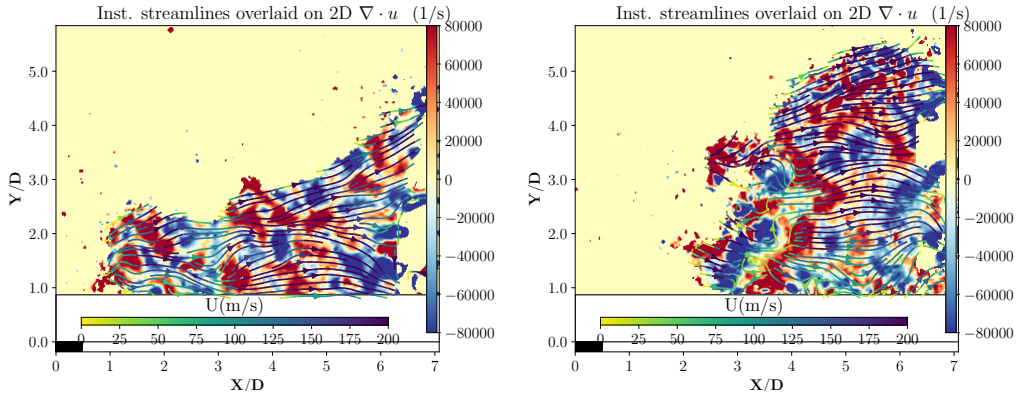


**(a)** 0µs $\phi_{AX}$ 1.73 $\phi_{AX,NG} = 1.45$ **(b)** 0µs $\phi_{AX}$ 2.69 $\phi_{AX,NG} = 2.0$

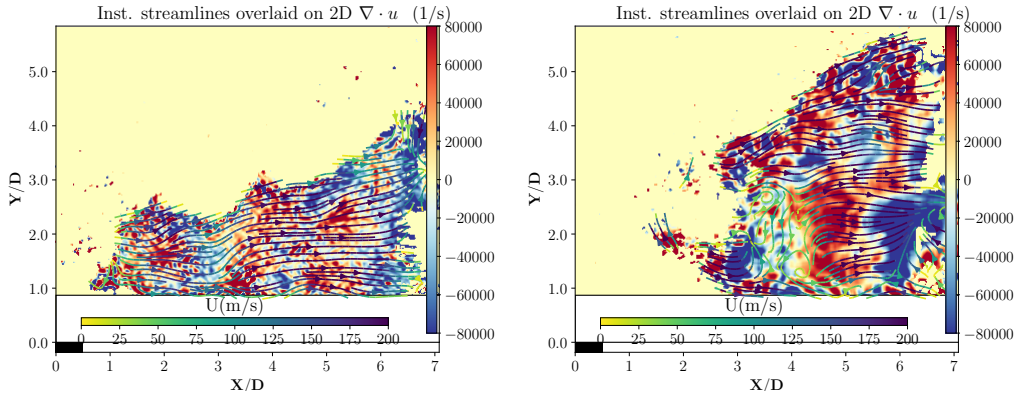


**(c)** 6.67 µs $\phi_{AX}$ 1.73 $\phi_{AX,NG} = 1.45$ **(d)** 6.67 µs $\phi_{AX}$ 2.69 $\phi_{AX,NG} = 2.0$

**Figure 8.19. :** Instantaneous divergence images at two different equivalence ratios with a fixed crossflow Mach number of 0.31

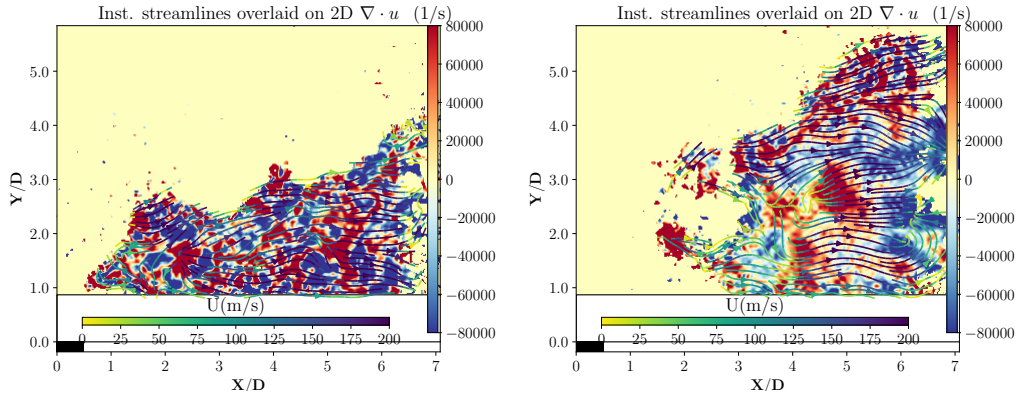


**(e)** 13.34 µs $\phi_{AX}$ 1.73 $\phi_{AX,NG} = 1.45$ **(f)** 13.34 µs $\phi_{AX}$ 2.69 $\phi_{AX,NG} = 2.0$

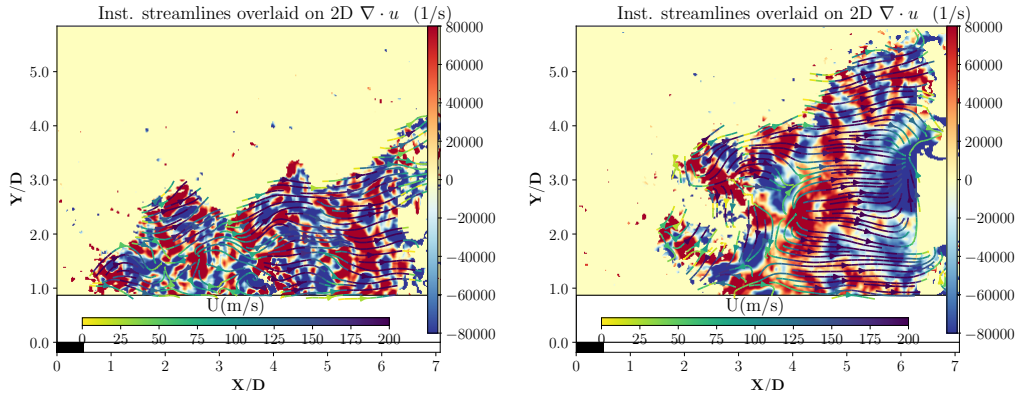


**(g)** 20.0 µs $\phi_{AX}$ 1.73 $\phi_{AX,NG} = 1.45$ **(h)** 20.0 µs $\phi_{AX}$ 2.69 $\phi_{AX,NG} = 2.0$

**Figure 8.19. :** ... contd Instantaneous divergence images at two different equivalence ratios with a fixed crossflow Mach number of 0.31

The images in Fig. 8.19 compare computations of the divergence of the velocity field at two equivalence ratios based on instantaneous OH* chemiluminescence images. There is evidence of intermittent detachment of the flame stabilized at the higher equivalence ratio. In addition, the streamlines point towards the incoming unburned fuel at the leading points. This is consistent with the prediction made in the previous section based on the reactivity of the fuel and the dynamics of partially premixed flames in high convective environments. Because the jet with the higher natural gas concentration is less diluted the stoichiometric surface lies further out radially from the core of the jet, causing the flame to stabilize near the wall. The large total fuel equivalence ratio is responsible for the size of fluid undergoing heat release. This large heat release (shown by the OH* chemiluminescence) is displaced from the

injector due to the lower reactivity resulting in the extension of the leading point towards the injector in response to new unburned fuel entering the wake of the jet. For the low equivalence ratio case, the flame is more attached and releases more heat gradually leading to the height of the flame increasing with downstream distance. Because the heat release is gradual, there are fewer attachment points to the injector. This may be an indication of differential burning due to hydrogen content. The leading point in the lower equivalence ratio flame may thus be stabilized more by flame propagation than autoignition.

The reaction propagation surface downstream of the leading point has some divergence for both equivalence ratios. The local expansion indicates motion of the flame base back towards the injector shortly after ignition at the attachment point. The distributed pattern of the expanding flame brush in Fig. 8.20 arises from the distribution of timescales over which the fluid undergoing heat release is carried along as flow history printed onto it. When the timescales of advection are shorter than those of expansion, the reaction front seems "frozen". This is rarely the case at the leading points. The flame expansion at the leading point and into the jet core is very large, and occurs frequently compared to the quenching of $OH^*$. The fluid carrying the expanding reaction front is then convected and stirred by turbulence through the flame brush. I am distinguishing the dilatation of fluid elements from the expansion of the flame surface within the brush. The first could be a result of the second, but is not natural to infer from the nature of the data. Some aperiodic divergence scalars arise due to the low resolution textured $OH^*$ chemiluminescence images which were used for generating these vectors. The wrinkled flame surface evident from these measurements is often present for a short fraction of the large advection duration. The spontaneous formation of autoignition kernels also adds detail to the analysis of the underlying flame surface: the presence of the autoignition kernels by themselves indicate the flame propagation mechanism at this level of reactivity. The convergence of the streamlines near the right boundary of the image is indication of the aliasing problem.

The velocity topology shows that autoignition kernels are more likely to occur at the higher equivalence ratios than at the lower equivalence ratios. Increased equivalence ratio in these transverse jet flames corresponds to increased natural gas equivalence ratio. For example, the higher equivalence ratio flame in Fig. 8.19 corresponds to the fuel jet with

the largest natural gas equivalence ratio, the least reactive apart from differential diffusion of hydrogen. It seems to indicate that decreased reactivity in a fuel jet tends to shift the stabilization mechanism towards autoignition if the flame is to be attached at all, moreso than equivalence ratio. The average divergence images in Fig 8.20 provide complementary results corroborating the distributed pattern of timescales downstream of the attachment point.

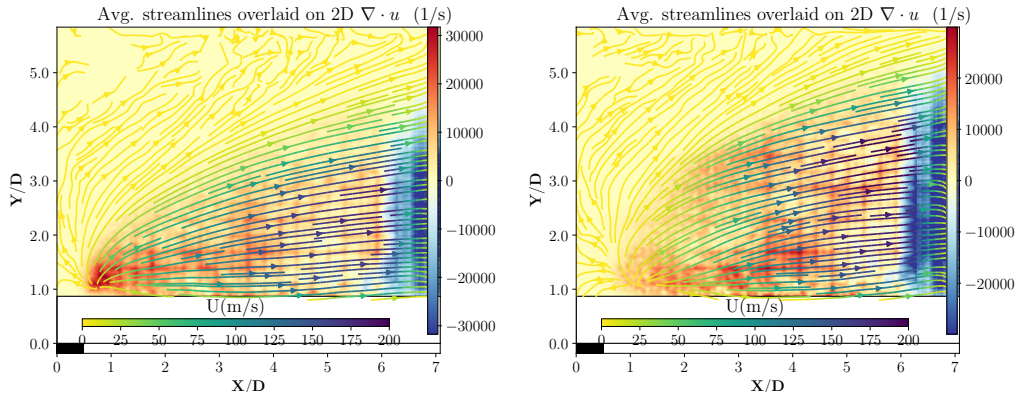


**(a)** $\phi_{AX}$ 1.73 $\phi_{AX,NG} = 1.45$ **(b)** $\phi_{AX}$ 2.69 $\phi_{AX,NG} = 2.0$

**Figure 8.20. :** Average divergence images at two different equivalence ratios and fixed crossflow Mach 0.31

A similar result is obtained for the instantaneous images of the 2D shear at these conditions in Fig. 8.21. The stream lines that respond to the change in local shear reveal the wrinkling and expansion of the flame brush. Other features that are occur on time scales too quick for the streamlines to respond to are interpreted as autoignition kernels or insufficient texturing of the image.

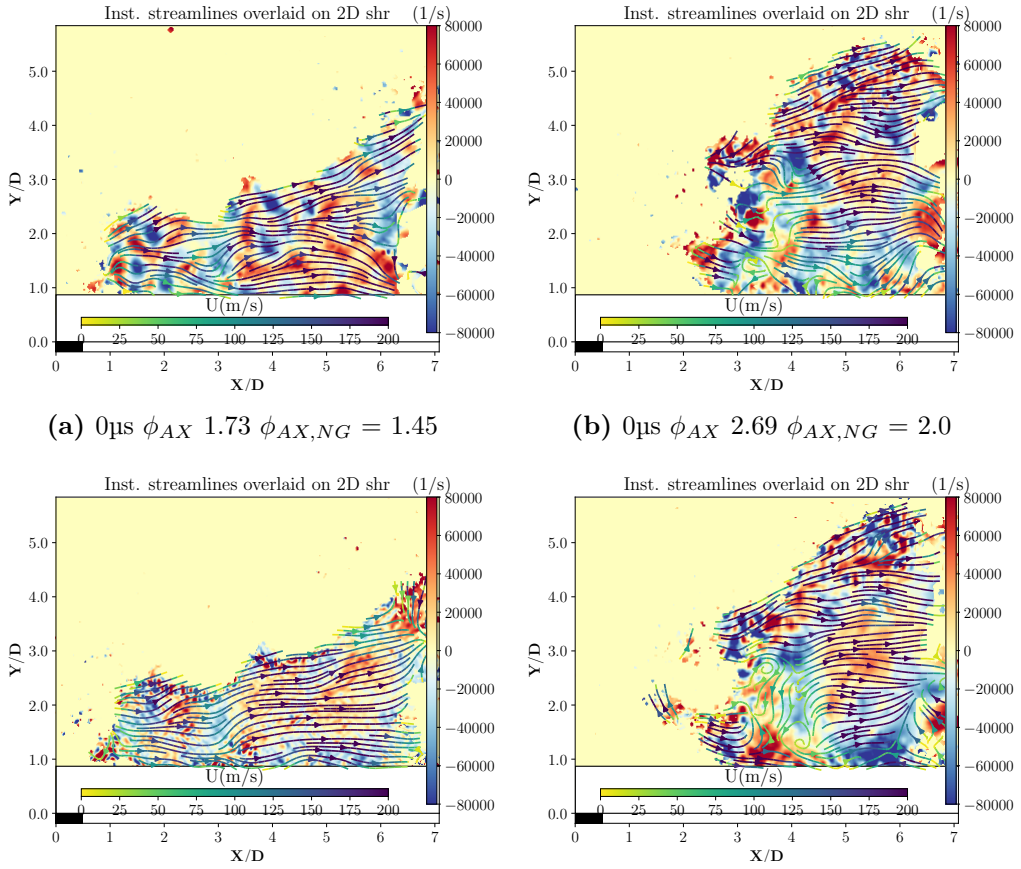


**(a)** 0µs $\phi_{AX}$ 1.73 $\phi_{AX,NG} = 1.45$ **(b)** 0µs $\phi_{AX}$ 2.69 $\phi_{AX,NG} = 2.0$

**(c)** 6.67µs $\phi_{AX}$ 1.73 $\phi_{AX,NG} = 1.45$ **(d)** 6.67µs $\phi_{AX}$ 2.69 $\phi_{AX,NG} = 2.0$

**Figure 8.21. :** Instantaneous shear images at two different equivalence ratios with a fixed Crossflow Mach number of 0.31

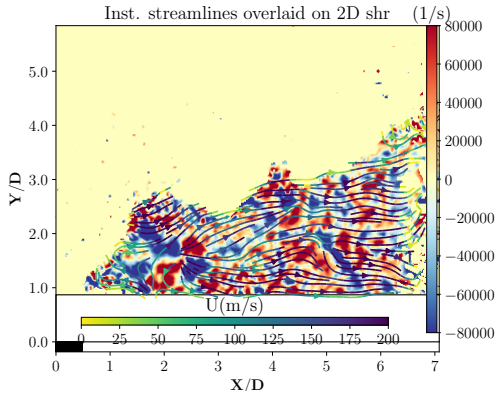


**(e)** 13.34µs $\phi_{AX}$ 1.73 $\phi_{AX,NG} = 1.45$

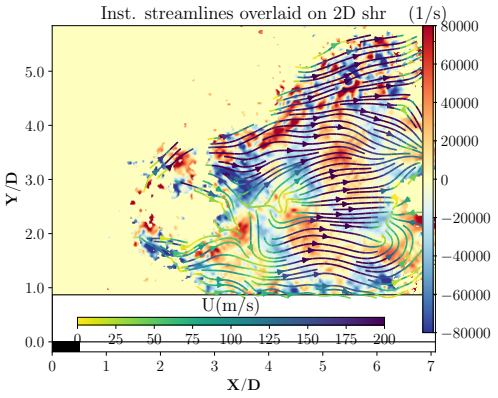


**(f)** 13.34µs $\phi_{AX}$ 2.69 $\phi_{AX,NG} = 2.0$

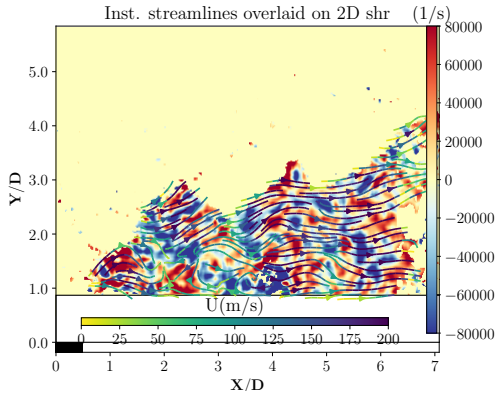


**(g)** 20.0µs $\phi_{AX}$ 1.73 $\phi_{AX,NG} = 1.45$

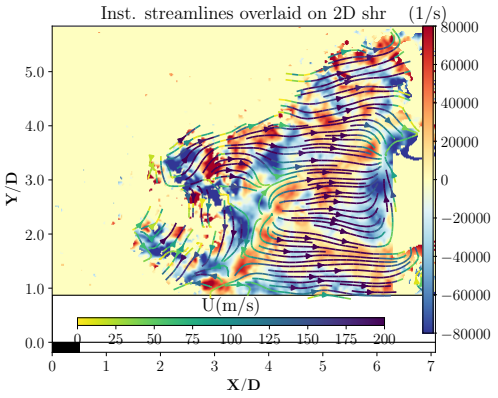


**(h)** 20.0µs $\phi_{AX}$ 2.69 $\phi_{AX,NG} = 2.0$

**Figure 8.21. :** ... contd Instantaneous shear images at two different equivalence ratios with a fixed crossflow Mach number of 0.31

Some more information about the dynamics of the jet can be extracted from the vorticity since wherever there is positive vorticity, the flame is moving towards the bottom wall. Even for the low equivalence ratio case, there is a lot of high negative vorticity near the bottom wall, indicating why the flame stays there. It is harder to extract information from the high equivalence ratio images due to the more stochastic nature of the flame. It is obvious though that a lot of the vorticity is located near the top of the flame brush.

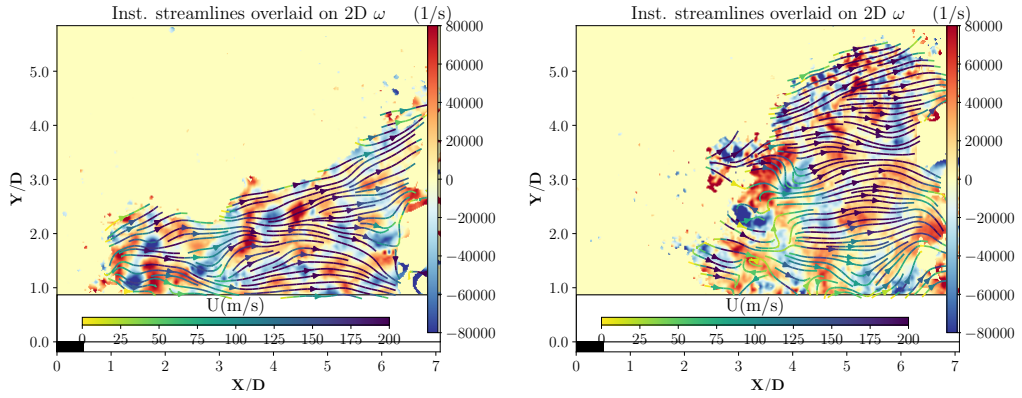


**(a)** 0µs $\phi_{AX}$ 1.73 $\phi_{AX,NG} = 1.45$ **(b)** 0µs $\phi_{AX}$ 2.69 $\phi_{AX,NG} = 2.0$

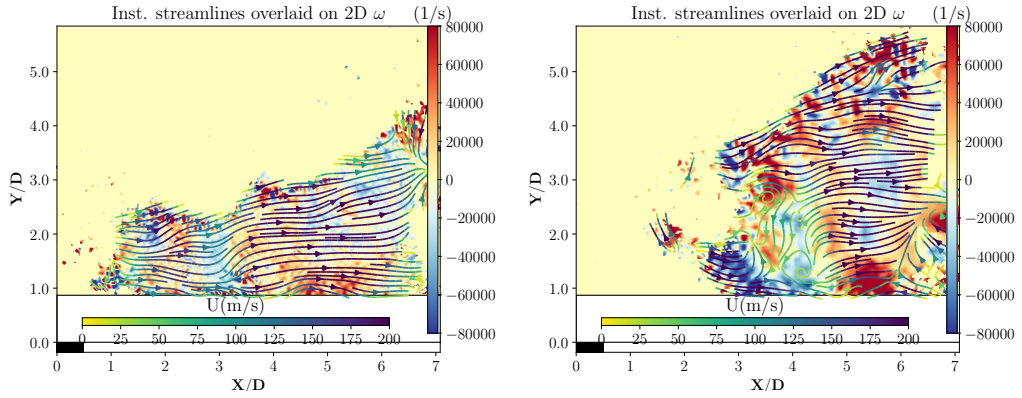


**(c)** 6.67µs $\phi_{AX}$ 1.73 $\phi_{AX,NG} = 1.45$ **(d)** 6.67µs $\phi_{AX}$ 2.69 $\phi_{AX,NG} = 2.0$

**Figure 8.22. :** Instantaneous vorticity images at two different equivalence ratios with a fixed crossflow Mach number of 0.31

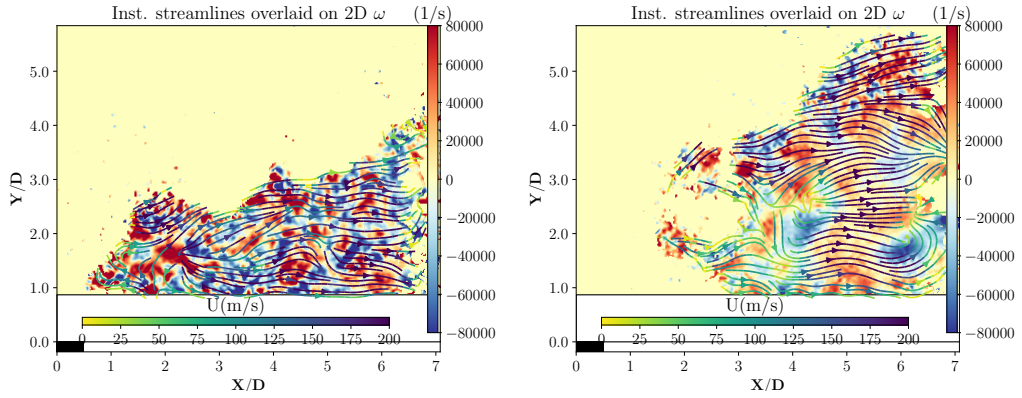


**(e)** 13.34µs $\phi_{AX}$ 1.73 $\phi_{AX,NG} = 1.45$ **(f)** 13.34µs $\phi_{AX}$ 2.69 $\phi_{AX,NG} = 2.0$

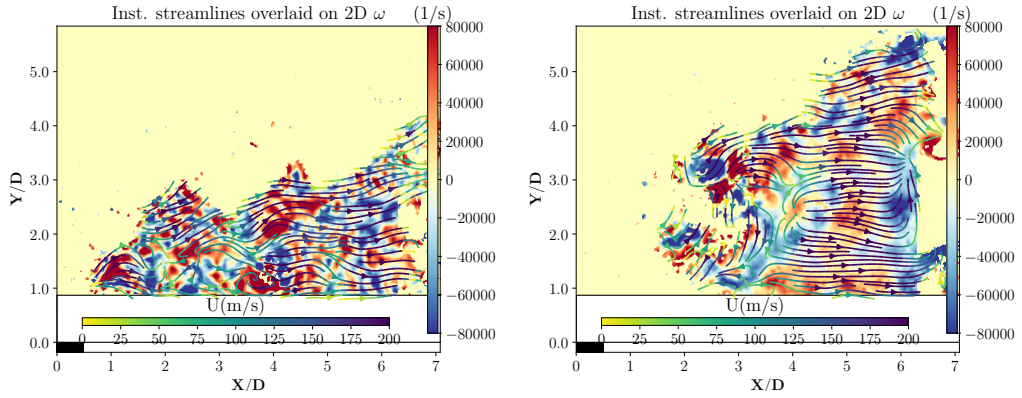


**(g)** 20.0µs $\phi_{AX}$ 1.73 $\phi_{AX,NG} = 1.45$ **(h)** 20.0µs $\phi_{AX}$ 2.69 $\phi_{AX,NG} = 2.0$

**Figure 8.22. :** ... contd Instantaneous vorticity images at two different equivalence ratios with a fixed crossflow Mach number of 0.31

The average shear images in Fig. 8.23 reveal the behavior of the flame at the edges of the flame brush where unlike the lowest equivalence ratio cases, vertical entrainment of the fluid from the walls is absent. In its place the flame pulls towards the wall for these higher natural gas equivalence ratio flames. The reaction propagation into the jet core pulls the top part of the flame brush upwards. At the highest equivalence ratio, the additional fuel (after the stoichiometric surface meets the the wall) burns into the downstream shear layer increasing the vertical extent of the flame. Together with the lower reactivity causing the delayed heat release and longer displacement from the injector face results in a more compact flame. The middle of the flame brush which has a positive shear, is the proposed downstream shear layer of the jet. The downstream shear layer again borders the reacting

fluid in the jet wake and serves as an entry point into which reactive fluctuations occur - following the lowest equivalence ratio picture from Fig. 8.18. This seems to suggest that more than the flamefront dynamics, flame reactivity is the dominant physics, such that the shear images for these lower reactivity flames are similar to that at the high Mach number - which features more natural gas. The picture is complemented by the average rotation images which show the flame adhering to the bottom wall in Fig. 8.23.

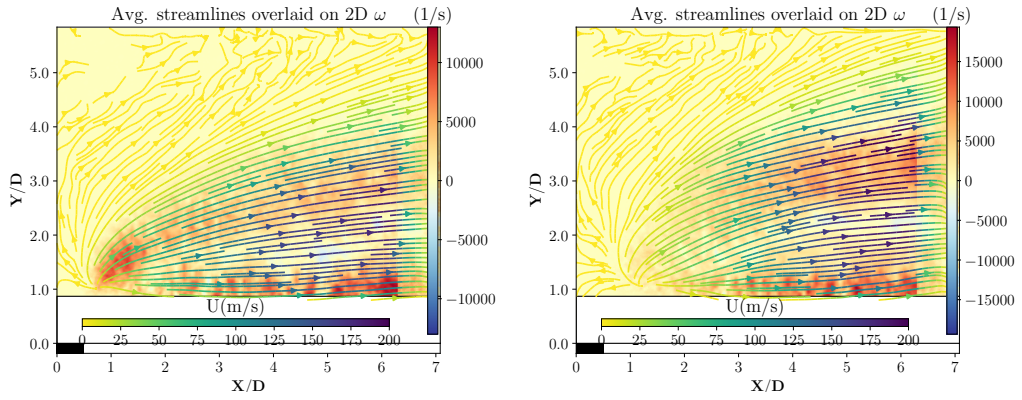


**(a)** $\phi_{AX}$ 1.73 $\phi_{AX,NG} = 1.45$ **(b)** $\phi_{AX}$ 2.69 $\phi_{AX,NG} = 2.0$

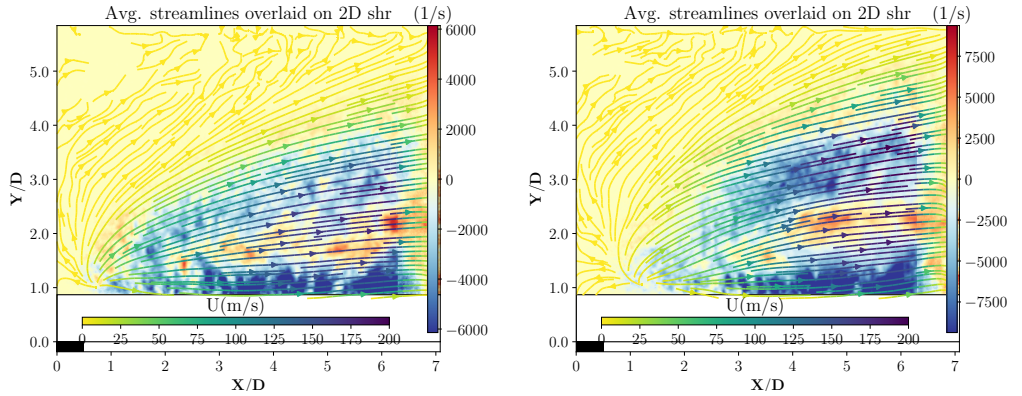


**(c)** $\phi_{AX}$ 1.73 $\phi_{AX,NG} = 1.45$ **(d)** $\phi_{AX}$ 2.69 $\phi_{AX,NG} = 2.0$

**Figure 8.23. :** Average rotation (top) and shear (bottom) of the velocity field generated by the jet flame at two different equivalence ratios with a fixed crossflow Mach number of 0.31

There are likely multiple stabilization fronts in this flame, each one dynamic because of inherent hydrodynamic and chemical instabilities within the highly strained shear layers. These chemical instabilities could result in the formation of spontaneous autoignition kernels

which have a higher reaction propagation speed than the average flame displacement speed because of thermal runaway, since the accompanying expansion of burnt gases behind the ignition kernel is not confined. In fact flame stabilization may be established by autoignition, flame propagation or a mixture of both for partially premixed combustion. Dominant variables that determine the stabilization of a transverse jet flame by autoignition include reactivity, inlet velocity and temperature [111]. In a recent publication by Minamoto et al. [81], it was shown via DNS that differential diffusion of hydrogen in both CO lean 1/0.06 and CO rich 1/1 $H_2-CO$ transverse jet flames forced the leeward stabilized flame to occur at the same position, with the bulk heat release located further downstream for the rich case. This result shows that despite conclusions based on global laminar flame speed, flame stabilization could be based on local flow reactivity. Most attached flames have been identified to be stabilized as partially premixed or premixed. In a recent paper by Schulz and Noiray [32], a 1-D 10 bar estimate of the role of temperature and mixture fraction on transverse jet flame regimes in a sequential burner revealed that with low ( 1200 K) vitiated crossflow temperatures, flames near the injector were stabilized via flame propagation evidenced by the fixed comparatively-low inlet velocity (equal to the laminar flame speed) able to sustain the flame. This result corroborated the 10 bar simulation in which a transient step reduction of the vitiated flow temperature uncoupled the transverse jet flame from its downstream leading edge position in an accompanying LES. At progressively higher vitiated flow temperatures, the 1-D analysis revealed the transverse jet flame capable of being sustained in different regimes. They showed that transverse jet flames with lower jet equivalence ratios sustained more likely by autoignition when displaced from their closest approach, and increasing the equivalence ratio relative to the stoichiometric condition the transverse jet flames stabilized more likely by flame propagation. Higher vitiated flow temperatures served to reduce the effect of jet equivalence ratio on the flame regime responsible for attachment, in general increasing the likelihood for autoignition to occur. The results also showed that increasing the flame speed by increasing the reactivity of the mixture increases the tendency to support flame-propagation stabilized flames. The results although applied to flames displaced from the injector in their paper, apply also to the current case.

In order to further explore the implications of the previous experimental and numerical results, a few hypotheses on the effects of the flowfield on the displacement velocity of the reacting transverse jet flame will be tested. Following the previous results, it could be hypothesized that the further out (radially) from the jet core the flame base is, the less exposed the leading points are to fluctuations in mixture fraction. This was the case in Yoo et al.'s 2009 paper [112] featuring DNS of a (less diluted) 65%/35% $H_2$–$N_2$ coflowing jet, where the region with stoichiometric mixture fraction was located further radially outward from the jet core, was hotter and featured lower velocities. The jet velocity was 347m/s and the coflow velocity was 4m/s. Here it was observed that the axial motion upstream and downstream of the leading point were similar in magnitude and timescale. The displacement speed was also similar to deflagration wave speeds where transport processes include both advection and diffusion. The magnitude of the displacement speed was also comparable to the fluctuation in normal velocities at the flame base so that the flame could propagate upstream. Here again $HO_2$ radicals were present upstream of OH radicals informing the reader about the stabilization mode of the partially premixed flame. These results indicated that the location of the leading points relative to the high velocity region can be inferred from the flame displacement velocity.

This result follows with the lower reactive fuel jets, which adhered to the bottom wall perhaps in an attempt to find hotter lower turbulent regions filled with radical pools sufficient for reaction propagation. In this case however, for the highest equivalence ratio, because the flame is comparatively less reactive, autoignition is the only the flame stabilization mode available leading to large fluctuations in leading point velocity.

To make claims about the flame stabilization mechanism in the DNS results, some analysis tools were designed. Chemical Explosive Mode Analysis (CEMA) can highlight limiting flame behavior such as local ignition, and extinction in reacting flow DNS. Using CEMA, the mixing layers upstream of the ignition point were identified as autoignitive in Lu et al.'s analysis of Yoo et al.'s 2009 data [112]. The timescales of the autoignitive mixture indicated partially premixed flame behavior at the leading point. Luo et al. [113] performed similar analysis of Yoo et al.'s 2011 data [109] identifying the abrupt transition from the autoignitive mixture to the diffusion flame via a partially premixed flame that made up the flame base

of the ethylene jet. The Takeno Flame Index (FI) was further used to identify the mode of flame propagation in Lu et al.[114]. Comparing the flame surface based on the FI to the ignition point based on CEMA, they noted that identifying the extents of the flame based on FI alone is insufficient.

Since these tools work on lifted jet flames, they can also be used to describe flame anchoring in transverse reacting jet flames. Lyra et al. [115] applied these analysis techniques to a reacting 70%/30% $H_2$–He jet whose 300 K core featured locations of high alignment of the fuel and oxidizer gradients, but at temperatures insufficient for ignition. The flame was stabilized as a diffusion flame in the wake of the jet and in the upstream shear layer based on OH. This was corroborated by CEMA timescale results which identified the upstream shear layer as a likely location for the jet ignition and identified the flame surface as the periphery of the jet tube within a few jet diameters of the injector orifice. In their analysis, the jet ignited both in the upstream shear layer and downstream in the near wake. Since the reacting transverse jet only ignites in the wake of the jet, the comparison is not exact, however a few inferences can be made. In the comparison of parameters of flame stabilization between inlet velocity, temperature and reactivity, reactivity often leads. In our results, I notice that the higher reactive flames travel towards the jet core and despite being more dilute do not feature the autoignitive advection cycle.

The purely leeward stabilized transverse jet flame as was observed in our results, was also observed in the DNS of a reacting 70%/30% $H_2$–$N_2$ transverse jet by Grout et al. [116]. The DNS conditions were matched closely in experimental efforts by Steinberg et al.[29] apart for example from the boundary layer thickness which differed 2mm to approximately 10mm between experiment and DNS. Steinberg et al.'s [29] experimental data did surprisingly feature upstream shear layer ignition leading Grout et al. [116] to hypothesize on the role of the boundary layer thickness on the stabilization point of the flame. We estimate that the temperature of the vitiated flow also had a role. It was also noted that the $HO_2$ radicals necessary for autoignition were observed in the windward side in the DNS and perhaps are available under some conditions for the windward stabilized flame. In a similar experiment by Solana-Perez et al. [33] the increase in hydrogen content of their atmospheric premixed $CH_4$–$H_2$ flame increased the tendency for the flame to attach in the windward side.

## 8.6 Benefits and Drawbacks of Interpreting Flame Behavior Using Velocity Fields From Chemiluminescence

In the last section, I demonstrated the potential results that could be obtained from analyzing properly textured chemiluminescence images to understand flame behavior. In addition to the general interpretation of the fluid kinematics, there are peculiar benefits associated with using a natural measurement of the flame for its analysis. For example, in contrast to seeded flowfields whose velocity topology may reveal effects of heat release on the flow, these measurements directly reveal the behavior of the flame without needing to infer from the effect on another flowfield with its own properties. The seeding of flowfields also suffers in highly strained or vortex processed regions where poor seeding density restricts the accuracy of the results. Because the results are generated from a dense technique, extracting information from spatial derivatives surpasses the results from correlation algorithms, which quite often are not sufficiently resolved, not meeting the 1/4 of the smallest scale resolution requirements. Large displacements are naturally handled using the multiresolution analysis built into the wavelet formalism.

On the other hand, the path averaged nature of chemiluminescence measurements contributes the the poor texture of the images. The long duration exposure may also result in image blurring further reducing the sharpness of the image. Near the edges of the image, the signal extension necessary for accurate results may be expensive to compute. Furthermore, the aliasing problem is particularly problematic for displacements near the edges. Evaluation of individual vectors to meet criteria is much harder with this technique. Significant improvements would have been afforded by using time resolved PLIF measurements for this analysis. Finally the lack of vectors in locations without the reactive scalar presents the data as similar to a poorly seeded flowfield. It prevents the interpretation using the rich physics of point statistics.

# 9. SUMMARY

In summary, I have shown some prominent design features and many detailed analyses of combustion in a novel high subsonic Mach number combustor. The design of this combustor was optimized using parametric sweeps from heat transfer and thermal stress analyses. The combustor handled high heat fluxes using active regenerative cooling and film cooling to reduce the thermal stresses in the material. The test section of the combustor was designed to handle high heat fluxes during the injection of additional fuel at high subsonic Mach number.

I also successfully demonstrated the continous operation of the previously mentioned high subsonic Mach number distributed combustor operating the secondary stage with high hydrogen enrichement of the premixed natural gas fuel. The first time the peak hydrogen enrichment of natural gas has been shown in literature at the peak Mach number achieved. The results will be submitted to the AIAA journal of propulsion and power. OH-PLIF of the attached and detached flames has been demonstrated as well as high repetition rate $OH^*$ chemiluminescence. The OH-PLIF of the attached flame revealed that the flame attaches on the leeward side exclusively at the crossflow and jet Mach numbers up to 0.68 for this distributed combustor configuration. The decrease in flow timescales with increase in crossflow Mach number was quantified by increasing the hydrogen content of the ffuel jet required to reestablish an attached jet flame. Jet flapping was observed in the near field of the jet flame which was attached in the leeward side exclusively. For the unattached jet flame, the OH PLIF revealed broken flamelets that occurred downstream of jet shear layer coherent structures. The flame was quite different from the attached flame, which required the bottom wall as an attachment point. Despite these differences the NOx, CO and UHC showed no change between attached and unattached jet flames.

From the $OH^*$ chemiluminescence results it was shown that the amount of hydrogen required to attach the flames from low to high subsonic crossflow Mach numbers increased drastically from about 60% by mole at the maximum for the low crossflow Mach number cases to about 80% at the maximum for the higher crossflow Mach number cases bearing in mind the infinite asymptote of mass required to approach unity mole fraction in a fuel

mixture. The shapes of the attached flames in these measurements were similar at the same relative reactivity, irrespective of the crossflow Mach number. The progression of the flame stabilization point into the high strain rate field near the jet injector provided results consistent with leading point theory of a high Lewis number instability in the flame. The instability was shown to propagate both towards the injector face as well as into the jet core potentially via the upright vortices in the wake of the jet. The amount of hydrogen required for attachment decreased first and then increased at the low crossflow Mach number while it decreased in the high crossflow Mach number. The distance of the attached jet flames from the injector did decrease with increased natural gas content in the average images. For the unattached jet flames, it was shown that at the 0.68 crossflow Mach number, only the lowest natural gas equivalence ratio case could establish an attached flame. The corresponding detached flame was out of the view at higher natural gas equivalence ratios at this crossflow Mach number. The flame brush shapes responded to the addition of natural gas by receding from the injector face. In addition, the delayed heat release caused a more compact flame that, together with the larger amount of fuel, resulted a vertical extension of the flame into the downstream shear layer.

The design of gas turbine combustors to benefit from lower NOx emissions at these high subsonic crossflow Mach numbers could also benefit from hydrogen enrichment. It has thus been shown that the dynamics of flame attachment can be made robust by addition of hydrogen, and that an attached flame can be kept attached at different natural gas compositions. If possible the unattached flame may be useful to gas turbine designers if the residence time of the flame can be kept low between the flame and the inlet guide vane. If the behavior scales with heat release in the axial stage, the attachment procedure may follow the hydrogen sweep progression with no detriment in NOx, CO or UHC emissions during and after this transient.

Inferences about the flame displacement velocities were made from the high repetition rate $OH^*$ chemiluminescence images. They were quantified using a wavelet optical flow. The wavelet used in this analysis is the coiflet with 5 vanishing moments. The wavelet optical flow algorithm as implemented was borrowed as is from HAL INRIA. The build was tested against a well known correlation algorithm by DAVIS used with particle displacement images.

It revealed the benefits of the higher spatial resolution on computed spatial gradients. The velocity gradients computed from the correlation algorithms suffered especially near the edges of the images, where the numerical derivatives are usually lower order. In addition, DMD spatial modes were reconstructed and compared against a lagrangian particle tracking at a fixed location in the image. The DMD reconstructed velocities were within the order of magnitude of the result from the wavelet optical flow measurement. From the results, it was clear that direct imaging of the flames allowed a direct interpretation of the results over the usual process which extracts flame information from the velocimetry of the underlying fluid motion. The results provided evidence that flame attachment at the wall is due to the movement of the stoichiometric surface outward for less reactive, higher equivalence ratio flames. Inferences in concert with these result appear to corroborate the results from the chemiluminescence measurements for example: at the stoichiometric surface, the prescence of high temperature gases and a constant source of radicals from the jet mixing with the crossflow makes it suitable for flame attachment. In addition to the flame adhering to the bottom wall, the delayed heat release of the flame due to the lower reactivity caused the flame to be more compact and heat release more localized. This resulted in the leading point dynamics being highlighted as the flame occassionally propagating towards the injector face. These behaviors are in contrast to the high reactivity low equivalence ratio flames which tended to burn near the downstream shear layer following the stoichiometric surface that was in those conditions closer to the jet core. It led to the flame pulling away from the wall with a thinner longer flame - signified by vertical displacement of the flame away from the wall. Quantifying uncertainty in the measurements showed the detriment of the poorly textured images obtained from the chemiluminescence mesurement. Future work should benefit from higher repetition rate measurements of OH-PLIF which provides better spatial gradients and a better textured image.

# REFERENCES


[1] L. B. Davis, "Dry low nox combustion systems for ge heavy-duty gas turbines," in *ASME 1996 International Gas Turbine and Aeroengine Congress and Exhibition*, vol. Volume 3: Coal, Biomass and Alternative Fuels; Combustion and Fuels; Oil and Gas Applications; Cycle Innovations, 1996. DOI: 10.1115/96-GT-027. [Online]. Available: https://doi.org/10.1115/96-GT-027.

[2] Y. Huang and V. Yang, "Dynamics and stability of lean-premixed swirl-stabilized combustion," *Progress in Energy and Combustion Science*, vol. 35, no. 4, pp. 293–364, 2009, ISSN: 0360-1285. DOI: https://doi.org/10.1016/j.pecs.2009.01.002. [Online]. Available: http://www.sciencedirect.com/science/article/pii/S0360128509000094.

[3] J. Marra, "Advanced hydrogen turbine development," Sep. 2015. DOI: 10.2172/1261639.

[4] T. Bradley and J. Marra, *Advanced hydrogen turbine development update*, Jun. 2012. PMID: ASMETurboExpo2012:TurbineTechnicalConferenceandExposition. [Online]. Available: https://doi.org/10.1115/GT2012-68169.

[5] C. A. Fugger, R. M. Gejji, J. E. Portillo, Y. Yu, R. P. Lucht, and W. E. Anderson, "A model combustor for studying a reacting jet in an oscillating crossflow," *Review of Scientific Instruments*, vol. 88, no. 6, p. 065 112, 2017, ISSN: 0034-6748.

[6] N. S. Rodrigues, O. Busari, W. C. B. Senior, C. T. Mcdonald, Y. Chen, A. J. North, W. R. Laster, S. E. Meyer, and R. P. Lucht, "Nox reduction in an axially staged gas turbine model combustor through increase in the combustor exit mach number," *Combustion and Flame*, vol. 212, pp. 282–294, 2020, ISSN: 0010-2180.

[7] W. G. Lamont, M. Roa, S. E. Meyer, and R. P. Lucht, "Emission measurements and ch chemiluminescence of a staged combustion rig for stationary gas turbine applications," *Journal of engineering for gas turbines and power*, vol. 134, no. 8, 2012, ISSN: 0742-4795.

[8] P. P. Panda, R. P. Lucht, and W. R. Laster, "Effect of the nature of vitiated crossflow on the flow-field of a transverse reacting jet," *Experiments in Fluids*, vol. 58, no. 2, p. 9, 2017, ISSN: 1432-1114. [Online]. Available: https://doi.org/10.1007/s00348-016-2288-4.

[9] N. Rodrigues, C. McDonald, O. Busari, A. Satija, A. North, W. Laster, S. Meyer, and R. Lucht, "An optically accessible secondary combustion zone for the transverse injection of reacting jets into a high-speed, vitiated crossflow within a staged, gas turbine model combustor.," accepted, 2020.

[10] J. Macomber, "A bibliography of transient effects in the resonant elastic response of matter to an intense light pulse," *IEEE Journal of Quantum Electronics*, vol. 4, no. 1, pp. 1–10, 1968, ISSN: 1558-1713.

[11] R. P. Lucht, D. W. Sweeney, and N. M. Laurendeau, "Balanced cross-rate model for saturated molecular fluorescence in flames using a nanosecond pulse length laser," *Appl. Opt.*, vol. 19, no. 19, pp. 3295–3300, 1980. [Online]. Available: http://ao.osa.org/abstract.cfm?URI=ao-19-19-3295.

[12] G. Berkooz, P. Holmes, and J. L. Lumley, "The proper orthogonal decomposition in the analysis of turbulent flows," *Annu. Rev. Fluid Mech.*, vol. 25, no. 1, pp. 539–575, Jan. 1993, ISSN: 0066-4189. DOI: 10.1146/annurev.fl.25.010193.002543. [Online]. Available: https://doi.org/10.1146/annurev.fl.25.010193.002543.

[13] P. J. Schmid, "Dynamic mode decomposition of numerical and experimental data," *Journal of Fluid Mechanics*, vol. 656, pp. 5–28, 2010, ISSN: 0022-1120. DOI: 10.1017/s0022112010001217. [Online]. Available: https://www.cambridge.org/core/article/dynamic-mode-decomposition-of-numerical-and-experimental-data/AA4C763B525515AD4521A6CC5E10DBD4.

[14] R. Zhang, I. Boxx, W. Meier, and C. D. Slabaugh, "Coupled interactions of a helical precessing vortex core and the central recirculation bubble in a swirl flame at elevated power density," *Combustion and Flame*, vol. 202, pp. 119–131, 2019, ISSN: 0010-2180. [Online]. Available: http://www.sciencedirect.com/science/article/pii/S0010218019300021.

[15] M. Sieber, C. O. Paschereit, and K. Oberleithner, "Spectral proper orthogonal decomposition," *Journal of Fluid Mechanics*, vol. 792, pp. 798–828, 2016, ISSN: 0022-1120. DOI: 10.1017/jfm.2016.103. [Online]. Available: https://www.cambridge.org/core/article/spectral-proper-orthogonal-decomposition/DCD8A6EDEFD56F5A9715DBAD38BD461A.

[16] M. Stöhr, K. Oberleithner, M. Sieber, Z. Yin, and W. Meier, "Experimental study of transient mechanisms of bistable flame shape transitions in a swirl combustor," *Journal of engineering for gas turbines and power*, vol. 140, no. 1, 2018, ISSN: 0742-4795.

[17] R. Z. Zhang, "Analysis Techniques for Characterizing High Power Turbulent Swirl Flames," Aug. 2019. DOI: 10.25394/PGS.8159288.v1. [Online]. Available:

.

[18] B. E. Schmidt, C. A. Towery, P. Hamlington, and J. A. Sutton, "Evaluation of wavelet-based optical flow velocimetry from oh scalar fields in reacting turbulent flows," in, ser. AIAA SciTech Forum 0, American Institute of Aeronautics and Astronautics, Jan. 2019. DOI: 10.2514/6.2019-0270. [Online]. Available: https://doi.org/10.2514/6.2019-0270.

[19] B. E. Schmidt, W. E. Page, and J. A. Sutton, "Seedless velocimetry in a turbulent jet using schlieren imaging and a wavelet-based optical flow method," in, ser. AIAA SciTech Forum 0, American Institute of Aeronautics and Astronautics, Jan. 2020. DOI: 10.2514/6.2020-2207. [Online]. Available: https://doi.org/10.2514/6.2020-2207.

[20] R. M. Kelso, T. T. Lim, and A. E. Perry, "An experimental study of round jets in cross-flow," *Journal of Fluid Mechanics*, vol. 306, pp. 111–144, 1996, ISSN: 0022-1120. DOI: 10.1017/s0022112096001255. [Online]. Available: https://www.cambridge.org/core/article/an-experimental-study-of-round-jets-in-crossflow/4301861CE913C315D60B390A77053977.

[21] T. F. Fric and A. Roshko, "Vortical structure in the wake of a transverse jet," *Journal of Fluid Mechanics*, vol. 279, pp. 1–47, 1994, ISSN: 0022-1120. DOI: 10.1017/s0022112094003800. [Online]. Available: https://www.cambridge.org/core/article/vortical-structure-in-the-wake-of-a-transverse-jet/79CFDA2A9200C76E5B16E2B2C4C2B515.

[22] F. Schlegel, W. Daehyun, Y. M. Marzouk, and A. F. Ghoniem, "Contributions of the wall boundary layer to the formation of the counter-rotating vortex pair in transverse jets," *Journal of Fluid Mechanics*, vol. 676, pp. 461–490, 2011, ISSN: 0022-1120. DOI: 10.1017/jfm.2011.59. [Online]. Available: https://www.cambridge.org/core/article/contributions-of-the-wall-boundary-layer-to-the-formation-of-the-counterrotating-vortex-pair-in-transverse-jets/CFB372F97339DE7888FC9E8F2E936377.

[23] L. Zhang and V. Yang, "Flow dynamics and mixing of a transverse jet in crossflow–part i: Steady crossflow," *J. Eng. Gas Turbines Power*, vol. 139, no. 8, Mar. 2017, ISSN: 0742-4795. [Online]. Available: https://doi.org/10.1115/1.4035808.

[24] C. Cárdenas, J. A. Denev, R. Suntz, and H. Bockhorn, "Study of parameters and entrainment of a jet in cross-flow arrangement with transition at two low reynolds numbers," *Experiments in Fluids*, vol. 53, no. 4, pp. 965–987, 2012, ISSN: 1432-1114. [Online]. Available: https://doi.org/10.1007/s00348-012-1333-1.

[25] S. H. A. N. JERRY W. and P. A. U. L. E. DIMOTAKIS, "Reynolds-number effects and anisotropy in transverse-jet mixing," *Journal of Fluid Mechanics*, vol. 566, pp. 47–96, 2006, ISSN: 0022-1120. DOI: 10.1017/s0022112006001224. [Online]. Available: https://www.cambridge.org/core/article/reynoldsnumber-effects-and-anisotropy-in-transversejet-mixing/EA7A625F2ECF8CADE4DC1285EAEA9387.

[26] S. Muppidi and K. Mahesh, "Direct numerical simulation of passive scalar transport in transverse jets," *Journal of Fluid Mechanics*, vol. 598, pp. 335–360, 2008, ISSN: 0022-1120. DOI: 10.1017/s0022112007000055. [Online]. Available: https://www.cambridge.org/core/article/direct-numerical-simulation-of-passive-scalar-transport-in-transverse-jets/252BF2CEC3B7EBBDAA98B8C88F095039.

[27] D. J. Forliti, D. V. Salazar, and A. J. Bishop, "Physics-based scaling laws for confined and unconfined transverse jets," *Experiments in Fluids*, vol. 56, no. 2, p. 36, 2015, ISSN: 1432-1114. [Online]. Available: https://doi.org/10.1007/s00348-014-1888-0.

[28] P. P. Panda, O. Busari, M. Roa, and R. P. Lucht, "Flame stabilization mechanism in reacting jets in swirling vitiated crossflow," *Combustion and Flame*, vol. 207, pp. 302–313, 2019, ISSN: 0010-2180. [Online]. Available: http://www.sciencedirect.com/science/article/pii/S0010218019302640.

[29] A. M. Steinberg, R. Sadanandan, C. Dem, P. Kutne, and W. Meier, "Structure and stabilization of hydrogen jet flames in cross-flows," *Proceedings of the Combustion Institute*, vol. 34, no. 1, pp. 1499–1507, 2013, ISSN: 1540-7489. [Online]. Available: http://www.sciencedirect.com/science/article/pii/S1540748912001344.

[30] M. D. Sirignano, V. Nair, D. Sunkara, B. L. Emerson, J. Seitzman, and T. C. Lieuwen, *Impact of flame lifting on nitrogen oxide emissions from premixed reacting jets in a vitiated crossflow*, Jun. 2019. PMID: ASMETurboExpo2019:TurbomachineryTechnicalConferenceandExposition. [Online]. Available: https://doi.org/10.1115/GT2019-90952.

[31] D. J. Micka and J. F. Driscoll, "Stratified jet flames in a heated (1390k) air cross-flow with autoignition," *Combustion and Flame*, vol. 159, no. 3, pp. 1205–1214, 2012, ISSN: 0010-2180. [Online]. Available: http://www.sciencedirect.com/science/article/pii/S001021801100318X.

[32] O. Schulz and N. Noiray, "Combustion regimes in sequential combustors: Flame propagation and autoignition at elevated temperature and pressure," *Combustion and Flame*, vol. 205, pp. 253–268, 2019, ISSN: 0010-2180. [Online]. Available: http://www.sciencedirect.com/science/article/pii/S0010218019301087.

[33] R. Solana-Pérez, L. Miniero, S. Shcherbanev, M. Bothien, and N. Noiray, *Morphology and dynamics of a premixed hydrogen-methane-air jet flame in hot vitiated turbulent crossflow*, Sep. 2020. PMID: ASMETurboExpo2020:TurbomachineryTechnicalConferenceandExposition. [Online]. Available: https://doi.org/10.1115/GT2020-16282.

[34] S. Lyra, B. Wilde, H. Kolla, J. M. Seitzman, T. C. Lieuwen, and J. H. Chen, "Structure of hydrogen-rich transverse jets in a vitiated turbulent flow," *Combustion and Flame*, vol. 162, no. 4, pp. 1234–1248, 2015, ISSN: 0010-2180. DOI: https://doi.org/10.1016/j.combustflame.2014.10.014. [Online]. Available: http://www.sciencedirect.com/science/article/pii/S0010218014003356.

[35] S. Megerian, J. Davitian, L. S. De B. Alves, and A. R. Karagozian, "Transverse-jet shear-layer instabilities. part 1. experimental studies," *Journal of Fluid Mechanics*, vol. 593, pp. 93–129, 2007, ISSN: 0022-1120. DOI: 10.1017/s0022112007008385. [Online]. Available: https://www.cambridge.org/core/article/transversejet-shearlayer-instabilities-part-1-experimental-studies/E1B78073918630A6BF25E6DCC8FD0DED.

[36] T. Shoji, E. W. Harris, A. Besnard, S. G. Schein, and A. R. Karagozian, "On the origins of transverse jet shear layer instability transition," *Journal of Fluid Mechanics*, vol. 890, no. A7, A7, 2020, ISSN: 0022-1120. DOI: 10.1017/jfm.2020.127. [Online]. Available: https://www.cambridge.org/core/article/on-the-origins-of-transverse-jet-shear-layer-instability-transition/FD9F28D1D2C69D58609C58468AA75ACC.

[37] M. D. Sirignano, V. Nair, B. Emerson, J. Seitzman, and T. C. Lieuwen, "Nitrogen oxide emissions from rich premixed reacting jets in a vitiated crossflow," *Proceedings of the Combustion Institute*, vol. 37, no. 4, pp. 5393–5400, 2019, ISSN: 1540-7489. [Online]. Available: http://www.sciencedirect.com/science/article/pii/S1540748918300890.

[38] H. Kolla, R. W. Grout, A. Gruber, and J. H. Chen, "Mechanisms of flame stabilization and blowout in a reacting turbulent hydrogen jet in cross-flow," *Combustion and Flame*, vol. 159, no. 8, pp. 2755–2766, 2012, ISSN: 0010-2180. [Online]. Available: http://www.sciencedirect.com/science/article/pii/S0010218012000260.

[39] M. Kolb, D. Ahrens, C. Hirsch, and T. Sattelmayer, "A model for predicting the lift-off height of premixed jets in vitiated cross flow," *Journal of engineering for gas turbines and power*, vol. 138, no. 8, p. 081 901, 2016, ISSN: 0742-4795.

[40] J. A. Wagner, S. W. Grib, M. W. Renfro, and B. M. Cetegen, "Flowfield measurements and flame stabilization of a premixed reacting jet in vitiated crossflow," *Combustion and Flame*, vol. 162, no. 10, pp. 3711–3727, 2015, ISSN: 0010-2180. [Online]. Available: http://www.sciencedirect.com/science/article/pii/S0010218015002114.

[41] M. G. Mungal and E. F. Hasselbrink, "Jets in crossflow – effects of heat release," in *Manipulation and Control of Jets in Crossflow*, A. R. Karagozian, L. Cortelezzi, and A. Soldati, Eds., Vienna: Springer Vienna, 2003, pp. 173–182. [Online]. Available:
.

[42] A. N. Kolmogorov, V. Levin, J. C. R. Hunt, O. M. Phillips, and D. Williams, "The local structure of turbulence in incompressible viscous fluid for very large reynolds numbers," *Proceedings of the Royal Society of London. Series A: Mathematical and Physical Sciences*, vol. 434, no. 1890, pp. 9–13, Jul. 1991. DOI: 10.1098/rspa.1991.0075. [Online]. Available: https://doi.org/10.1098/rspa.1991.0075.

[43] J. O. Hinze, *Turbulence: an introduction to its mechanism and theory.* New York: McGraw-Hill, 1959.

[44] S. Chandrasekhar, "The fluctuations of density in isotropic turbulence," *Proceedings of the Royal Society of London. Series A, Mathematical and Physical Sciences*, vol. 210, no. 1100, pp. 18–25, 1951, ISSN: 00804630. [Online]. Available: http://www.jstor.org.ezproxy.lib.purdue.edu/stable/98946.

[45] G. A. Richards, M. M. McMillian, R. S. Gemmen, W. A. Rogers, and S. R. Cully, "Issues for low-emission, fuel-flexible power systems," *Progress in Energy and Combustion Science*, vol. 27, no. 2, pp. 141–169, 2001, ISSN: 0360-1285. [Online]. Available: http://www.sciencedirect.com/science/article/pii/S0360128500000198.

[46] U. EPA, "Health criteria (final report, 2016)," in *Integrated Science Assessment (ISA) For Oxides of Nitrogen*, Washington, DC, 2016, pp. 1–1148. [Online]. Available:
.

[47] N. Zarzalis, T. Ripplinger, S. Hohmann, M. Hettel, K. Merkle, W. Leuckel, G. Klose, R. Meier, R. Koch, S. Wittig, M. Carl, T. Behrendt, C. Hassa, U. Meier, R. Lückerath, and W. Stricker, "Low-nox combustor development pursued within the scope of the engine 3e german national research program in a cooperative effort among engine manufacturer mtu, university of karlsruhe and dlr german aerospace research center," *Aerospace Science and Technology*, vol. 6, no. 7, pp. 531–544, 2002, ISSN: 1270-9638. [Online]. Available: http://www.sciencedirect.com/science/article/pii/S1270963802011793.

[48] C. E. Baukal Jr., *The John Zink Hamworthy Combustion Hand book*. Baton Rouge: Taylor & Francis Group, 2013.

[49] E. C. Zabetta, M. Hupa, and K. Saviharju, "Reducing nox emissions using fuel staging, air staging, and selective noncatalytic reduction in synergy," *Ind. Eng. Chem. Res.*, vol. 44, no. 13, pp. 4552–4561, Jun. 2005, ISSN: 0888-5885. DOI: 10.1021/ie050051a. [Online]. Available: https://doi.org/10.1021/ie050051a.

[50] J. M. Beér, "Minimizing nox emissions from stationary combustion; reaction engineering methodology," *Chemical Engineering Science*, vol. 49, no. 24, Part A, pp. 4067–4083, 1994, ISSN: 0009-2509. [Online]. Available: http://www.sciencedirect.com/science/article/pii/S0009250905800065.

[51] S. Hayashi and H. Yamada, "Nox emissions in combustion of lean premixed mixtures injected into hot burned gas," *Proceedings of the Combustion Institute*, vol. 28, no. 2, pp. 2443–2449, 2000, ISSN: 1540-7489. [Online]. Available: http://www.sciencedirect.com/science/article/pii/S008207840080658X.

[52] K. P. Geigle, W. Meier, M. Aigner, C. Willert, M. Jarius, P. Schmitt, and B. Schuermans, "Phase-resolved laser diagnostic measurements of a downscaled, fuel-staged gas turbine combustor at elevated pressure and comparison to les predictions," *Journal of engineering for gas turbines and power*, vol. 129, no. 3, pp. 680–687, 2007, ISSN: 0742-4795.

[53] P. Therkelsen, T. Werts, V. McDonell, and S. Samuelsen, "Analysis of nox formation in a hydrogen-fueled gas turbine engine," *J. Eng. Gas Turbines Power*, vol. 131, no. 3, Feb. 2009, ISSN: 0742-4795. [Online]. Available: https://doi.org/10.1115/1.3028232.

[54] O. O. Busari, N. S. Rodrigues, C. T. McDonald, A. North, W. R. Laster, A. Satija, and R. P. Lucht, "Characterizing leeward stabilized transverse jet flames in vitiated crossflows at high subsonic mach numbers," *AIAA Journal*, AIAA Journal, 2020, submitted.

[55] C. K. Law, "Dynamics of stretched flames," *Symposium (International) on Combustion*, vol. 22, no. 1, pp. 1381–1402, 1989, ISSN: 0082-0784. [Online]. Available: http://www.sciencedirect.com/science/article/pii/S0082078489801493.

[56] A. N. Lipatnikov and J. Chomiak, "Molecular transport effects on turbulent flame propagation and structure," *Progress in Energy and Combustion Science*, vol. 31, no. 1, pp. 1–73, 2005, ISSN: 0360-1285. [Online]. Available: http://www.sciencedirect.com/science/article/pii/S0360128504000486.

[57] E. R. Hawkes and J. H. Chen, "Direct numerical simulation of hydrogen-enriched lean premixed methane-air flames," *Combustion and Flame*, vol. 138, no. 3, pp. 242–258, 2004, ISSN: 0010-2180. [Online]. Available: http://www.sciencedirect.com/science/article/pii/S0010218004001154.

[58] T. Kathrotia, *Reaction kinetics modeling of OH*, CH*, and $C_2$* chemiluminescence*, 2011.

[59] H. N. Najm, O. M. Knio, P. H. Paul, and P. S. Wyckoff, "A study of flame observables in premixed methane - air flames," *Combustion Science and Technology*, vol. 140, no. 1-6, pp. 369–403, 1998, ISSN: 0010-2202.

[60] S. Sardeshmukh, M. Bedard, and W. Anderson, "The use of OH* and CH* as heat release markers in combustion dynamics," *International Journal of Spray and Combustion Dynamics*, vol. 9, no. 4, pp. 409–423, Jul. 2017, ISSN: 1756-8277. DOI: 10.1177/1756827717718483. [Online]. Available: https://doi.org/10.1177/1756827717718483.

[61] M. J. Black and A. Rangarajan, "On the unification of line processes, outlier rejection, and robust statistics with applications in early vision," *International Journal of Computer Vision*, vol. 19, no. 1, pp. 57–91, 1996, ISSN: 1573-1405. [Online]. Available: https://doi.org/10.1007/BF00131148.

[62] B. K. Horn and B. G. Schunck, "Determining optical flow," *Artificial Intelligence*, vol. 17, no. 1, pp. 185–203, 1981, ISSN: 0004-3702. DOI: https://doi.org/10.1016/0004-3702(81)90024-2. [Online]. Available: http://www.sciencedirect.com/science/article/pii/0004370281900242.

[63] D. Geman and G. Reynolds, "Constrained restoration and the recovery of discontinuities," *IEEE Transactions on Pattern Analysis and Machine Intelligence*, vol. 14, no. 3, pp. 367–383, 1992, ISSN: 1939-3539.

[64] S. Geman and D. McClure, "Statistical methods for tomographic image reconstruction," *Bulletin of the International Statistical Institute*, vol. 52, no. 4, pp. 5–21, 1987, ISSN: 0373-0441.

[65] Y. G. Leclerc, "Constructing simple stable descriptions for image partitioning," *International Journal of Computer Vision*, vol. 3, no. 1, pp. 73–102, 1989, ISSN: 1573-1405. [Online]. Available: https://doi.org/10.1007/BF00054839.

[66] E. Memin and P. Perez, "Dense estimation and object-based segmentation of the optical flow with robust techniques," *IEEE Transactions on Image Processing*, vol. 7, no. 5, pp. 703–719, 1998. DOI: 10.1109/83.668027.

[67] D. Sun, S. Roth, and M. J. Black, "A quantitative analysis of current practices in optical flow estimation and the principles behind them," *International Journal of Computer Vision*, vol. 106, no. 2, pp. 115–137, 2014, ISSN: 1573-1405. [Online]. Available: https://doi.org/10.1007/s11263-013-0644-x.

[68] P. Dérian, *Wavelets and fluid motion estimation*, 2012.

[69] A. Haar, "Zur theorie der orthogonalen funktionensysteme," *Mathematische Annalen*, vol. 69, no. 3, pp. 331–371, 1910, ISSN: 1432-1807. [Online]. Available: https://doi.org/10.1007/BF01456326.

[70] I. Daubechies, *Ten Lectures on Wavelets*. Society for Industrial and Applied Mathematics, Jan. 1992, p. 369. DOI: 10.1137/1.9781611970104. [Online]. Available: https://doi.org/10.1137/1.9781611970104.

[71] M. Stéphane, "Chapter 1 - sparse representations," in *A Wavelet Tour of Signal Processing (Third Edition)*, M. Stéphane, Ed., Third Edition, Boston: Academic Press, 2009, pp. 1–31, ISBN: 978-0-12-374370-1. DOI: https://doi.org/10.1016/B978-0-12-374370-1.00005-7. [Online]. Available: https://www.sciencedirect.com/science/article/pii/B9780123743701000057.

[72] G. R. Lee, R. Gommers, F. Waselewski, K. Wohlfahrt, and A. O'Leary, "Pywavelets: A python package for wavelet analysis," *Journal of Open Source Software*, vol. 4, no. 36, p. 1237, 2019. DOI: 10.21105/joss.01237. [Online]. Available: https://doi.org/10.21105/joss.01237.

[73] W. Anderson and S. Meyer, "Propulsion test facilities at purdue university," in, ser. Joint Propulsion Conferences 0, American Institute of Aeronautics and Astronautics, Jul. 2002. DOI: 10.2514/6.2002-4280. [Online]. Available: https://doi.org/10.2514/6.2002-4280.

[74] T. Pourpoint, S. Meyer, and C. Ehresman, "Propulsion test facilities at the purdue university maurice j. zucrow laboratories," in, ser. Joint Propulsion Conferences 0, American Institute of Aeronautics and Astronautics, Jul. 2007. DOI: 10.2514/6.2007-5333. [Online]. Available: https://doi.org/10.2514/6.2007-5333.

[75] S. E. Meyer, S. D. Heister, C. Slabaugh, R. P. Lucht, A. Pratt, R. M. Gejji, M. Bedard, and A. Lemcherfi, "Design and development of the high pressure combustion laboratory at purdue university," in, ser. AIAA Propulsion and Energy Forum 0, American Institute of Aeronautics and Astronautics, Jul. 2017. DOI: 10.2514/6.2017-4965. [Online]. Available: https://doi.org/10.2514/6.2017-4965.

[76] N. S. Rodrigues, O. Busari, W. C. B. Senior, C. T. McDonald, A. J. North, Y. Chen, W. R. Laster, S. E. Meyer, and R. P. Lucht, "The development and performance of a perforated plate burner to produce vitiated flow with negligible swirl under engine-relevant gas turbine conditions," *Review of Scientific Instruments*, vol. 90, no. 7, p. 075 107, 2019. DOI: 10.1063/1.5100180. eprint: https://doi.org/10.1063/1.5100180. [Online]. Available: https://doi.org/10.1063/1.5100180.

[77] E. Witoszynski, "ber strahlerweiterung und strahlablenkung," in *Vorträge aus dem Gebiete der Hydro- und Aerodynamik (Innsbruck 1922)*, T. v. Kármán and T. Levi-Civita, Eds., Berlin, Heidelberg: Springer Berlin Heidelberg, 1924, pp. 248–251. [Online]. Available: .

[78] P. G. ( G. Hill, *Mechanics and thermodynamics of propulsion*, eng, Second edition. 1992, ISBN: 0201146592.

[79] E. W. Lemmon, I. H. Bell, M. L. Huber, and M. O. McLinden, *Nist standard reference database 23: Reference fluid thermodynamic and transport properties-refprop, version 10.0, national institute of standards and technology*, 2018. DOI: https://doi.org/10.18434/T4/1502528. [Online]. Available: https://www.nist.gov/srd/refprop.

[80] T. A. Davidson and U. States., *A simple and accurate method for calculating viscosity of gaseous mixtures*, ser. Report of investigations / Bureau of Mines ;9456 12 p. [Washington, DC]: U.S. Dept. of the Interior, Bureau of Mines, 1993, 12 p. [Online]. Available: http://hdl.handle.net/2027/osu.32435025835810%20(no.9456%201993).

[81] Y. Minamoto, H. Kolla, R. W. Grout, A. Gruber, and J. H. Chen, "Effect of fuel composition and differential diffusion on flame stabilization in reacting syngas jets in turbulent cross-flow," *Combustion and Flame*, vol. 162, no. 10, pp. 3569–3579, 2015, ISSN: 0010-2180. [Online]. Available: http://www.sciencedirect.com/science/article/pii/S0010218015001947.

[82] O. Schulz, E. Piccoli, A. Felden, G. Staffelbach, and N. Noiray, "Autoignition-cascade in the windward mixing layer of a premixed jet in hot vitiated crossflow," *Combustion and Flame*, vol. 201, pp. 215–233, 2019, ISSN: 0010-2180. DOI: https://doi.org/10.1016/j.combustflame.2018.11.012. [Online]. Available: http://www.sciencedirect.com/science/article/pii/S0010218018304875.

[83] M. Gamba and M. G. Mungal, "Ignition, flame structure and near-wall burning in transverse hydrogen jets in supersonic crossflow," *Journal of Fluid Mechanics*, vol. 780, pp. 226–273, 2015, ISSN: 0022-1120. DOI: 10.1017/jfm.2015.454. [Online]. Available: https://www.cambridge.org/core/article/ignition-flame-structure-and-nearwall-burning-in-transverse-hydrogen-jets-in-supersonic-crossflow/57CED283345524387010C3C4EBB84C1A.

[84] T. Kathrotia, U. Riedel, A. Seipel, K. Moshammer, and A. Brockhinke, "Experimental and numerical study of chemiluminescent species in low-pressure flames," *Applied Physics B*, vol. 107, no. 3, pp. 571–584, 2012, ISSN: 1432-0649. [Online]. Available: https://doi.org/10.1007/s00340-012-5002-0.

[85] K. H. Becker, D. Haaks, and T. Tatarczyk, "The natural lifetime of (OH $^2\Sigma^+$, $\nu = 0$, N = 2, J = 32) and its quenching by atomic hydrogen," *Chemical Physics Letters*, vol. 25, no. 4, pp. 564–567, 1974, ISSN: 0009-2614. [Online]. Available: http://www.sciencedirect.com/science/article/pii/0009261474853686.

[86] P. W. Fairchild, G. P. Smith, and D. R. Crosley, "Collisional quenching of $A^2\Sigma^+$ OH at elevated temperatures," *J. Chem. Phys.*, vol. 79, no. 4, pp. 1795–1807, Aug. 1983, ISSN: 0021-9606. DOI: 10.1063/1.446025. [Online]. Available: https://doi.org/10.1063/1.446025.

[87] B. L. Hemming, D. R. Crosley, J. E. Harrington, and V. Sick, "Collisional quenching of high rotational levels in $A^2\Sigma^+$ OH," *J. Chem. Phys.*, vol. 115, no. 7, pp. 3099–3104, Aug. 2001, ISSN: 0021-9606. DOI: 10.1063/1.1386783. [Online]. Available: https://doi.org/10.1063/1.1386783.

[88] M. Tamura, P. A. Berg, J. E. Harrington, J. Luque, J. B. Jeffries, G. P. Smith, and D. R. Crosley, "Collisional quenching of ch(a), oh(a), and no(a) in low pressure hydrocarbon flames," *Combustion and Flame*, vol. 114, no. 3, pp. 502–514, 1998, ISSN: 0010-2180. [Online]. Available: http://www.sciencedirect.com/science/article/pii/S0010218097003246.

[89] P. Dérian, C. F. Mauzey, and S. D. Mayor, "Wavelet-based optical flow for two-component wind field estimation from single aerosol lidar data," English, *Journal of Atmospheric and Oceanic Technology*, vol. 32, no. 10, pp. 1759–1778, [Online]. Available:
.

[90] L. T. Chang, B. Macdonald, and V. Perez-Mendez, "Axial tomography and three dimensional image reconstruction," *IEEE Transactions on Nuclear Science*, vol. 23, no. 1, pp. 568–572, 1976. DOI: 10.1109/TNS.1976.4328307.

[91] G. Gilabert, G. Lu, and Y. Yan, "Three-dimensional tomographic reconstruction of the luminosity distribution of a combustion flame," *IEEE Transactions on Instrumentation and Measurement*, vol. 56, no. 4, pp. 1300–1306, 2007. DOI: 10.1109/TIM.2007.900161.

[92] X. Yan, H. Li, L. He, D. Li, X. Dai, and X. Zhang, "Acquiring and processing of light field images in a tissue equalent scintillator based on 3d dosimetry," in *2019 IEEE Nuclear Science Symposium and Medical Imaging Conference (NSS/MIC)*, 2019, pp. 1–3. DOI: 10.1109/NSS/MIC42101.2019.9059741.

[93] P. M. Brisley, Gang Lu, Yong Yan, and S. Cornwell, "Three-dimensional temperature measurement of combustion flames using a single monochromatic ccd camera," *IEEE Transactions on Instrumentation and Measurement*, vol. 54, no. 4, pp. 1417–1421, 2005. DOI: 10.1109/TIM.2005.851074.

[94] B. Christophe, *Wavelets and ill posed problems: Optic flow and scattered data interpolation*, 1999.

[95] K. Kohse-Höinghaus, "Quantitative laser-induced fluorescence: Some recent developments in combustion diagnostics," *Applied Physics B*, vol. 50, no. 6, pp. 455–461, 1990, ISSN: 1432-0649. [Online]. Available: https://doi.org/10.1007/BF00408771.

[96] J. M. Fisher, M. E. Smyser, M. N. Slipchenko, S. Roy, and T. R. Meyer, "Burst-mode femtosecond laser electronic excitation tagging for khz–mhz seedless velocimetry," *Opt. Lett.*, vol. 45, no. 2, pp. 335–338, Jan. 2020. DOI: 10.1364/OL.380109. [Online]. Available: http://ol.osa.org/abstract.cfm?URI=ol-45-2-335.

[97] D. J. Fleet, *Measurement of Image Velocity*, eng, 1st ed. 1992., ser. The Springer International Series in Engineering and Computer Science, 169. 1992, ISBN: 0-7923-9198-5.

[98] H. David, *Notes on motion estimation*, 1998. [Online]. Available: http://www.cns.nyu.edu/~david/handouts.motion.pdf.

[99] S. Cai, E. Mémin, P. Dérian, and C. Xu, "Motion Estimation under Location Uncertainty for Turbulent Fluid Flow," *Experiments in Fluids*, pp. 1–17, 2017. [Online]. Available: https://hal.inria.fr/hal-01589642.

[100] M. Sutton, J. Yan, V. Tiwari, H. Schreier, and J. Orteu, "The effect of out-of-plane motion on 2d and 3d digital image correlation measurements," *Optics and Lasers in Engineering*, vol. 46, no. 10, pp. 746–757, 2008, ISSN: 0143-8166. DOI: https://doi.org/10.1016/j.optlaseng.2008.05.005. [Online]. Available: https://www.sciencedirect.com/science/article/pii/S0143816608000985.

[101] F. S. Tardu, "Concomitance of the local spanwise velocity and production in wall turbulence," *Physics of Fluids*, vol. 28, no. 1, p. 015 108, 2016. DOI: 10.1063/1.4939715. eprint: https://doi.org/10.1063/1.4939715. [Online]. Available: https://doi.org/10.1063/1.4939715.

[102] A. M. Ruiz, G. Lacaze, and J. C. Oefelein, "Flow topologies and turbulence scales in a jet-in-cross-flow," *Physics of Fluids*, vol. 27, no. 4, p. 045 101, 2015. DOI: 10.1063/1.4915065. eprint: https://doi.org/10.1063/1.4915065. [Online]. Available: https://doi.org/10.1063/1.4915065.

[103] P. Dérian, P. Héas, C. Herzet, and E. Mémin, "Wavelets and optical flow motion estimation," *Numerical Mathematics: Theory, Methods and Applications*, vol. 6, no. 1, pp. 116–137, 2013, ISSN: 2079-7338. DOI: https://doi.org/10.4208/nmtma.2013.mssvm07. [Online]. Available: .

[104] S. Kadri-Harouna, P. Dérian, P. Héas, and E. Mémin, "Divergence-free wavelets and high order regularization," *International Journal of Computer Vision*, vol. 103, no. 1, pp. 80–99, 2013, ISSN: 1573-1405. [Online]. Available: https://doi.org/10.1007/s11263-012-0595-7.

[105] M. Son, W. Armbruster, J. Hardi, and M. Oschwald, "Measuring the velocity field of a shear-coaxial, cryogenic flame in a high-pressure rocket thrust chamber," *Proceedings of the Combustion Institute*, 2020, ISSN: 1540-7489. [Online]. Available: https://www.sciencedirect.com/science/article/pii/S1540748920305265.

[106] J. Tu, C. Rowley, D. Luchtenburg, S. Brunton, and J. Kutz, "On dynamic mode decomposition: Theory and applications," *Journal of Computational Dynamics*, vol. 1, Nov. 2013.

[107] G. Beylkin, R. Coifman, and V. Rokhlin, "Fast wavelet transforms and numerical algorithms i," eng, *Communications on pure and applied mathematics*, vol. 44, no. 2, pp. 141–183, 1991, ISSN: 0010-3640.

[108] L. K. Su, O. S. Sun, and M. G. Mungal, "Experimental investigation of stabilization mechanisms in turbulent, lifted jet diffusion flames," *Combustion and Flame*, vol. 144, no. 3, pp. 494–512, 2006, ISSN: 0010-2180. [Online]. Available: http://www.sciencedirect.com/science/article/pii/S0010218005002178.

[109] C. S. Yoo, E. S. Richardson, R. Sankaran, and J. H. Chen, "A dns study on the stabilization mechanism of a turbulent lifted ethylene jet flame in highly-heated coflow," *Proceedings of the Combustion Institute*, vol. 33, no. 1, pp. 1619–1627, 2011, ISSN: 1540-7489. [Online]. Available: http://www.sciencedirect.com/science/article/pii/S154074891000310X.

[110] L. M. Pickett, S. Kook, H. Persson, and Ö. Andersson, "Diesel fuel jet lift-off stabilization in the presence of laser-induced plasma ignition," *Proceedings of the Combustion Institute*, vol. 32, no. 2, pp. 2793–2800, 2009, ISSN: 1540-7489. [Online]. Available: http://www.sciencedirect.com/science/article/pii/S1540748908001752.

[111] A. Krisman, E. R. Hawkes, and J. H. Chen, "Two-stage autoignition and edge flames in a high pressure turbulent jet," *Journal of Fluid Mechanics*, vol. 824, pp. 5–41, 2017, ISSN: 0022-1120. DOI: 10.1017/jfm.2017.282. [Online]. Available: https://www.cambridge.org/core/article/twostage-autoignition-and-edge-flames-in-a-high-pressure-turbulent-jet/831AE0D2A1E1290D1C2D6B601949C549.

[112] Y. C. S., R. SANKARAN, and C. J. H., "Three-dimensional direct numerical simulation of a turbulent lifted hydrogen jet flame in heated coflow: Flame stabilization and structure," *Journal of Fluid Mechanics*, vol. 640, pp. 453–481, 2009, ISSN: 0022-1120. DOI: 10.1017/s0022112009991388. [Online]. Available: https://www.cambridge.org/core/article/threedimensional-direct-numerical-simulation-of-a-turbulent-lifted-hydrogen-jet-flame-in-heated-coflow-flame-stabilization-and-structure/F90F81BFEB5324713BC67D3B8A762579.

[113] Z. Luo, C. S. Yoo, E. S. Richardson, J. H. Chen, C. K. Law, and T. Lu, "Chemical explosive mode analysis for a turbulent lifted ethylene jet flame in highly-heated coflow," *Combustion and Flame*, vol. 159, no. 1, pp. 265–274, 2012, ISSN: 0010-2180. [Online]. Available: http://www.sciencedirect.com/science/article/pii/S0010218011001696.

[114] L. T. F., Y. C. S., C. J. H., and L. C. K., "Three-dimensional direct numerical simulation of a turbulent lifted hydrogen jet flame in heated coflow: A chemical explosive mode analysis," *Journal of Fluid Mechanics*, vol. 652, pp. 45–64, 2010, ISSN: 0022-1120. DOI: 10.1017/s002211201000039x. [Online]. Available: https://www.cambridge.org/core/article/threedimensional-direct-numerical-simulation-of-a-turbulent-lifted-hydrogen-jet-flame-in-heated-coflow-a-chemical-explosive-mode-analysis/447BD0E7DA9E1599A9F61786AA62AF79.

[115] S. Lyra, B. Wilde, H. Kolla, J. M. Seitzman, T. C. Lieuwen, and J. H. Chen, "Structure of hydrogen-rich transverse jets in a vitiated turbulent flow," *Combustion and Flame*, vol. 162, no. 4, pp. 1234–1248, 2015, ISSN: 0010-2180. [Online]. Available: http://www.sciencedirect.com/science/article/pii/S0010218014003356.

[116] R. W. Grout, A. Gruber, C. S. Yoo, and J. H. Chen, "Direct numerical simulation of flame stabilization downstream of a transverse fuel jet in cross-flow," *Proceedings of the Combustion Institute*, vol. 33, no. 1, pp. 1629–1637, 2011, ISSN: 1540-7489. [Online]. Available: http://www.sciencedirect.com/science/article/pii/S1540748910000192.

# VITA

Oluwatobi's major research interests are in the area of combustion diagnostics using and developing such techniques for harsh environments. His experience with these techniques includes: Longitudinal magneto optical Kerr effect for monitoring light polarization changes after reflection from a magnetized surface, planar laser induced fluorescence (PLIF) of reacting fuel jets in crossflow for describing their structure and dynamics, a growing interest in femtosecond Coherent Antistokes Raman Scattering (fs-CARS) using decoherence for temperature measurement and Seeded Mie scattering for velocimetry in reacting fuel jets in crossflow, also as a simultaneous technique with Planar LIF.

**Oluwatobi Busari**
West Lafayette, IN | tbusari@purdue.edu
https://www.linkedin.com/in/oluwatobi-busari-768b4318

## EDUCATION

**Purdue University**
Doctor of Philosophy: **Aeronautics and Astronautics** Mar 2021
*Dissertation: Design And Analysis Of A Staged Combustor Featuring A Premixed Transverse Reacting Fuel Jet Injected Into A Vitiated Confined Crossflow*
Master of Science: **Aeronautics and Astronautics** May 2016

**University at Buffalo (SUNY)**
Bachelor of Science: **Aerospace Engineering (Honors College)** Dec 2012
University at Buffalo (SUNY) Magna Cum Laude
Undergraduate Research and Scholarship Award of Distinction (2011/2012)
*Thesis: Analysis of Carbon/Carbon Composites by Thermogravimetry*
Bachelor of Arts: **Physics (Honors College)** Dec 2012
Magna Cum Laude

## SKILLS AND INTERESTS

**Computer**: Matlab | Python | C++ | FORTRAN | LabVIEW | CUDA | Maple | Mathematica (UNIX and Windows OS)
**Research Interests**:
Combustion diagnostics | Laser measurement techniques | Developing laser measurement techniques for harsh environments
**Experience**:

- Longitudinal magneto optical Kerr effect for monitoring light polarization changes after reflection from a magnetized surface.
- Planar laser induced fluorescence of reacting fuel jets in crossflow for describing their structure and dynamics.
- Femtosecond Coherent Anti-stokes Raman Scattering using decoherence for temperature measurement.
- Seeded Mie scattering for velocimetry in reacting fuel jets in crossflow, also as a simultaneous technique with Planar LIF.

## PROJECTS & RESEARCH

**Graduate Research Assistant:** *Fall 2014 – Current*
**Laser diagnostic imaging of fuel jet in vitiated crossflow w. Prof R. Lucht, multi-year project renewed yearly after milestones were met.** *For each phase: Design to extensive hot-fire test matrix of hardware.*

- Progressed through Aerospace Engineering design milestones from conceptual review to critical design review for three manufactured combustor rigs.
- Consulted with machine shops for manufacturability of optically accessible hardware during subsequent project phase.
- Assembled and Instrumented hardware for monitoring and diagnostics.
- Performed hot fire experiments with multiple combustors performing initial emissions map per project phase.
- Performed laser diagnostics non-intrusive experiments with multiple optically accessible combustor rigs per project phase using advanced laser diagnostic techniques for flame imaging and measurement.
- Managed statement of work and cost accounting during project tenure.
- Reported results in academic open literature.

- Collaborated with international colleagues towards applying computer vision techniques to flame images.

**Graduate Research Assistant:** *Current*

***Femtosecond* CARS measurement of temperature and species composition at rocket injector w. Prof R. Lucht**

- Participated in extended setup for representative diagnostics.

**Class Research**

**FTIR analysis of green hypergolic rocket fuel via drop test w. Prof T Pourpoint** *Spring 2015*

*From early phase design to extensive drop-test test matrix of green hypergolic fuels.*

- Assembled cost effective experimental hardware used in obtaining drop test samples for spectrometry.
- Used thorough review of literature to evince measurement limits and room for improvement.
- Performed TEAB-WFNA drop test experiments gaining familiarity with proper PPE and use of a fume hood.
- Measured product species in gaseous effluent using FTIR spectrometer.
- Reported results in academic open literature.

**Design of 3-D printer for hybrid rocket w. Prof T Pourpoint** *Spring 2014*

*From early phase design of printer to hot-fire test of paraffin hybrid rocket grain.*

- Ran 3-D printer software program for hybrid fuel grain with no additives.
- Performed hot-fire experiments with printed grain creating initial performance map.
- Reported results in academic open literature.

## TEACHING

**Graduate Teaching Assistant:** *Fall 2019*

**Hypersonic aerothermodynamics. AAE 51900 (27 students)**

Responsibilities included giving lectures, grading scripts and proctoring exams.

**Thermal Sciences. AAE 33800 (70 students)** *Spring 2020*

Responsibilities included, grading exams and holding office hours creatively during COVID 19 pandemic.

## REFREED PUBLICATION TITLES

- (planned) Characterizing leeward stabilized flush transverse jet flames in vitiated crossflows at high subsonic Mach numbers. AIAA Journal of Propulsion and Power
- (planned) Flame stabilization modes of a reacting fuel jet in confined vitiated crossflow at high subsonic Mach number: Measurement of flame displacement speeds using wavelet optical flow velocimetry. Combustion and Flame Journal
- (planned) Characterizing the distribution of fuel downstream of a premixed-diffusion coannular swirling fuel nozzle using acetone PLIF. Journal of gas turbine and power
- Effect of the nature of vitiated crossflow on the flow-field of a transverse reacting jet Experiments in Fluids 58 (2), 9
- Flame stabilization mechanism in reacting jets in swirling vitiated crossflow Combustion and Flame 207, 302-313
- The development and performance of a perforated plate burner to produce vitiated flow with negligible swirl under engine relevant gas turbine conditions. Review of Scientific Instruments
- NOx reduction in an axially staged gas turbine model combustor through increase in the combustor exit Mach number. Combustion and Flame